UNIVERSITY OF SOUTHAMPTON

FACULTY OF ENGINEERING AND PHYSICAL SCIENCES

Maritime Engineering and Ship Science
Fluid Structure Interactions Research Group

Energy Harvesting Using Ship Motions Applying a Gimballed Pendulum System as an Energy Conversion Mechanism

by

Trewut Anurakpandit

Thesis for the degree of Doctor of Philosophy

April 2019

UNIVERSITY OF SOUTHAMPTON

ABSTRACT

FACULTY OF ENGINEERING AND PHYSICAL SCIENCES
Maritime Engineering and Ship Science
Fluid Structure Interactions Research Group

Doctor of Philosophy

ENERGY HARVESTING USING SHIP MOTIONS APPLYING A GIMBALLED PENDULUM SYSTEM AS AN ENERGY CONVERSION MECHANISM

by Trewut Anurakpandit

This research describes a novel methodology of assessing the mechanical power contributed by the multiple-degree-of-freedom dynamics of a ship in waves concerning the directional responses of the ship oscillatory motions. It is motivated by the limited understanding of the potential use of wave energy harvesting using wave-induced ship motions, and the quantitative assessment of the ship motions energy in the real sea has never been explored. By adopting the seakeeping analysis and the statistical technique as the standard wave spectrum, therefore, the contributed mechanical power of a ship in a sea state can be quantified. It is found that the magnitude of mechanical power of a ship in waves varies proportionally to the ship scale, but the power is contributed by the different dynamic determinants depending on the scale or size of the ship. Importantly, it is also discovered that the number of the involved degree-of-freedoms is able to magnify the mechanical power of a ship in waves that is available to be harvested.

Typically, the wave energy harvesting system onboard a marine vessel is designed to operate in a limited degree-of-freedom. This contrasts to the dynamics of a floating ship in the variance real sea condition as it could lose to potential to harvest more energy. Consequently, the concept of using a multiple-degree-of-freedom system as a 2-axis gimballed pendulum mechanism has recently been introduced. However, its dynamics has never been investigated as a multiple-degree-of-freedom system. Therefore, the research examines the dynamics of a gimballed pendulum system in an aspect of an energy conversion mechanism regarding its directional responses and applies it as an onboard energy conversion mechanism for ship motions energy harvesting.

Moreover, in this thesis, a novel numerical model of a gimballed pendulum system is indicated which is validated by a set of experimental testings of a prototype of a gimballed pendulum energy harvester based on the directional harmonic excitations on a motion simulator. At the sufficient angle, the gimballed pendulum created coupled motions between two referenced pivots. Outside resonance, the coupled motions are small and are found to be beneficial in the simultaneous power generations by the pivots. At resonance, the motions are more significant. Also, the coupling relationships between the two referenced rotational axes become more influential which diminishes the pendulum responses compared to when it performs as a single-degree-of-freedom system at the identical disturbance. This behaviour can be numerical and experimentally confirmed. However, the numerical prediction of the coupled pendulum motions at around resonance has been found to be inaccurate compared to the experiment. This is because of the simplified assumption that is made to form the equations of motion using geometric coupling relationships of two inertial perpendicular pendulum dynamics around two horizontal axes (2-DOF). Yet, with the potential asymmetric inertial properties between the gimballed pivots, the determination of the equations of motion which are included all DOFs is theoretically complex and not straightforward.

Then, the gimballed pendulum system has been applied onboard a ship model as the numerical and experimental investigations have been carried out. Based on the result, it shows that the multiple-degree-of-freedom ship dynamics offers the potential to generate more energy that reflects the simultaneous power generations by the coupled motions of the gimballed pendulum. Also, this proves that the energy harvesting using ship motions applying a gimballed pendulum as an energy conversion mechanism is practicable.

Contents

List of Figures

List of Tables

Declaration of Authorship

I, Trewut Anurakpandit , declare that the thesis entitled *Energy Harvesting Using Ship Motions Applying a Gimballed Pendulum System as an Energy Conversion Mechanism* and the work presented in the thesis are both my own, and have been generated by me as the result of my own original research. I confirm that:

- this work was done wholly or mainly while in candidature for a research degree at this University;
- where any part of this thesis has previously been submitted for a degree or any other qualification at this University or any other institution, this has been clearly stated;
- where I have consulted the published work of others, this is always clearly attributed;
- where I have quoted from the work of others, the source is always given. With the exception of such quotations, this thesis is entirely my own work;
- I have acknowledged all main sources of help;
- where the thesis is based on work done by myself jointly with others, I have made clear exactly what was done by others and what I have contributed myself;
- parts of this work have been published as: Anurakpandit et al. (under review)

Signed:...

Date:..

Acknowledgements

Firstly, I would like to express my sincere gratitude to the Royal Thai Navy, Prof. Philip A. Wilson, and the University of Southampton for this PhD opportunity. Secondly, I would like to extend my thankfulness to both of my supervisors, again, Prof. Philip A Wilson, and Dr. Niclolas C. Townsend for the full support, strong motivation, and extreme guidance throughout this PhD study.

Also, I would like to thank my PhD companions, Dr. James A. Bowker, Dr. Catherine J. Hollyhead, Dr. Rittirong Ariyatanapol, Dr. Prin Kanyoo, Dr. Ponprot Boonpratpai, Dr. Kantapon Tanakitkorn, and many of non-mentions for the aids in the experimental works, academic advices, and invaluable friendships.

Importantly, I would especially like to thank my family including my girlfriend, Saritsana Witoonchat, for the endless encouragement, inspiration, understanding, and support in every aspect of my life.

Abbreviations

1-D	One- or Single-Dimensional
2-D	Two-Dimensional
3-D	Three-Dimensional
ASV	Autonomous Surface Vehicle
AUV	Autonomous Underwater Vehicle
AWS	Archimedes Wave Swing
BEM	Boundary Element Method
CCC	Complex Conjugate Control
CFD	Computational Fluid Dynamics
CG	Centre of Gravity
CW	Capture Width
DC	Direct Current
DEG	Dielectric Elastomer Generator
DOF	Degree-of-Freedom
FLEUR	Flapping Energy Utilisation and Recovery
HFRU	Human Factors Research Unit
IMU	Inertial Measurement Unit
ISVR	Institute of Sound and Vibration Research
ITTC	International Towing Tank Conference
JONSWAP	Joint North Sea Wave Project
LCG	Longitudinal Centre of Gravity
LIMPET	Land Installed Marine Power Energy Transmitter
MEMS	Micro-Electro-Mechanical-System
ODE	Ordinary Differential Equation
OTEC	Ocean Thermal Energy Conversion
OWC	Oscillating Water Column
PTO	Power Take-Off
RAO	Response Amplitude Operator
RMS	Root-Mean-Square
RPM	Revolutions per Minute
SD	Standard Deviation
SEAKERS	SEA Kinetic Energy Recovery System

SSG	Sea Slot-Cone Generator
SWL	Still Water Level
TAPCHAN	Tapered Channel Wave Power Plant
TF	Transfer Function
USV	Unmanned Surface Vehicle
VCG	Vertical Centre of Gravity
WDPS	Wave Devouring Propulsion System
WEC	Wave Energy Conversion
WITT	Whatever Input to Torque Transfer

Nomenclature

a_{ij}	Hydrodynamic mass or inertia coefficient matrix
a'_{ij}	Sectional added mass
A_{WP}	Waterplane area
b	Wave crest width
b_{ij}	Hydrodynamic damping coefficient matrix
b'_{ij}	Sectional damping coefficient
B_{OA}	Ship beam overall
B_{WL}	Ship waterline beam
c	Wave celerity or phase velocity
c_g	Group velocity
c_{ij}	Hydrostatic restoring coefficient matrix
c'_{ij}	Sectional hydrostatic restoring force or moment
C_B	Block coefficient
CW	Capture width
d	Ship draft
D	Ship moulded depth
E_k	Kinetic energy transmitted in one wave length
E_p	Potential energy transmitted in one wave length
E_w	Total energy transmitted in one wave length
E_{w/m^2}	Wave energy per unit wave area
f_3	Sectional Froude-Krylov force
F_{coulomb}	Coulomb friction component
F_e	External force
F_i	Sum of forces or moments in direction i
F_{h_i}	Hydromechanical forces or moments in direction i
F_{H_i}	Horizontal force referenced to generalised coordinate i
$F_{mech,z}$	Force of heave motion created by a ship in waves
F_s	Static friction force
F_{viscous}	Viscous friction force component
F_{V_i}	Vertical force referenced to generalised coordinate i
F_{w_i}	Wave exciting force or moment in direction i
F_{wa_i}	Wave exciting force or moment amplitude in direction i

g	Acceleration due to gravity or gravitational constant
G	Centre of gravity of a ship
GM_T	Transverse metacentric height
h	Water depth
h_i	Vertical distance of pendulum mass referenced to generalised coordinate i
h_3	Sectional diffraction force
H	Wave height
$H_{1/3}$	Significant wave height
$\bar{H}_{1/3}$	Average significant wave height
I_{WP}	Second moment of area about transverse axis at centre of gravity
I_{xx}	Moment of inertia about x-axis
I_{yy}	Moment of inertia about y-axis
I_{zz}	Moment of inertia about z-axis
k	Wave number
$\bar{k}$	Average wave number
$k_{n,i}$	Speed constant of generator referenced to generalised coordinate i
k_{xx}	Radian of gyration about x-axis
k_{yy}	Radian of gyration about y-axis
k_{zz}	Radian of gyration about z-axis
KE	Kinetic energy
l_p	Pendulum length
L	Lagrangian
L_a	Mutual inductance
L_{OA}	Ship overall length
L_{WL}	Ship waterline length
m	Pendulum mass
m_{ij}	Solid mass and inertia matrix of a ship
m_p	Pendulum mass
m_{θ_p}	Pendulum mass on θ_p-plane reference
m_{ϕ_p}	Pendulum mass on ϕ_p-plane reference
M_{WP}	First moment of area about transverse axis at centre of gravity
n_i	Driven speed at generator referenced to generalised coordinate i
P_E	Ship effective power
P_i	Generated power referenced to generalised coordinate i
$P_{mech,i}$	Mechanical power generated by i motion
P_{total}	Total generated power
P_w	Total wave power transmitted in one wave length
$P_{w/m}$	Wave power per unit wave crest
$\bar{P}_{w/m}$	Average wave power per unit wave crest
PE	Potential energy
Q_i	Generalised force or torque referenced to generalised coordinate i

R	Dimension ratio or scaling factor
R_{Load}	Load resistance
$R_{Terminal}$	Terminal resistance
S_{r_i}	Motion energy or response spectrum of i motion
$S_{P_{mech,i}}$	Response mechanical power spectrum of i motion
S_α	Wave slope spectrum
$S_{\alpha,ITTC}$	ITTC wave slope spectrum
$S_{\alpha,JONS}$	JONSWAP wave slope spectrum
S_ζ	Wave energy spectrum or spectral ordinate
$S_{\zeta,ITTC}$	ITTC two-parameter wave energy spectrum
$S_{\zeta,JONS}$	JONSWAP wave energy spectrum
t	Time
T	Wave period
$\bar{T}$	Average wave period
T_e	Period of encounter or encountering period
T_p	Peak period
$\bar{T}_p$	Average peak period
T_z	Zero crossing period
$\bar{T}_z$	Average zero crossing period
T_*	Natural period of oscillation
TF_i	Transfer function of i motion
u_i	Gear ratio of gear head referenced to generalised coordinate i
U	Ship speed
v	Velocity component
v_i	Velocity referenced to generalised coordinate i
$\mathbf{v}_i$	Velocity vector in i direction
V_i	Induced voltage referenced to generalised coordinate i
VCG	Vertical centre of gravity of a ship
x	Surge displacement of a ship
x_a	Surge motion amplitude of a ship
$\dot{x}$	Surge velocity of a ship
$\ddot{x}$	Surge acceleration of a ship
$\ddot{x}_j$	Linear or angular acceleration of a ship in direction j
X_B	Position of moving based
$X_\circ$	Base excitation amplitude
X_p	Excitation amplitude at pendulum pivot along x_p-axis
$\dot{X}_p$	Excitation velocity at pendulum pivot along x_p-axis
$\ddot{X}_p$	Excitation acceleration at pendulum pivot along x_p-axis
y	Sway displacement of a ship
y_a	Sway motion amplitude of a ship
$\dot{y}$	Sway velocity of a ship

$\ddot{y}$	Sway acceleration of a ship
$\hat{y}$	Sectional outward normal unit vector in y-direction
Y_p	Excitation amplitude at pendulum pivot along y_p-axis
$\dot{Y}_p$	Excitation velocity at pendulum pivot along y_p-axis
$\ddot{Y}_p$	Excitation acceleration at pendulum pivot along y_p-axis
z	Heave displacement of a ship
z_a	Heave motion amplitude of a ship
$\dot{z}$	Heave velocity of a ship
$\dot{z}_a$	Heave velocity amplitude of a ship
$\ddot{z}$	Heave acceleration of a ship
$\ddot{z}_a$	Heave acceleration amplitude of a ship
$\hat{z}$	Sectional outward normal unit vector in z-direction
Z_p	Excitation amplitude at pendulum pivot along z_p-axis
$\dot{Z}_p$	Excitation velocity at pendulum pivot along z_p-axis
$\ddot{Z}_p$	Excitation acceleration at pendulum pivot along z_p-axis
α	Wave slope at the water's surface
α_a	Wave slope amplitude
Δ	Ship displacement weight
ε_i	Phase lag of force or moment in direction i
$\eta_{P_w,i}$	Wave power conversion efficiency of i motion
ξ	Longitudinal distance from longitudinal centre of gravity of a ship hull
ξ_i	Damping ratio referenced to generalised coordinate i
ζ	Wave elevation or profile at the water's surface
ζ_a	Wave amplitude
θ	Pitch angular displacement of a ship
θ_a	Pitch angular motion amplitude of a ship
θ_p	Pendulum angular displacement on θ_p-plane
$\dot{\theta}$	Pitch angular velocity of a ship
$\dot{\theta}_a$	Pitch angular velocity amplitude of a ship
$\dot{\theta}_p$	Pendulum angular velocity on θ_p-plane
$\ddot{\theta}$	Pitch angular acceleration of a ship
$\ddot{\theta}_a$	Pitch angular acceleration amplitude of a ship
$\ddot{\theta}_p$	Pendulum angular acceleration on θ_p-plane
λ	Wavelength
$\bar{\lambda}$	Average wavelength
μ	Heading angle relative to wave or excitation direction
ρ	Mass density of water
$\tau_{\mathrm{coulomb,i}}$	Frictional torque referenced to generalised coordinate i
$\tau_{mech,\theta}$	Torque created by pitch motion of a ship in waves
$\tau_{mech,\phi}$	Torque created by roll motion of a ship in waves
ϕ	Roll angular displacement of a ship

ϕ_a	Roll angular motion amplitude of a ship
ϕ_p	Pendulum angular displacement on ϕ_p-plane
$\dot{\phi}$	Roll angular velocity of a ship
$\dot{\phi}_a$	Roll angular velocity amplitude of a ship
$\dot{\phi}_p$	Pendulum angular velocity on ϕp-plane
$\ddot{\phi}$	Roll angular acceleration of a ship
$\ddot{\phi}_a$	Roll angular acceleration amplitude of a ship
$\ddot{\phi}_p$	Pendulum angular acceleration on ϕp-plane
ϕ_{30}	Amplitude of 2-D velocity potential of the section in heave
ψ	Yaw angular displacement of a ship
ψ_a	Yaw angular motion amplitude of a ship
ψ_p	Pendulum angular displacement on polar coordinate around vertical axis
$\dot{\psi}$	Yaw angular velocity of a ship
$\dot{\psi}_p$	Pendulum angular velocity on polar coordinate around vertical axis
$\ddot{\psi}$	Yaw angular acceleration of a ship
$\ddot{\psi}_p$	Pendulum angular acceleration on polar coordinate around vertical axis
ω	Circular wave frequency
$\bar{\omega}$	Average circular wave frequency
ω_e	Encountering frequency
$\omega_{n,p}$	Natural frequency of a pendulum
$\omega_{n,i}$	Natural frequency of a pendulum referenced to generalised coordinate i
ω_*	Oscillation frequency
ω_{*4}	Natural frequency of roll motion
∇	Ship displacement volume

Chapter 1

Introduction

1.1 Research Background

With the depletion and the impact on the environment from the use of conventional energy resources such as fuel oil and coal, seeking clean and sustainable energy sources is a necessity nowadays. In fact, various of clean, natural energy sources that have been harvested and utilised, for example, solar, wind, tidal, and wave energies.

Solar energy can be considered as the most promising source of renewable energy, which is influenced by the reduction in the technology costs annually (IEA, 2014). REN21 (2017) claims that, during 2016, more than 31,000 solar panels were installed worldwide in every hour with current development aiming to reduce the environmental impact during the cell making process. For wind energy, with the cost-effective in power generation, the technology status is not so different from the level of the development of that the solar energy (Edelstein et al., 2003). A number of wind farms can be seen in many countries around the world (Hernández et al., 2017). The present research based on utilising wind energy is aiming to improve wind forecasting for a better energy management strategy (National Grid, 2006) and to reduce the initial cost through the advancement of the materials (Sun et al., 2012). Moreover, the technology status of tidal energy can also be considered as well-developed even it is limited to the location where the tidal range is sufficient (Bryden et al., 2007). The current development of this technology is focused on optimising performance through the design with the aid of the present advanced computational tool (Gebreslassie et al., 2013, 2015). However, in comparison to that of the wave, the development of wave energy technology is somewhat behind those prior examples mostly as demonstration projects (REN21, 2012).

For the potential resource, ocean waves are reported to contain energy density of approximately 2-3 kW/m^2 over an area perpendicular to the wave propagation greater than the energy densities of solar (0.1-0.3 kW/m^2 of a horizontal area) and wind (0.5

kW/m^2 of an square area of the wind direction) energies (Falnes, 2007). Besides, other report claims that that wave energy could globally offer 2 kW/m of the wave crest for 90% of the year (Zheng et al., 2014). Moreover, wave energy is indicated to be the most conspicuous form of clean energy (McCormick, 2007).

Regarding the attractive property, however, the utilisation of ocean waves energy can be considered as unsuccessful with the several main concepts, i.e., overtopping, oscillating water column, and oscillating body system (Falcão, 2010; Levitan, 2014). Typically, this is because of the massive operating cost to maintain WEC systems including the cost of installation, survivability, and energy transfer from the location where the energy is created generally in the offshore site (Como et al., 2015; Xu, 2005). Besides, most of the introduced techniques are designed to operate in an idealistic condition that is in a limited degree-of-freedom (DOF). This contrasts to the variance of the sea surface which is the combination of wave height, period, and direction. Although a concept to harvest energy from random wave condition using a multiple-DOF pendulum with gimballed pivots has been introduced by WITT Energy Ltd. (2018), its dynamics and performance as a multiple-DOF system have never been theoretically and experimentally investigated. Therefore, to overcome the limitations and to fulfil the knowledge gap of the uninvestigated WEC system are still major challenges to improve the development status of wave energy utilisation.

1.2 Motivation

The dynamics of a ship at sea is the result of the interaction between the vessel and ambient wave condition. Hence, it can be stated that a ship moving in waves is directly related to ocean waves energy. Besides, utilising wave energy onboard a sea-going ship could eliminate the cost of transferring energy to the shore as it will be locally consumed where it is generated. Furthermore, when considering the potential amount of energy contributed by waves reported by numerous studies (e.g. Brooke (2003); Burman and Walker (2009); Falnes (2007); Muetze and Vining (2006); Zheng et al. (2014)), discovering the means to utilise this energy for a ship in a seaway might be one of the ways to increase the potential use and development status of wave energy utilisation.

However, the understanding of the potential use of the wave energy harvesting using ship motions is limited, and the quantitative assessment of ship motions energy in the real sea state has never been explored. The work presented in this thesis, therefore, firstly focuses on the theoretical investigation of a ship dynamics in waves leading to the assessment of the available energy or power from ship multiple-DOF dynamics in a seaway based on seakeeping analysis. Secondly, this research also focuses on the investigation of the passive dynamics of a multiple-DOF energy conversion mechanism, a gimballed pendulum system, and apply this concept to ship motions energy harvesting application.

Moreover, it should be emphasised that the level of wave power absorption of interest in this research represents a small fraction of the ideal limit of the absorbed power for a particular motion. This is because of there is no performance optimisation technique applied. As can be seen from Figure 1.1, the absolute performance limit of an oscillating body in waves provided by Falnes (2007) shows the limit absorbed power that is bounded to the area under the ideal performance curves (solid lines). The two dashed curves within the ideal limit represent the examples of the wave power absorption level of a spherical shape heaving buoy with (the upper dashed curve) and without (the lower dashed curve) applying performance control optimisation algorithm latching or phase control in this case).

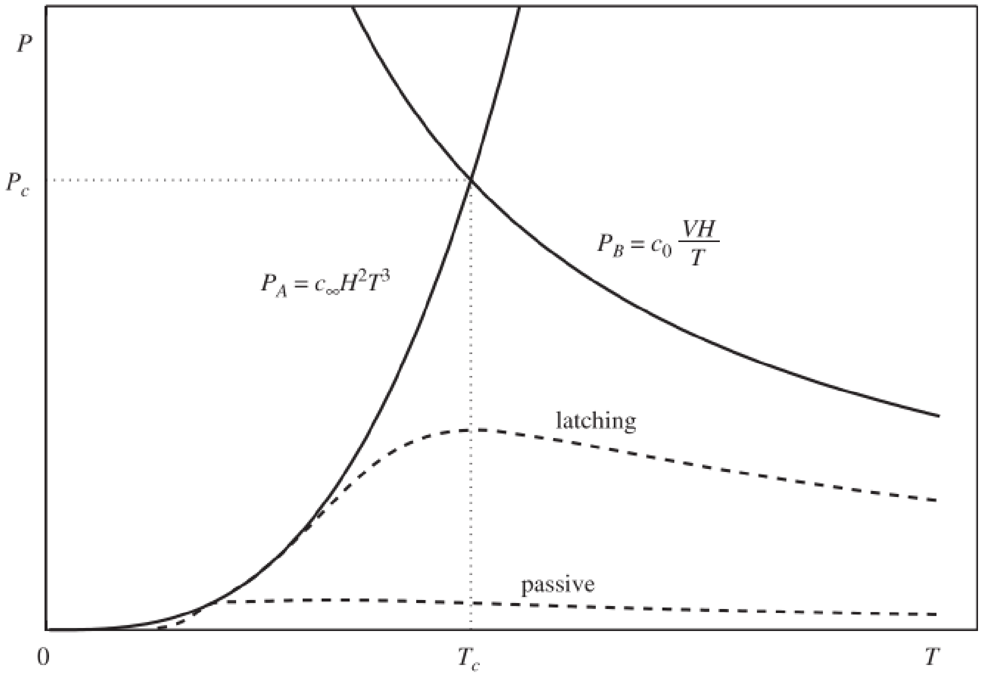

Figure 1.1: Absolute performance limit of an oscillating body wave energy converter in waves by Falnes (2007).

1.3 Aim and Objectives

The aim of this research is to investigate energy harvesting using ship motions applying a gimballed pendulum as an energy conversion mechanism. In this case, the research scope can be related to, first, the assessment of the potential available energy or power of ship motions in waves. Second, the investigation of the passive dynamics of a gimballed pendulum as an energy conversion system. Third, the investigation of the energy harvesting using a gimballed pendulum induced by multiple-DOF ship dynamics in waves.

To achieve the aim, the required objectives are identified as:

- Defining a method of assessing available power from ship motions in a seaway based on seakeeping analysis.
- Understanding the passive dynamics of a gimballed pendulum system as an energy harvester and developing a numerical model that is able to simulate the pendulum motion which is validated by experimental investigation.
- Developing a numerical model of the coupled ship and onboard energy harvester validating by experimental testing.

1.4 Structure of the Thesis

Chapter 2 provides a review of previous research regarding wave energy conversion (WEC) technologies and the technologies or techniques that have been applied to marine vessel application.

Chapter 3 details a theoretical overview of the numerical treatment of both regular and irregular waves and the dynamics of a ship in the waves.

Chapter 4 presents a numerical analysis of assessing the available mechanical power of ship motions with consideration of the ship directional responses in sea state.

Chapter 5 indicates a numerical modelling and experimental validation/investigation of a gimballed pendulum system in an aspect of an energy conversion mechanism with the concern of directional responses.

Chapter 6 demonstrates an numerical modelling of the dynamics of a ship and an onboard gimballed pendulum energy harvester with a set of wave tank experiments aiming to validate the numerical model.

Chapter 7 discusses the key areas that are identified in this research.

Chapter 8 summarises the key outcomes and recommended areas for future research.

Chapter 2

Literature Review

This chapter reviews the general concepts of WEC techniques and technologies that have been researched and developed to the present day. The review details the categorisation of these developed techniques based on the working principles of how they convert wave energy into the useful forms. Then, the WEC techniques that have been applied to marine vehicle application are critically described and discussed.

2.1 Wave Energy Conversion Technologies

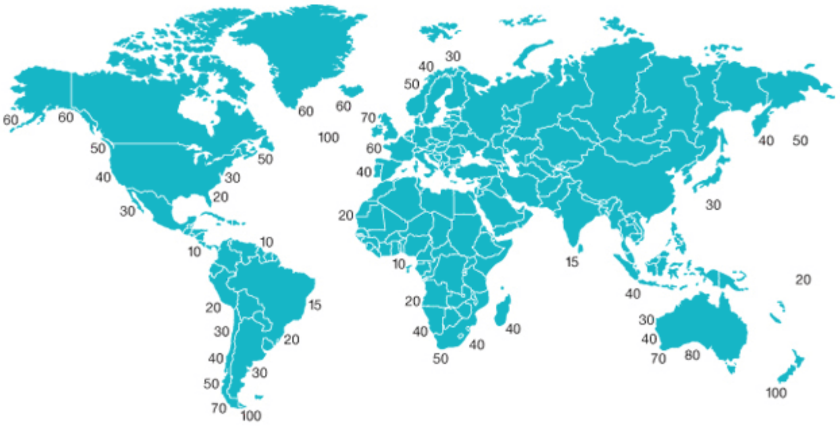

Figure 2.1: The global average annual wave power levels (kW/m) of the wave front on locations over the world's oceans (Ocean Power Technologies Inc.).

Despite the fact that there are many renewable energy resources (e.g., solar, wind, ocean current, tidal, thermal, and wave energies) available on the ocean for maritime domain, energy from waves with over 70 per cent covered the earth's surface has a massive potential (Burman and Walker, 2009). Regarding energy density, ocean waves provide 15-20 times more energy per square metre than solar or wind energy (Muetze and Vining, 2006). Thus, it might not be erroneous to declare that the ocean is the biggest energy storage on earth. Figure 2.1 shows the average annual wave power levels of the wavefront over the world's oceans with the approximated power of 2 TW available to be harvested and utilised (Ocean Power Technologies Inc.; Drew et al., 2009). Moreover, it is estimated that ocean wave energy could cover 40 per cent of the global electric power generation (Rahm, 2010).

In this research, a ship moving in waves is considered as a type of WEC system. Motions of a ship are induced by experiencing or incoming waves, and the ship simultaneously absorbs energy from the waves. To convert the wave energy via motions of a ship, understanding the existing WEC techniques is essential. The WEC techniques that have been developed so far generally have different principles of operations such as deployed locations, energy transfer and PTO methods as well as structural related. A number of works (e.g. Brooke (2003); Burman and Walker (2009); Cheung and Childress (2007); Drew et al. (2009); Falcão (2010); Khan and Bhuyan (2009); Lagoun et al. (2010); McCormick (2007); Muetze and Vining (2006); Multon (2012); Rodrigues (2008); Thorpe (1999)) suggest the categorisations of these WEC systems. In summary, three main WEC types have been classified in common as presented in Figure 2.2.

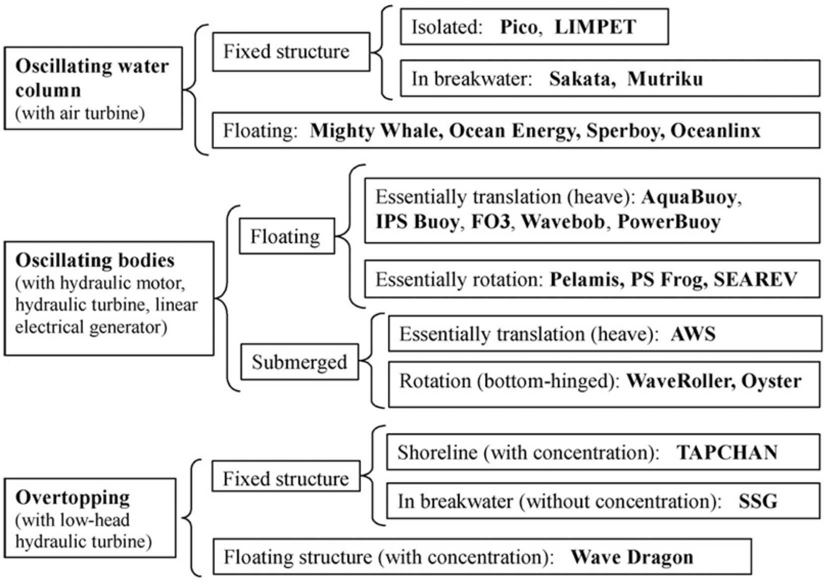

Figure 2.2: The classification of WEC technologies (Falcão, 2010).

2.1.1 Overtopping System

This WEC technique can be compared to the hydroelectric system as both convert the potential energy from the water stored at a higher level referenced to the PTO unit (Brooke, 2003). This WEC system is normally consisted of overtopping ramp, reservoir, and low-head axial flow turbine as illustrated in Figure 2.3. As waves are allowed to spill via ramp and store onto reservoir elevated from the mean water level, the energy in the

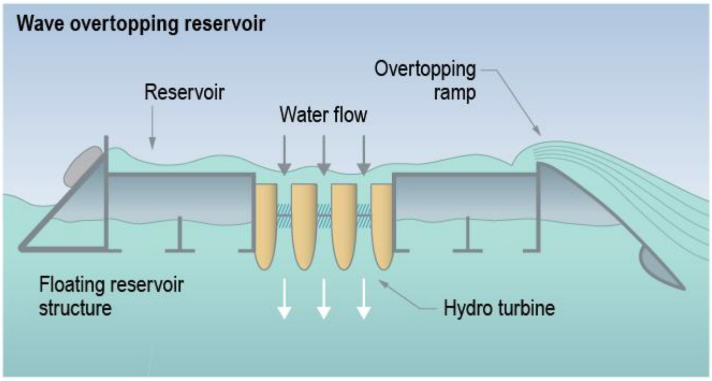

Figure 2.3: Schematic drawing of overtopping WEC system (Como et al., 2015).

form of potential energy is converted by low-head turbine once the water flows back to the ocean and simultaneously drive the turbine which is coupled to the electric generator. This reservoir-filled energy conversion concept has been developed as fixed and floating structures (Falcão, 2014; Rahm, 2010). Theoretically, there is no wave-induced motion related to the energy generation by this WEC concept (Como et al., 2015).

Although various projects and prototypes of overtopping WEC system, for instance, Tapered Channel (TAPCHAN) wave power plant (Evans and Falcão, 1986), Wave Dragon device (Falcão, 2010), Sea Slot-Cone Generator (SSG) project (Margheritini et al., 2007) etc., have been emerged, they still remain at the development stages.

2.1.2 Oscillating Water Column System

Oscillating water column (OWC) or cavity resonance wave energy converter is considered as the first generation of modern WEC system regarding the prototypes of Masuda (1971, 1979). Similar to the previous technique, this WEC system appears in both fixed and

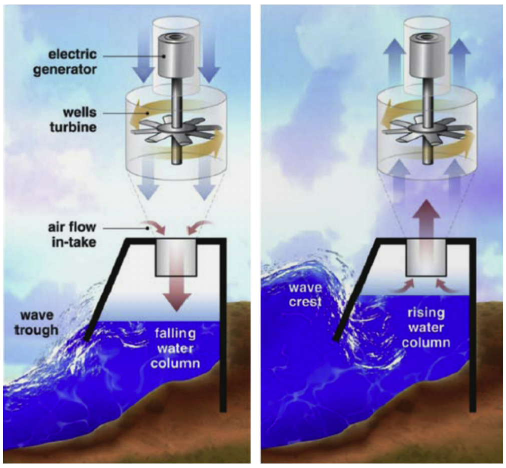

Figure 2.4: Schematic drawing of the working principle of oscillating water column system (Fadaeenejad et al., 2014).

floating applications. The main structure of this WEC system is partially submerged with opened-bottom chamber placed below the mean water level and PTO unit at the top-end. As illustrated in Figure 2.4, the approaching and retreating waves cause the water oscillation inside the chamber (water column) pressuring the internal air which is utilised to drive the PTO unit (Heath, 2012). Several projects and prototypes have been deployed, tested, and some commercialised in many locations around the world such as Oceanlinx project (Oceanlinx Ltd), LIMPET (The Queen's University of Belfast, 2002), Pico (Wave Energy Centre (WavEC), 2006), and a ship-like OWC prototype called as 'Mighty Whale' (Washio et al., 2001). It should be highlighted that, to maximise the energy conversion efficiency, the geometry of OWC must be designed to match the local ocean climate concerning wave height and wavelength characteristics where the system is deployed (Muetze and Vining, 2006).

Typically, this pneumatic system employs an air turbine connected to an electric generator as an energy conversion mechanism as the 'Wells' turbine (see Figure 2.4), an axial flow single-directional rotation turbine, is the most commonly used (Falcão, 2010). However, air turbine is not the only possible energy conversion technique for OWC system. A concept of smart material has been applied to this OWC system as PTO unit so-called 'Dielectric Elastomer Generator (DEG)' as presented in Figure 2.5. This dielectric elastomer is able to convert mechanical energy (from pneumatic pressure in this case) to electrical energy by its deformation, reducing thickness by expansion (Koh et al., 2011). Papini et al. (2013) and Vertechy et al. (2013) performed the numerical simulations of the dynamic of DEG-based OWC system. Furthermore, the study of Vertechy and Fontana (2015) carried out an experimental validation of the previous works using a floating OWC collector with DE membrane PTO unit in a wave tank. Besides, they also claimed that this PTO technique for OWC has the advantages over the typical design as it has a large energy density, fewer step of energy conversion, silent operation, and low maintained cost.

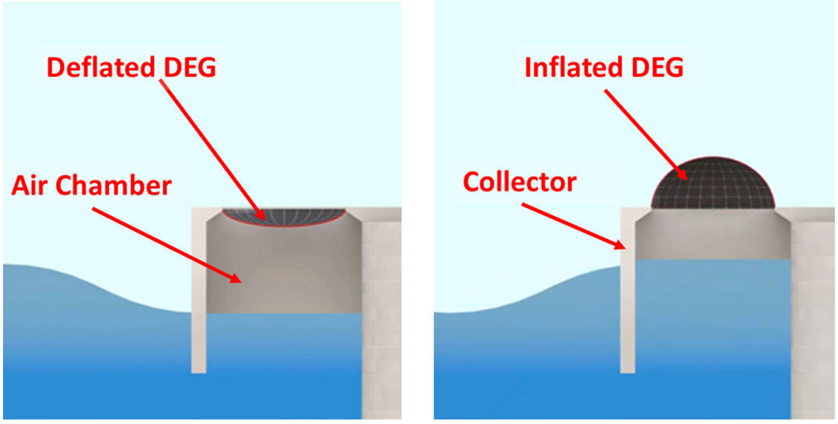

Figure 2.5: Graphical drawing of dielectric elastomer generator for OWC system (Vertechy et al., 2013).

2.1.3 Oscillating Body System

Oscillating body energy harvesting system is a typical energy conversion technique regarding many applications and types of energy conversion mechanism. This technique utilised relative motions between moving host and mounted PTO mechanism to generate the useful form of energy. The classic application for this energy conversion method can be referred to the portable self-winding or rotating-mass device, see Figure 2.6, powered by vibration source as human motion (Romero-Ramirez, 2010; Watkins, 2013; Xie et al., 2009; Yeatman, 2008; Zhu, 2011). Moreover, the energy harvesting for high-frequency machinery vibration can also be referred to this oscillating body system (Priya and Inman, 2009).

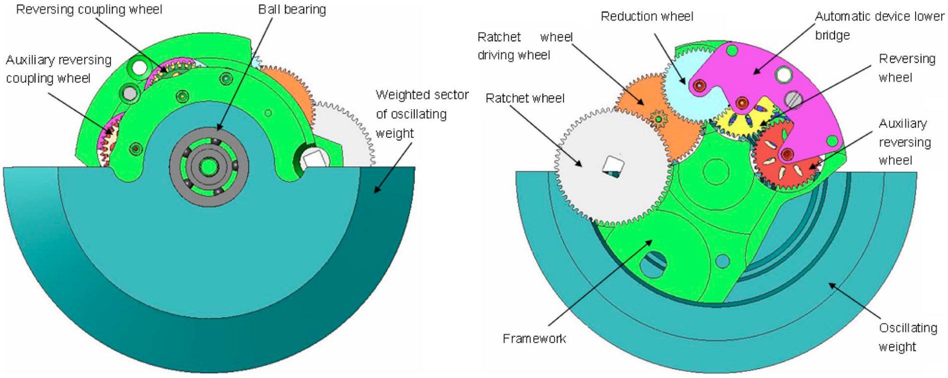

(a) Front view. (b) Back view.

Figure 2.6: The typical design of automatic winding device (Xie et al., 2009).

For WEC application, a body moving in waves is considered as a host body energised by the surrounding waves. Due to the dynamics of a body in waves can be related to a combination of motions regarding degree-of-freedom (DOF), types of wave-induced motion have been utilised to generate energy.

Heave motion is one of the options. Various designs of heaving WEC have been developed. Generally, the concepts converting vertical translational motion can be related to two designs, one-body and two-body heaving systems (Falcão, 2010). First, the one-body heaving system is the most straightforward oscillating body system converting a heaving body on the wave surface against a fixed part at the seabed. The upper buoy or moving part is allowed to vertically move along the waves and drive PTO unit, linear generator or hydraulic pump, at the bottom part via cable as can be seen in Figure 2.7(a) (Waters et al., 2007; Waters, 2008). Next, the two-body heaving system is utilised where the distance between free-surface and seafloor is high or in the deepwater region. The relative motions of two attached bodies, usually floating buoy and submerged body, are used to convert to useful energy as illustrated in Figure 2.7(b) (Falcão, 2010).

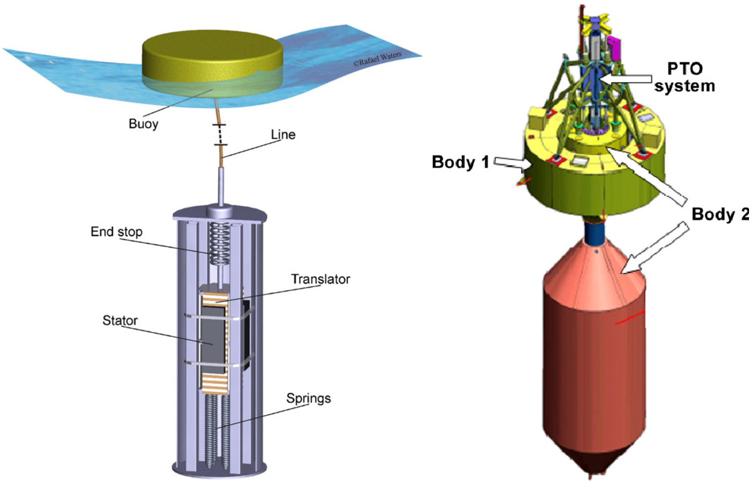

(a) One-body heaving system. (b) Two-body heaving system.

Figure 2.7: Examples of heaving buoy WEC system (Falcão, 2010).

Another option for WEC design is the usage of rotational motion of a floating body. This oscillating body system ideally moves (pitch or roll depending on the definition of designed orientation) along the direction of incident waves. Typically, this type of WEC devices mainly consists of a floating host which is enclosed entirely with an internal PTO mechanism. Therefore, the system is not exposed to the water and harsh environment. The first simple technique to be introduced is the sliding mass type WEC device. The concept of sliding mass energy harvesting is a very intimated concept as the self-rechargeable shaking flashlight is a comparable one (Yan and Wang, 2007). For the linear-sliding mass type, it comes with the similar PTO method, the direct-drive linear generator, to the mentioned heaving body system. McCabe et al. (2006) introduced an offshore pitching WEC device called as 'PS Frog Mk 5' presented in Figure 2.8. The PS Frog Mk 5 is a paddle shape point absorber that produces electrical energy by utilising the relative motions between wave induced pitch motion of the host and a linear-sliding mass generator. However, this sliding-mass PTO unit is allowed to move along a guided

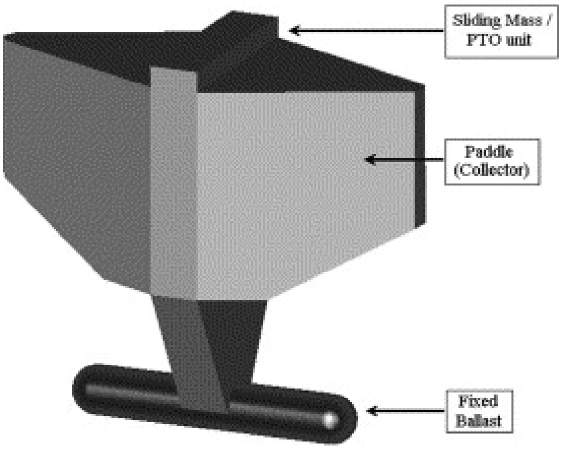

Figure 2.8: The graphical drawing of the PS Frog Mk 5 by McCabe et al. (2006).

path, so there is only one possibility to capture the wave energy in a single direction. Besides, the PTO mass could create undesirable sound and vibration when it hits the end-stop at both sides; as a result, this could be a problem in scaling issue.

Alternatively, to avoid the end-stop issue, a circular-sliding mass system has been suggested. Chen and DelBalzo (2013a,b) proposed a theoretical model of a WEC device with a sealed circular-path sliding mass PTO mechanism. They adopted the wave-induced pitch/roll motion of a buoy to excite the tracked mass which rotates responding to gravity. This PTO technique is modelled to operate as a horizontal-plane pendulum that is mounted to a gearbox and generator as shown in Figure 2.9. Clearly, the guided circular motion is able to eliminate the end-stop problem for the PTO mass and also increase the possibility to generate energy from multiple or random wave direction (Chen and DelBalzo, 2013b).

Nevertheless, regarding the system arrangement, optimum wave slope and frequency are required for the WEC device to maintain continuous circular motion of the PTO mass. Also, zero energy production can be expected under pure heave condition. Furthermore, the performance of this WEC system is only simulated as a 2-D model under the ideal condition as it has never been built and tested as a physical prototype. Hence, the actual performance operating in real sea conditions or even in a controlled environment in a laboratory is doubtful.

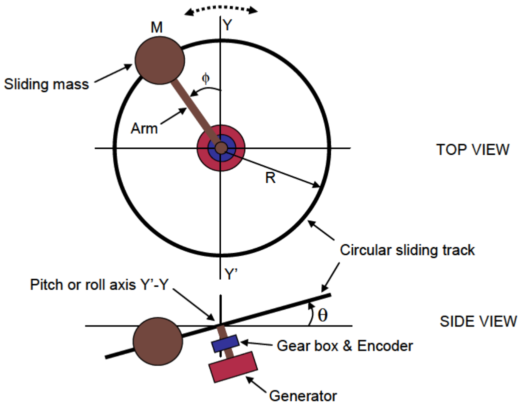

(a) Design layout.

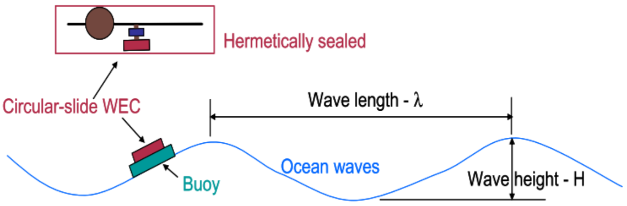

(b) The opearational basis.

Figure 2.9: The general design of the circular sliding-mass WEC device (Chen and DelBalzo, 2013a,b).

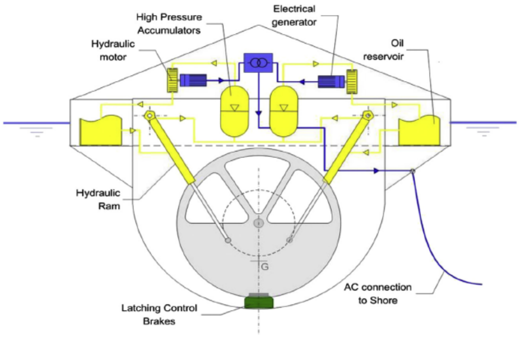

Figure 2.10: Schematic arrangement of the SEAREV G1 and internal components (Cordonnier et al., 2015).

One of the simplest mechanical arrangement PTO concepts for oscillating body energy harvesting system utilising rotational motion can be attributed to pendulum-like or vertical-plane rotating mass (similar to the example in Figure 2.6). Fundamentally, this mechanical arrangement is comparable to the previous technique regarding principal components, and it is not restricted in angular displacement around its pivot point. In discrepancy, for non-to-low damping case, a simple pendulum always oscillates about (for harmonic excitation) and rests at (for non-disturbance) its equilibrium position. Therefore, it could provide better balancing on such a floating WEC device. A floating WEC device called the ‘SEAREV[1] G1’ is a an example for pitching body system using vertical-plane pendulum PTO mechanism. The concept design of the SEAREV was numerically developed and then built as a model-scaled prototype in France 2006 (Durand et al., 2007) as can be seen in Figures 2.10 and 2.11. Its PTO components in a chain of the hydraulic system are driven by an unbalanced heavy disk or a compound pendulum that moves followed the response of the enclosed host (Ruellan et al., 2010). Later, Cordonnier et al. (2015) has presented a study of the second- and third generations of the SEAREV called as ‘SEAREV G21’ and ‘SEAREV G3’. The theoretical and experimental of this studies show that the performance of the device can be improved by optimising the hull shape to minimise slamming and waves breaking effects causing the loss of energy.

Figure 2.11: The prototype of the SEAREV G1 (Durand et al., 2007).

---

[1] SEAREV is an abbreviation of the French term, *Système Electrique Autonome de Récupération de l’Energie des Vagues* (autonomous electric wave energy recovery system) (Cordonnier et al., 2015).

Besides, this vertical-plane pendulum energy conversion mechanism also appears in the research of Crowley et al. (2013, 2014). They combined the ideas of the pendulum principle and pneumatic application to their PTO system which is numerically applied to the WEC device called the 'Bristol Cylinder' theoretically developed by Clare et al. (1982); Evans et al. (1979). The modified Bristol Cylinder is designed to be moored to the seabed and lie parallel to wavefront which allows the cylinder to surge and roll. In this way, the internal pendulum mass will rotate and circulate the air inside the cylinder which drives the PTO unit, an air turbine. Obviously, both examples of WEC designs have the similar limitation in responsive DOF to generate energy constrained by a fixed reference plane of rotation of simple pendulum energy conversion technique.

Figure 2.12: The prototype of the WITT device (WITT Energy Ltd., 2018).

In general, the excitation from the surrounding environment as ocean waves is not always unidirectional. Therefore, to design a system to operate in the limited responsive condition as a 1-DOF system like a simple pendulum might not be sufficient. In this regard, a mechanism is known as '2-axis gimbals' has been applied to a vertical pendulum system to enhance multiple-DOF responsiveness. This mechanical arrangement allows a pendulum mass to rotate respecting the perpendicular horizontal pivots thus spherical or orbital rotation can be achieved. Likewise, the WITT (Whatever Input to Toque Transfer) device, see Figure 2.12, introduced by WITT Energy Ltd. (2018) is a prototype of a gimballed energy harvesting device designed for converting energy from random disturbance vibration. Also, this device can transmit its spherical rotation into unidirectional output via a gearbox mechanism connected at the pivots. Further, the theoretical and experimental works to investigate the feasibility of using the WITT device for WEC has been conducted by Crowley et al. (2018). In this work, however, the device is treated and analysed as a 1-DOF pendulum WEC system. So, the dynamics of the mechanical design as a multiple- or coupled-DOF energy conversion performance is uninvestigated and hypothetical.

Figure 2.13: The graphical design of the nodding Duck (Taylor, 2009).

In addition, the utilisation of gyroscopic moment, or gyroscopic generator, is another option that has been adapted into energy scavenging and WEC applications. This type of energy conversion technique generates energy by using the torque produced by the gyroscopic effect of a spinning mass and input rotational excitation. For energy scavenging from the miniature vibrating system, Yeatman (2006, 2008) theoretically suggested a potential implementation of a gyroscopic generator for micro-electro-mechanical-system (MEMS) with the advantage over the typical linear displacement energy conversion mechanism as there is no limit in angular motion. This leads to the possibility to increase the amount of energy production, but the minimised level of internal drag is necessarily required. For WEC, a famous design of pitching body WEC device generating energy by gyroscopic effect, the Salter's Duck, as shown in Figure 2.13 introduced by Stephen Salter from the University of Edinburgh (Salter, 1974). Moreover, Kanki et al. (2009) deployed and tested several prototypes of the gyroscopic moment WEC system in coastal regions in Japan, see one example in Figure 2.14. The results show that it is practical to generate energy from gyroscopic moment but, importantly, the gyroscopic generator also requires electrical power to drive the mass and maintain the effect thus the net of the generated power output is marginally reduced. To be highlighted, the presented examples of gyroscopic effect WEC system are designed to operate in a single directional wave condition.

Figure 2.14: The gyroscopic moment WEC system by Kanki et al. (2009).

Note that, the relative motions between the multi-body system on waves, i.e. the Pelamis, has also been used by converting the torque at the joints of the bodies via hydraulic motors. (Henderson, 2006). Additionally, the fully-submerged oscillating body WEC systems such as Archimedes Wave Swing (AWS), WaveRoller, and Oyster are also the alternative techniques. These designs use the fluctuation of the water pressure under the wave to create relative motion reference to a fixed point at the seabed and drive PTO unit (AW-Energy Oy, 2018; Cameron et al., 2010; Falcão, 2010).

2.1.4 Wave Energy Conversion Control Fundamentals for Power Take-off System

The main objective of a WEC system is to generate the maximum power from the dynamic behaviour of the WEC at a given circumstance. As most of power production by vibration system as WEC devices happens during resonant oscillation in which the excitation force by waves is in phase with the device velocity (Falnes, 2002; Ringwood et al., 2014). However, sea waves are made up of a spectrum of frequencies. Therefore, in order to alter the system dynamics to achieve resonance, a control strategy as feedback control is required (Coe et al., 2017).

The simplest fundamental of the control technique for PTO system can be referred to as ‘resistive damping control’. In this control strategy, the value of PTO damping will be tuned proportional to gain at a particular exciting condition to achieve the optimal damping constant that provides a lower bound power absorption rate. Theoretically, this can be performed in the time-domain model of a particular motion of a 1WEC system (Coe et al., 2017).

For an upper limit representation of the power production performance of a wave device, a technique called ‘complex conjugate control (CCC)’ strategy is typically employed (Falnes, 2002). The maximum useful power or optimal power absorption rate can be obtained by setting the intrinsic impedance of the PTO system equals to the complex conjugate of the incoming short term waves (Ringwood et al., 2014). This can be derived from the frequency-domain force-to-velocity model of a WEC system (Coe et al., 2017; Falnes, 2002; Ringwood et al., 2014). However, with the physical constraints such as the displacement limit of PTO mechanism and the irregularity of sea state, a numerical optimisation algorithm is essentially needed. Ringwood et al. (2014) provides an example of a control structure for WEC system as illustrated in Figure 2.15. The optimal velocity profile is calculated in the upper branch of the structure and fed to the controller (servo) to control the PTO force to achieve the optimal set point.

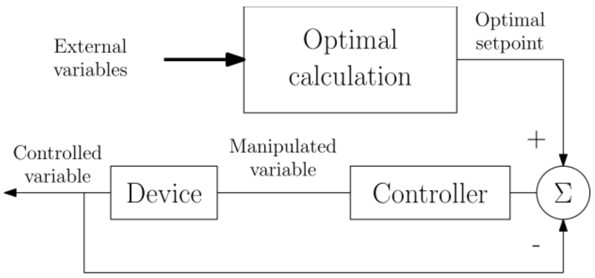

Figure 2.15: Control structure for WEC system by Ringwood et al. (2014).

2.1.5 Wave Energy Conversion Technologies Review Summary

The review of the existing WEC technologies has identified the principles of how wave energy is converted. In the interest of this research, the remarked summary from the review can be listed as:

- Fixed structure WEC systems (fixed structure overtopping and OWC systems) only appear in shoreline WEC application.
- Floating structure overtopping WEC system do not gain benefit from the wave-induced motion of the host in energy conversion process due to it only converts potential energy from the falling water from the higher level by axial flow low-head turbine. So, it can be dismissed from this research.
- Two types of energy conversion system that have been applied to the OWC system:
  - Air turbine based; Well turbine.
  - Material based; DEG.
- The dynamics of the pneumatic application based on floating OWC system are coupled between floating structure (water column) and internal fluid inside the column.
- Types of energy conversion mechanism for floating oscillating body WEC system can be summarised as:
  - Linear-sliding mass system.
  - Circular-sliding mass or horizontal-plane pendulum system.
  - Vertical-plane pendulum mass system.
  - Gyroscopic moment generator.
- The working principle of fully-submerged oscillating body WECs are treated as irrelevant to this research.

2.2 Wave Energy Conversion for Marine Vehicles

To compare with the WEC system, a ship or marine vehicle moving in waves always associates with wave energy regarding a combination of motions or DOFs. The concepts of using wave energy for the sea-going vessels can be grouped into two main categories, wave-assist propulsion system and wave energy recovering for onboard power generation. The prior listed category, the wave-assist propulsion system, has been well developed as the extension of the wave devouring propulsion system (WDPS) or flapping foil technology which is normally activated by wave-induced heave and pitch motions of a surface vehicle (Bowker, 2018). In recent years, its success reflected in various of commercial maritime autonomous system programmes (e.g. Wave Glider (Liquid Robotics Inc., 2018), AutoNaut (AutoNaut Ltd., 2018)).

The wave energy recovering for onboard power generation for a marine vessel, on the other hand, is still at the development stage. Following the concept of the WDPS, Bowker et al. (2015, 2016) have evaluated the potential of using submerged flapping foils for a wave energy recovery onboard autonomous surface vehicle (ASV). They performed experimental investigations of a system called as ‘Flapping Energy Utilisation and Recovery (FLEUR)’. The purpose of the system was to use the relative motions between the ASV and the submerged foils in power generation mode which can be used to recover the energy from wave induced motion, see Figure 2.16.

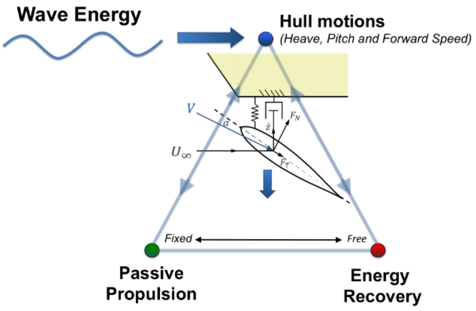

(a) The working principle.

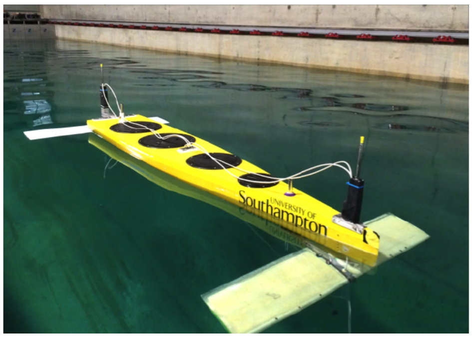

(b) The prototype.

Figure 2.16: The Flapping Energy Utilisation and Recovery (FLEUR) by Bowker et al. (2016).

Figure 2.17: The water quality monitorin USV with an onboard pendulum energy harvester by Toh et al. (2011).

For other concepts for marine vessels, a number of recent researches have focused on single-DOF energy conversion systems. For instance, Mitcheson et al. (2011) and Toh et al. (2011) introduced a prototype of a motion energy conversion system for water quality monitoring unmanned surface vehicle (USV), in Figure 2.17, aiming to provide electrical power support for the more extended mission deployment. This onboard energy harvester is a simple pendulum system as shown in Figure 2.18 that is designed to purely harness energy from the roll motion of the vessel. During oscillation due to wave-induced motion, the pendulum directly drives the rotary direct current (DC) generators by a tracked pinion. This system has been tested both in laboratory and field experiments. In the controlled environment, the pendulum was tested with a set of simulated motions over a frequency range with an applied frequency tuning technique. In the field test, the USV with the onboard pendulum was launched into the open sea. The average power generation of 0.3 mW was recorded during the test. According to the design, however, this 1-DOF pendulum system is reported to be limited to a specific angular displacement level (Kaphengst et al., 2012; Toh et al., 2011).

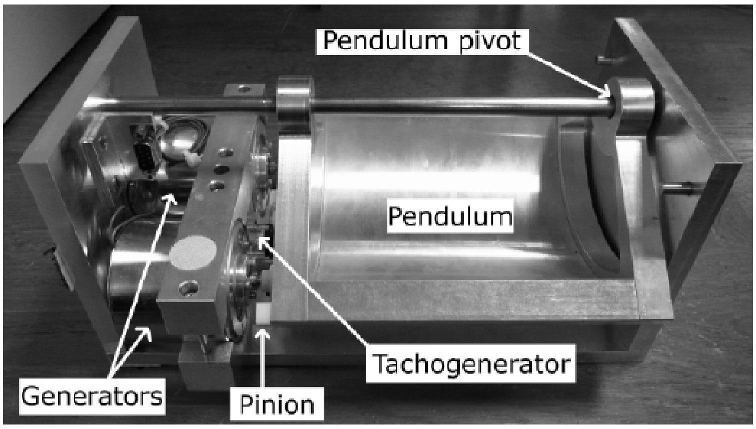

Figure 2.18: The prototype of the inertia pendulum energy harvester (Kaphengst et al., 2012; Toh et al., 2011).

Karami and Inman (2012) suggested a theoretical design of a hybrid rotary-translational energy harvester as shown in Figure 2.19(a). The energy is created by the magnetic tip passes over the electromagnetic coils. The advantage of that this device is able to generate energy from the combination of translational and rotational excitations is claimed in their literature. Besides, the simulated results show that the system performs a periodic response to low-frequency ambient oscillation. However, the response of the device to translational and rotational motions are modelled separately. Later on, Yerrapragada et al. (2017) have applied this concept to their physical prototype as can be seen in Figure 2.19(b). The pendulum-like prototype was installed on a three-quarter-metre ship model and tested in a wave tank in head waves condition with the power generation of 4.7 mW is reported. Noticeably, even the system is claimed to be operated in the combination of translation and rotational ambient vibration, the system itself is a 1-DOF. Also, the concept of this design can be compared to the horizontal pendulum based or circular sliding-mass WEC system in Figure 2.9.

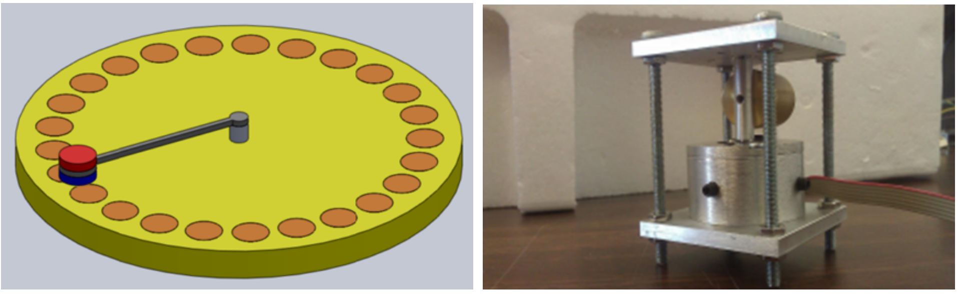

(a) Theoretical design. (b) Physical design.

Figure 2.19: The hybrid rotary-translational vibration energy harvester (Karami and Inman, 2012; Yerrapragada et al., 2017).

Another pendulum energy harvesting device for ship motion application is designed by Lu et al. (2011) called as 'eccentric disk generator'. Potentially, this design is comparable to the previous example by Karami and Inman (2012) with the similar main components (magnetic rotor and wired coils), but it is intended to operate on an only vertical plane. For the initial work, the numerical model of this device has been validated by experimental testing on a test rig which creates translational harmonic oscillation. Then, Wang and Hao (2014) theoretically applied this eccentric disk concept to harvest energy from the roll motion of a ship. Based on their ship characteristics in this work, a 185-metre cargo ship (42,184 tonnes) was selected. The investigated roll motion of the ship is investigated under regular waves condition with motion amplitude of 7° at 0.2 Hz. Therefore, the size of this pendulum based device becomes relatively large, 15.2 m of the pendulum arm length, in order to guarantee the occurrence of the pendulum response. The simulated power production is estimated to produce 2.3 W which is very low comparing to the scale of the investigated ship.

Townsend and Shenoi (2012, 2013, 2016) conducted numerical studies of a wave energy recovery system using gyroscopic precession for marine vessels. By utilising wave-induced rotational motion, the gyro system can create relative motion that is used to generate energy. Their study theoretically shows that gyroscopic system can be used as motion stabiliser and onboard power regeneration. They also stated that, as the gyro is internally installed, there is no direct exposure to the harsh marine environment and it does not create any additional drag to the host vessel. However, as stated earlier, this type of system requires power management and recharging strategies to achieve positive power out in power generation mode. Also, the investigation was proposed based on a chosen DOF excitation condition of a 2-metre torpedo-shape AUV. In wave tank test experiment, the gyroscopic generator achieved a maximum of 8 W power generation with negative net gain from pitch motion of the AUV at stationary with 0.01 m wave amplitude (Townsend, 2016).

For a speculated concept, Sharon et al. (2011) have published an idea of using a 50-metre boat connected to outboard heaving buoys for WEC application as presented in Figure 2.20. Based on the detail in this publication, the study mainly focuses on assessing the feasibility of deploying this energy harvesting idea in the economic point of view. In terms of the system dynamics, the initial development of the numerical model is insisted to be formed as a heaving WEC system while the other techniques to investigate its behaviour such as computational fluid dynamics (CFD) and wave tank experiment are mentioned. Nevertheless, there is no technical detail or result provided. Therefore, the realisation of the system as the dynamics of a ship in waves subjecting to energy harvesting aspect is unclear. Moreover, from the naval architect point of view, the outboard heaving buoys could add a major drag to the ship.

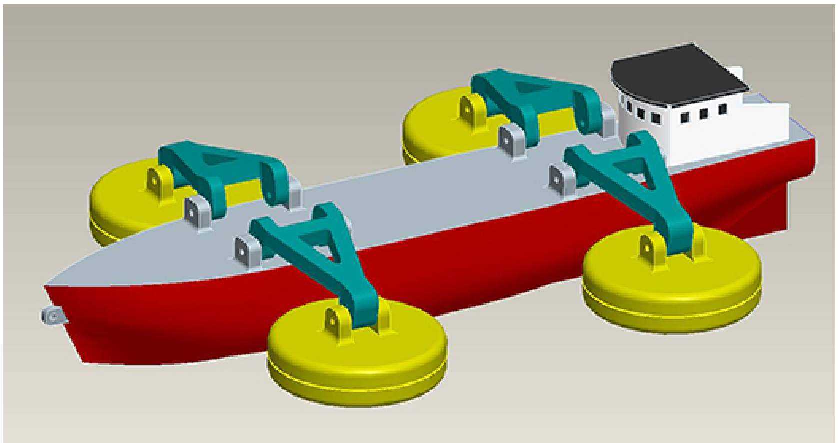

Figure 2.20: Mobile wave energy harvesting system by Sharon et al. (2011).

2.2.1 Wave Energy Conversion for Marine Vehicles Review Summary

A ship or marine vessel in seaway can be considered as an oscillating body in waves. However, wave energy utilisation for marine vehicles has been well developed only as wave-assist propulsion system using flapping wave foil. The level of development for this type of system reflects the number of projects in the private sector or the commercialised technologies (AutoNaut Ltd., 2018; Liquid Robotics Inc., 2018). This system also subjects to the research of potential use of the flapping foil as an onboard wave power recovery system (Bowker et al., 2015, 2016; Bowker, 2018).

For the other developing approaches based on the reviewed literature, the energy conversion techniques for marine vehicles that have been theoretically and physically applied as energy harvesting system can be compared to the existing oscillating WEC systems. These WEC concepts for marine vessels and the utilised motion can be summarised as:

- Onboard system:
    - Onboard system does not create additional drag to the host body or, in this case, ship and it could prevent damage by the marine environment as it is internally installed.
    - The onboard WEC systems for marine vehicles are mainly designed to utilise 1-DOF wave-induced rotational motion, roll or pitch, of the vessels to excite the systems (Kaphengst et al., 2012; Karami and Inman, 2012; Lu et al., 2011; Mitcheson et al., 2011; Toh et al., 2011; Townsend and Shenoi, 2012, 2013, 2016; Townsend, 2016; Wang and Hao, 2014; Yerrapragada et al., 2017).
    - Most of the WEC for marine vessels are potentially 1-DOF pendulum systems (Kaphengst et al., 2012; Karami and Inman, 2012; Lu et al., 2011; Mitcheson et al., 2011; Toh et al., 2011; Yerrapragada et al., 2017). These pendulum systems do not require input power to operate as their responses depend on excitation frequency.
    - The gyroscopic generator for the AUV proposed by Townsend and Shenoi (2012, 2013, 2016); Townsend (2016) requires input power to maintain the gyroscopic effect. Based on the reports, positive power generations were not achieved.
- Outboard system:
    - Outboard system potentially creates major drag.
    - The design introduced by Sharon et al. (2011), the outboard heaving buoys, is theoretically modelled as a individual heaving buoy with the unclear utilising ship motion provided.

2.3 Concluding Remarks and Scope of Research

The review of previous research has identified areas that have not been focused on and investigated. Based on the related literature, it can be summarised that

- Most of the studies generally focus on applying various designs of WEC system onboard marine vessels. Also, the understanding of the coupled dynamics between the vessel body and the onboard energy harvesting system of these systems are yielded by either numerical and experimental investigations.
- The on-going researches mainly design and model energy conversion system for a marine vehicle as 1-DOF.
- As the dynamics of a ship in waves is considered as a multiple-DOF system, however, there is no research evidence of assessing the potential energy or power level of using the associated motions.
- The multiple-DOF energy conversion system as the gimballed pendulum has never been investigated and applied onboard a ship.

Within the scope of this research, the following points are considered to be essentially importance, and are addressed in this thesis:

- Ship dynamics in waves as an aspect of WEC system:
    - A method to theoretically assess and quantify the available mechanical power created by multiple-DOF ship dynamics in waves.
- Multiple-DOF energy conversion system (a gimballed pendulum system):
    - A concept design of a gimballed pendulum energy harvester.
    - A method to model, understand and predict the dynamics of a multiple-DOF system, a gimballed pendulum, in the aspect of energy conversion mechanism which can be done through numerical and experimental investigation.
- The feasibility of energy harvesting using multiple-DOF ship dynamics in waves applying a gimballed pendulum as an energy conversion mechanism:
    - A method to model, understand and predict the dynamics of the coupled ship and onboard gimballed pendulum system which can be done through numerical and experimental investigation.

Chapter 3

Numerical Modelling of Ship Dynamics in Waves

This chapter describes the theories that are used to numerically model the dynamics of a ship in seaway. First, the referenced coordinate systems of a ship in waves used throughout this research are detailed. Next, the simplified mathematical approach of explaining the ideal wave characteristics as regular or linear wave theory and the statistical techniques for analysing the variation of actual sea or irregular waves are described. Furthermore, the equations that govern the motions of a ship in both regular and irregular waves called as seakeeping theory are lastly stated.

3.1 Frames of Reference

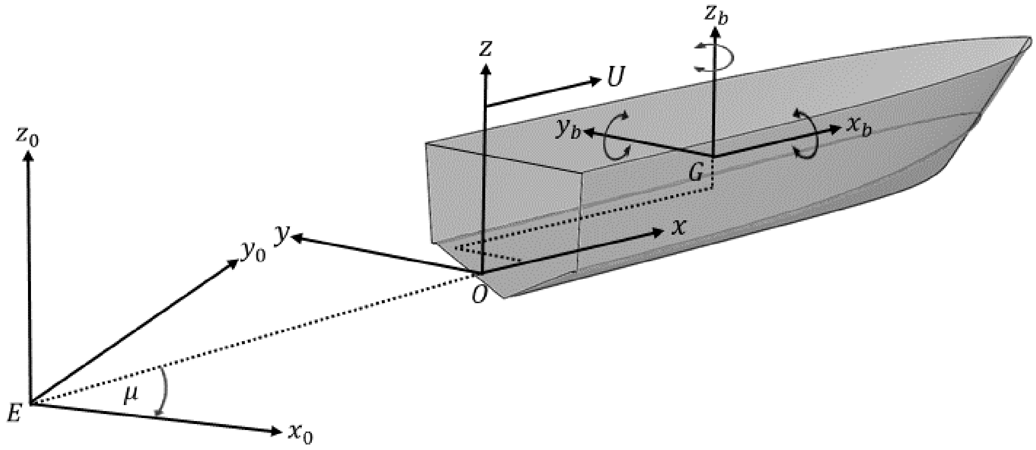

Figure 3.1: Referenced coordinate systems of a ship in a seaway.

At a particular ship's track, a ship is treated as a rigid body in 3-D space. The centre of gravity (G) of the ship is a referenced point relating to three right-handed orthogonal coordinates, see Figure 3.1, detailed as:

- **Earth-fixed** or **global** coordinate ($E(x_0, y_0, z_0)$): The horizontal plane of this coordinate system lies on the still water level (SWL). x_0 positive is in the direction of wave propagation with the angle (μ) relative to the steadily translating coordinate system ($O(x, y, z)$) or heading angle of the ship.
- **Body-fixed** or **local** coordinate ($G(x_b, y_b, z_b)$): The original point of this system is located in the centre of gravity of the ship (G). At still water condition, this coordinate system is parallel to the still water surface.
- **Steadily Translating** coordinate ($O(x, y, z)$): The point O lies on the mean water level and moves along the vector Sx with the ship speed (U, m/s). The coordinates $O(x, y, z)$ and $G(x_b, y_b, z_b)$ are in the same alignment if the ship is at zero speed condition. In addition, at particular sea stage, the position of the ship's centre of gravity (G) oscillates around the origin of this coordinate system (O).

3.2 Wave Theory

Ocean waves are generated by the linked natural phenomena. As the sun transfers energy via sunshine to the surface of the earth, the temperature differences of the heated air creates the movement of the air so called 'winds'. Then, the blowing winds over the ocean's surface establish small waves. Over times, these small waves are energised by the others natural effects (e.g., a resonant effect from the blowing winds and seismic disturbances) which induce them to grow and move away from where they are generated (McCormick, 2007). Finally, when the moving waves reach shallow water area, the shape of the waves will change with increased amplitude and decreased speed. Then, they start to break due to the lost of stability and the friction from the shallower seafloor (Hagerman, 1995; von Sydow, 2014) as illustrated in Figure 3.2.

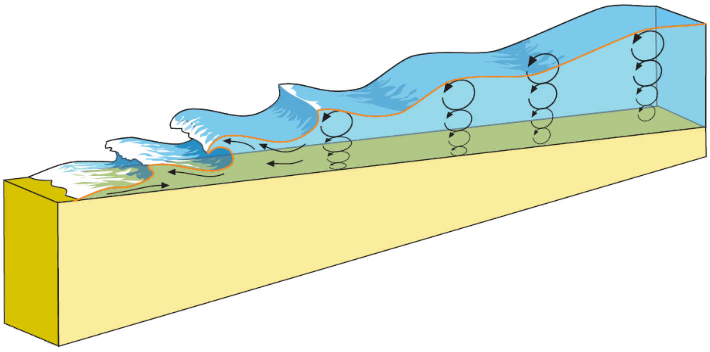

Figure 3.2: An illustration of ocean waves generation (Aqua-RET, 2012).

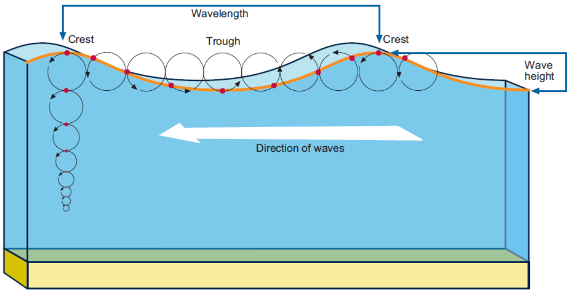

Figure 3.3: Regular wave profile (Aqua-RET, 2012).

Ocean waves can be categorised into two basic types. The first is so called ‘swell’. This type of wave is the waves that travels away from the storm area. The individual wave profile of the swell has round crest with relatively great wavelength, small height and it can be considered as a regular wave as shown in Figure 3.3. Next, so called ‘sea’, is the waves with various heights, periods that travel in different directions as it can be referred to sea stage or irregular waves. The sea can be theoretically considered as the combination or superposition of a number of different regular waves. Both of the ocean waves types are detailed and discussed in this section.

3.2.1 Regular Wave

Regular or linear wave theory is widely used to mathematically model a wave travelling along a referenced space with a constant wave amplitude and frequency or a progressive wave. This theory provides excellent accuracy in predicting the kinematic properties of waves for the condition of a wave height to wave length ratio (H/λ) of 1/50 or less. Figure 3.4 shows the configuration of a progressive wave definition. The coordinate system for a progressive wave can be referred to the earth-fixed or global coordinate detailed in Section 3.1. The water depth (h) is noted to be negative below the SWL. For the depth to wave length ratio (h/λ) more than half of the wave length, $h/\lambda > 1/2$ or $\lambda/h < 2$, the wave is considered as ‘deep water wave’ as it is not influenced by seabed. Unless, for $h/\lambda < 1/20$ or $\lambda/h > 20$, the wave is assumed to be ‘shallow water wave’ which seabed has great influence to its overall characteristics (Holthuijsen, 2007; Journée and Massie, 2001; Lloyd, 1989; McCormick, 2007). Note that, the assumption of deep water wave is used in all of the wave analyses in this research.

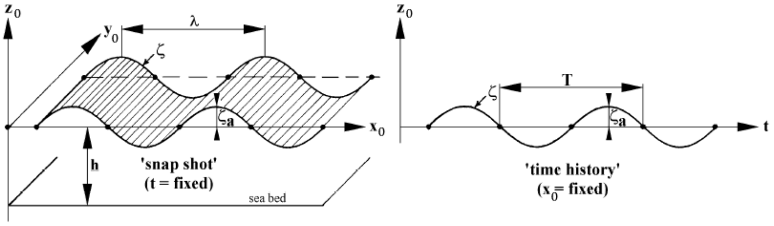

Figure 3.4: Regular or linear wave definition (Journée and Massie, 2001).

The wave height (H, m) is the vertical distance from wave trough to wave crest and it is twice to the wave amplitude (ζ_a, m). So, the wave height mathematically is

$$H = 2\zeta_a. \tag{3.1}$$

Furthermore, the wavelength (λ, m) is measured from the distance of the two successive wave crest and the wave period (T, s) is the distance lying on time axis that a wave travel in one cycle. In terms of angular argument, they can be expressed in the relationships as:

$$k\lambda = 2\pi \quad \text{or} \quad k = \frac{2\pi}{\lambda} \tag{3.2}$$

$$\omega T = 2\pi \quad \text{or} \quad \omega = \frac{2\pi}{T} \tag{3.3}$$

where k is the wave number (rad/m) and ω is the circular wave frequency (rad/s). Also, the wave celerity or phase velocity (c, m/s) of individual travelling waves is described as:

$$c = \frac{\lambda}{T} = \frac{gT}{2\pi}\tanh(kh) \tag{3.4}$$

and the relationship between the circular wave frequency (ω) and the wave number is

$$\omega^2 = kg\tanh(kh) \tag{3.5}$$

as the relationship is called ‘dispersion relation’ and, in case of deep water ($\tanh(kh) \approx 1$), Equation 3.5 becomes

$$\omega^2 = kg \quad \text{or} \quad \omega = \sqrt{kg}. \tag{3.6}$$

So, when waves move in the positive x_0-direction according to Figure 3.4, the waves elevation or profile (ζ, m) at the water’s surface in deep water region can be represented as:

$$\zeta(t) = \zeta_a \cos(kx - \omega t) \tag{3.7}$$

and the wave slope (α, rad) at the surface is

$$\alpha(t) = \alpha_a \cos(kx - \omega t) \tag{3.8}$$

where the frequency-dependant wave slope amplitude (α_a, rad) is

$$\alpha_a = k\zeta_a \tag{3.9}$$

as the maximum wave slope occurs when the wave elevation or surface depression is zero and vice versa.

Energy and Power in Regular Wave

The standard mathematical expression for the total energy (E_w, J) in a regular wave can be expressed (see Journée and Massie (2001) or Lloyd (1989) for the derivation) as:

$$E_w = E_k + E_p = \frac{\rho g H^2 \lambda b}{8} \tag{3.10}$$

where E_k and E_p are the kinetic and potential energies (J) transmitted in one wave length, ρ is the mass density of water (kg/m^3), and b is the width of the wave crest (m). The total energy transmitted in a wave is normally presented in the wave energy transmitted per unit area (E_{w/m^2}, J/m^2); that is

$$E_{w/m^2} = \frac{E_w}{\lambda b} = \frac{\rho g H^2}{8}. \tag{3.11}$$

Then, the total wave power transmitted in a wave (P_w, W) can be calculated as:

$$P_w = \frac{\rho g H^2 c_g b}{8} \tag{3.12}$$

as it is normally presented as the wave power per unit wave crest or wave front ($P_{w/m}$, W/m) which is

$$P_{w/m} = \frac{P_w}{b} = \frac{\rho g H^2 c_g}{8} \quad \text{or} \quad P_{w/\mathrm{m}} = c_g E_{w/\mathrm{m}^2} \tag{3.13}$$

where c_g is the group velocity (m/s^2) which is

$$c_g = \frac{c}{2}\left(1 + \frac{2kh}{\sinh(2kh)}\right). \tag{3.14}$$

For a deep water wave ($2kh/\sinh(2kh) \approx 0$), Equation 3.14 becomes

$$c_g = \frac{c}{2}. \tag{3.15}$$

As can be seen from Equation 3.13, the total wave power per unit wave front is proportional to the wave height squared and the group velocity as the later is related to wavelength or wave frequency detailed in Equation 3.4. Therefore, from the deep water approximation, Equation 3.13 can be expressed as:

$$P_{w/m} = \frac{\rho g^2}{32\pi} H_{1/3}^2 T. \tag{3.16}$$

It should be noted that Equation 3.24 provides the upper limit or peak of the magnitude of the total wave power. So, the average wave power per wave front of a sea area can be estimated as:

$$\bar{P}_{w/m} = \frac{\rho g^2}{64\pi} \bar{H}_{1/3}^2 \bar{T}. \tag{3.17}$$

Additionally, Equation 3.17 is sometimes estimated as $\frac{1}{2}\bar{H}_{1/3}^2\bar{T}$ (kW/m) (Brooke, 2003; Faizal et al., 2014; Rodrigues, 2008).

3.2.2 Irregular Wave

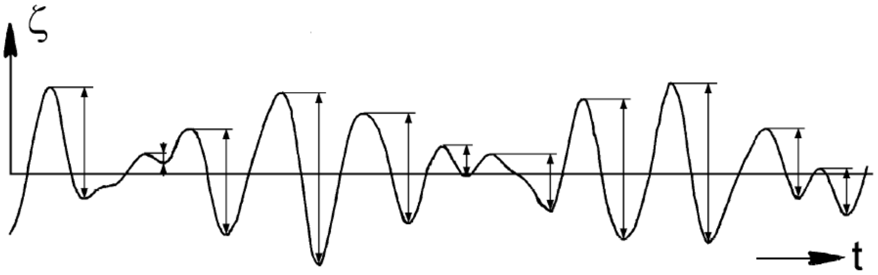

Figure 3.5: Example of waves record in real sea (Journée and Massie, 2001).

The waves in the middle of the ocean, especially in storm and windy regions, are normally observed to be random and irregular as an example of the real sea waves record presented in Figure 3.5. The generated sea waves are theoretically considered as the sum of the random variation in wave height, period, and direction. To determine the ocean waves condition, the standard statistical methods or spectral analysis techniques can be used with the wave record in a particular sea area (Bhattacharyya, 1978; Holthuijsen, 2007; Journée and Massie, 2001; Lloyd, 1989; McCormick, 2007, 2010).

For fully developed or open sea area, waves are typically modelled using the 'Bretschneider' or often called 'ITTC two-parameter' wave energy spectrum ($S_{\zeta,ITTC}$, $\mathrm{m}^2/(\mathrm{rad/s})$) which is defined as:

$$S_{\zeta,ITTC}(\omega) = 172.75\frac{\bar{H}_{1/3}^2}{\bar{T}^4}\omega^{-5}\exp\left(\frac{-691}{\bar{T}^4}\omega^{-4}\right) \tag{3.18}$$

where $\bar{H}_{1/3}$ is the average significant wave height (m) which the significant wave height ($H_{1/3}$, m) is defined as the mean value of the highest 1/3 of the waves record and $\bar{T}$ is the average wave period (s) which is related to the average zero crossing period ($\bar{T}_z$, s); that is

$$\bar{T}_z = \frac{1.296}{1.410}\bar{T} \approx 0.92\bar{T}. \tag{3.19}$$

Besides, for the coastal area with limited fetch, the Joint North Sea Wave Project (JONSWAP) wave spectrum ($S_{\zeta,JONS}$, $\mathrm{m}^2/(\mathrm{rad/s})$) is used which is

$$S_{\zeta,JONS}(\omega) = 320\frac{\bar{H}_{1/3}^2}{\bar{T}_p^4}\omega^{-5}\exp\left(\frac{-1950}{\bar{T}_p^4}\omega^{-4}\right)3.3^{\exp\left(\frac{-1}{2\gamma^2}\left(\frac{\omega\bar{T}_p}{2\pi}-1\right)^2\right)} \tag{3.20}$$

where $\bar{T}_p$ is the average peak period (s) defined as:

$$\bar{T}_p = 1.296\bar{T} \tag{3.21}$$

and γ is a step function of

$$\gamma = \begin{cases} 0.07 & \text{for} \quad \omega < 2\pi/\bar{T}_p \\ 0.09 & \text{for} \quad \omega > 2\pi/\bar{T}_p. \end{cases} \tag{3.22}$$

For the wave slope spectra (S_α) for both standard wave spectra can be obtained by multiply Equations 3.18 and 3.20 by ω^4/g^2.

Energy and Power in Irregular Wave

For a particular sea area, the wave energy per unit area (E_{w/m^2}) regarding the irregular wave record can then be calculated as:

$$E_{w/m^2} = \rho g \int_0^\infty S_\zeta(\omega) d\omega = \rho g m_\circ \tag{3.23}$$

where $m_\circ$ is the total variance of the wave energy spectrum (m^2) or the area under the wave energy spectrum curve. Then, the wave power spectrum (S_{P_w}, m^3/rad) can be calculated by multiply Equation 3.23 by group velocity (c_g). Thus, the wave power per unit wave front ($P_{w/\mathrm{m}}$) of a particular sea area can be expressed as:

$$P_{w/m} = \rho g \int_0^\infty S_{P_w}(\omega) d\omega = \rho g \int_0^\infty c_g(\omega) S_\zeta(\omega) d\omega. \tag{3.24}$$

3.3 Ship Motions in Seaway

A ship dynamics in seaway is generally defined as a combination of two types of ship motions using the frames of reference detailed in Section 3.1. First, three linear displacements or translational motions along the steadily translating coordinate, namely, surge (x, m), sway (y, m), and heave (z, m) motions which are the motions along x-, y-, and z-axes respectively. Second, three angular displacements or rotational motions, namely, roll (ϕ, rad), pitch (θ, rad), and yaw (ψ, rad) motions, the angular motions about x-, y-, and z-axes respectively. Note that, for a ship dynamics in this research, ship is always assumed to have port-starboard symmetry property.

3.3.1 Encountering Frequency

The frequency of oscillation for a ship in seaway is called 'frequency of encounter' or 'encountering frequency'. At stationary or zero speed condition, this encountering frequency (ω_e, rad/s) is equivalent to the experiencing wave frequency ($\omega_e = \omega$). However, if the ship is travelling at speed (U, m/s), the encountering frequency is no longer equal

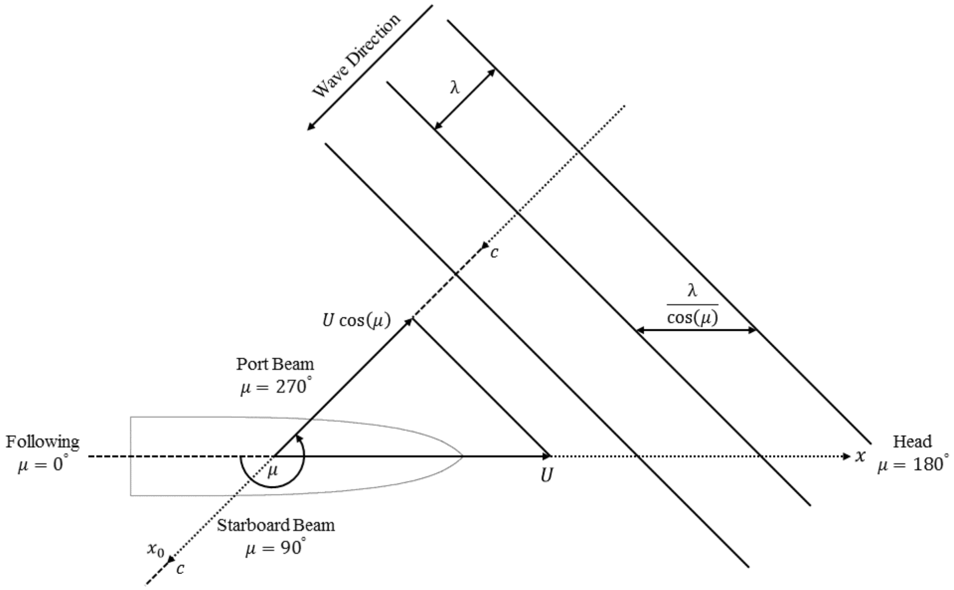

Figure 3.6: Relationship between encountering frequency and heading angle of a ship relative to wave direction.

to that the wave ($\omega_e \neq \omega$). The encountering frequency, in this case, also relates to the heading angle (μ, Deg) of the ship relative to the experiencing wave direction.

Figure 3.6 illustrates the relationships of the involved parameters relating to the change of encountering frequency of a ship moving on a track. Assuming a ship is experiencing a train of regular waves at a speed (U) with heading angle (μ), the period of encounter (T_e) of the ship relating to the waves can be defined as:

$$T_e = \frac{\lambda}{c - U\cos(\mu)}. \tag{3.25}$$

So, the encountering frequency (ω_e) is

$$\omega_e = \frac{2\pi}{T_e} = \frac{2\pi}{\lambda}\Big(c - U\cos(\mu)\Big). \tag{3.26}$$

Besides, Equation 3.26 can be presented in the relationship of circular wave frequency (ω) as:

$$\omega_e = \omega - kU\cos(\mu) \tag{3.27}$$

or with the dispersion relation in deep water, Equation 3.6, as:

$$\omega_e = \omega - \frac{\omega^2 U}{g}\cos(\mu). \tag{3.28}$$

Then, the wave elevation (ζ) along the ship's track in the translating coordinate ($O(x, y, z)$) is

$$\zeta(t) = \zeta_a \sin\big(\omega_e t - kx\cos(\mu) + ky\sin(\mu)\big). \tag{3.29}$$

3.3.2 Ship Motions in Regular Waves

General Equations of Ship Motions

Considering a conventional ship with port-starboard symmetry in body-fixed or local coordinate ($G(x_b, y_b, z_b)$) based on the Newton's second law of motion, the governing equation of motion of a 6-DOF ship motion in waves is defined by:

$$\sum_{j=1}^{6} m_{ij}\ddot{x}_j(\omega_e, t) = F_i(\omega_e, t) \quad \text{for} \quad i = 1, ...6 \tag{3.30}$$

where m_{ij} is the matrix of solid mass (for $i = 1$ to 3, kg) and inertia (for $i = 4$ to 6, kg·m^2) of the ship, $\ddot{x}_j$ is the motion acceleration (linear motions for $i = 1$ to 3, m/s^2, and angular motions for $i = 4$ to 6, rad/s^2) of the ship in the direction j, and F_i is the sum of the forces (for $i = 1$ to 3, N) or moments (for $i = 4$ to 6, N·m) acting on the ship in direction i. Note that, the forcing term (F_i) in Equation 3.30 consists of the hydrodynamic reaction and hydrostatic linear restoring forces or moments (F_{h_i}) and the wave exciting force or moment (F_{w_i}). In addition, the index numbers 1 to 6 respectively represent surge, sway, heave, roll, pitch, yaw motions of the ship.

Typically, the solid mass matrix of a ship in 6-DOF is given as:

$$m = \begin{bmatrix} \rho\nabla & 0 & 0 & 0 & 0 & 0 \\ 0 & \rho\nabla & 0 & 0 & 0 & 0 \\ 0 & 0 & \rho\nabla & 0 & 0 & 0 \\ 0 & 0 & 0 & I_{xx} & -I_{xy} & -I_{xz} \\ 0 & 0 & 0 & -I_{yx} & I_{yy} & -I_{yz} \\ 0 & 0 & 0 & -I_{zx} & -I_{zy} & I_{zz} \end{bmatrix} \tag{3.31}$$

by the product moments of inertia ($I_{xy} = I_{yx}$, $I_{xz} = I_{zx}$, and $I_{yz} = I_{zy}$) are relatively small and are generally neglected (Bhattacharyya, 1978; Journée and Massie, 2001; Lloyd, 1989). Hence, the mass distribution matrix, Equation 3.31, becomes

$$m = \begin{bmatrix} \rho\nabla & 0 & 0 & 0 & 0 & 0 \\ 0 & \rho\nabla & 0 & 0 & 0 & 0 \\ 0 & 0 & \rho\nabla & 0 & 0 & 0 \\ 0 & 0 & 0 & I_{xx} & 0 & 0 \\ 0 & 0 & 0 & 0 & I_{yy} & 0 \\ 0 & 0 & 0 & 0 & 0 & I_{zz} \end{bmatrix}. \tag{3.32}$$

For convenience, the moments of inertia about x_b-, y_b-, and z_b-axes of a ship are often approximated as:

$$I_{xx} = k_{xx}^2 \rho \nabla \quad \text{by} \quad k_{xx} \approx 0.3 B_{WL} \tag{3.33}$$

$$I_{yy} = k_{yy}^2 \rho \nabla \quad \text{by} \quad k_{yy} \approx 0.225 L_{WL} \tag{3.34}$$

$$I_{zz} = k_{zz}^2 \rho \nabla \quad \text{by} \quad k_{zz} \approx 0.225 L_{WL} \tag{3.35}$$

where ∇ is the displacement volume (m^3) of a ship, B_{WL} is the maximum waterline beam (m), L_{WL} is the water line length (m), and k_{xx}, k_{yy}, and k_{zz} are the radii of gyration of the ship about x_b-, y_b-, and z_b-axes respectively.

Giving the exciting simple harmonic force or moment (F_{w_i}) due to a train of regular waves as:

$$F_{w_i}(\omega_e, t) = F_{wa_i}(\omega_e) \cos\big(\omega_e t + \varepsilon_i(\omega_e)\big) \quad \text{for} \quad i = 1, ...6 \tag{3.36}$$

where F_{wa_i} is the amplitude of wave exciting force (N) or moment (N·m) in direction i, and ε_i is the phase (rad) of force or moment in direction i. Besides, the hydrodynamic reaction and hydrostatic linear restoring forces or moments (F_{h_i}) is given as:

$$F_{h_i}(\omega_e, t) = -a_{ij}(\omega_e)\ddot{x}_j(\omega_e, t) - b_{ij}(\omega_e)\dot{x}_j(\omega_e, t) - c_{ij}x_j(\omega_e, t) \quad \text{for} \quad i = 1, ...6 \tag{3.37}$$

where x_j is the motion displacement (m or rad) in direction j, $\dot{x}_j$ is the motion velocity (m/s or rad/s) in direction j, a_{ij} is hydrodynamic or added mass/inertia coefficient, b_{ij} is hydrodynamic damping coefficient, and c_{ij} is the hydrostatic restoring or stiffness coefficient in 6×6 matrices.

Then, substituting Equations 3.36 and 3.37 into Equation 3.30, the general equation of 6-DOF motion of a ship in regular waves is obtained in the form of a linear second-order ordinary differential equation (ODE) as:

$$\begin{aligned}\sum_{j=1}^{6} \big((m_{ij} + a_{ij}(\omega_e))\ddot{x}_j(\omega_e, t) + b_{ij}(\omega_e)\dot{x}_j(\omega_e, t) + c_{ij}x_j(\omega_e, t)\big) \\ = F_{wa_i}(\omega_e) \cos\big(\omega_e t + \varepsilon_i(\omega_e)\big) \quad \text{for} \quad i = 1, ...6.\end{aligned} \tag{3.38}$$

Coupled Equations of Ship Motions

Equation 3.38 can be expressed into coupled 6-DOF equations of motion. Therefore, there are 108 complex hydrodynamic and hydrostatic coefficients in total (from 3 6×6 matrices) to be identified. However, for a port-starboard symmetry ship, there are zero and small coupling coefficients which can be neglected for simplification (Bhattacharyya, 1978; Lloyd, 1989). So, the less complex forms of the equations of motions of a conventional ship in regular waves can be finalised as:

- **Surge Motion**:

$$
\begin{aligned}
&\big(\rho\nabla + a_{11}(\omega_e)\big)\ddot{x}(\omega_e,t) + b_{11}(\omega_e)\dot{x}(\omega_e,t) \\
&\qquad = F_{wa_1}(\omega_e)\cos\big(\omega_e t + \varepsilon_1(\omega_e)\big)
\end{aligned} \tag{3.39}
$$

- **Sway Motion**:

$$
\begin{aligned}
&\big(\rho\nabla + a_{22}(\omega_e)\big)\ddot{y}(\omega_e,t) + b_{22}(\omega_e)\dot{y}(\omega_e,t) \\
&\qquad +a_{24}(\omega_e)\ddot{\phi}(\omega_e,t) + b_{24}(\omega_e)\dot{\phi}(\omega_e,t) \\
&\qquad +a_{26}(\omega_e)\ddot{\psi}(\omega_e,t) + b_{26}(\omega_e)\dot{\psi}(\omega_e,t) + c_{26}\psi(\omega_e,t) \\
&\qquad = F_{wa_2}(\omega_e)\cos\big(\omega_e t + \varepsilon_2(\omega_e)\big)
\end{aligned} \tag{3.40}
$$

- **Heave Motion**:

$$
\begin{aligned}
&\big(\rho\nabla + a_{33}(\omega_e)\big)\ddot{z}(\omega_e,t) + b_{33}(\omega_e)\dot{z}(\omega_e,t) + c_{33}z(\omega_e,t) \\
&\qquad +a_{35}(\omega_e)\ddot{\theta}(\omega_e,t) + b_{35}(\omega_e)\dot{\theta}(\omega_e,t) + c_{35}\theta(\omega_e,t) \\
&\qquad = F_{wa_3}(\omega_e)\cos\big(\omega_e t + \varepsilon_3(\omega_e)\big)
\end{aligned} \tag{3.41}
$$

- **Roll Motion**:

$$
\begin{aligned}
&\qquad a_{42}(\omega_e)\ddot{y}(\omega_e,t) + b_{42}(\omega_e)\dot{y}(\omega_e,t) \\
&\big(I_{xx} + a_{44}(\omega_e)\big)\ddot{\phi}(\omega_e,t) + b_{44}(\omega_e)\dot{\phi}(\omega_e,t) + c_{44}\phi(\omega_e,t) \\
&\qquad +a_{46}(\omega_e)\ddot{\psi}(\omega_e,t) + b_{46}(\omega_e)\dot{\psi}(\omega_e,t) + c_{46}\psi(\omega_e,t) \\
&\qquad = F_{wa_4}(\omega_e)\cos\big(\omega_e t + \varepsilon_4(\omega_e)\big)
\end{aligned} \tag{3.42}
$$

- **Pitch Motion**:

$$
\begin{aligned}
&\qquad a_{53}(\omega_e)\ddot{z}(\omega_e,t) + b_{53}(\omega_e)\dot{z}(\omega_e,t) + c_{53}z(\omega_e,t) \\
&\big(I_{yy} + a_{55}(\omega_e)\big)\ddot{\theta}(\omega_e,t) + b_{55}(\omega_e)\dot{\theta}(\omega_e,t) + c_{55}\theta(\omega_e,t) \\
&\qquad = F_{wa_5}(\omega_e)\cos\big(\omega_e t + \varepsilon_5(\omega_e)\big)
\end{aligned} \tag{3.43}
$$

- **Yaw Motion**:

$$
\begin{aligned}
&\qquad a_{62}(\omega_e)\ddot{y}(\omega_e,t) + b_{62}(\omega_e)\dot{y}(\omega_e,t) \\
&\qquad a_{64}(\omega_e)\ddot{\phi}(\omega_e,t) + b_{64}(\omega_e)\dot{\phi}(\omega_e,t) \\
&\big(I_{zz} + a_{66}(\omega_e)\big)\ddot{\psi}(\omega_e,t) + b_{66}(\omega_e)\dot{\psi}(\omega_e,t) + c_{66}\psi(\omega_e,t) \\
&\qquad = F_{wa_6}(\omega_e)\cos\big(\omega_e t + \varepsilon_6(\omega_e)\big).
\end{aligned} \tag{3.44}
$$

The remaining frequency-dependant hydrodynamic coefficients (a_{ij} and b_{ij}), hydrostatic coefficients (c_{ij}), and the wave excitation components (F_{wa_i}) for each DOF or motion can be referred as global coefficients. These coefficients can be experimentally determined by model testing. Nevertheless, it consumes time and requires suitable resources such as model, testing facility, cost, and precise measuring system and technique. Another option is the mathematical method (computer aiding) as the 2-D strip theory which is that is used for the coefficients calculations throughout this research.

From the coupled equations of motions of a ship in regular waves, Equations 3.39 to 3.44, only surge motion is not influenced by any other motions or it is independent. Sway motion is affected by roll and yaw motions and vice versa. Likewise, heave and pitch motions are coupled. Furthermore, when the ship is travelling with constant speed, course, and heading angle, it should be highlighted that only heave, roll, and pitch motions are pure oscillatory as the restoring terms (c_{ij}) contained in their equations of motion and yaw motion is considered to be zero.

Motion Transfer Functions

Once all of the parameters as ship particulars, wave or exciting condition, and hydrodynamics and hydrostatic coefficients are identified, the equations of motion detailed in Section 3.3.2 can be solved in time-domain using numerical methods for ODEs, e.g., the Euler method, the forth-order RungeKutta or RK4 method etc. The steady-state resulting motions of a ship over a range of wave frequencies are normally presented in the form of dimensionless parameter so called ‘Transfer Function (TF)’.

The transfer function is able to provide an idea of scalable linear relationships of a ship motions proportional to the wave amplitude. For the translational motions, the transfer functions of surge (x_a), sway (y_a), and heave (z_a) motions are obtained by dividing the responded motion amplitudes by the wave amplitude (ζ_a). For the angular motions, the transfer functions of roll (ϕ_a), pitch (θ_a), and yaw (ψ_a) motions are calculated by dividing the motion amplitudes by the wave slope amplitude (α_a or $k\zeta_a$). Therefore, the transfer functions (TF_i) of a 6-DOF ship motion are

- **For Translational Motions**:

$$TF_x(\omega_e) = \frac{x_a(\omega_e)}{\zeta_a(\omega_e)} \tag{3.45}$$

$$TF_y(\omega_e) = \frac{y_a(\omega_e)}{\zeta_a(\omega_e)} \tag{3.46}$$

$$TF_z(\omega_e) = \frac{z_a(\omega_e)}{\zeta_a(\omega_e)} \tag{3.47}$$

- **For Angular Motions**:

$$TF_{\phi}(\omega_e) = \frac{\phi_a(\omega_e)}{\alpha_a(\omega_e)} \tag{3.48}$$

$$TF_{\theta}(\omega_e) = \frac{\theta_a(\omega_e)}{\alpha_a(\omega_e)} \tag{3.49}$$

$$TF_{\psi}(\omega_e) = \frac{\psi_a(\omega_e)}{\alpha_a(\omega_e)}. \tag{3.50}$$

3.3.3 Ship Motions in Irregular Waves

As described in section 3.2.2, ocean waves condition in reality is random and irregular and the statistical technique as wave energy spectrum is deployed to estimate the waves characteristics in particular sea area based on available wave record. Furthermore, if a ship travelling conditions, i.e., speed (U) and heading angle (μ) in the sea area are identified, wave energy spectrum of the area can be transformed to the spectral ordinate that experiences by the moving ship called as ‘encountering wave spectrum’.

Encountering Wave Spectrum

The wave spectrum experienced by a moving ship in a particular sea area is not equal to the static wave spectrum due to corresponding frequency of encounter. However, transforming the static wave spectrum to the moving or translating coordinate of the moving ship, the energies contained in both wave spectra are even. So, they can be mathematically expressed as:

$$S_{\zeta}(\omega_e)d\omega_e = S_{\zeta}(\omega)d\omega. \tag{3.51}$$

Hence,

$$S_{\zeta}(\omega_e) = S_{\zeta}(\omega)\frac{d\omega}{d\omega_e} \tag{3.52}$$

and, from Equation 3.28, therefore,

$$\frac{d\omega_e}{d\omega} = 1 - \frac{2\omega U}{g}\cos(\mu). \tag{3.53}$$

Then, substitute Equation 3.53 into 3.52, the encountering wave spectrum is

$$S_{\zeta}(\omega_e) = \frac{S_{\zeta}(\omega)}{\left(1 - \frac{2\omega U}{g}\cos(\mu)\right)}. \tag{3.54}$$

Motion Energy Spectrum

Under the linear relationships, the motion energy or response spectrum (S_{r_i}, $\mathrm{m}^2/(\mathrm{rad/s})$) the ship is equal to the product of the encountering wave energy spectrum and the motion transfer function squared of a particular ship motion that is

$$S_{r_i}(\omega_e) = S_{\zeta}(\omega_e) TF_i^2 \quad \text{for} \quad i = 1, ...6 \tag{3.55}$$

by TF_i^2 is called the 'response amplitude operator' or 'RAO'.

3.4 Summary

The theories relating to the numerical modelling of a ship dynamics in waves which are detailed in this chapter and are employed throughout this research can be summarised as:

- Wave theories:
    - Linear or regular waves based on idealised wave profile and deep water approximation.
    - Irregular waves regarding the standard wave energy spectrum formula.
- Ship dynamics:
    - Ship responses in regular waves based on the Newton's second law of motion and seakeeping analysis.
    - Ship responses in irregular waves or sea state based on the seakeeping and statistical analyses.

Chapter 4

Assessment of Available Power from Ship Motions in a Seaway

This chapter describes a novel theoretical assessment of the available mechanical power of ship motions in sea state. As a ship in waves can be considered as a wave energy converter, the directional responses of the ship in different heading condition can be directly converted to motion mechanical power. With the adoption of the theories indicated in Chapter 3, the directional response mechanical power spectrum and power magnitude can, therefore, be quantified.

4.1 Assumptions

In order to assess the available mechanical power generated by a ship in a seaway, the ship particular and ship responses in particular wave condition are needed to be identified. Therefore, for convenience, the relevant theories detailed in Chapter 3 are employed following the assumptions that

- The ship is mono hull with slender shape.
- The speed is zero.
- The hull of the ship is rigid with port-starboard symmetry and wall-sided.
- The course or heading angle is stable.
- The responded motions of the ship in waves are small and harmonic.
- The deep water approximations are applied.
- The hull provides no effect on the incident waves (the Froude-Krylov hypothesis).
- The ocean is fully-developed in deep and open water regions.

4.2 Mechanical Power Determination Methodology

4.2.1 Motion Mechanical Power

The dynamics of a ship in waves are theoretically treated as 6-DOF dynamics which are the combination of surge, sway, heave, roll, pitch, and yaw motions. However, followed the assumptions made in Section 4.1, the non-oscillatory motions as surge and sway and also the lateral-plane motion as yaw are negligible. Therefore, in this research, only coupled heave-pitch, and roll motions are included in the consideration. Basically, the mechanical power from the motions ($P_{mech,i}$, W) created by the ship over a range of frequencies can be calculated as:

$$P_{mech,i}(\omega_e) = \begin{cases} F_{mech,z}(\omega_e)\dot{z}_a(\omega_e) & \text{for} \quad \text{heave} \\ \tau_{mech,\theta}(\omega_e)\dot{\theta}_a(\omega_e) & \text{for} \quad \text{pitch} \\ \tau_{mech,\phi}(\omega_e)\dot{\phi}_a(\omega_e) & \text{for} \quad \text{roll} \end{cases} \tag{4.1}$$

where

$$F_{mech,z}(\omega_e) = \Delta\ddot{z}_a(\omega_e) \tag{4.2}$$

$$\tau_{mech,\theta}(\omega_e) = I_{yy}\ddot{\theta}_a(\omega_e) \tag{4.3}$$

$$\tau_{mech,\phi}(\omega_e) = I_{xx}\ddot{\phi}_a(\omega_e) \tag{4.4}$$

where $F_{mech,z}$ is the mechanical force (N) created by heave motion, Δ is the displacement (kg) of the ship, $\tau_{mech,\theta}$ and $\tau_{mech,\phi}$ are the mechanical torques (N·m) created by pitch and roll motions, I_{xx} and I_{yy} are the moments of inertia (kg·m^2) about x_b- and y_b-axes of the ship, and $\dot{z}_a$, $\ddot{z}_a$, $\dot{\theta}_a$, $\ddot{\theta}_a$, $\dot{\phi}_a$ and $\ddot{\phi}_a$ are the amplitudes of heave, pitch, and roll velocities (m/s or rad/s) and accelerations (m/s^2 or rad/s^2) of the ship respectively. Moreover, the motions amplitudes (z_a, θ_a, and ϕ_a) can be obtained by the motion transfer functions, Equations 3.47 to 3.49. By assuming the responded motions are harmonic, hence, the velocity and acceleration amplitudes of the motions can be calculated as:

$$\dot{z}_a(\omega_e) = z_a(\omega_e)\omega_e \quad \text{and} \quad \ddot{z}_a(\omega_e) = z_a(\omega_e)\omega_e^2 \tag{4.5}$$

$$\dot{\theta}_a(\omega_e) = \theta_a(\omega_e)\omega_e \quad \text{and} \quad \ddot{\theta}_a(\omega_e) = \theta_a(\omega_e)\omega_e^2 \tag{4.6}$$

$$\dot{\phi}_a(\omega_e) = \phi_a(\omega_e)\omega_e \quad \text{and} \quad \ddot{\phi}_a(\omega_e) = \phi_a(\omega_e)\omega_e^2. \tag{4.7}$$

4.2.2 Capture Width

The wave power that is absorbed by a WEC system or a ship in this case is typically defined as the product of wave power per unit wave front ($P_{w/m}$, W/m) expressed in Equation 3.13 or 3.24 multiply by the absorption length or width of the ship facing the

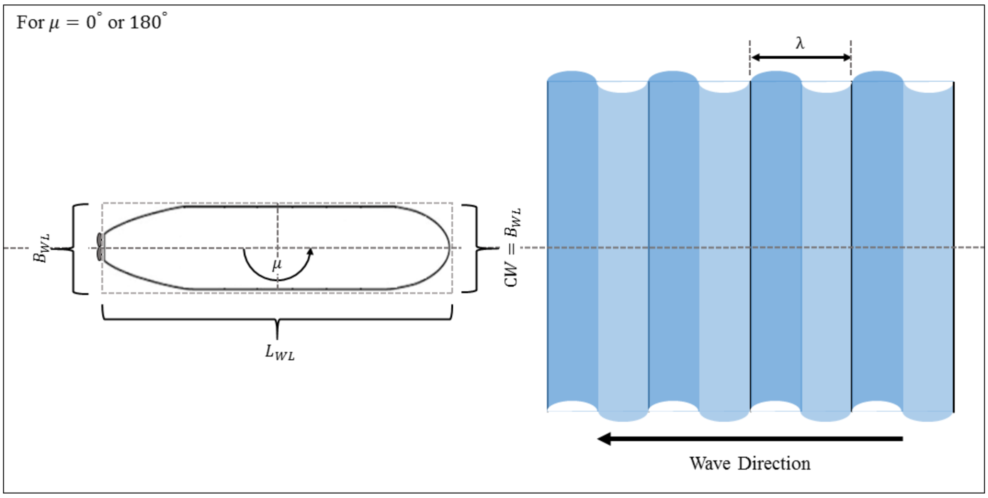

(a) For $\mu = 0°$ or 180°.

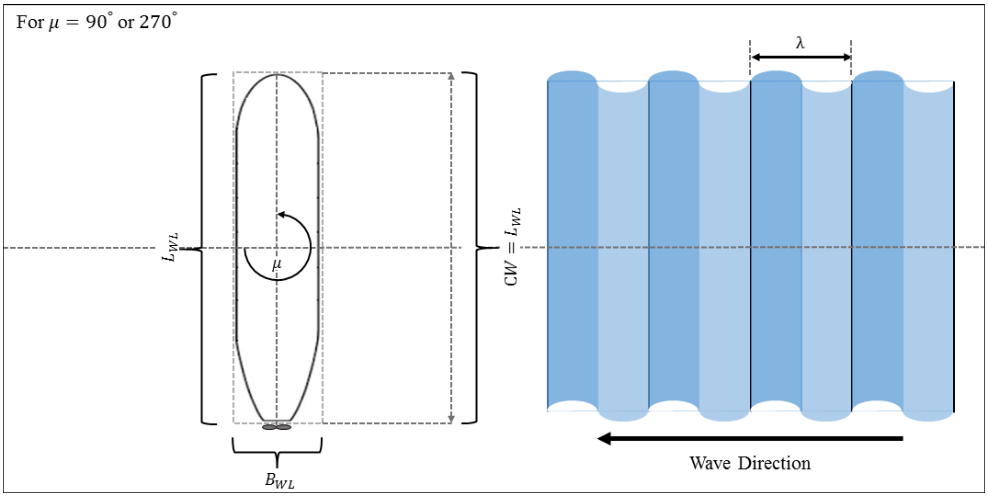

(b) For $\mu = 90°$ or 270°.

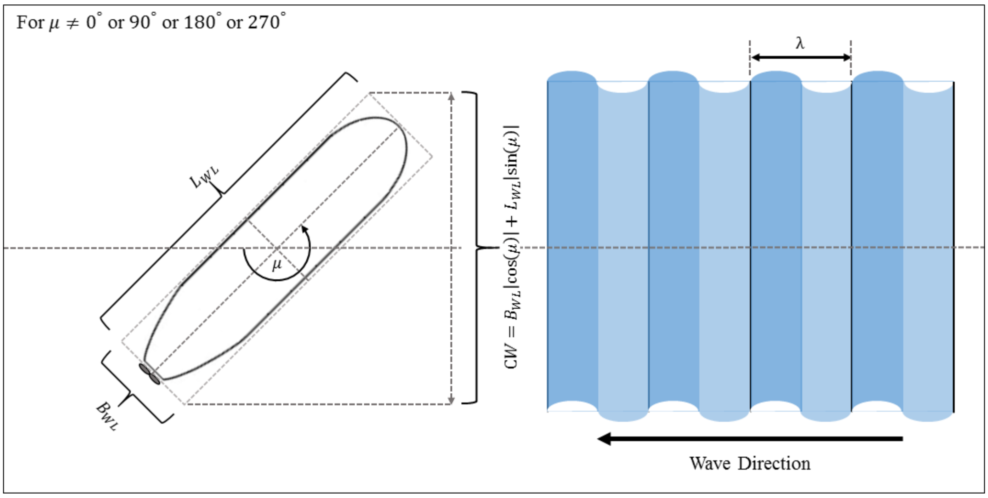

(c) For $\mu \neq 0°$ or 90° or 180° or 270°.

Figure 4.1: Relationship between capture width and heading angle of a ship relative to wave direction.

wave front. The concept of the width of absorption was first introduced by Budar and Falnes (1975) and then also be applied in the work of Babarit (2015) as it is called the 'Capture Width (CW)'.

Considering a moving ship in a train of waves, the capture width of the ship is a function of the heading angle relative to the wave direction. This is because of the vertical or waterline plane profile of ship's hull is slender as the length is assumed to be much greater than the beam. For simplification, the vertical profile of an arbitrary ship is considered as a rectangular shape with the length and width are equal to the waterline length (L_{WL}) and the waterline beam (B_{WL}) of the ship as illustrated in Figure 4.1. Therefore, the capture width (CW) of an arbitrary ship can be numerically expressed as a function of heading angle (μ) as:

$$CW(\mu) = B_{WL}|\cos(\mu)| + L_{WL}|\sin(\mu)|. \tag{4.8}$$

4.2.3 Wave Power Conversion Efficiency

The wave power conversion or hydrodynamic efficiency ($\eta_{P_w,i}$) of a motion in a regular wave condition relative to the capture width can be defined as:

$$\eta_{P_w,i}(\omega_e,\mu) = \frac{P_{mech,i}(\omega_e,\mu)}{P_{w/m}(\omega_e,\mu)CW(\mu)}. \tag{4.9}$$

This parameter is able to reflect the fraction of wave power flowing through and being absorbed by the ship.

4.2.4 Response Mechanical Power Spectrum

Once wave power conversion efficiency of a motion ($\eta_{P_w,i}$) and wave power spectrum (S_{P_w}, m^3/rad) at particular sea area are obtained, the response mechanical power spectrum ($S_{P_{mech,i}}$, m^3/rad) can be calculated as:

$$S_{P_{mech,i}}(\omega_e,\mu) = \eta_{P_w,i}(\omega_e,\mu)S_{P_w}(\omega_e,\mu) \tag{4.10}$$

and, with the similar manner in Section 3.2.2, the response mechanical power of a motion at particular sea area or sea state in a function of heading angle of a ship relative to waves direction can be now calculated as:

$$P_{mech,i}(\mu) = \rho g CW(\mu) \int_0^\infty S_{P_{mech,i}}(\mu) d\omega_e. \tag{4.11}$$

Note that, the value provided by Equation 4.11 is the upper limit or peak of the total response power. Therefore, the average of the magnitude of the response mechanical power can be calculated by taking half of the Equation 4.11.

4.3 Mechanical Power from Ship Motions in Seaway

4.3.1 Global Wave Power Resource

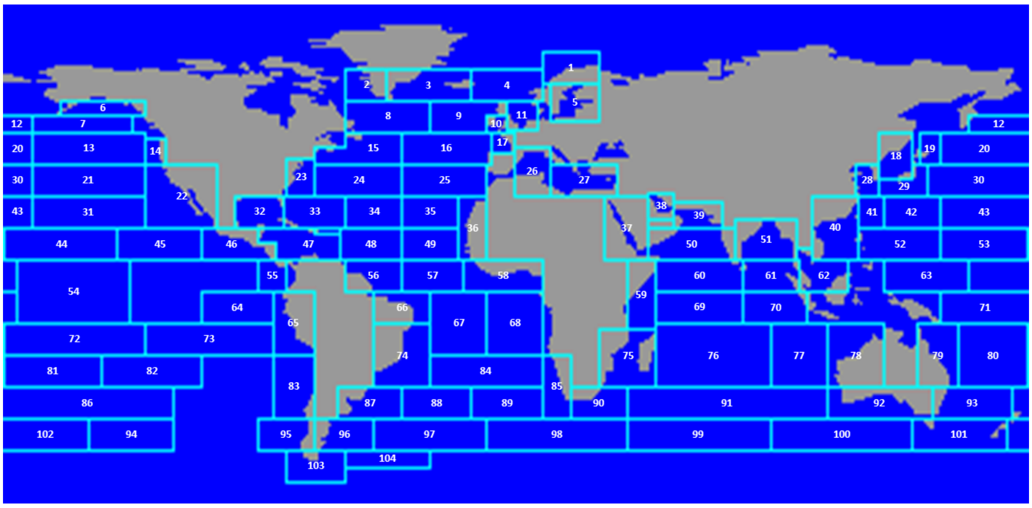

Figure 4.2: 104 discretised sea areas of global wave statistics (BMT Fluid Mechanics Limited, 2011).

The global wave record that is used in this research is the global wave statistics published in the work of Hogben et al. (1986) based on the 30-year visual observations by merchant ships of the voluntary fleet. Besides, this database is also digitally published by BMT Fluid Mechanics Limited (2011). This wave record consists of the data of significant wave heights ($H_{1/3}$) and zero crossing periods (T_z) covering 104 discretised sea or ocean areas across the world as can be seen in Figure 4.2. The normal distributions, mean, and standard deviations of the global average significant wave height and zero crossing period are presented in Figures 4.3(a) and 4.3(b), see Appendix A for raw data for the individual sea area.

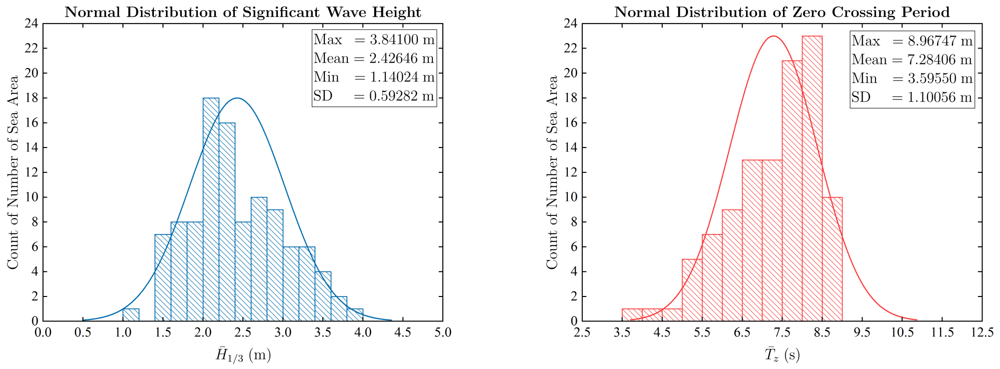

(a) Signficant wave height.

(b) Zero crossing period.

Figure 4.3: Global wave statistics of all directional waves of 104 discretised sea areas based on Hogben et al. (1986); BMT Fluid Mechanics Limited (2011).

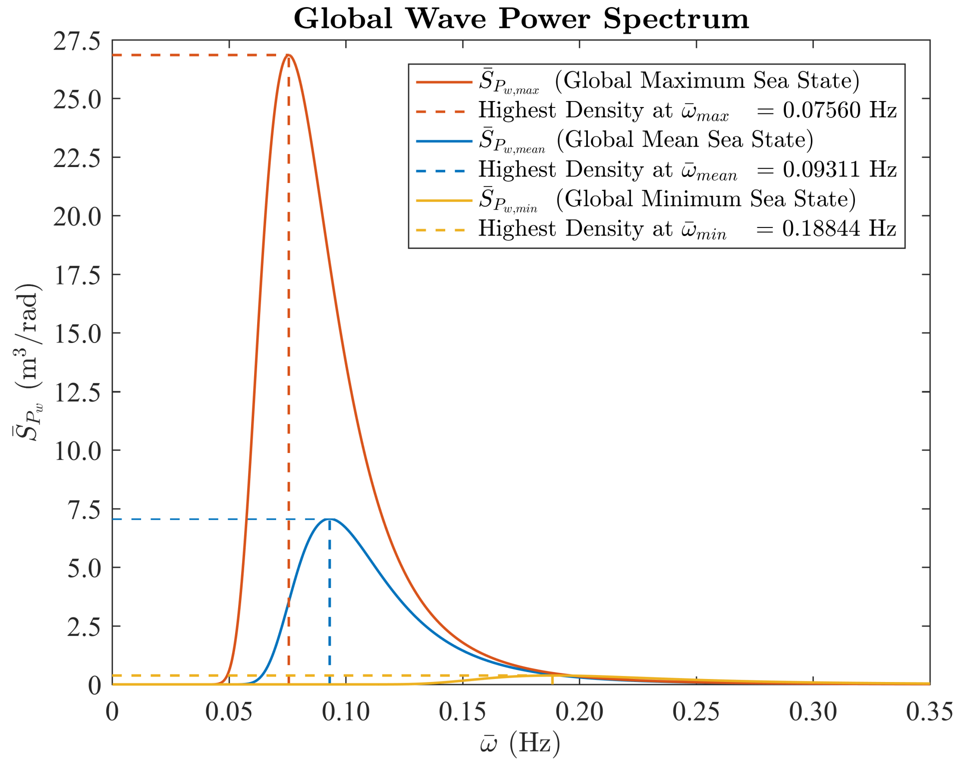

Figure 4.4: Global wave power spectrum based on the global wave statistics of Hogben et al. (1986).

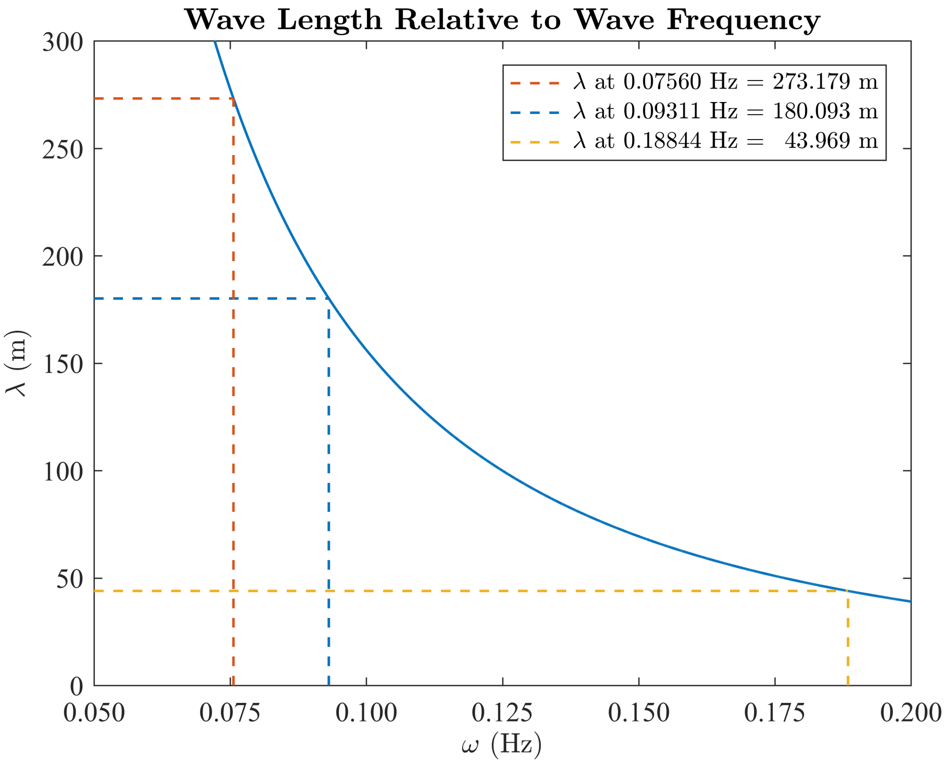

Figure 4.5: Wave length relative to wave frequency.

Using the mean values of the average significant wave height and zero crossing period, the global average spectral ordinate of the fully-developed sea state can be calculated by Equation 3.18. Consequently, the global average wave power spectrum of the global average sea state can be obtained based on Equation 3.24 as plotted in Figure 4.4 (blue line). The highest density of this global average wave power spectrum occurs at 0.09311 Hz of the average wave frequency of the global average sea state ($\bar{\omega}_{mean}$). Moreover, Figure 4.4 also presents the possible maximum and minimum wave power spectra of the sea states based on the maximum and minimum values of significant wave height and zero crossing periods of the global wave statistics. Also, the wavelengths ($\bar{\lambda}_i$[1]) at the wave frequencies (ω) where the highest wave power densities contained in each wave power spectra can be found from the mathematical relationships showing in Figure 4.5.

4.3.2 Generic Ship Representation

In order to predict the available mechanical power generated by motions of a ship in the sea states, reference ship model particular is necessary to be identified. In this research, a naval architecture software package, MAXSURF Modeller Advanced, has been used as a tool for this investigation (Bentley Systems, 2015a). As can be seen in Figure 4.6, a reference standard design provided by the software, 1-surface displacement ship type (the software's terminology) with no bulbous bow, is selected and assumed as a generic ship hull form representation with length-to-beam ratio (L_{OA}/B_{OA}) and beam-to-depth (B_{OA}/D) equal to 6.535 and 1.427 respectively. Also, the reference draft (d) is given by half of the moulded depth (D).

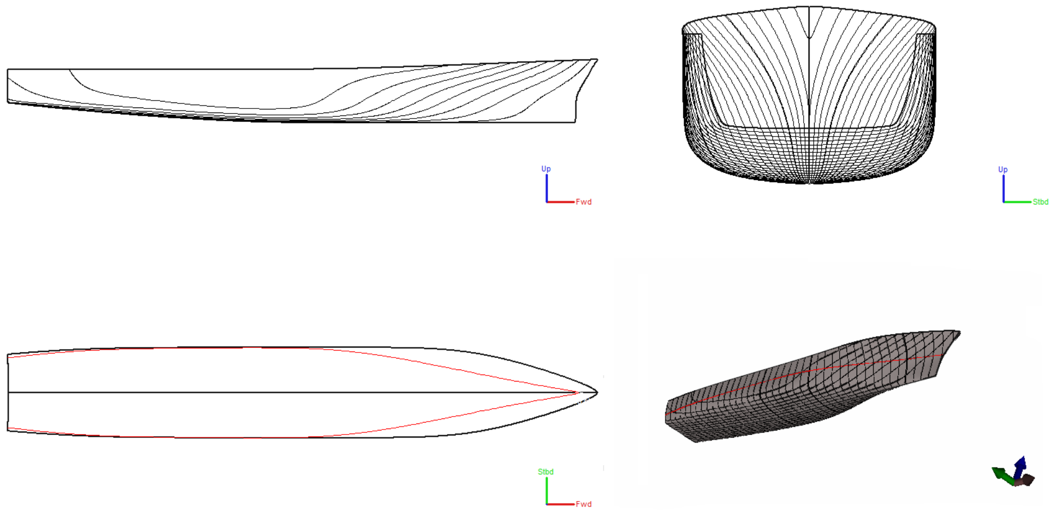

Figure 4.6: The reference ship hull form geometry (top-left: side profile; top-right: body plan; bottom-left: top plan; bottom-right: perspective view; red line is reference waterline).

---

[1] The subscription i is the representation of the value at sea state; *mean* is mean sea state; *min* is minimum sea state; *max* is maximum sea state.

4.3.3 Influence of Ship Geometry to Ship Responses

Ship Geometries of Interest

The numerical analysis is initially conducted upon the different values of a dependent variable that is the length-to-beam ratio ($L_{OA,i}/B_{OA,i}$) to provide the idea of how can the shape of a ship affect the ship responses in sea state. Based on the reference geometry in Figure 4.6, the ship has been varied respecting to top plan geometry with ±25% of $B_{OA,i}$ and ±25% of $L_{OA,i}$, as visualised in Figure 4.7, by keeping the moulded depth constant. Therefore, 5 different length-to-beam ratios are investigated as:

- $L_{OA,i}/B_{OA,i} = 8.169$ (+25% of reference $L_{OA,i}$).
- $L_{OA,i}/B_{OA,i} = 5.228$ (+25% of reference $B_{OA,i}$).
- $L_{OA,i}/B_{OA,i} = 6.535$ (reference $L_{OA,i}$, $B_{OA,i}$)[2].
- $L_{OA,i}/B_{OA,i} = 8.714$ (−25% of reference $B_{OA,i}$).
- $L_{OA,i}/B_{OA,i} = 4.902$ (−25% of reference $L_{OA,i}$).

First, the ships responses in global mean sea state are investigated. Furthermore, the reference waterline length of the reference ship equals to the wavelength that contained the highest wave power density in the sea state ($L_{WL,mean} = 1.00\bar{\lambda}_{mean}$). Additionally, to provide equitable comparison, the volume displacements of the ships are given to be equivalent respecting to the reference ship geometry (at $L_{OA,i}/B_{OA,i} = 6.535$). This can be achieved by tuning the design waterline or draft of the ships (d). The ships particulars are detailed in Table 4.1.

Ship Heading Conditions

There are 5 main heading conditions in interest which are

- Following Waves ($\mu = 0°$).
- Stern-Oblique Waves ($\mu = 45°$ and $315°$).
- Beam Waves ($\mu = 90°$ and $270°$).
- Bow-Oblique Waves ($\mu = 135°$ and $225°$).
- Head Waves ($\mu = 180°$).

---

[2] The reference ship geometry

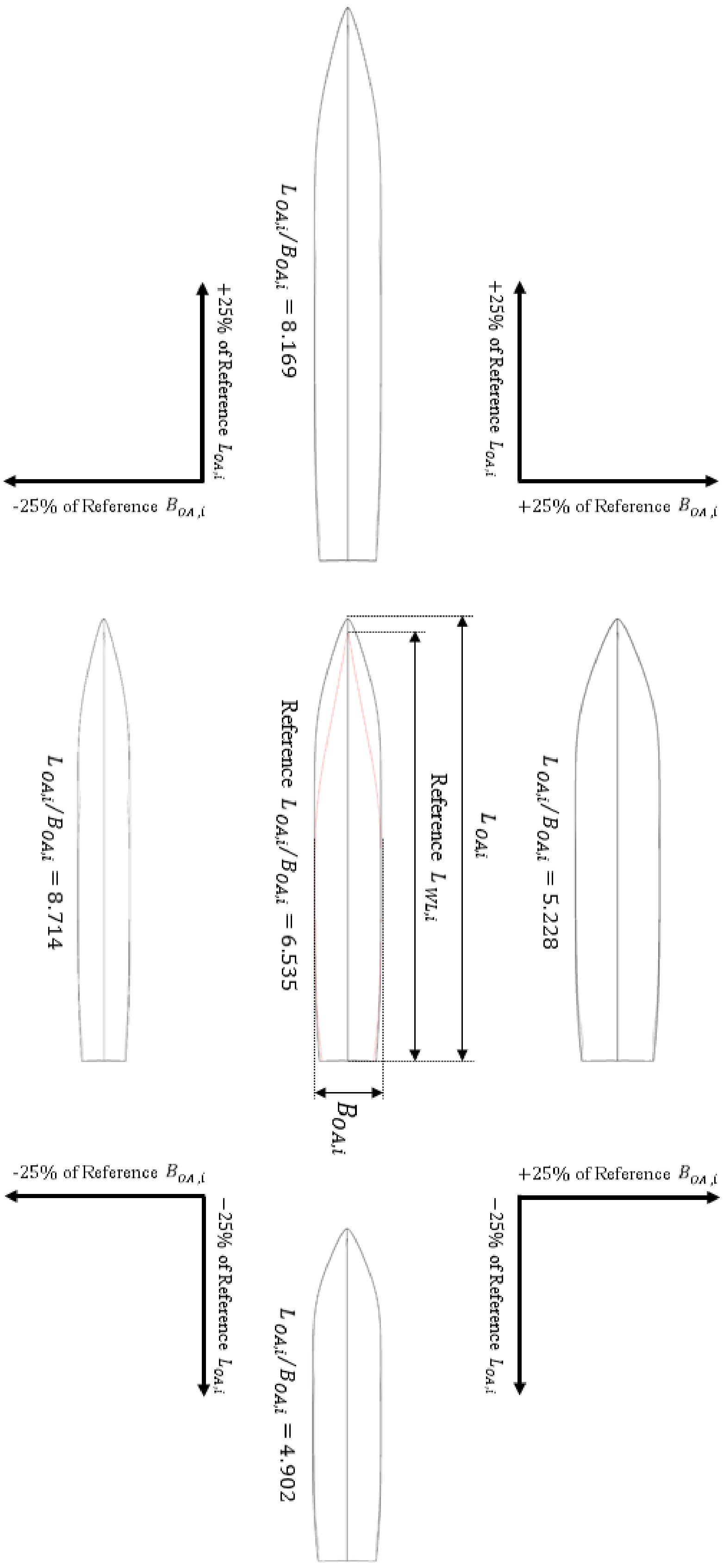

Figure 4.7: Investigated ship geometries based on varied length-to-beam ratios.

Table 4.1: Investigated ship particulars at mean sea state (note that: $i = mean$).

Parameter	Symbol	Ref. $L_{WL,i} = 1.00 \times \bar{\lambda}_i$					Unit	Corresponding scaling laws
		$L_{OA,i}/B_{OA,i}$						
		8.169	5.228	6.535[a]	8.714	4.902		
Remark	-	+25% Ref. $L_{OA,i}$	+25% Ref. $B_{OA,i}$	-	-25% Ref. $B_{OA,i}$	-25% Ref. $L_{OA,i}$	-	-
Length Overall	L_{OA}	232.422	185.938	185.938	185.938	139.453	m	$1/R$
Beam Overall	B_{OA}	28.451	35.563	28.451	21.338	28.451	m	$1/R$
Moulded Depth	D	19.938	19.938	19.938	19.938	19.938	m	$1/R$
Draft	d	8.547	8.546	9.969	12.253	12.253	m	$1/R$
Block Coefficient	C_B	0.504	0.504	0.537	0.577	0.577	-	-
Volume Displacement	∇	27,344.078	27,344.078	27,344.078	27,344.078	27,344.078	m^3	$1/R^3$
Displacement Weight	Δ	28,028.000	28,028.000	28,028.000	28,028.000	28,028.000	tonnes	$1/R^3$
Waterline Length	L_{WL}	224.387	179.509	180.093[b]	181.333	136.000	m	$1/R$
Waterline Beam	B_{WL}	28.272	35.340	28.366	21.324	28.432	m	$1/R$
Vertical Centre of Gravity	VCG	10.557	15.665	9.969	7.033	9.743	m	$1/R$
Transverse Metacentric Height	GM_T	3.772	3.772	3.772	3.772	3.772	m	$1/R$
Radius of Gyration about x-axis	k_{xx}	8.482	10.602	8.510	6.397	8.530	m	$1/R$
Radius of Gyration about y-axis	k_{yy}	50.487	40.390	40.521	40.800	30.600	m	$1/R$
Moment of Inertia about x-axis	I_{xx}	2,016,242,307.150	3,150,378,604.923	2,029,671,979.646	1,147,009,478.440	2,039,127,961.670	$kg \cdot m^2$	$1/R^5$
Moment of Inertia about y-axis	I_{yy}	71,441,007,440.570	45,721,939,114.791	46,019,919,125.504	46,655,825,622.724	26,243,998,397.982	$kg \cdot m^2$	$1/R^5$
Roll Damping Coefficient	b_{44}	0.075	0.075	0.075	0.075	0.075	-	-

[a] Reference Ship Geometry

[b] Reference Waterline Length

Verification of Seakeeping Analysis for Ship Motion Transfer Functions

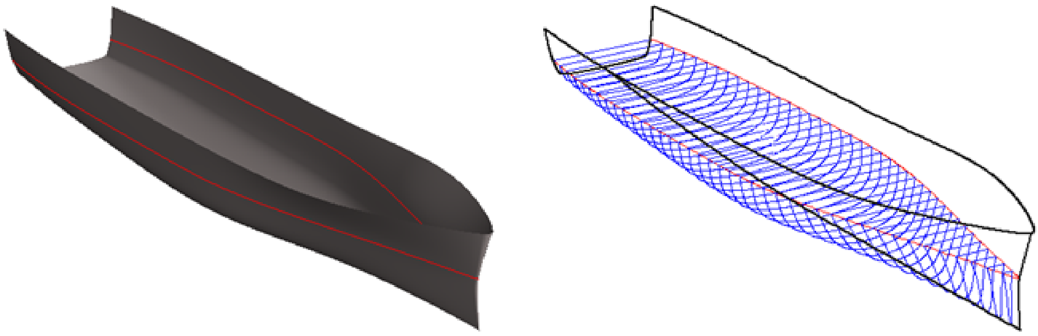

(a) 3-D render surface.

(b) 3-D drawing with devided hull sections.

Figure 4.8: The reference ship hull form (red line is waterline and blue line is below waterline sectional areas).

For this investigation, seakeeping analysis is used to simulated the ships responses in the identified sea state. The hydrodynamic and hydrostatic coefficients of the ships are calculated using the 2-D strip theory (for coupled heave-pitch) and the estimation based on hydrostatic properties of the ships (for roll) described in Appendix B. The calculation and estimation techniques are implemented in a ship motion software package called 'MAXSURF Motions Advanced'. Another option for calculating seakeeping prediction is a panel method. The panel method is a first-order diffraction/radiation hydrodynamic analysis based on boundary element method (BEM) which could provide all 6-DOF ship dynamics. However, this method requires high resolution 3-D model and high computational cost.

To calculate the ships motion transfer functions using the MAXSURF software based on the 2-D strip theory, the number of hull sections of 3-D hull forms is needed to be stated as the example in Figure 4.8. As an initial input parameter for 2-D strip theory method (for coupled heave-pitch), more number of hull sections are able to increase the accuracy of the simulation, but it also requires a longer time to simulate. Therefore, it is vital to compromise between acceptable accuracy and simulation time. In this case, the number of hull sections of 51 sections is set as a reference for which these hull sections are assumed that the results achieve acceptable convergence.

Figures 4.9(a) and 4.9(b) show the convergences of the relative errors of the average heave and pitch transfer functions over the frequency range for each input number of hull sections. The significant errors occur at the number of hull sections from fewer than 31 sections, and therefore a number of hull sections of 41 sections are selected. The selected number is able to provide an acceptable relative error of less than 0.02 % and achieve a manageable computation time as can be seen in Figure 4.9(c).

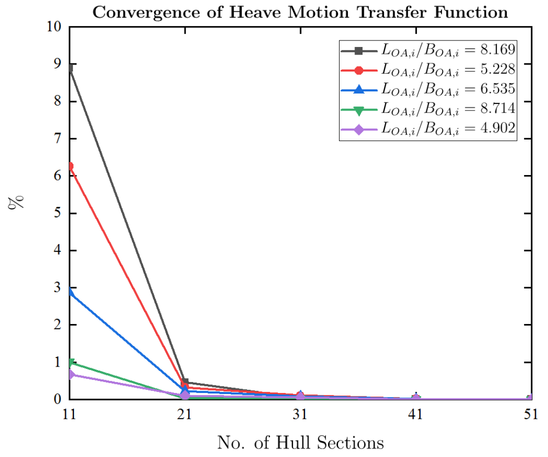

(a) For heave motion transfer function.

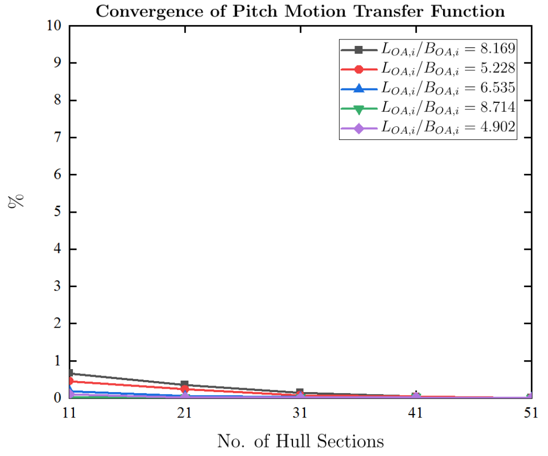

(b) For pitch motion transfer function.

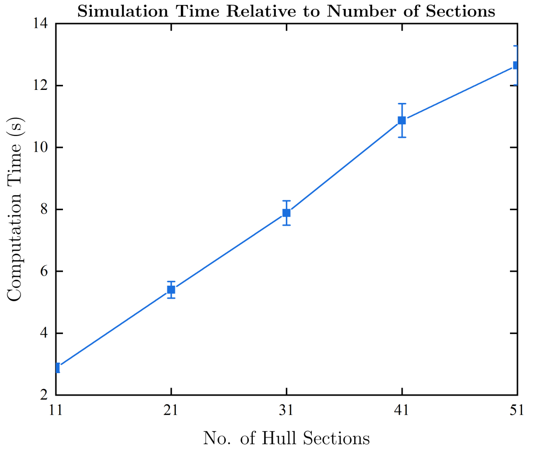

(c) Computation time running on a desktop computer with Intel Core i7-4770 CPU (3.40 GHz) and 16.00 GB DDR4 RAM.

Figure 4.9: Numerical sensitivity tests of number of hull sections.

Capture Width of the Ships

The capture width of the ships respecting to heading angles are calculated by Equation 4.8. As the ships are port-starboard symmetry, the capture widths between both sides of the ships ($0° \leqslant \mu \leqslant 180°$ and $180° \leqslant \mu \leqslant 360°$) are also symmetric as demonstrated in Figure 4.10. The dips of the capture widths at 90° and 270° can be observed due to the simplified assumption for ship waterline shape made in Section 4.2.2.

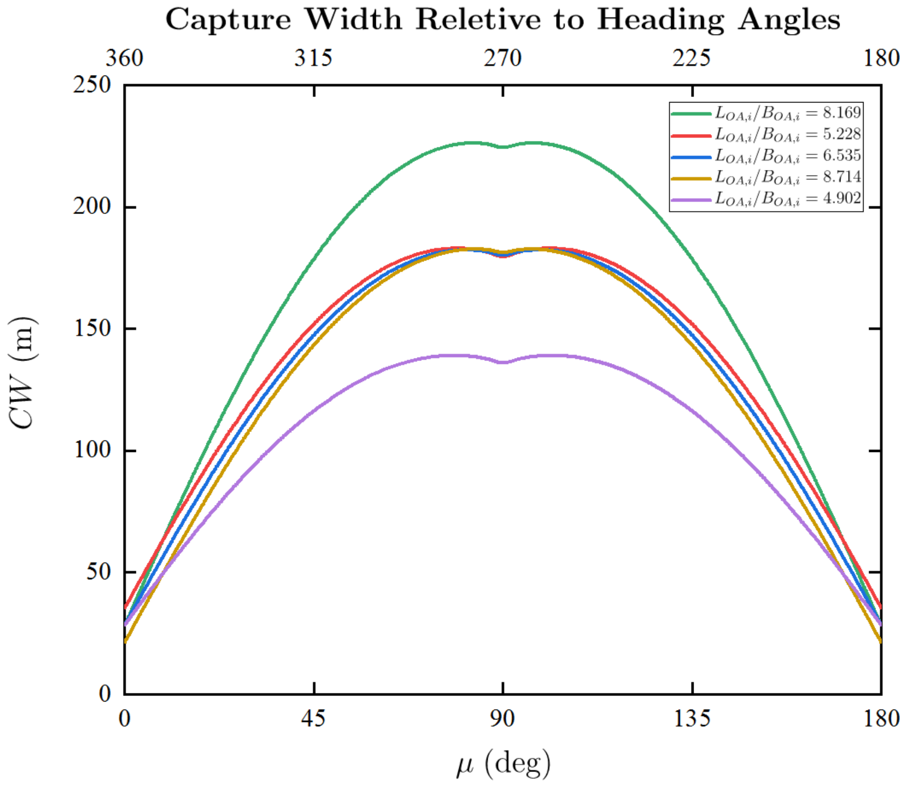

Figure 4.10: Capture widths relative to heading angles of the ships in the case of $L_{OA,mean} = 1.00\bar{\lambda}_{mean}$.

Effect of Ship Geometry on Motion Responses

Regarding the ship geometries and heading conditions of interest, the motion transfer functions, wave power conversion efficiencies, response mechanical power spectra, and magnitude of available mechanical powers in the global mean sea state are plotted in Figures 4.11 to 4.14.

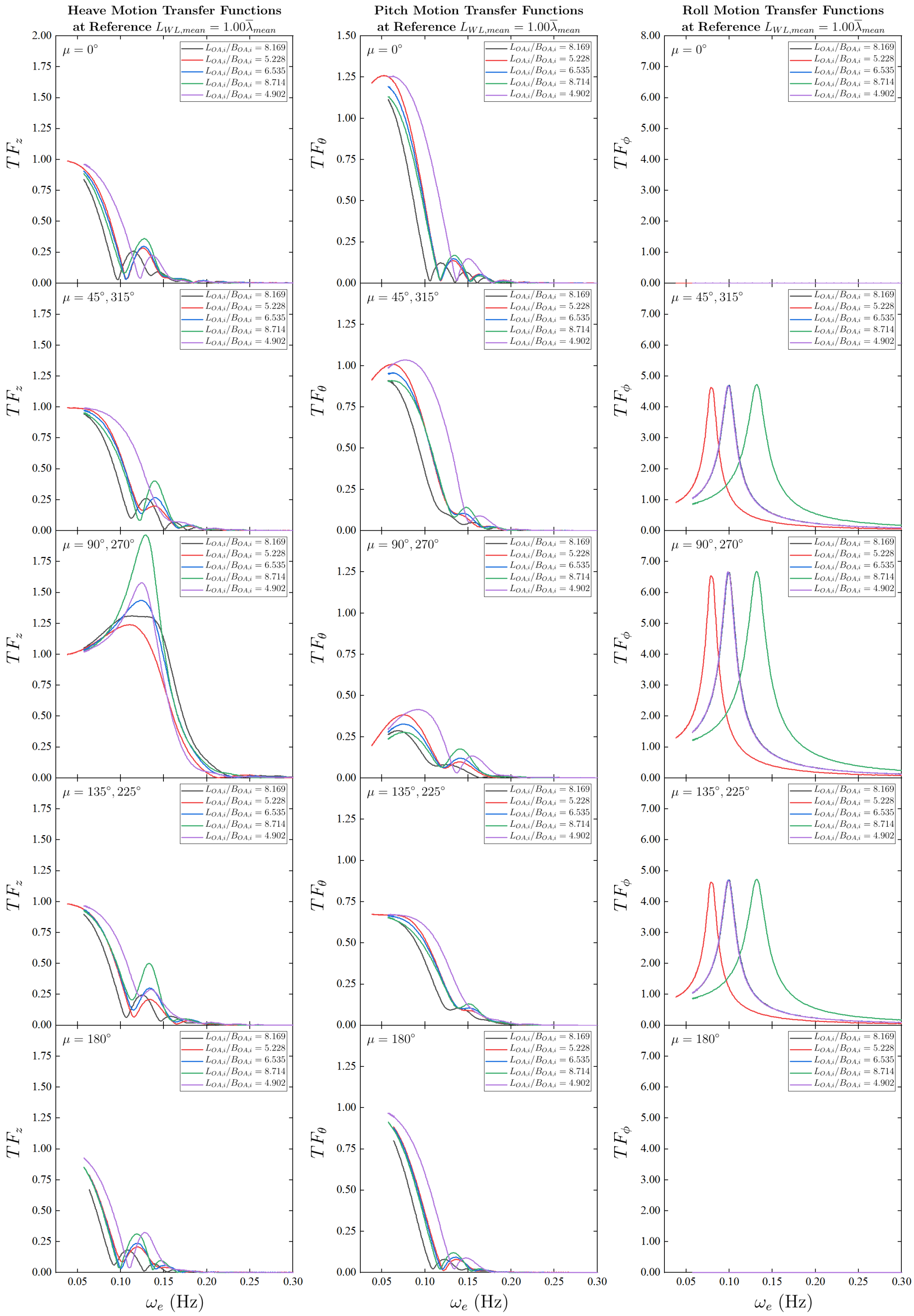

Figure 4.11: Motion transfer functions of the ships at mean sea state at the reference $L_{OA,mean} = 1.00\bar{\lambda}_{mean}$ (note that: plots for each motion are not in the similar scale).

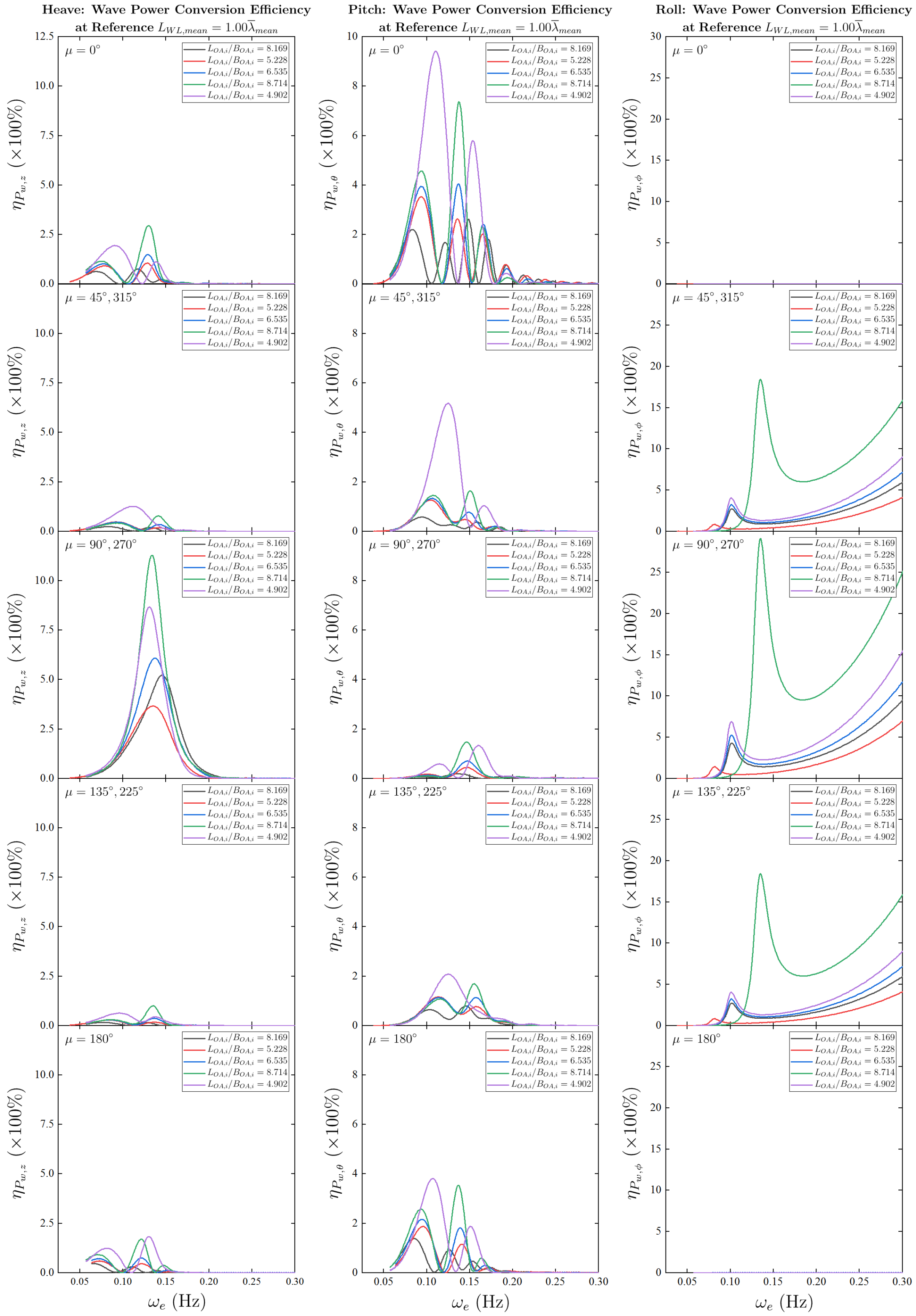

Figure 4.12: Wave power conversion efficiencies in regular waves at global mean significant wave height ($\bar{H}_{1/3} = 2.42646$ m) over frequency range of the ships at the reference $L_{OA,mean} = 1.00\bar{\lambda}_{mean}$ (note that: plots for each motion are not in the similar scale).

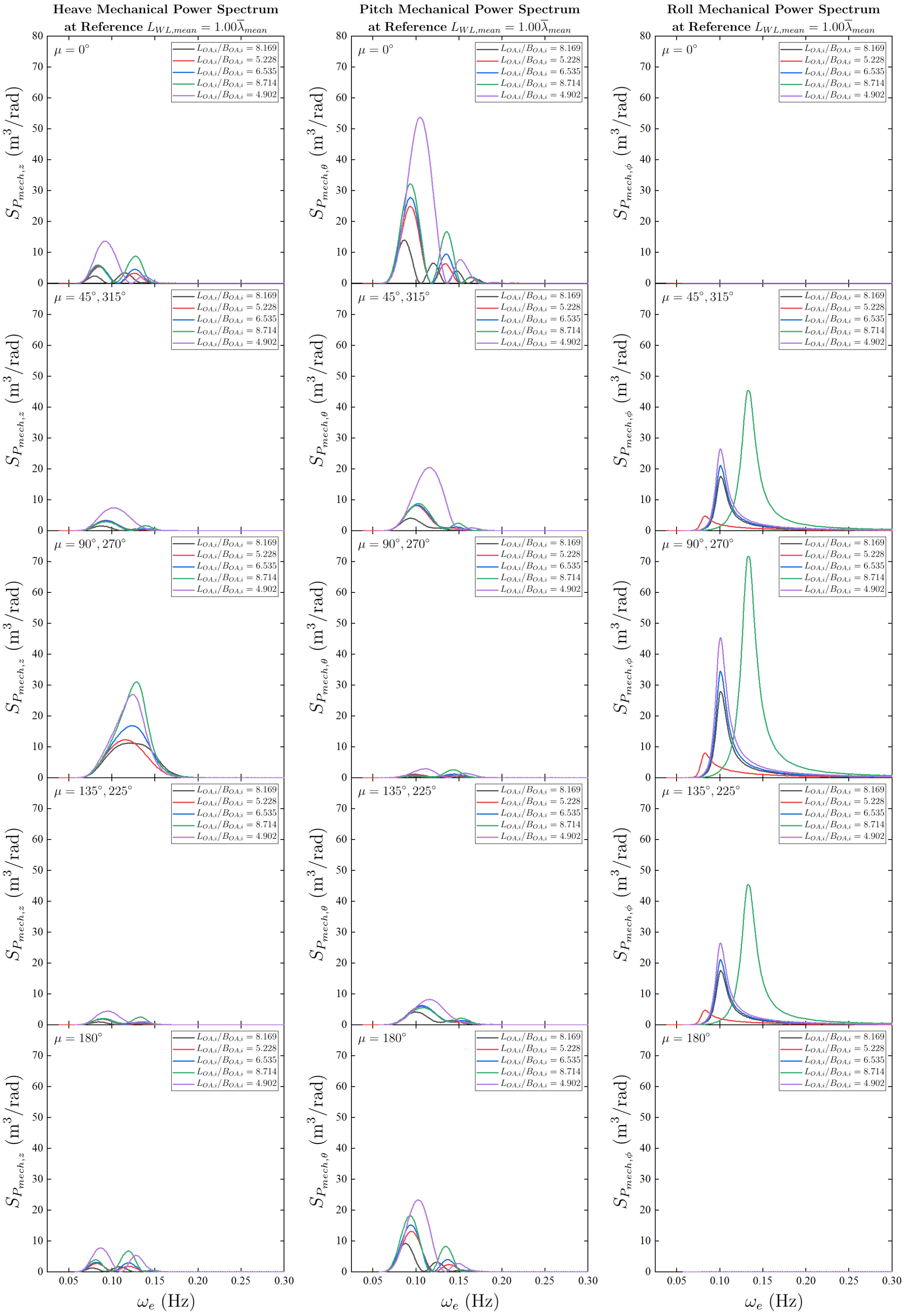

Figure 4.13: Motion mechanical power spectra of the ships at mean sea state and the reference $L_{OA,mean} = 1.00\bar{\lambda}_{mean}$.

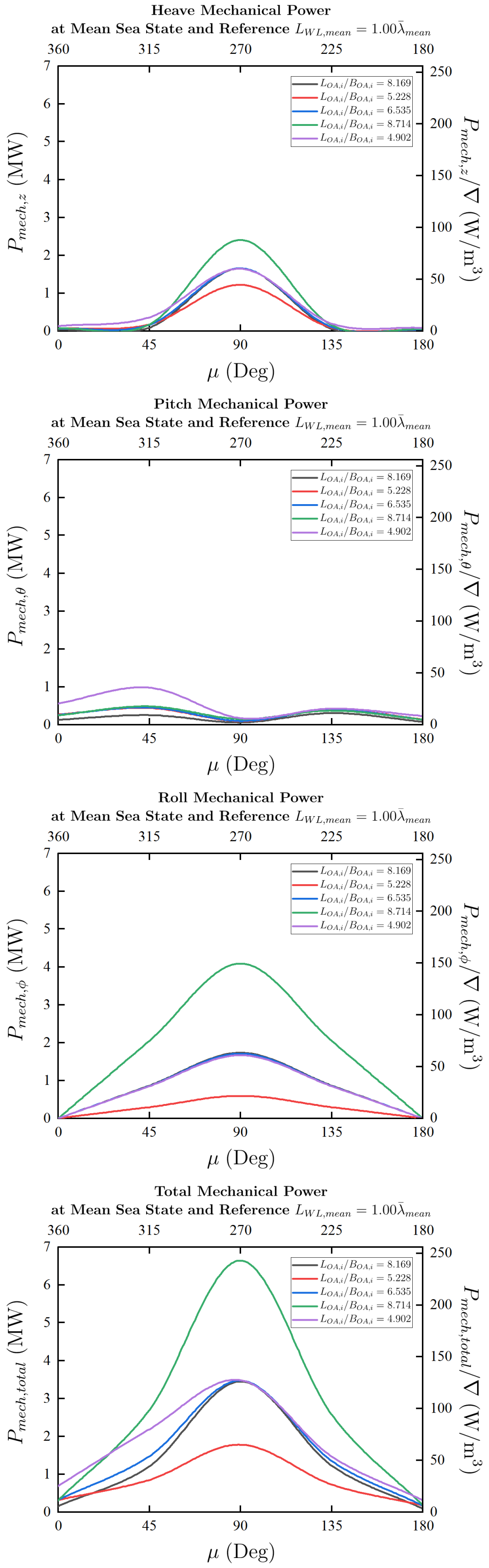

Figure 4.14: Motion mechanical power and power per unit volume displacement of the ships at mean sea state and the reference $L_{OA,mean} = 1.00\overline{\lambda}_{mean}$.

Figure 4.11 shows the transfer functions of the ships at zero speed over the encountering frequency range (in this case $\omega_e = \omega$) in the investigated heading conditions. The significant changing in ship responses or transfer functions with different ship geometries can be observed.

With the changing in the beam (B_{OA}), the variations of the transfer functions of heave and roll motions can be seen especially in the conditions of oblique waves ($45°, 315°$ and $135°, 225°$) and beam waves ($90°$ and $270°$). For heave motion responses, changing in beam does not change the characteristics of the frequency responses, but it provides the variation in response magnitudes. By the same volume displacements, the smaller beam length contributes more heave responses and, on the other hand, the more massive beam provides the opposite at the similar frequency. For roll motion at a particular heading angle, the limit or peak of the transfer functions are not altered following the transverse dimension due to the value of roll damping coefficient is constant. However, the location of the peak (resonance) of roll response shifts toward higher frequency range when the ship is more slender. This is because of the location of natural roll frequency depends on the value of the moment of inertia about x-axis (I_{xx}) which is defined in Equation B.21. In case of pitch motion, generally, there is no major effect in the changing of pitch transfer functions with the varied beam lengths. The most observable change of pitch responses, in this case, occurs at the beam wave condition. The pitch motion at this heading condition is relatively low and merely negligible.

By the changing in length (L_{OA}) in a similar manner, this results in a shift in the frequency responses for heave and pitch motions. Generally, the ship with longer longitudinal dimension responses to the lower frequency range. In contrast to the shorter, the motion transfer functions cover the broader range toward higher response frequencies. Nonetheless, for roll motion, this does not affect to the motion response characteristics.

Once the motions transfer functions are obtained, the wave power conversion efficiencies in regular waves ($\bar{H}_{1/3,mean} = 2.42646$ m) over the frequency responses in Figure 4.12 are calculated by Equation 4.9. It should be noted that this non-dimensional parameter is calculated by the mechanical power produced by the whole ship based on linear relationships of motion transfer function over the wave power absorbed by the ship related to the capture width at a particular heading angle and encountering frequency. Therefore, the proportions between the powers of the motions are relatively high. Besides, the noticeable trends of wave power conversion efficiencies of roll motion after the peaks in the direction of high-frequency responses (to the right) are identified. This is due to the ratios between resulting motion and wave slope amplitude after the resonance calculated by uncoupled second-order ODE (Equation B.19) decays to a constant positive value, not zero. In this frequency region, this theoretically reflects in a constant motion amplitude oscillating with more cycle, and hence more power magnitude can be expected. Also, the differences in the roll motion power conversion efficiencies of the variation of ship length are caused by the numerical measures of the roll moments of inertia.

Then, with the relationship in Equation 4.10, the response mechanical power spectra of the ships in mean sea state can be calculated as indicated in Figure 4.13. These motion mechanical power spectra related to the heading conditions imply the range of frequency responses and the responded power components at the sea state. Thereby, the higher value of the power spectrum indicates that the motion response at that encountering frequency experiencing in the sea state could provide more available mechanical power. Besides, the magnitude of the created power at particular heading condition relates to the area under the power spectrum curve and the capture width length. Subsequently, from Equation 4.11, the available mechanical powers from the motions in the mean sea state at different heading conditions is quantified as presented in Figure 4.14.

For heave motion, the highest responded power magnitudes occur at beam wave conditions compared to any other investigated heading conditions especially following and head waves. At this angle, the significant change in power magnitude is observed when varying the size of the ship beam. The slimmer ship provides more heave response as a result in higher power level. In case of following, oblique, and head waves conditions, the ship with shorter length delivers greater responses with the slightly higher magnitudes when waves approach from the stern part ($0° \leqslant \mu \leqslant 90°$ and $270° \leqslant \mu \leqslant 360°$). While, at these heading conditions, the variation of transverse dimension does not influence the heave response characteristics.

In comparison, pitch motion also transmits higher powers at the stern waves conditions with the ship with shorter length but the pitch power magnitude peaks at stern-oblique waves (45° and 315°). However, at beam sea, the small level of pitch power is created by the ship. Moreover, due to the size of ship beam insignificantly correlates with pitch response at any angle, the levels of the power are therefore comparable in this regard.

The power from roll motion related to the heading angle is port-starboard symmetric and straightforward. The highest power magnitude of roll motion can be surely expected at beam waves conditions and becomes higher with the ship with the more slender shape. The measurement of roll power proportionally decreases from the highest to zero measures at the following and head waves.

The nature of the motion responses of a typical port-starboard symmetry vessel reflects on the characteristics of the resulting power generations regarding DOFs. In this investigation, the transverse dimension of a ship shows to be a dominated factor for the responses in the roll power in most cases except following and head waves, and heave at beam sea, but not in pitch. The changing in the longitudinal dimension, nonetheless, significantly influences the heave and pitch response powers in the stern wave conditions as this is independent for the roll. Ultimately, by summing up the individual source of power generated by each motion, it is shown that the level of the available mechanical power resource of a ship in the sea state can be clearly magnified. Also, this is able to support the setup hypothesis of the higher potential power resource respecting to associated DOFs of a ship in waves.

4.3.4 Influence of Ship Scale based on Reference Waterline Length to Ship Responses

Ship geometry is not the only parameter that affects ship responses at particular sea state, but also the scale of the ship is needed to be considered.

Geometric Scaling

In this investigation, the scales are geometrically referenced to the percentage or fraction of the reference waterline length ($L_{WL,i}$) of the ship. In this case, the reference waterline length is chosen to be of 180.093 m (reference $L_{WL,mean} = 1.00\bar{\lambda}_{mean}$). By this means, Lloyd (1989) has provided the definition of the dimension ratio or scaling factor (R) compared between two ships which can be defined as:

$$R = \frac{\text{Reference Waterline Length}}{\text{Target Waterline Length}}. \tag{4.12}$$

This scaling factor can be used to calculated geometric dimension, mass, and inertia properties of the scaled ship comparing to the reference one based on the parameter-related corresponding scaling laws as provided in Table 4.1. Also, the full list of scaling laws based on dimension ratio can be found in Appendix C. In terms of the ship geometry, the scaled ships are geometrically identical to the reference ships (with the different length-to-beam ratios stated in Section 4.3.3) in all aspect. In this case, the investigated fractions of the reference waterline length are selected within the range of 0.25 to 1.25 (with 0.25 increment). Therefore, the scaling factors of the ships related to the identified numbers of the fraction can be determined as detailed in Table 4.2. Besides, it should be noted that the capture width is also relatively scaled accordingly.

Table 4.2: Scaling factors of the ships at mean sea state.

Fraction of Waterline Length compared to $\bar{\lambda}_i$	$L_{WL,mean}$ (m)	$L_{OA,mean}$ (m)	R
0.25	45.023	46.485	4.000
0.50	90.047	92.969	2.000
0.75	135.069	139.454	1.333
1.00	180.093*	185.938	1.000
1.25	225.116	232.423	0.800

*Reference Waterline Length

Effect of Ship Scale on Motion Responses

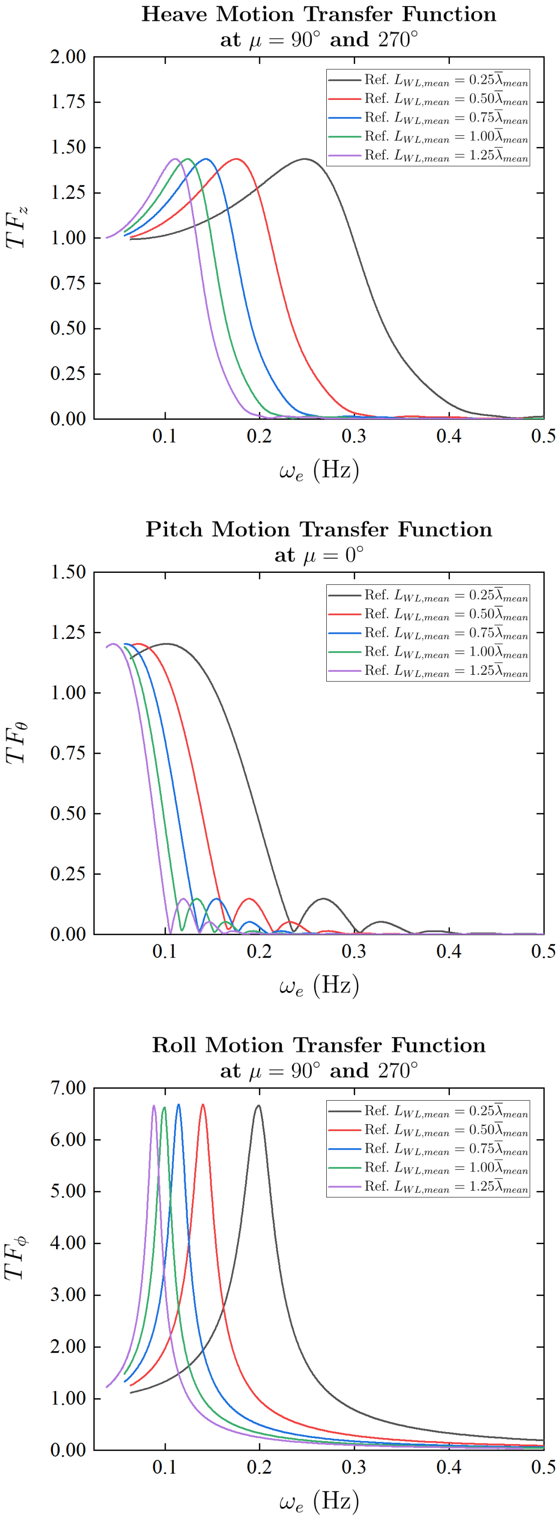

Figure 4.15: Effect of ship scale on motion transfer functions.

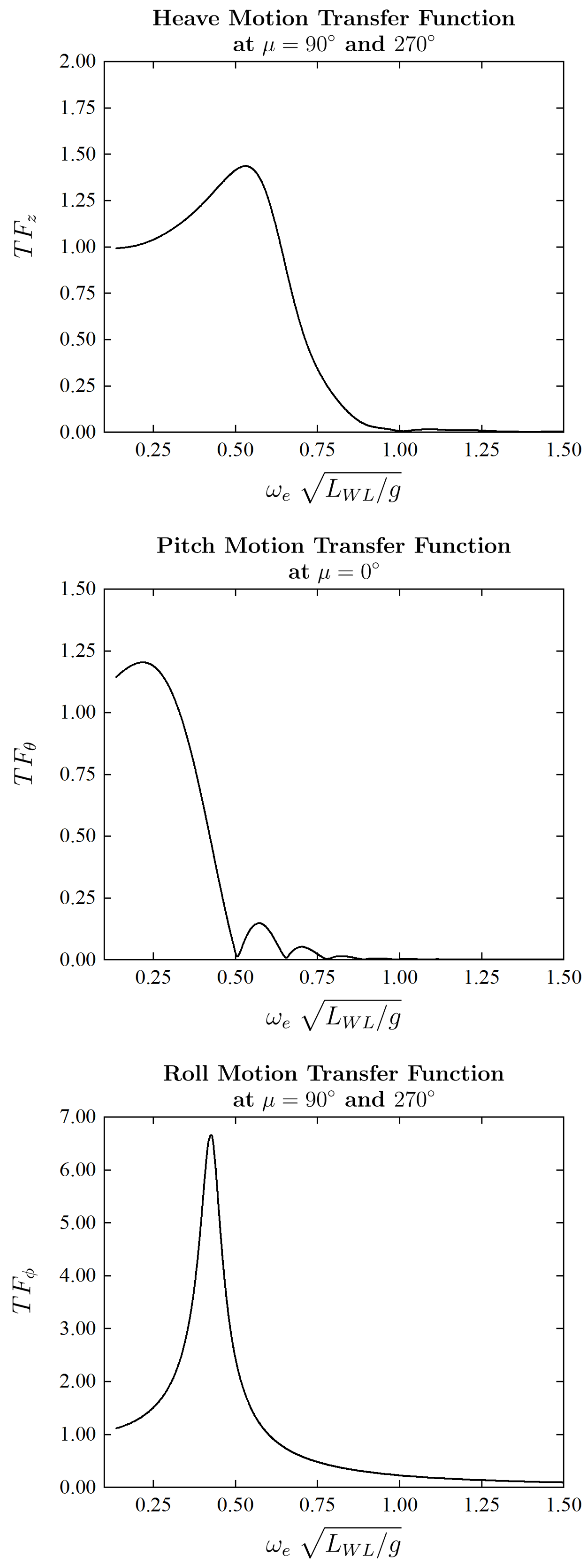

Heave Motion Transfer Function at $\mu = 90°$ and $270°$

Pitch Motion Transfer Function at $\mu = 0°$

Roll Motion Transfer Function at $\mu = 90°$ and $270°$

Figure 4.16: Motion transfer functions against non-dimensional encountering frequencies

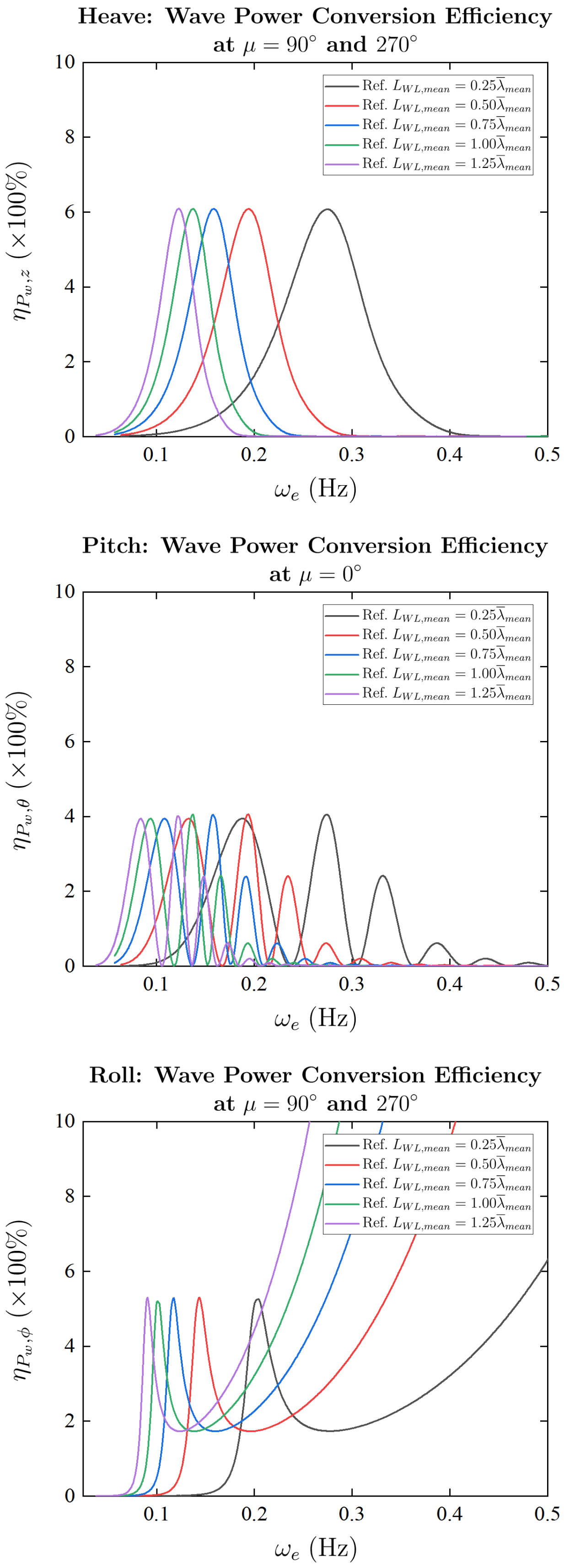

Figure 4.17: Effect of ship scale on wave power conversion efficiencies.

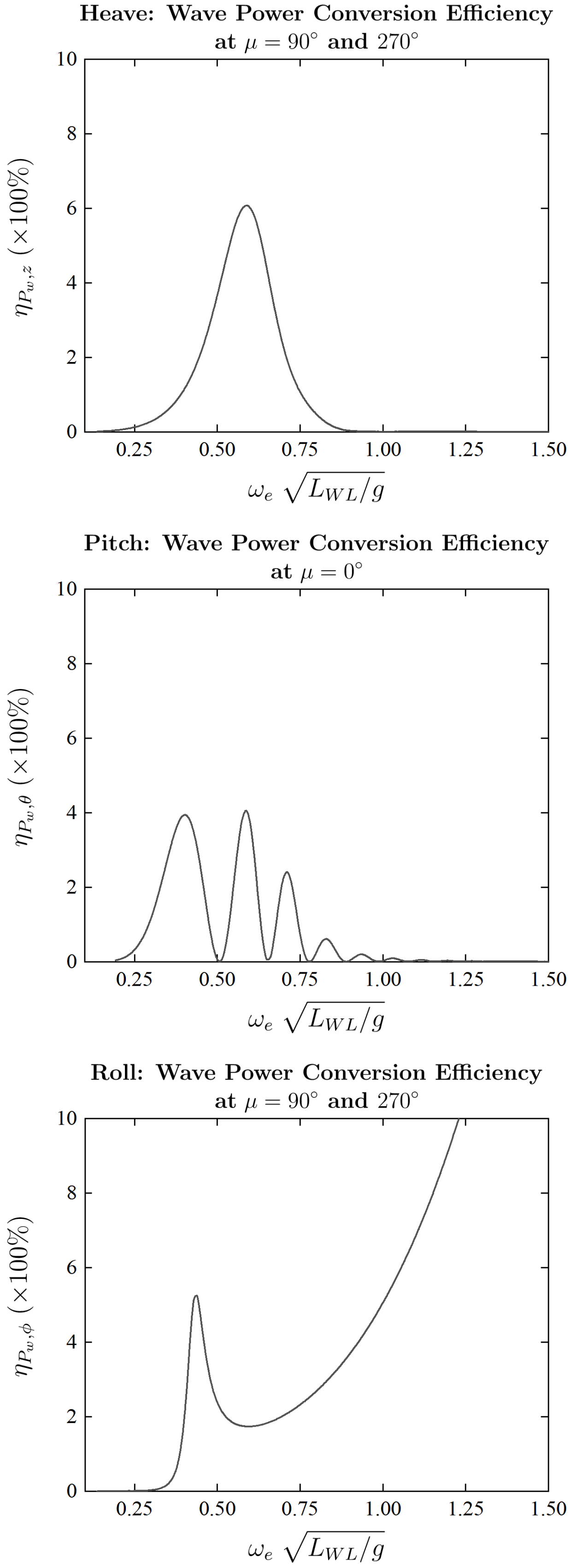

Heave: Wave Power Conversion Efficiency at $\mu = 90^\circ$ and 270°

Pitch: Wave Power Conversion Efficiency at $\mu = 0^\circ$

Roll: Wave Power Conversion Efficiency at $\mu = 90^\circ$ and 270°

Figure 4.18: Wave power conversion efficiencies against non-dimensional encountering frequencies.

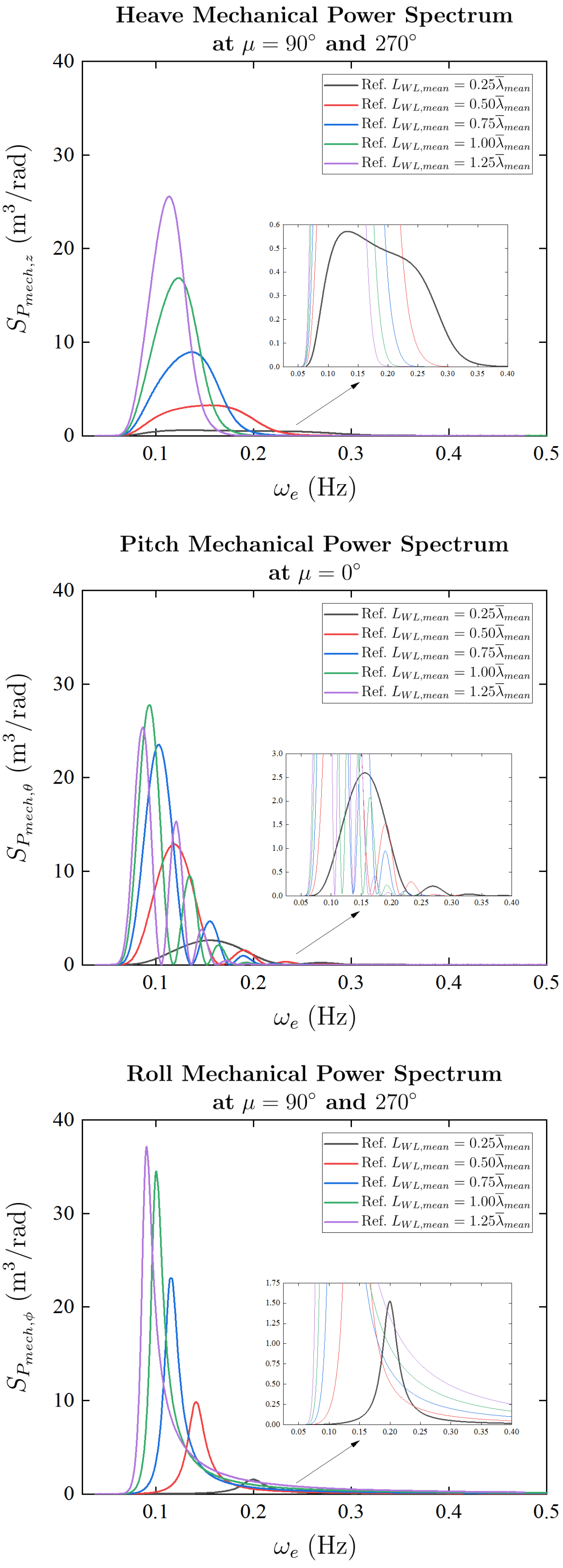

Figure 4.19: Effect of ship scale on motion mechanical power spectra.

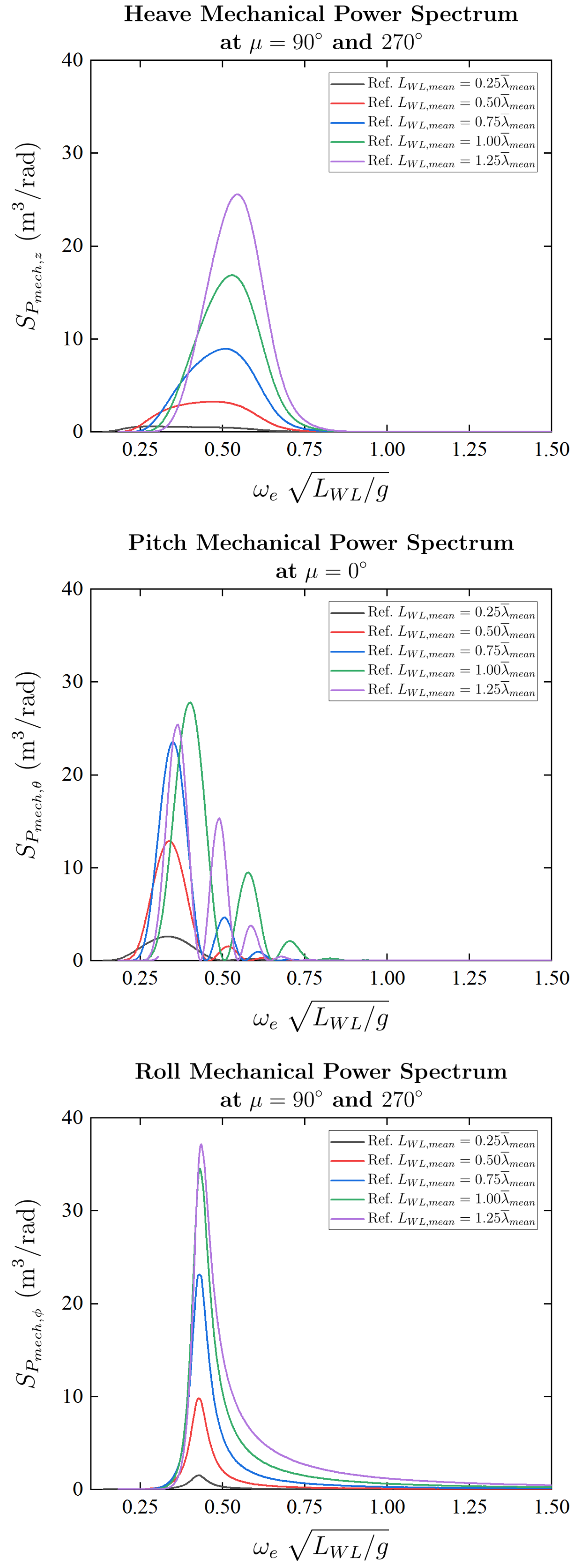

Figure 4.20: Motion mechanical power spectra against non-dimensional encountering frequencies.

Figure 4.15 illustrates the effect of ship scale on the motion transfer functions. The transfer functions generally stretch toward higher frequency response following the reducing geometric scale. This numerical phenomenon can be referred to as the scaling laws provided in Appendix C that is the frequency response of the geometrically scaled vessels changes proportionally to the square-root of scaling factor as shown in Figure 4.21 by remaining the similar response characteristic. Hence, by the linear relationship, the wave power conversion efficiencies of the response motions also change with similar scaling relationship as can be seen in Figure 4.17. To be notice at this point for roll motion, the decaying motion transfer function approach a constant positive value and this causes the large increasing wave power conversion efficiency behaviour toward high encountering frequency as discussed in Section 4.3.3.

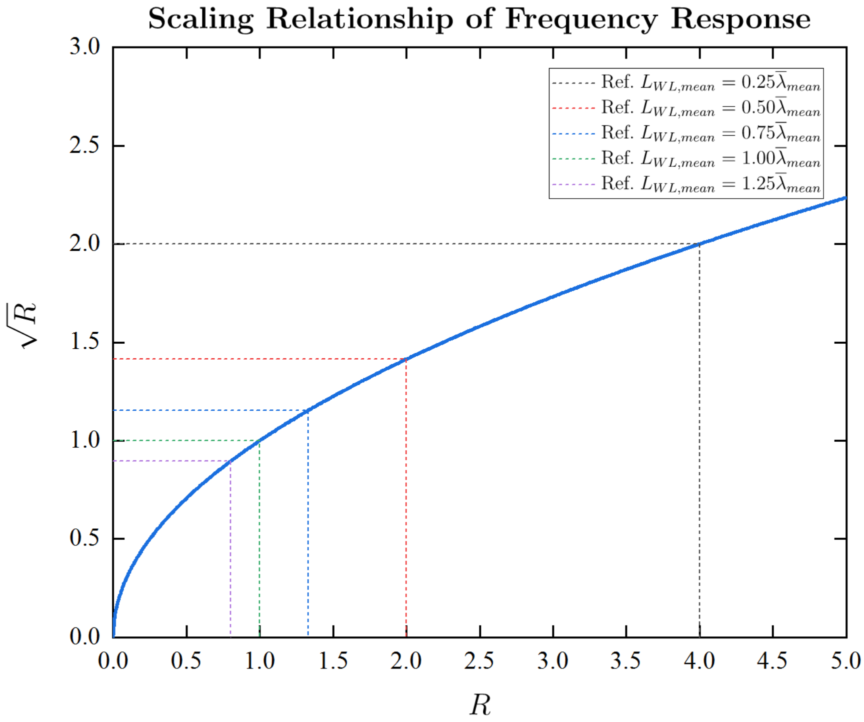

Figure 4.21: Scaling relationship of frequency response.

However, for the motion mechanical spectra, the scaling relationship cannot be here applied. This is due to the wave power spectrum of the sea state is invariable as it is not scaled up and down followed the investigated ship dimension ratios. Also, the motion power spectrum is the product of the wave power spectrum multiply by the wave power conversion efficiency. Observably, the motion power spectra relatively vary to scale of the ship as expected as demonstrated in Figure 4.19. It can be seen that a larger ship responds to low-frequency waves with a narrow responsive band. On the other hand, in the case of a smaller ship, the effect is shown to be reversed.

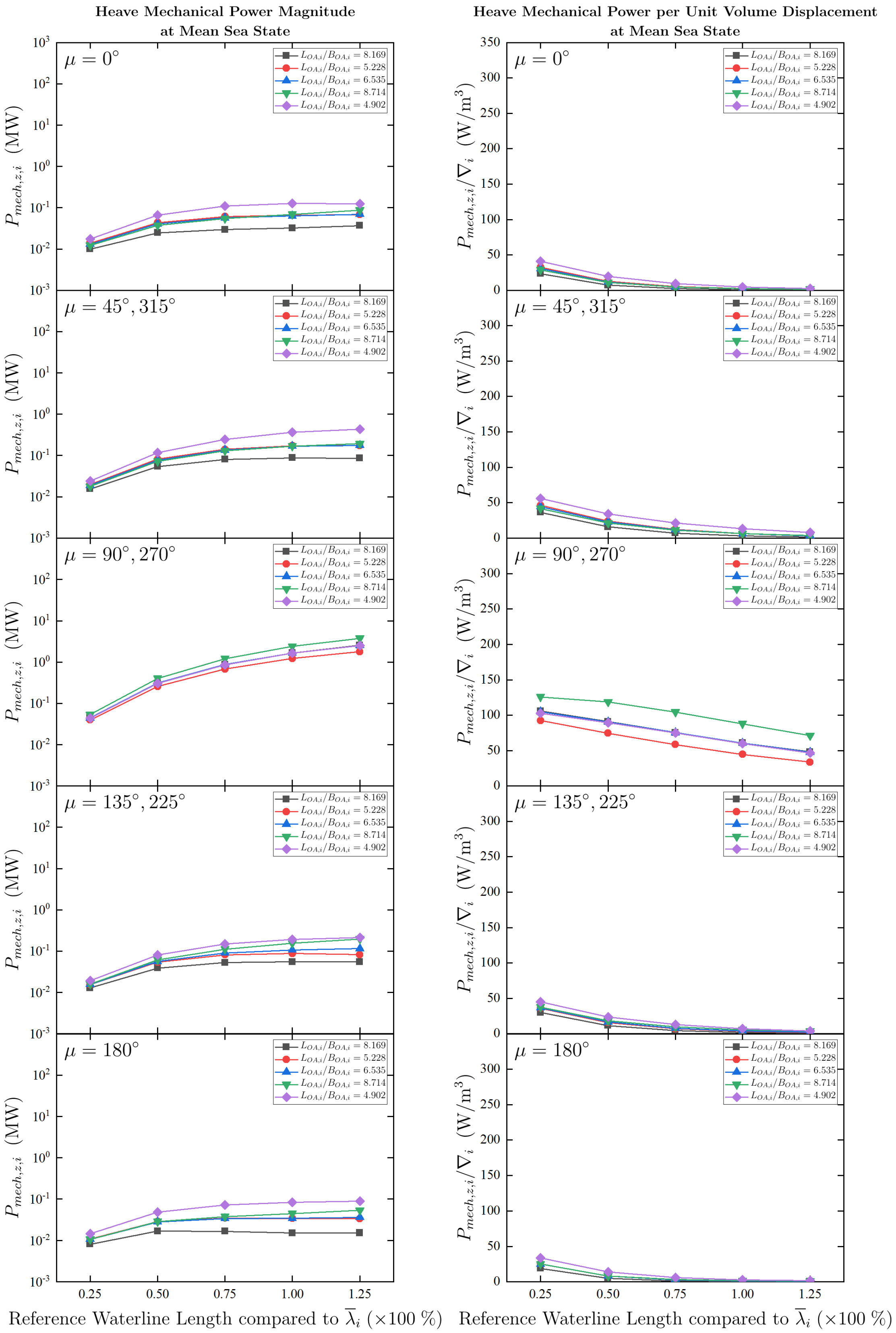

(a) Heave power magnitude (in logarithmic scale).

(b) Heave power per unit volume displacement.

Figure 4.22: Effect of ship scale with different length-to-beam ratios on heave mechanical power at the global mean sea state.

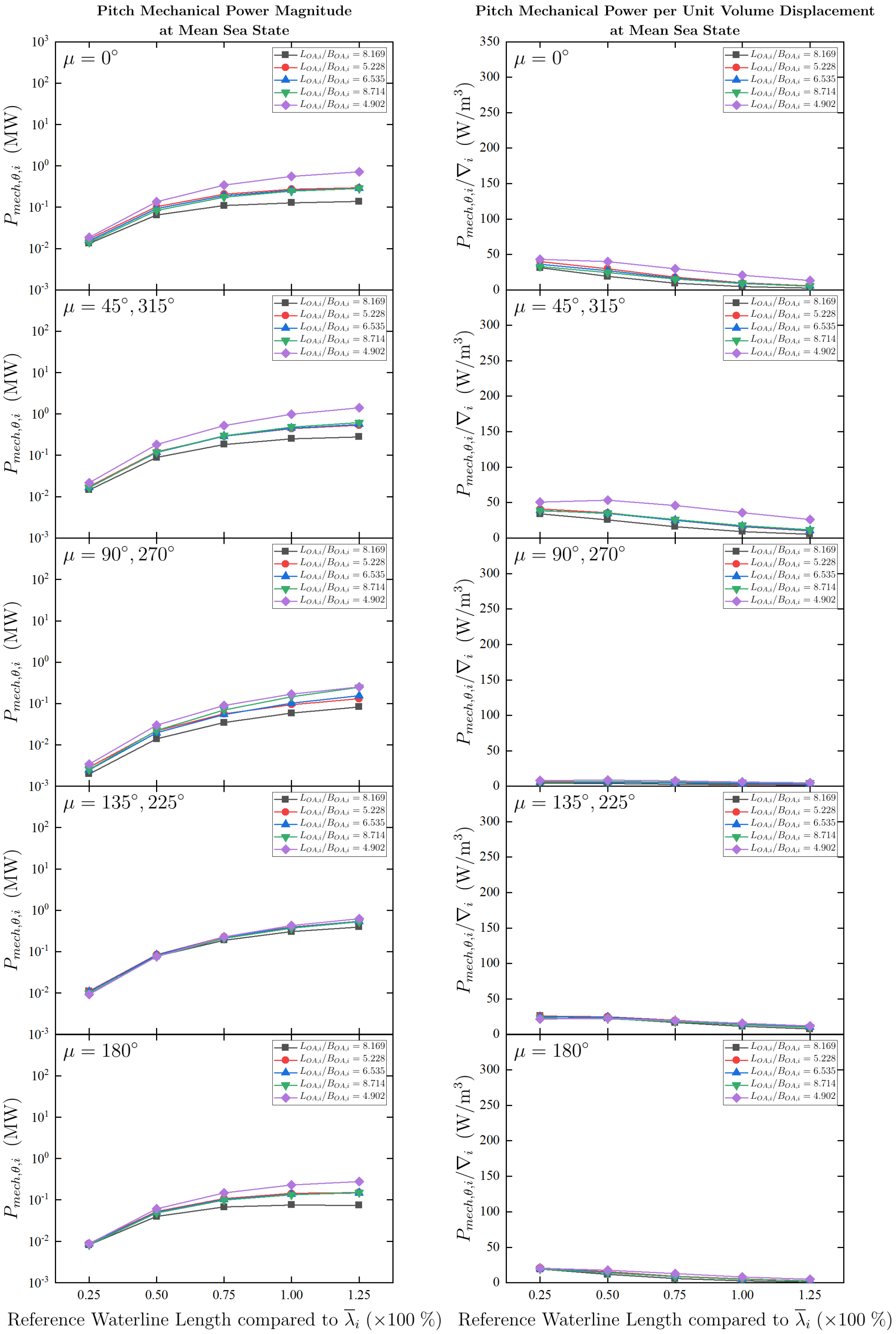

(a) Pitch power magnitude (in logarithmic scale).

(b) Pitch power per unit volume displacement.

Figure 4.23: Effect of ship scale with different length-to-beam ratios on pitch mechanical power at the global mean sea state.

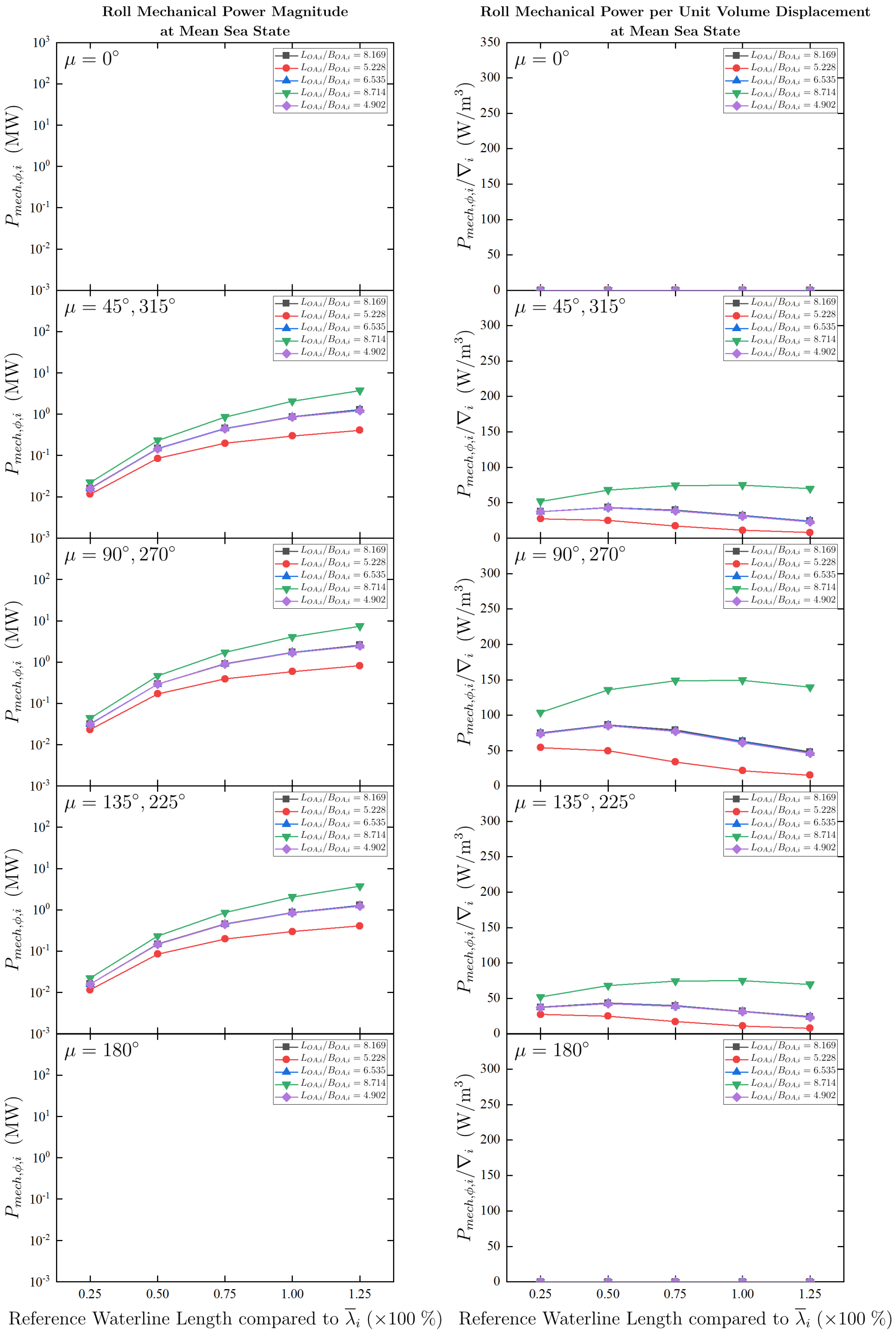

(a) Roll power magnitude (in logarithmic scale).

(b) Roll power per unit volume displacement.

Figure 4.24: Effect of ship scale with different length-to-beam ratios on roll mechanical power at the global mean sea state.

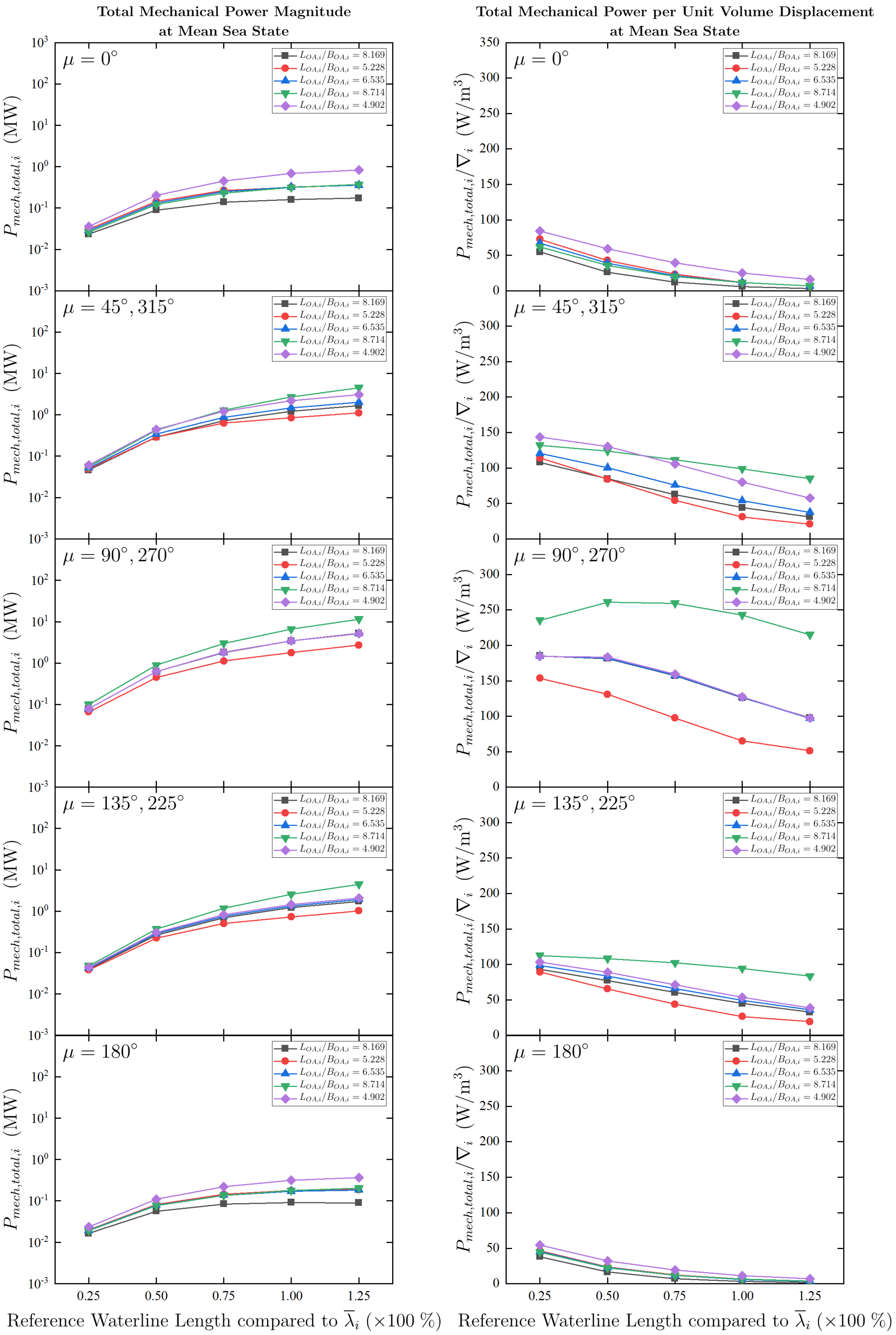

(a) Total power magnitude (in logarithmic scale).

(b) Total power per unit volume displacement.

Figure 4.25: Effect of ship scale with different length-to-beam ratios on total mechanical power at the global mean sea state.

Figures 4.22(a) to 4.25(a) show the available heave, pitch, roll, and total mechanical power magnitudes generated by the ships with the different geometrically scaled and the varied length-to-beam ratios. As a reflection of the motion power spectrum, the level of the motion power magnitude also alters relative to the size of the ship. A larger scale of vessel generates a higher level of available mechanical power from motion and vice versa. Considering the relationships of power from both linear and angular motions in Equation 4.1 with the association of non-dimensional analysis based on scaling relationships in Appendix C, the mechanical power dependent factors can be plotted as shown in Figure 4.26. It can be seen that the power generated by the larger size of a ship is dominated by force, torque, and velocity of linear or the heave motion in this case. The force and torque can be referred to the mass and moments of inertia of the ship. For the smaller vessel, angular velocities of rotational motions as pitch and roll motions are the primary sources of mechanical powers which directly correlate to the angular motion amplitudes and encountering frequency.

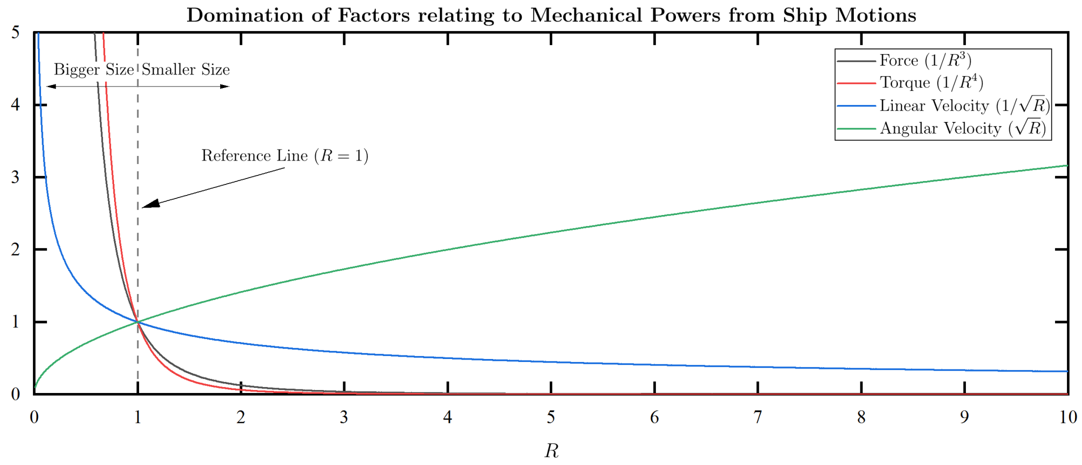

Figure 4.26: Mechanical power dependant factors regarding the ship scale.

In terms of the power generation per unit volume, the motion power generation of the scaled ships are compared by using the power per unit volume displacement or power generation density as shown in Figures 4.22(b) to 4.25(b). Interestingly, the power generation density generally increases followed the smaller scaled of geometric dimension except for the one of roll motion of the most slender vessel, the length-to-beam ratio of 8.714, at the beam and oblique waves. At this length-to-beam ratio, the optimal reference waterline length for the motion appears to be around the length equals to the fraction of 0.75 to 1.00 of the average wavelength that contains the highest wave power density in the global mean sea state ($\bar{\lambda}_{mean}$). Considering the total power generation density at beam sea, however, the optimal reference waterline length of this top-view geometry is at 50% of the average wavelength. For the other cases, the smallest scale of investigated ships exhibits the highest power generation density.

4.3.5 Influence of Sea State to Ship Responses

The ship responses in the global mean sea state have already been analysed in Sections 4.3.3 and 4.3.4. Therefore, in this section, the investigation aims to demonstrate the ship motion responses in the representations of different sea area based on the global wave statistics detailed in Appendix A. As summarised in Figure 4.3, the wave record contains the upper and lower bounds of the average significant wave heights and zero crossing wave periods over the sea areas. The maximum numbers of both the wave height and period can be referred to the deep water region far away from the shore (area no. 99). Moreover, the minimal record was measured from the coastal waters (area no. 5 and 38). Thus, these pairs of the upper and lower limits are presumably used to represent the world possible maximum and minimum sea states.

For convenient comparison, the assumption of adopting the standard wave spectrum formula made in Section 4.3.1 still remains. By using these datasets, the maximum and minimum wave energy and wave power spectra can be calculated as plotted in Figure 4.4. It can be seen that the average wave frequency where the highest wave power contained depends on the average wave period while the vertical ordinate relies on the value of the average significant wave height of the sea area. Note that, the investigated geometric dimensions are proportionally scaled respecting to the fractions of the average wavelengths that comprise the highest wave power densities of the sea states as indicated in Table 4.3.

Table 4.3: Scaling factors of the ships relating to different sea states.

Sea state	Subscription i	$\bar{H}_{1/3}$ (m)	$\bar{T}_z$ (s)	Fraction of waterline length compared to $\bar{\lambda}_i$	$L_{WL,i}$ (m)	$L_{OA,i}$ (m)	R
Minimum	min	1.14024	3.59550	0.25	10.992	11.349	16.384
				0.50	21.985	22.698	8.192
				0.75	32.977	34.047	5.461
				1.00	43.969	45.396	4.096
				1.25	54.961	56.745	3.277
Mean	mean	2.42646	7.28406	0.25	45.023	46.485	4.000
				0.50	90.047	92.969	2.000
				0.75	135.070	139.454	1.333
				1.00	180.093*	185.938*	1.000*
				1.25	225.116	232.423	0.800
Maximum	max	3.84100	8.96747	0.25	68.295	70.511	2.637
				0.50	136.590	141.023	1.318
				0.75	204.884	211.534	0.879
				1.00	273.179	282.045	0.659
				1.25	341.474	352.556	0.527

*Reference ship geometry

Effect of Sea State on Motion Responses

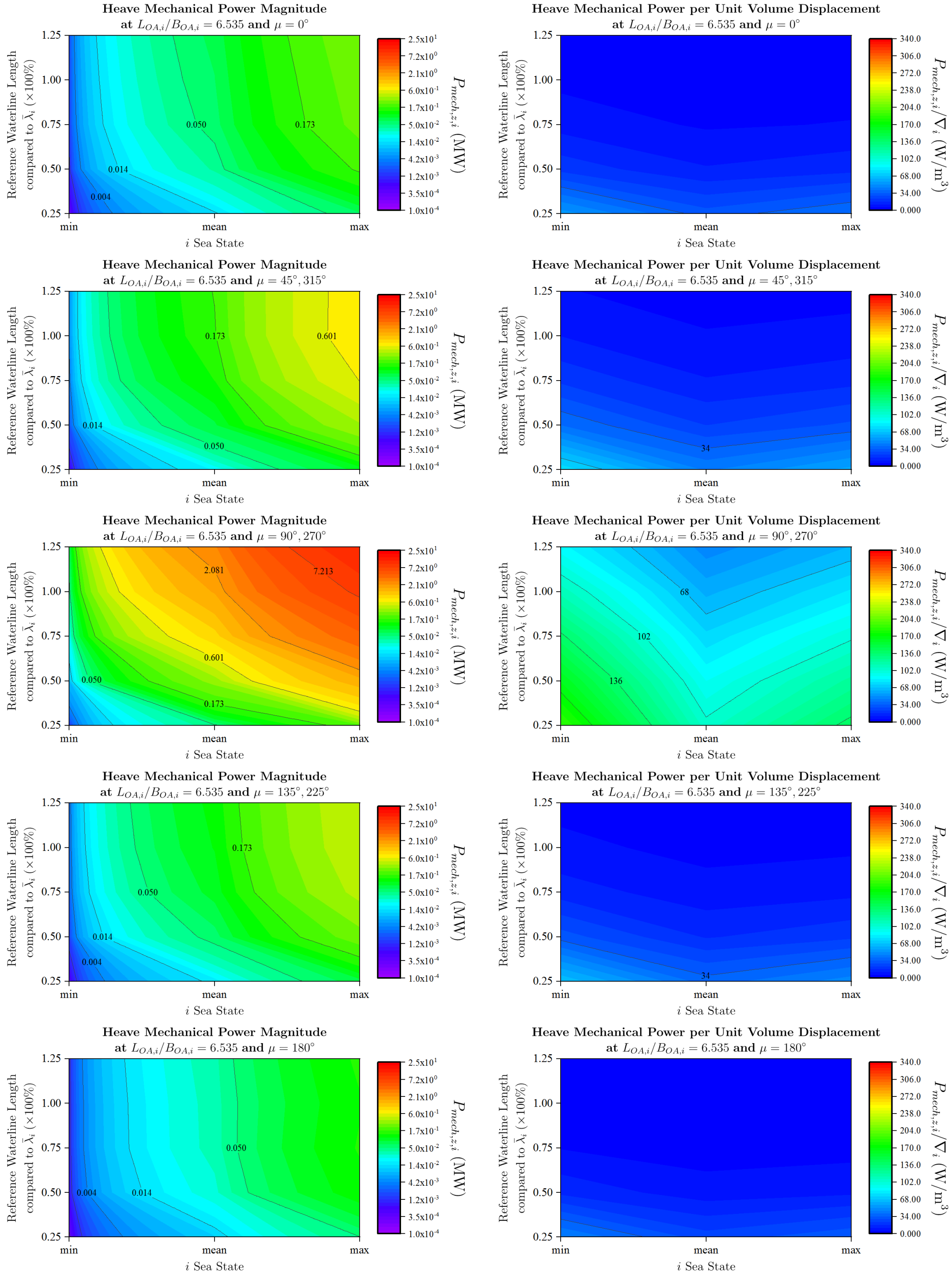

Heave Mechanical Power Magnitude at $L_{OA,i}/B_{OA,i} = 6.535$ and $\mu = 0°$

Heave Mechanical Power per Unit Volume Displacement at $L_{OA,i}/B_{OA,i} = 6.535$ and $\mu = 0°$

Heave Mechanical Power Magnitude at $L_{OA,i}/B_{OA,i} = 6.535$ and $\mu = 45°, 315°$

Heave Mechanical Power per Unit Volume Displacement at $L_{OA,i}/B_{OA,i} = 6.535$ and $\mu = 45°, 315°$

Heave Mechanical Power Magnitude at $L_{OA,i}/B_{OA,i} = 6.535$ and $\mu = 90°, 270°$

Heave Mechanical Power per Unit Volume Displacement at $L_{OA,i}/B_{OA,i} = 6.535$ and $\mu = 90°, 270°$

Heave Mechanical Power Magnitude at $L_{OA,i}/B_{OA,i} = 6.535$ and $\mu = 135°, 225°$

Heave Mechanical Power per Unit Volume Displacement at $L_{OA,i}/B_{OA,i} = 6.535$ and $\mu = 135°, 225°$

Heave Mechanical Power Magnitude at $L_{OA,i}/B_{OA,i} = 6.535$ and $\mu = 180°$

Heave Mechanical Power per Unit Volume Displacement at $L_{OA,i}/B_{OA,i} = 6.535$ and $\mu = 180°$

(a) Heave power magnitude (in logarithmic scale).

(b) Heave power per unit volume displacement.

Figure 4.27: Effect of sea state to heave mechanical power.

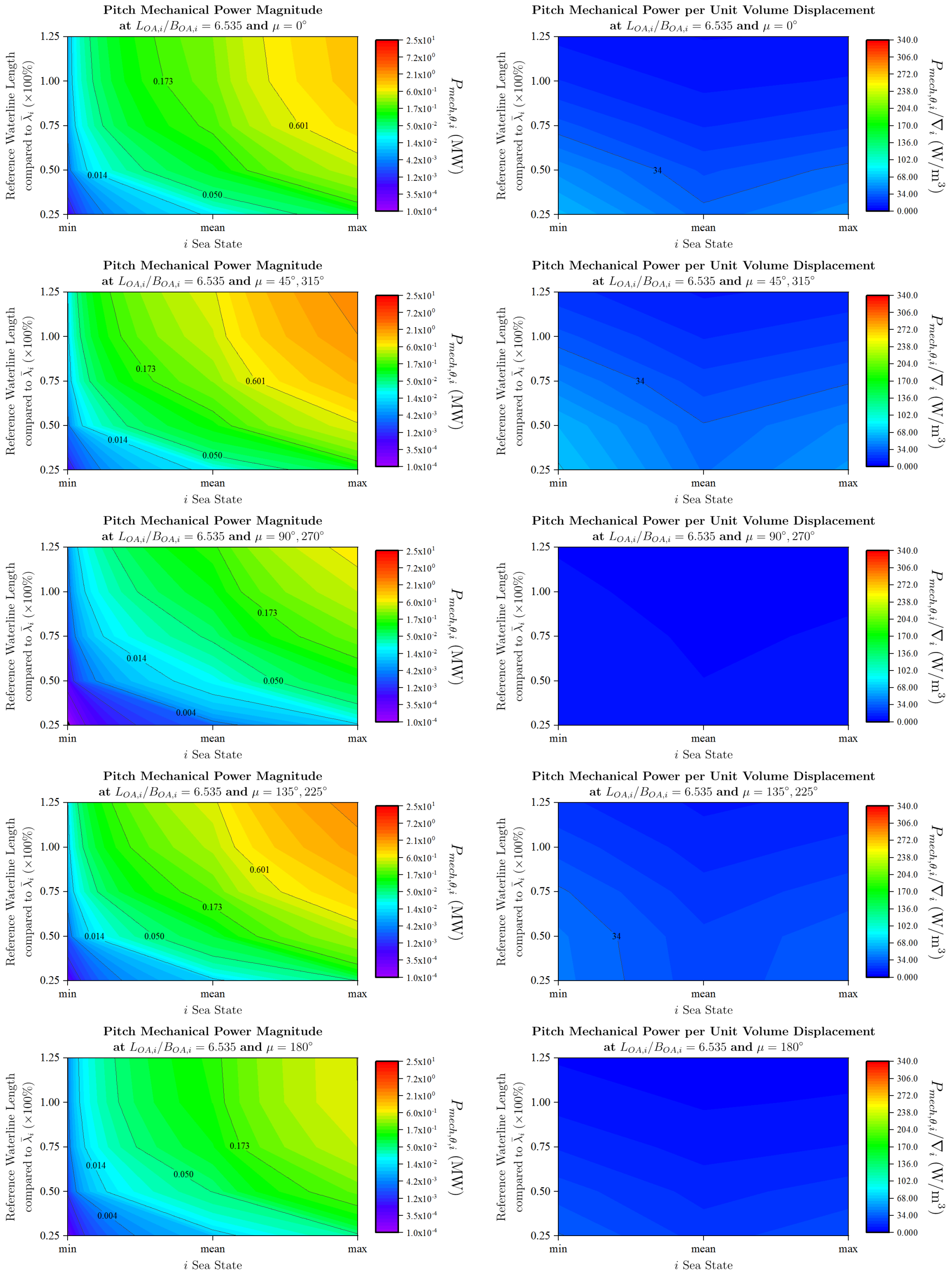

(a) Pitch power magnitude (in logarithmic scale).

(b) Pitch power per unit volume displacement.

Figure 4.28: Effect of sea state to pitch mechanical power.

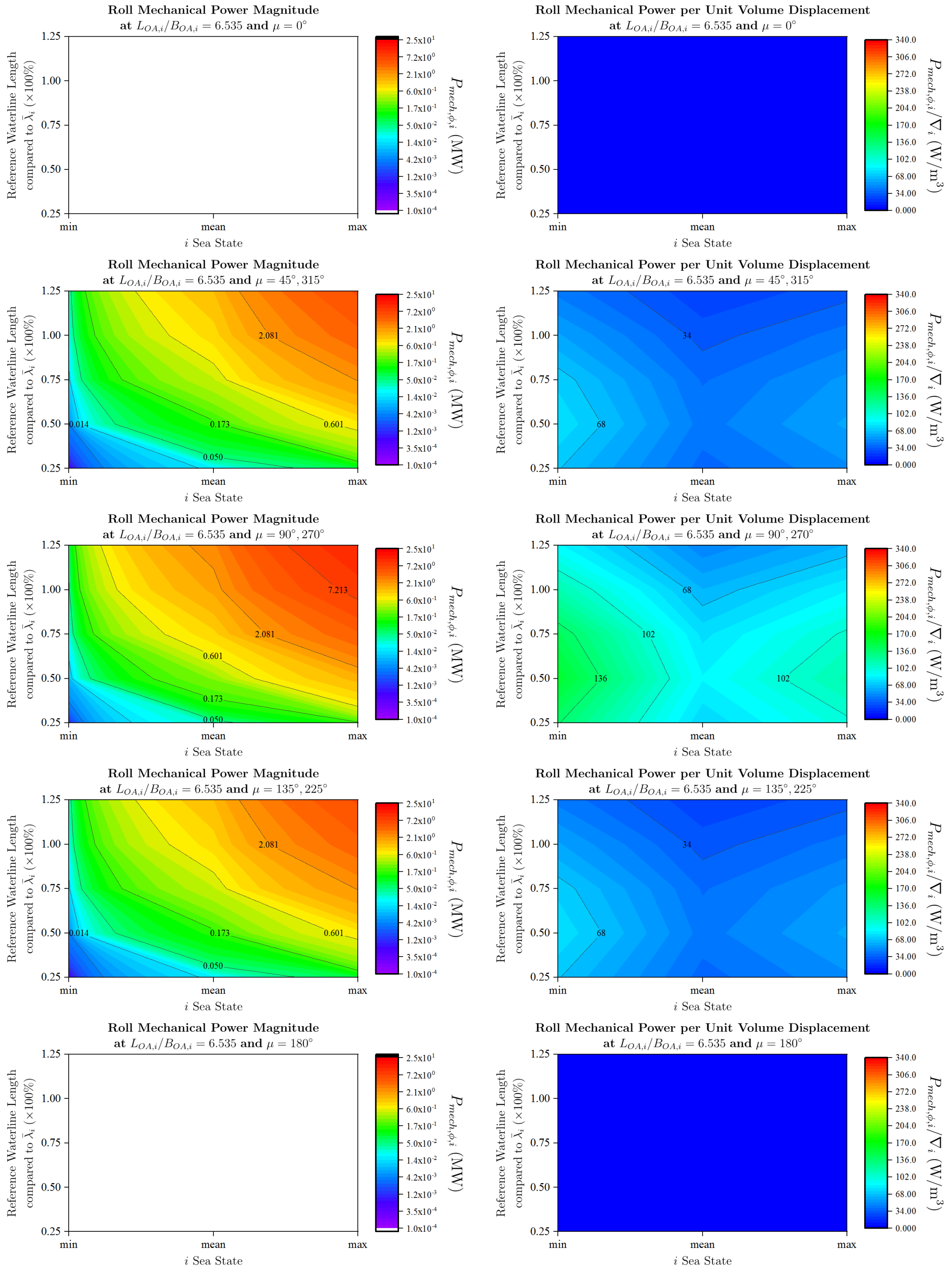

(a) Roll power magnitude (in logarithmic scale).

(b) Roll power per unit volume displacement.

Figure 4.29: Effect of sea state to roll mechanical power.

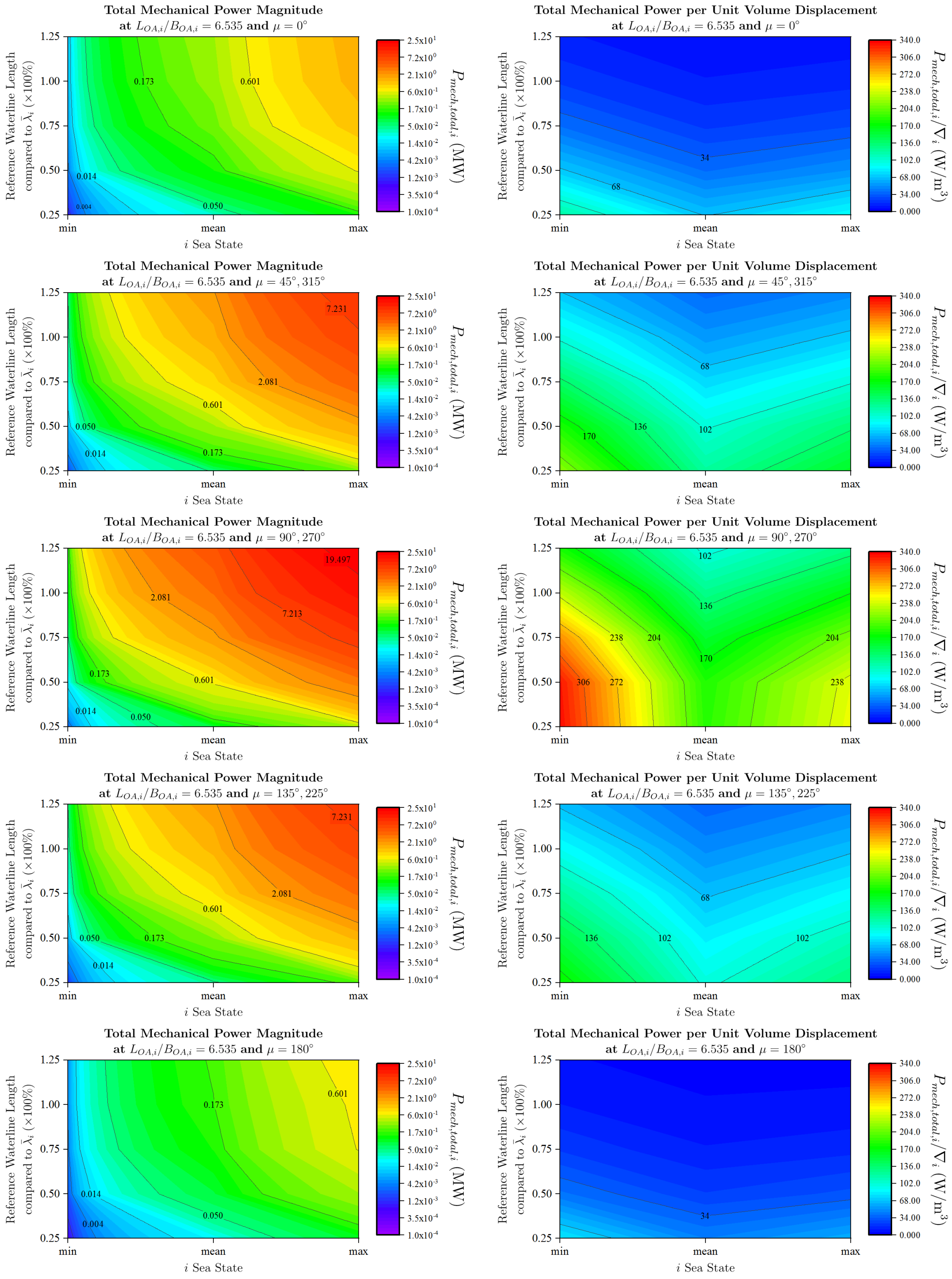

(a) Total power magnitude (in logarithmic scale). (b) Total power per unit volume displacement.

Figure 4.30: Effect of sea state to total mechanical power.

Figures 4.27 to 4.30 display the contour plots of the available motion mechanical powers and power generation densities of the ship respecting to the variations of geometric scale and reference sea state. Similar to the results previously presented in Section 4.3.4, as expected, the dependence of the motion mechanical power level on the size of the ship is still corroborated in any sea state. In this case, this also relates to the wave power spectrum of the sea state. Besides, regarding the power per volume displacement at an individual sea state, the power density concentrates more on the smaller scaled ship. However, in comparison, the scaled ship operating in the minimum sea state provides the highest power generation density, and the lowest is the ship at the mean sea state.

In this manner, therefore, a small ship operating in the sea state along the coastal water could offer more available mechanical power per volume that predominated by rotational motions than a mass possessed power by a larger scaled ship which has the operational basis in the middle of the ocean. This could be a beneficial factor for the design consideration for an energy conversion mechanism using motions of a ship in the real sea state.

4.4 Summary

A novel methodology of assessing available mechanical power from the motions of a ship in a sea state is provided. This assessment method adopts the statistical technique of describing the characteristic of the irregular sea and the seakeeping analysis of ship responses in the waves in a wave energy conversion aspect. Therefore, the available mechanical powers from the motions of a ship in a sea state can be determined. The numerical investigation is proposed upon the variations of heading condition, ship geometry, and ship scale relative to the applied sea state at zero speed.

With the consideration of utilising oscillatory motions (heave, pitch, and roll motions) for a port-starboard symmetry ship, the results show that the responses of the motions vary as a function of heading condition and also the geometry of the ship. By keeping ship volume displacement and transverse metacentric height constant, the changing in the transverse dimension, the ship beam, typically affects the motion response amplitude in heave and pitch and the frequency response in roll. Moreover, the changing in ship length does not contribute significant effect on the roll but influence the frequency response of the heave and pitch. This is because of the response transfer functions of the coupled heave and pitch motions are calculated based on the linear 2-D strip theory that directly relates to the immersed or underwater part of the ship. However, for the roll motion, it is modelled from the contribution of the ship inertial and hydrostatic properties, and it is uncoupled.

In terms of available mechanical powers from the motions, these oscillatory motions are able to individually and simultaneously offer an enormous level of mechanical power that is available to be harvested. Nonetheless, the magnitudes of the power also vary by the ship directional responses respecting the heading conditions. In the beam sea, the powers from the heave and roll motions are much higher than the one of the pitch. In contrast, for the following and head waves, pitch motion generates more power compared to the heave and, especially, to the roll which is nothing. However, by including the powers from the associated motions, the directional available mechanical power is obviously elevated. Therefore, the consideration of the harvesting energy from the multiple-DOF ship dynamics is encouraged as the expectation of having a uni-directional excitation and single-DOF ship dynamics in the real sea is too idealistic.

Based on the non-dimensional analysis, the magnitudes of the mechanical powers from the large-scaled ship are controlled by the mass distribution (weight and moment of inertia) and the velocity of linear or heave motion. Nevertheless, for the smaller vessel, the angular motions (pitch and roll) and encountering frequency are the dominant factors of the power sources from the ship dynamics in waves. For the available power per volume, generally, a small-scaled ship operating in the coastal water zone which contains high wave frequency could offer higher power density compared to a relatively large ship in the faraway shore sea state with high wave period.

Chapter 5

Numerical Modelling and Experimental Valodation of a Gimballed Pendulum System

This chapter describes the numerical modelling and a set of experimental investigations of a gimballed pendulum system which is the energy conversion mechanism used for harvesting energy from ship motions for this research. First, a general concept design of a 2-axis gimbal mechanism applying to a pendulum system is introduced, and it is compared to the existing numerical model, spherical pendulum model, based on its working principle. Next, a novel theoretical model of a gimballed pendulum is presented and detailed. Then, a set of experimental investigations for the model validation is indicated with the results are lastly shown and discussed.

5.1 Introduction of 2-Axis Gimbal Mechanism

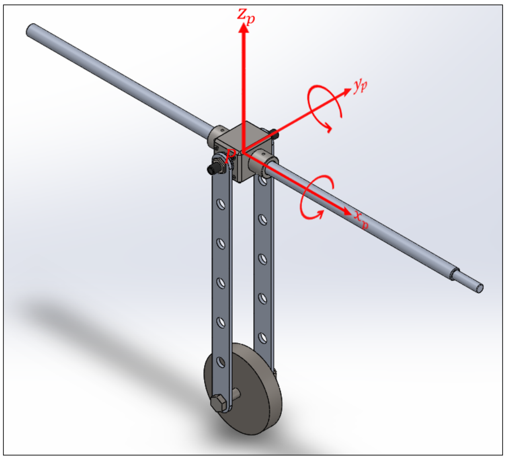

Figure 5.1: Graphical design of a 2-axis gimbal mechanism.

A 2-axis gimbal mechanism (or universal joint) is a support point consisted of a set of two orthogonal pivots that allows a mounted object to rotate around the two reference crossing axes. As in this way, the object is able to achieve spherical-path rotation.

5.2 Governing Equation and Existing Numerical Models of Spherical-path Pendulum Systems

Note that, the equations of motion of pendulum systems that are used in this research are non-linear solution as the pendulum motion is considered as not always small and therefore linearised equation of a pendulum motion is not valid, see Appendix D.1.1 for detail.

5.2.1 Introduction of Lagrange's Equation

Lagrange's equation is a second-order partial differential equation that is used to solve dynamic problems. Moreover, it is equivalent to the Newton's laws of motion but it has the advantage of having similar form in any generalised coordinate or DOF of a dynamic system. This governing equation relates to the difference between the kinetic and potential energies evolved from a known initial state to a identified final state. The standard form of Lagrange's equation in a generalised coordinate is defined as:

$$\frac{d}{dt}\left(\frac{\partial L}{\partial \dot{q}_i}\right) - \frac{\partial L}{\partial q_i} = Q_i \tag{5.1}$$

where L is a mathematic function called 'Lagrangian' which is

$$L = KE - PE \tag{5.2}$$

where KE is the total kinetic energy (J), PE is the potential energy (J) of the system, and Q_i is the generalised force or torque that is normally defined as frictional damping and control force or torque applied to the system (Inman, 2014).

5.2.2 Spherical Pendulum System

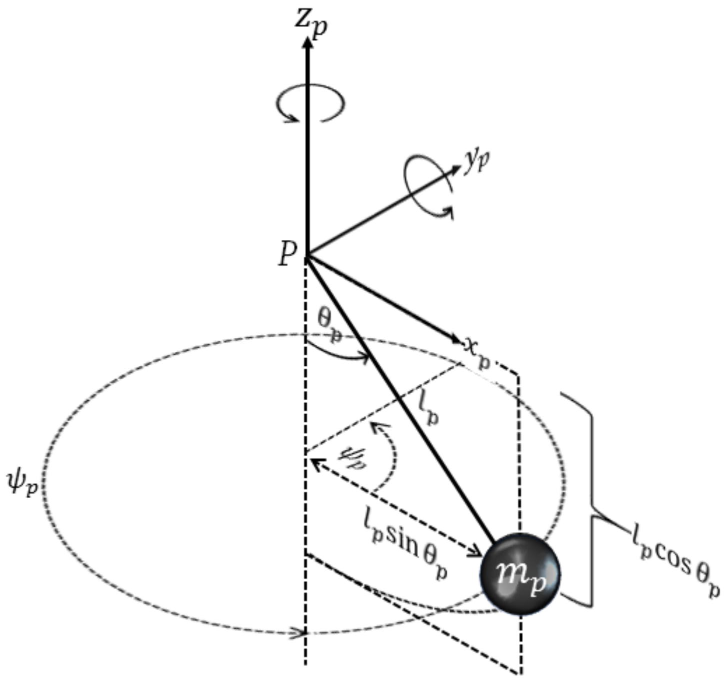

Figure 5.2: Schematic diagram of a spherical pendulum system.

The dynamics of a spherical-path pendulum is usually referred to as a spherical or conical pendulum system defined in both three-dimensional (3-D) Cartesian and polar coordinate systems as illustrated in Figure 5.2. The motion of this pendulum system can be mathematically expressed as 2-DOF dynamics system as:

$$m_p l_p^2 \ddot{\theta}_p(t) + m_p g l_p \sin(\theta_p(t)) - m_p l_p^2 \sin(\theta_p(t)) \cos(\theta_p(t)) \dot{\psi}_p(t)^2 = Q_{\theta_p}, \tag{5.3}$$

$$m_p l_p^2 \sin(\theta_p(t))^2 \ddot{\psi}_p(t) = Q_{\psi_p} \tag{5.4}$$

by the numerical derivation of the equations of motion, equations 5.3 and 5.4 can be found in Section E.1 in Appendix E where m_p is the pendulum mass (kg), l_p is the length of the pivot-to-CG of the pendulum or the pendulum arm (m), g is the acceleration due to gravity (m/s^2). The angular motions of this pendulum system are defined regarding two generalised coordinates; θ_p and ψ_p are the DOFs describing the angular position of the pendulum respecting the vertical axis (z_p-axis) and the angular position on the horizontal plane ($x_p y - p$-plane) that is referenced to the x_p-axis or azimuth angle with the generalised torques, Q_θ and Q_ψ, respectively.

5.2.3 Driven Spherical Pendulum System

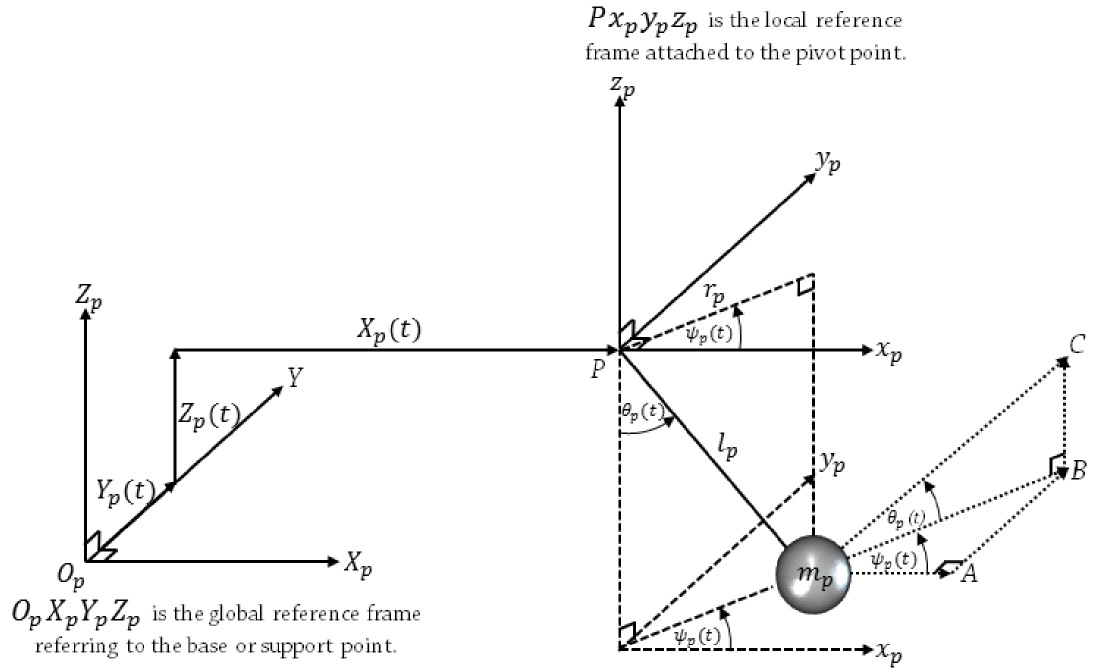

Figure 5.3: Schematic diagram of a driven spherical pendulum system.

The extension of the previous pendulum model is to applied external excitation. The externally excited or driven spherical pendulum can be diagrammatically indicated in Figure 5.3 and can also be numerically represented in the equations of motion as:

$$
\begin{aligned}
&m_pl_p^2\ddot{\theta}_p(t) + m_pgl_p\sin(\theta_p(t)) - m_pl_p^2\sin(\theta_p(t))\cos(\theta_p(t))\dot{\psi}_p(t)^2 \\
&+ m_{\theta_p}l_{\theta_p}\Big(\ddot{X}(t)\cos(\theta_p(t))\cos(\psi_p(t)) + \ddot{Y}(t)\cos(\theta_p(t))\sin(\psi_p(t)) \\
&+ \ddot{Z}(t)\sin(\theta_p(t))\Big) = Q_{\theta_p},
\end{aligned}
\tag{5.5}
$$

$$
\begin{aligned}
&m_pl_p^2\sin(\theta_p(t))^2\ddot{\psi}_p(t) + 2m_pl_p^2\sin(\theta_p(t))\cos(\theta_p(t))\dot{\theta}_p(t)\dot{\psi}_p(t) \\
&- m_pl_p\sin(\theta_p(t))\Big(\ddot{X}(t)\sin(\psi_p(t)) + m_pl_p\ddot{Y}(t)\cos(\psi_p(t))\Big) = Q_{\psi_p}
\end{aligned}
\tag{5.6}
$$

where the definitions of the property and orientation of the pendulum are identical to the non-driven case. In addition, $\ddot{X}$, $\ddot{Y}$, and $\ddot{Z}$ are the accelerations (m/s^2) of the external excitation along x-, y-, and z-axes. Note that, the full derivation of this driven pendulum system is provided in Section E.2 in Appendix E.

5.2.4 Remark Discussion of the Existing Pendulum Models

The existing spherical pendulum models indicated in both Sections 5.2.2 and 5.2.3 are unable to theoretically explain the dynamics of a pendulum hanged on a gimballed pendulum. Due to, first, the rotating definition made in the spherical pendulum models not representing the rotating arrangement provided by a 2-axis gimbal mechanism. Second, a gimbal mechanism potentially creates asymmetric inertial properties of two perpendicular pivots, but the existing models only suggest symmetric inertia. Therefore, to numerically model a gimballed pendulum system and to understand its coupled dynamics are major challenges.

5.3 Dynamics of a Gimballed Pendulum System

Consider a system of a compound or physical pendulum hanging on a support point representing local coordinate ($Px_py_pz_p$) in a 3-D Cartesian coordinate system as illustrated in Figure 5.4. The pendulum is allowed to rotate around both horizontal axes (x_p- and y_p-axes) via two perpendicular pivots representing a gimbal mechanism. The dual perpendicular pivots ideally enable the directional response based on the multi-directional disturbance or excitation in the 3-D space along x_p-, y_p-, and z_p-axes. The presence of the gimballed pivots virtually creates two perpendicular projected simple or 1-DOF pendulum systems with a shared vertical referenced axis (z_p-axis). Importantly, from this mechanical arrangement, the physical properties such as mass distributions and damping terms of these two individual pendulum systems are not necessarily symmetric.

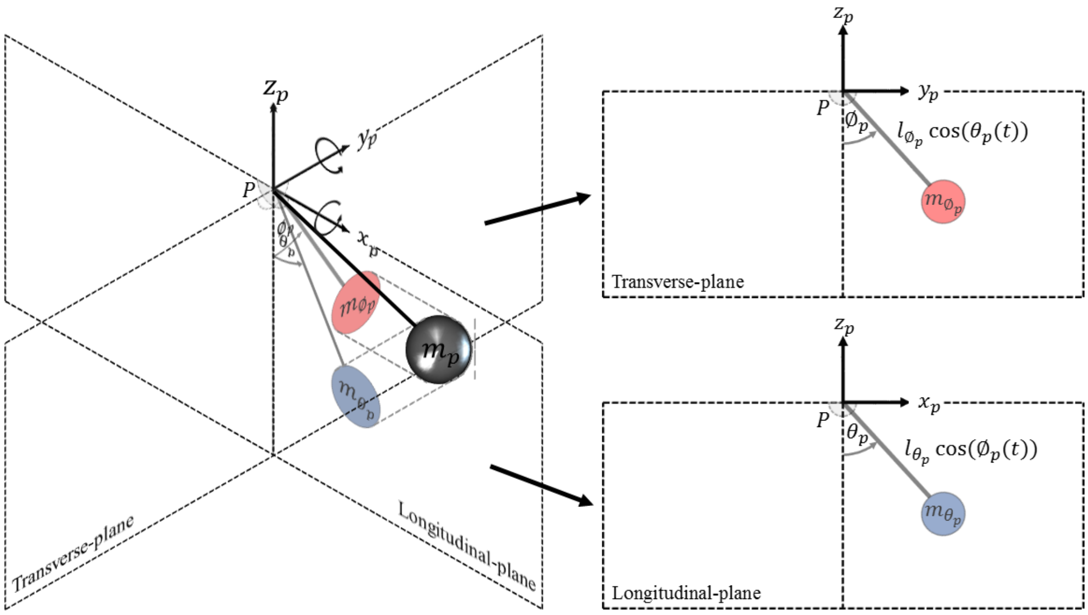

Figure 5.4: Schematic diagram of a driven gimballed pendulum system.

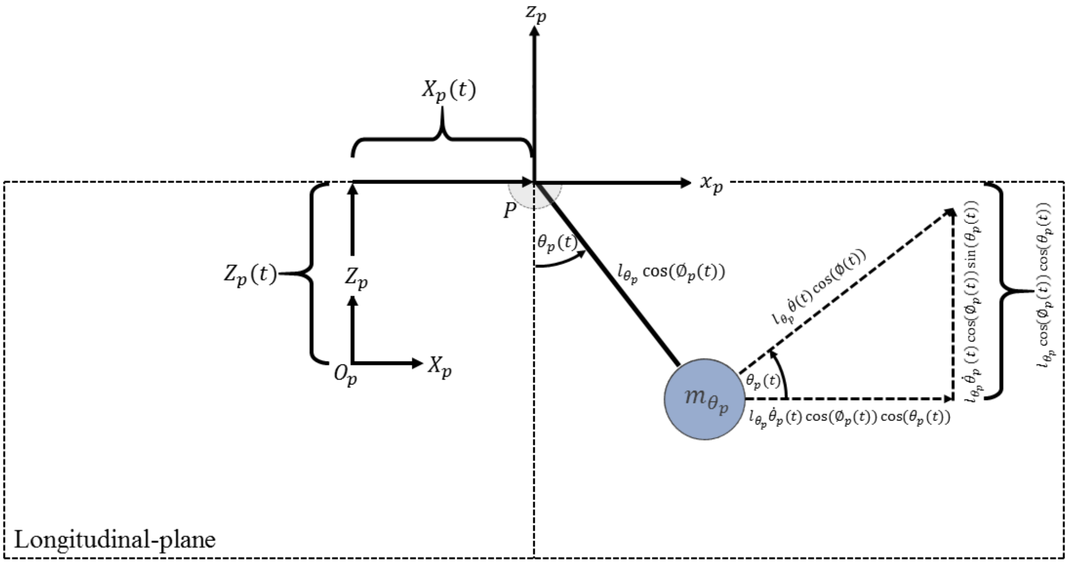

(a) Longitudinal-plane or θ_p-plane pendulum reference.

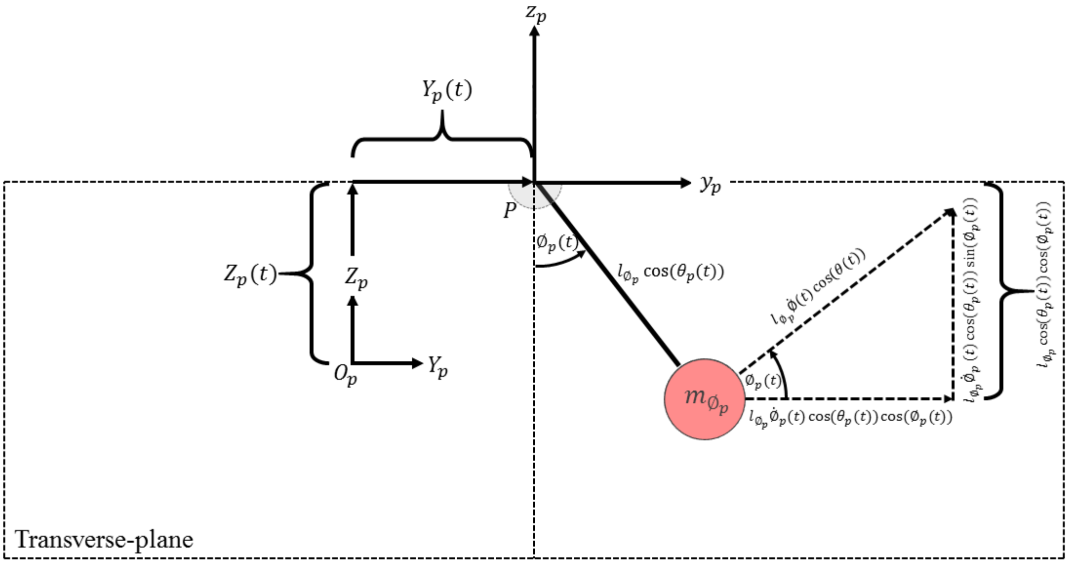

(b) Transverse-plane or ϕ_p-plane pendulum reference.

Figure 5.5: Coupled pendulum references.

The pendulum system graphically presented in Figure 5.4 is simplified and divided into two coupled planar pendulum systems which are 'longitudinal-plane' and 'transverse-plane' given as θ_p- and ϕ_p-planes pendulum systems respectively as illustrated in Figures 5.5(a) and 5.5(b). The local coordinates of the two pendulum references are defined as Px_pz_p for θ_p-plane and Py_pz_p for ϕ_p-plane. Each pendulum system consists of a mass (m_{θ_p} or m_{ϕ_p}) supported at a pivot from a distance away from the CG (l_{θ_p} or l_{ϕ_p}). So, there are two generalised coordinates, θ_p and ϕ_p, defined for these coupled pendulum systems.

Once the axial excitations along x_p-, y_p-, and z_p-axes are applied, the pivoted point (P) is moved away from the initial position representing global coordinate $OX_pY_pZ_p$ with the distances in X_p, Y_p, and Z_p. As both pendulum dynamics are coupled with the cosine functions, $\cos(\theta_p(t))$ and $\cos(\phi_p(t))$, the kinetic and potential energies for the θ_p-plane pendulum can therefore be calculated as:

$$\begin{aligned}
KE_{\theta_p}(t) &= \frac{1}{2}m_{\theta_p}v_{\theta_p}(t)^2 \\
&= \frac{1}{2}m_{\theta_p}\Big(\mathbf{v}_{x_p}(t) + \mathbf{v}_{z_p}(t)\Big)^2 \\
&= \frac{1}{2}m_{\theta_p}\Big(\big(\dot{X}_p(t) + l_{\theta_p}\dot{\theta}_p(t)\cos(\phi_p(t))\cos(\theta_p(t))\big) \\
&\qquad + \big(\dot{Z}_p(t) + l_{\theta_p}\dot{\theta}_p(t)\cos(\phi_p(t))\sin(\theta_p(t))\big)\Big)^2 \\
&= \frac{1}{2}m_{\theta_p}\Big(\dot{X}_p(t) + \dot{Z}_p(t) + l_{\theta_p}^2\dot{\theta}_p(t)^2\cos(\phi_p(t))^2 \\
&\qquad + 2l_{\theta_p}\dot{\theta}_p(t)\cos(\phi_p(t))\big(\dot{X}_p(t)\cos(\theta_p(t)) + \dot{Z}_p(t)\sin(\theta_p(t))\big)\Big), \qquad (5.7)
\end{aligned}$$

$$\begin{aligned}
PE_{\theta_p}(t) &= m_{\theta_p}gh_{\theta_p}(t) \\
&= m_{\theta_p}gZ_p(t) + m_{\theta_p}gl_{\theta_p}\cos(\phi_p(t))\Big(1 - \cos(\theta_p(t))\Big), \qquad (5.8)
\end{aligned}$$

and, from Equation 5.2, the Lagrangian of the longitudinal-plane reference (L_{θ_p}) is

$$\begin{aligned}
L_{\theta_p}(t) = \frac{1}{2}m_{\theta_p}\Big(&\dot{X}_p(t) + \dot{Z}_p(t) + l_{\theta_p}^2\dot{\theta}_p(t)^2\cos(\phi_p(t))^2 \\
&+ 2l_{\theta_p}\dot{\theta}_p(t)\cos(\phi_p(t))\big(\dot{X}_p(t)\cos(\theta_p(t)) + \dot{Z}_p(t)\sin(\theta_p(t))\big)\Big) \\
&- m_{\theta_p}gZ_p(t) + m_{\theta_p}gl_{\theta_p}\cos(\phi_p(t))\Big(1 - \cos(\theta_p(t))\Big). \qquad (5.9)
\end{aligned}$$

Likewise, for the ϕ-plane pendulum, as:

$$\begin{aligned}
KE_{\phi_p}(t) &= \frac{1}{2}m_{\phi_p}v_{\phi_p}(t)^2 \\
&= \frac{1}{2}m_{\phi_p}\Big(\mathbf{v}_{y_p}(t)+\mathbf{v}_{z_p}(t)\Big)^2 \\
&= \frac{1}{2}m_{\phi_p}\Big(\big(\dot{Y}_p(t)+l_{\phi_p}\dot{\phi}_p(t)\cos(\theta_p(t))\cos(\phi_p(t))\big) \\
&\qquad +\big(\dot{Z}_p(t)+l_{\phi_p}\dot{\phi}_p(t)\cos(\theta_p(t))\sin(\phi_p(t))\big)\Big)^2 \\
&= \frac{1}{2}m_{\phi_p}\Big(\dot{Y}_p(t)+\dot{Z}_p(t)+l_{\phi_p}^2\dot{\phi}_p(t)^2\cos(\theta_p(t))^2 \\
&\qquad +2l_{\phi_p}\dot{\phi}_p(t)\cos(\theta_p(t))\big(\dot{Y}_p(t)\cos(\phi_p(t))+\dot{Z}_p(t)\sin(\phi_p(t))\big)\Big), \qquad (5.10)
\end{aligned}$$

$$\begin{aligned}
PE_{\phi_p}(t) &= m_{\phi_p}gh_{\phi_p}(t) \\
&= m_{\phi_p}gZ_p(t)+m_{\phi_p}gl_{\phi_p}\cos(\theta_p(t))\Big(1-\cos(\phi_p(t))\Big), \qquad (5.11)
\end{aligned}$$

and, therefore, the Lagrangian of the transverse-plane reference (L_{ϕ_p}) is

$$\begin{aligned}
L_{\phi_p}(t) = \frac{1}{2}m_{\phi_p}\Big(&\dot{Y}_p(t)+\dot{Z}_p(t)+l_{\phi_p}^2\dot{\phi}_p(t)^2\cos(\theta_p(t))^2 \\
&+2l_{\phi_p}\dot{\phi}_p(t)\cos(\theta_p(t))\big(\dot{Y}_p(t)\cos(\phi_p(t))+\dot{Z}_p(t)\sin(\phi_p(t))\big)\Big) \\
&-m_{\phi_p}gZ_p(t)+m_{\phi_p}gl_{\phi_p}\cos(\theta_p(t))\Big(1-\cos(\phi_p(t))\Big). \qquad (5.12)
\end{aligned}$$

From the Lagrange equation (Equation 5.1), the governing equations in the two generalised coordinates for this pendulum system are

$$\frac{d}{dt}\left(\frac{\partial L_{\theta_p}}{\partial\dot{\theta}_p}\right)-\frac{\partial L_{\theta_p}}{\partial\theta_p}=Q_{\theta_p}, \qquad (5.13)$$

$$\frac{d}{dt}\left(\frac{\partial L_{\phi_p}}{\partial\dot{\phi}_p}\right)-\frac{\partial L_{\phi_p}}{\partial\phi_p}=Q_{\phi_p}. \qquad (5.14)$$

Finally, the equations of motion of this gimballed pendulum system can be formulated as:

$$\begin{aligned}
&\ddot{\theta}_p(t) + \frac{m_{\theta_p} g l_{\theta_p}}{I_{\theta_p} \underbrace{\cos(\phi_p(t))}_{\text{Coupling Term}}} \sin(\theta_p(t)) + \frac{m_{\theta_p} l_{\theta_p}}{I_{\theta_p} \underbrace{\cos(\phi_p(t))}_{\text{Coupling Term}}} \Big(\ddot{X}_p(t)\cos(\theta_p(t)) + \ddot{Z}_p(t)\sin(\theta_p(t))\Big) \\
&\quad \underbrace{-\dot{\phi}_p(t)\sin(\phi_p(t))\Big(\frac{2\dot{\theta}_p(t)}{\cos(\phi_p(t))} + \frac{m_{\theta_p} l_{\theta_p}}{I_{\theta_p}\cos(\phi_p(t))^2}\big(\dot{X}_p(t)\cos(\theta_p(t)) + \dot{Z}_p(t)\sin(\theta_p(t))\big)\Big)}_{\text{Coupling Term}} \\
&\quad = \frac{Q_{\theta_p}}{I_{\theta_p} \underbrace{\cos(\phi_p(t))^2}_{\text{Coupling Term}}},
\end{aligned} \tag{5.15}$$

$$\begin{aligned}
&\ddot{\phi}_p(t) + \frac{m_{\phi_p} g l_{\phi_p}}{I_{\phi_p} \underbrace{\cos(\theta_p(t))}_{\text{Coupling Term}}} \sin(\phi_p(t)) + \frac{m_{\phi_p} l_{\phi_p}}{I_{\phi_p} \underbrace{\cos(\theta_p(t))}_{\text{Coupling Term}}} \Big(\ddot{Y}_p(t)\cos(\phi_p(t)) + \ddot{Z}_p(t)\sin(\phi_p(t))\Big) \\
&\quad \underbrace{-\dot{\theta}_p(t)\sin(\theta_p(t))\Big(\frac{2\dot{\phi}_p(t)}{\cos(\theta_p(t))} + \frac{m_{\phi_p} l_{\phi_p}}{I_{\phi_p}\cos(\theta_p(t))^2}\big(\dot{Y}_p(t)\cos(\phi_p(t)) + \dot{Z}_p(t)\sin(\phi_p(t))\big)\Big)}_{\text{Coupling Term}} \\
&\quad = \frac{Q_{\phi_p}}{I_{\phi_p} \underbrace{\cos(\theta_p(t))^2}_{\text{Coupling Term}}}
\end{aligned} \tag{5.16}$$

where $\dot{X}_p$, $\dot{Y}_p$, $\dot{Z}_p$, $\ddot{X}_p$, $\ddot{Y}_p$, and $\ddot{Z}_p$ are the first and second time-derivatives of the excitations along the local x_p-, y_p-, and z_p-axes respectively and I_{θ_p} and I_{ϕ_p} are the mass moments of inertia of the compound pendulum systems. Also, with the absence of damping, the natural frequencies of the coupled pendulum systems in Equations 5.15 and 5.16 are

$$\omega_{n,\theta_p} = \sqrt{\frac{m_{\theta_p} g l_{\theta_p}}{I_{\theta_p}\cos(\phi_p(t))}} \quad \text{and} \quad \omega_{n,\phi_p} = \sqrt{\frac{m_{\phi_p} g l_{\phi_p}}{I_{\phi_p}\cos(\theta_p(t))}}. \tag{5.17}$$

It should be noted that the uncoupled natural frequencies of both pendulum references can be referred to when θ_p and ϕ_p equal to zero as the cosine terms for the both in equation 5.17 numerically become one.

5.3.1 Verification

The derived equations of motion, Equations 5.15 and 5.16, are defined in the form of ordinary second-order differential equation (ODE). These ODEs for the dynamics of a gimballed pendulum system are solved using fourth-order RungeKutta (RK4) numerical method based on MATLAB software package. This numerical method requires an optimal time-step size that is able to provide an acceptable accuracy and reasonable computational time. In this analysis, a comparable small time-step size of 0.001 of a second is set as a reference as it is assumed that the numerical model achieves acceptable convergence.

Figure 5.6 shows the convergence of the numerical results for the decreasing time-step size. The significant errors occur at the time increments greater than 0.025 seconds. Therefore, a time-step of 0.01 seconds is chosen which achieves a manageable simulation time and an acceptable relative error of overall less than 0.5% for the whole range of investigated excitation frequencies. This analysis provides confidence that, with the selected time-step size, the numerical model and the mathematical solver is numerically stable.

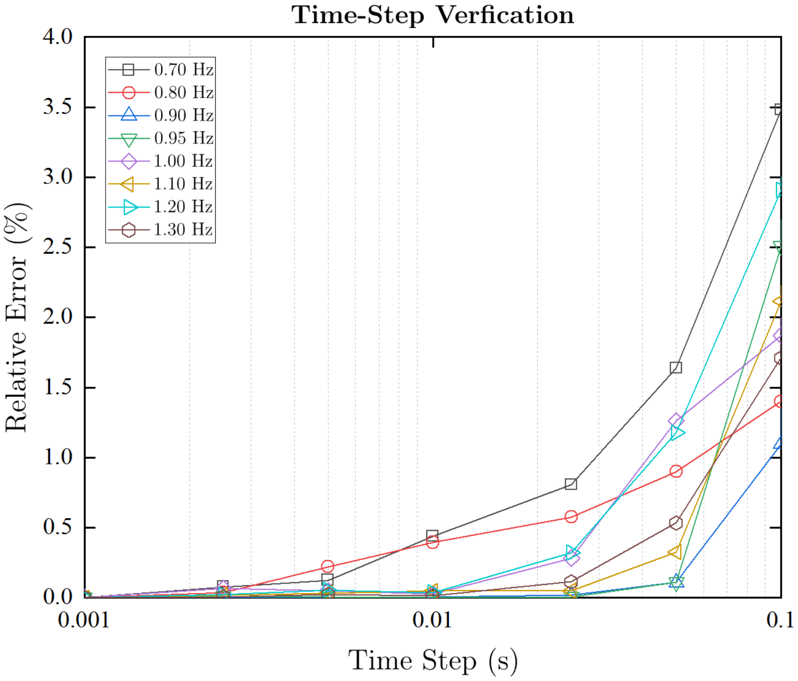

Figure 5.6: Time-step verification for the numerical method.

5.4 Experimental Validation and Investigation of a Gimballed Pendulum System

5.4.1 Experimental Set-up

A prototype of a gimballed pendulum energy harvester was experimentally investigated to validate the pendulum response predicted by the equations of motion described in Section 5.3 and to provide more understanding of the coupled dynamics of the pendulum system. Figure 5.7(a) and 5.7(b) illustrate the graphical and manufactured designs of the investigated gimballed pendulum system. The pendulum system comprises a metal hub with a long shaft through the middle supported by two rigid aluminium frames at both ends. The hub is connected to two sets of perpendicular bearings creating two horizontal axes gimballed pivots with a disk-shaped mass bracing with two aluminium arms hanged in the middle. At the pivots, angular motion sensors (rotary potentiometers for non-PTO condition) or PTO units (electric generators with encoders for applied PTO condition) can be attached and directly driven via transmission systems that consist of 1:1 ratio pulley wheels with rubber belts. Moreover, each pivot can be constrained to perform as a 1-DOF dynamics system. The drawing of the design of the gimballed pendulum energy harvester and the technical details of the involved components are provided in Appendix F.

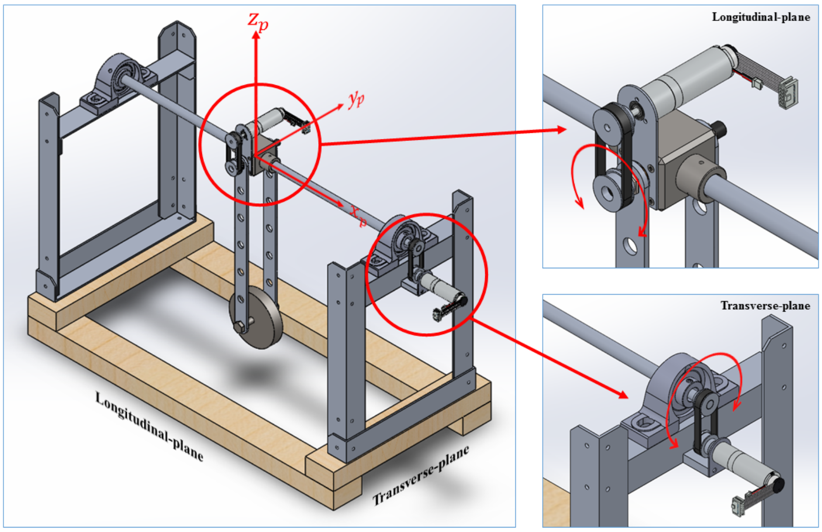

(a) 3-D Graphical design.

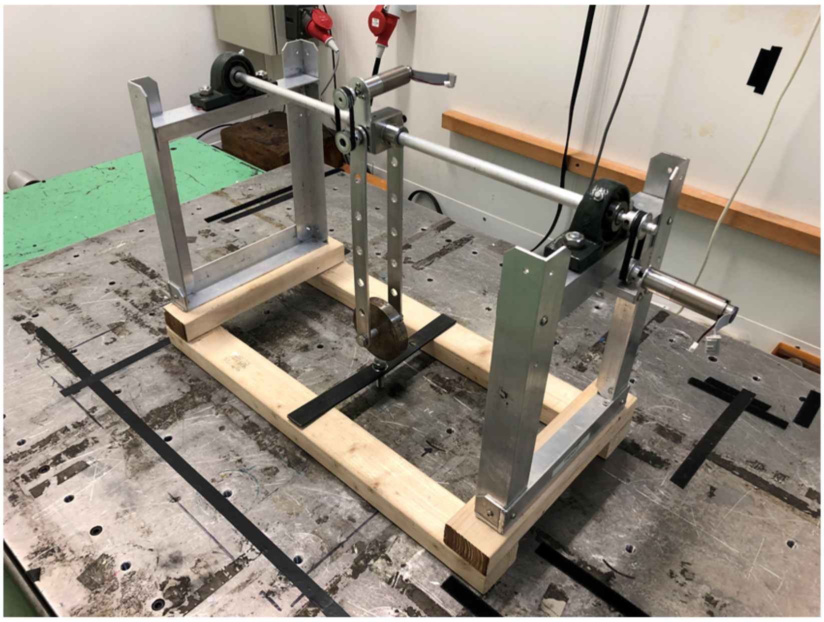

(b) Manufactured design on the test rig.

Figure 5.7: Design of the investigated gimballed pendulum system.

A series of experimental testing was carried out in the Human Factors Research Unit (HFRU) laboratory of the University of Southampton, UK. The pendulum prototype was attached to a 1 m x 1.75 m horizontal motion simulator that is capable of producing single-axis harmonic motion up to 1 m and peak accelerations up to 10 m/s^2 with frequency content from 0 to 50 Hz (University of Southampton, 2018). The two MAXON DCX22L-EB-KL-12V DC motors with 1:44 planetary gearhead operating as generators were used as PTO units with the load resistance (terminal resistance) 1.84 Ω, see Appendix F for more detail. All the data was acquired using a National Instruments' NI cRIO-9022 unit and LabVIEW software package with a sampling rate of 100 Hz.

5.4.2 Power Generation Measurement

Electric Generator Model

The model of the DC generator can be referred to the electrical equivalent diagram in Figure 5.8. The components in the circuit of the DC generator that is driven by an oscillating pendulum with rotational speed or frequency (Ω) consist of terminal resistance ($R_{Terminal}$), mutual inductance (L_a), and load resistance (R_{Load}) Bastankhah and Porté-Agel (2018). In this investigation, there is no extra load is applied ($R_{Load} = 0$) and therefore the electrical power generated by the DC generator is calculated based on the induced voltage across the terminal resistance.

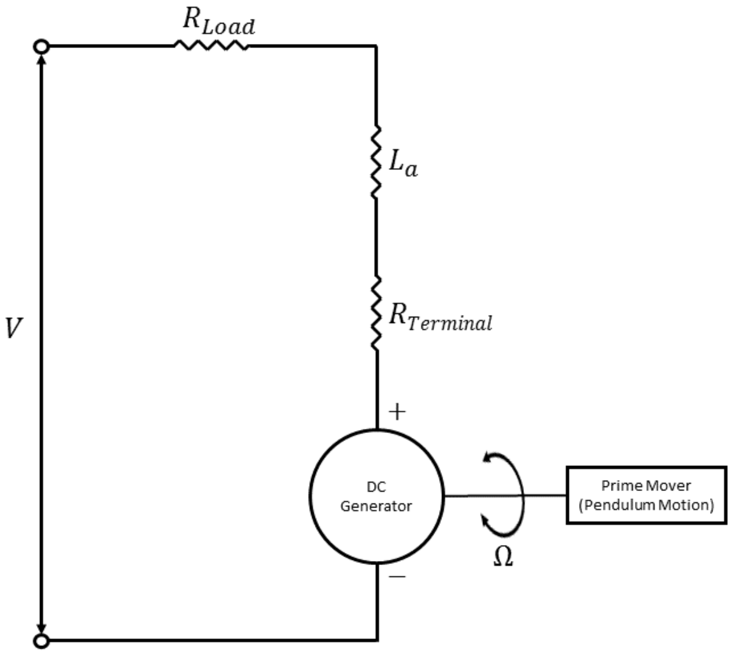

Figure 5.8: Electrical equivalent model of the DC generator.

The power generations from the generators driven by both pendulum references were measured across a constant load resistance and calculated using Ohm's law as:

$$P_i = \frac{V_i^2}{R_i} \quad \text{by} \quad i = \theta_p \text{ or } \phi_p \tag{5.18}$$

where P_i is the generated power (W), V_i is the induced voltage (V), and R_i is the terminal resistance of the generator. For the numerical model in this manner, the induced voltage can be calculated by

$$V_i = \frac{n_i u_i}{k_{n,i}} \quad \text{by} \quad i = \theta_p \text{ or } \phi_p \tag{5.19}$$

where n_i is the driven speed (rpm), u_i is the gear ratio of the gearhead, and $k_{n,i}$ is the speed constant of the generator (rpm/V).

5.4.3 Pendulum Property Measurement

Physical Property Determination

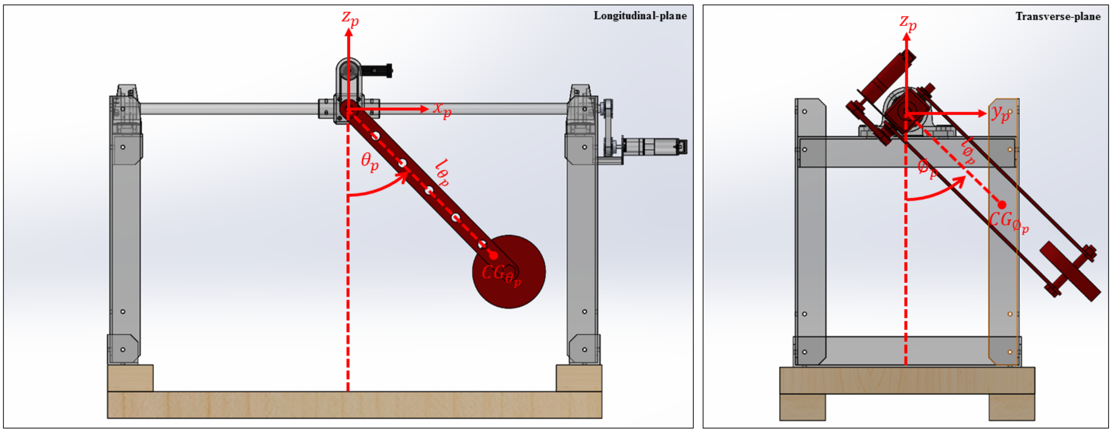

(a) θ_p-plane pendulum. (b) ϕ_p-plane pendulum.

Figure 5.9: Pendulum rotating references (movable parts respecting to the rotating references are highlighted in red).

The physical parameters such as the individual pendulum weights, pivot-to-CG lengths, and mass moments of inertia are obtained based on the experimental measurements respecting two pendulum references as presented in Figures 5.9(a) and 5.9(b).

Frictional Force Models

A number of mathematical models have been introduced for describing the phenomenon of friction or frictional damping. A classical models of friction can be referred to three main types of friction as:

- **Viscous friction** is the results viscous effect of a fluid lubricant layer of two surfaces as well as the effect of surrounding air that an object moving pass. Viscous friction is mathematically presented as a linear function of velocity as:

$$Q_{\text{viscous}} = F_{\text{viscous}} v \tag{5.20}$$

  where F_v is the viscous friction component that is proportional to velocity (v). This viscous friction equals to zero at zero velocity.

- **Coulomb friction** is the friction effect that depends on the direction of the velocity, not the magnitude. Therefore, the mathematical model of this coulomb friction as a static map between the sign of the velocity as:

$$Q_{\text{coulomb}} = F_{\text{coulomb}} \text{sgn}(v) \tag{5.21}$$

  where F_{coulomb} is frictional force (or torque for rotational system denoted as τ_{coulomb}) and sgn(v) is the signum function of the velocity.

- **Static friction** or **stiction** is the friction of stationary object in contact that needs to be overcome to enable relative motion. This type of friction is independent of the velocity as the mathematical model can be represented as:

$$Q_{\text{stiction}} = \begin{cases} F_e & \text{if} \quad v = 0 \text{ and } |F_e| \ < \ F_s \\ F_s \text{sgn}(F_e) & \text{if} \quad v = 0 \text{ and } |F_e| \ \geq \ F_s. \end{cases} \tag{5.22}$$

  where F_e is an external force and F_s is static friction force.

Due to the complexity of experimentally quantifying the magnitude of stiction, this research therefore focuses on a suitable frictional force or damping model for a pendulum system based on viscous and coulomb frictions and it is treated as independent as detailed in the next section.

Damping Constants Determination

A set of dynamic measurement, pendulum free decay test, has been performed for both referenced planes regarding two conditions, without and with PTO units. These tests were done in order to understand the decay characteristics leading to the most appropriate and valid damping model that could theoretically represent the actual dynamics of the individual pendulum.

Initially, the commonly used types of damping model, viscous and Coulomb dampings, for a pendulum dynamics are investigated. Both of the damping coefficients are determined based on the slope of the successive decay peaks in free decay test (see Inman (2014) for more details) as can be summarised as:

- **Viscous damping**: the determination of viscous damping coefficient (ξ) can be referred to the concept of logarithmic decrement. The decay envelope of the successive peaks of viscous drag dominant system decays exponentially to the equilibrium position. For simplified variation, the viscous damping coefficient can be calculated as:
$$\xi_i = \frac{\ln(\text{Slope}_i)}{\pi} \quad \text{by} \quad i = \theta_p \text{ or } \phi_p. \tag{5.23}$$
Therefore, by this approach, the generalised torque is
$$Q_{\text{viscous},i} = -2\xi_i \omega_{n,i} \frac{di(t)}{dt} \quad \text{by} \quad i = \theta_p \text{ or } \phi_p. \tag{5.24}$$

- **Coulomb damping**: this type of frictional damping typically represents sliding or dry friction. The characteristics of the slope regarding the deployment of Coulomb damping decays linearly to a complete stop at a potentially different equilibrium position unlike in the case of viscous damping. The Coulomb damping coefficient for a pendulum system can be denoted as a frictional torque (τ_{coulomb}) which can be determined as:
$$\tau_{\text{coulomb},i} = \frac{\text{Slope}_i \pi m_i g l_i}{2\omega_{n,i}} \quad \text{by} \quad i = \theta_p \text{ or } \phi_p. \tag{5.25}$$
Hence, the generalised torque for this type of damping can be mathematically written as:
$$Q_{\text{coulomb},i} = -\tau_{\text{coulomb},i} \text{sgn}(\frac{di(t)}{dt}) \quad \text{by} \quad i = \theta_p \text{ or } \phi_p, \tag{5.26}$$
where $\text{sgn}(\frac{di(t)}{dt})$ is called 'signum function' which theoretically defined as:
$$\text{sgn}(\frac{di(t)}{dt}) = \begin{cases} -1 & \text{for} \quad \frac{di(t)}{dt} > 0 \\ 0 & \text{for} \quad \frac{di(t)}{dt} = 0 \\ 1 & \text{for} \quad \frac{di(t)}{dt} < 0 \end{cases} \quad \text{by} \quad i = \theta_p \text{ or } \phi_p. \tag{5.27}$$

By applying the identified damping models, the comparison of experimental measurements and numerical predictions based on the damping models, Equations 5.24 and 5.26, is examined in Figure 5.10.

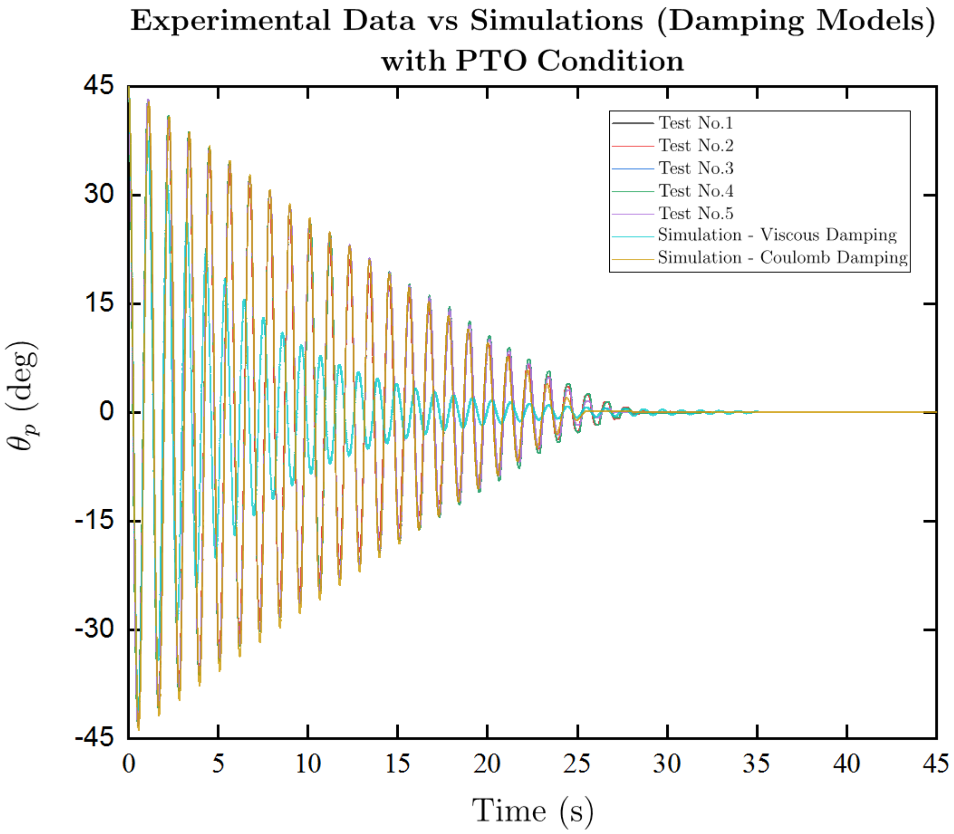

Figure 5.10: Comparison of experimental results and simulations based on damping models selection.

As can be seen from Figure 5.10, the comparison of the uses of frictional damping models shows that both investigated damping models provide a good agreement concerning decay duration to complete stops. However, a valid correspondence between experimental measurements and the numerical model is only yielded by the applied Coulomb damping. This shows that the sliding or dry friction dominates the characteristics of the pendulum dynamics and therefore this type of friction is considered as a suitable damping model for the investigated pendulum prototype.

The experimental and numerical results of the free decay tests of both pendulum references without and with PTO units are demonstrated in Figures 5.11 to 5.14. Additionally, the asymmetric inertial properties of two pendulum references are summarised in Table 5.1.

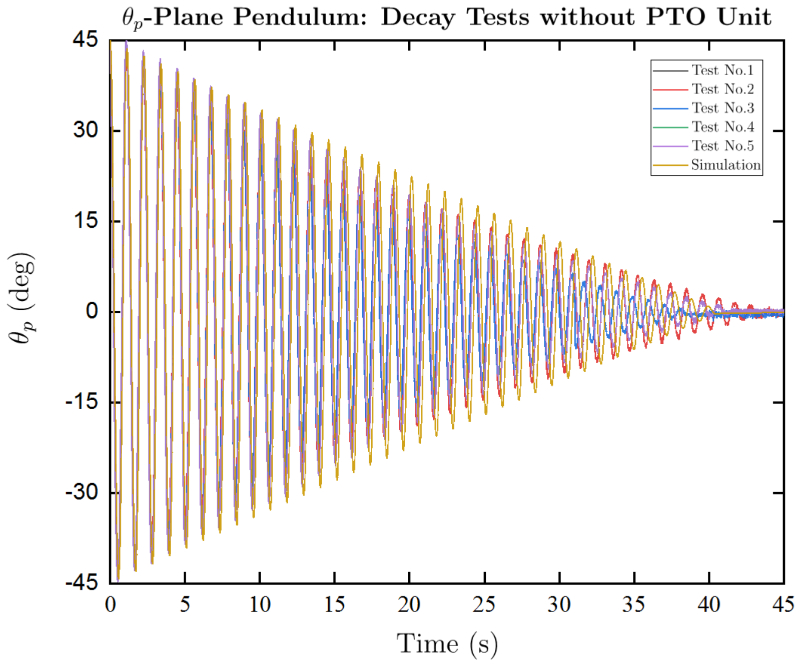

(a) θ_p-plane pendulum angular displacments.

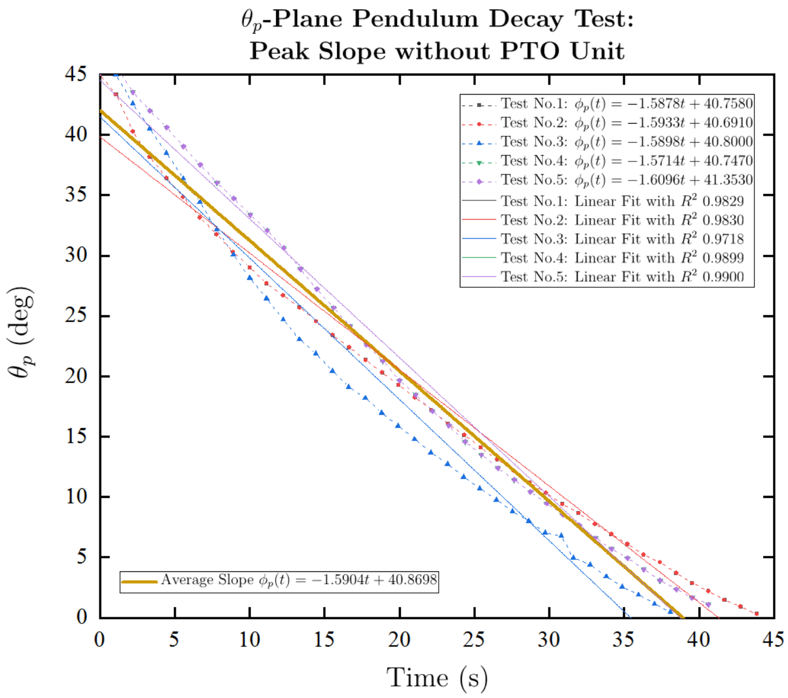

(b) θ_p-plane pendulum decay slopes.

Figure 5.11: θ_p-plane pendulum free decay tests without PTO unit.

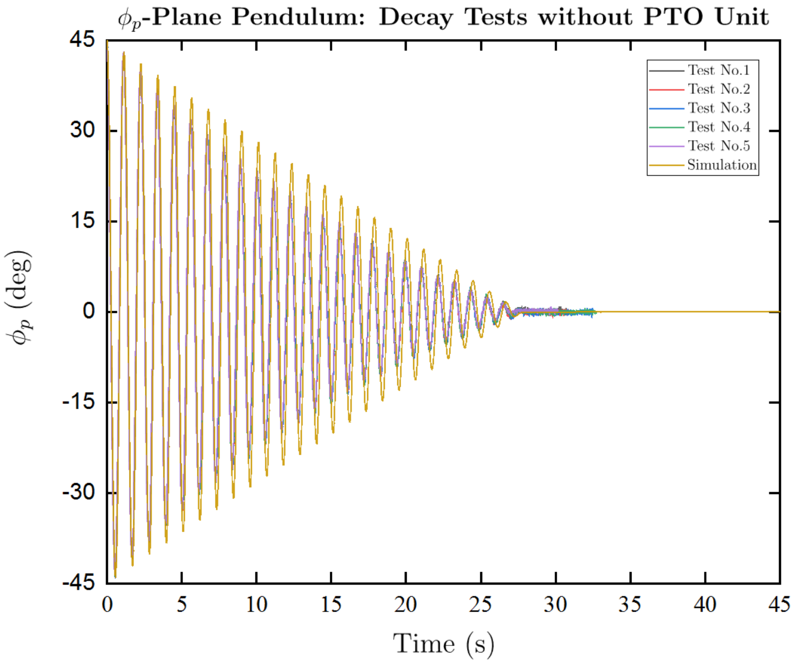

(a) ϕ_p-plane pendulum angular displacments.

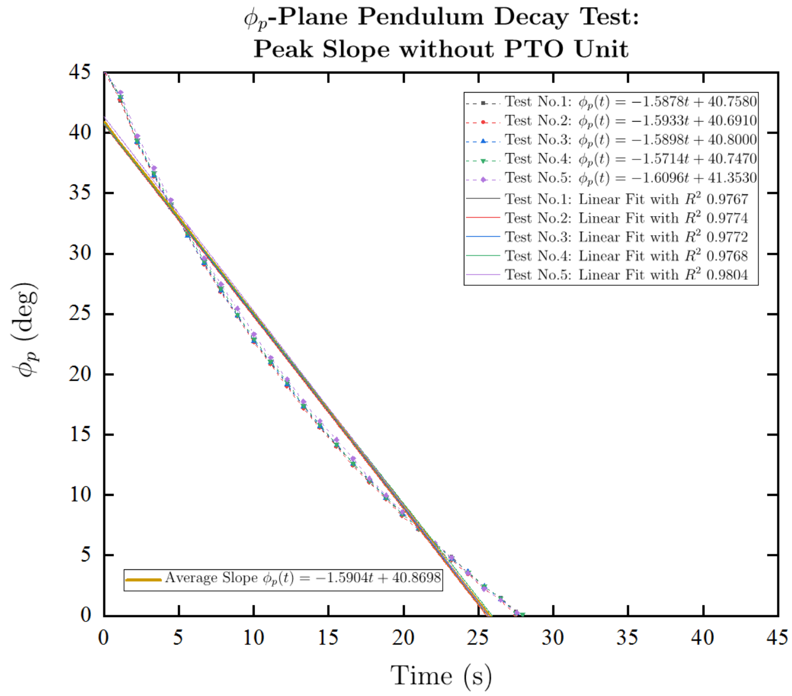

(b) ϕ_p-plane pendulum decay slopes.

Figure 5.12: ϕ_p-plane pendulum free decay tests without PTO unit.

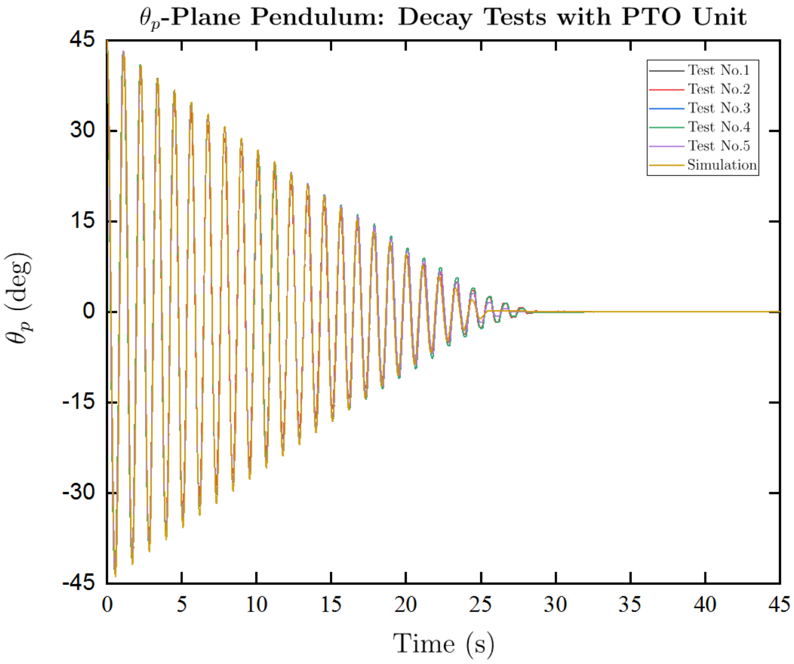

(a) θ_p-plane pendulum angular displacments.

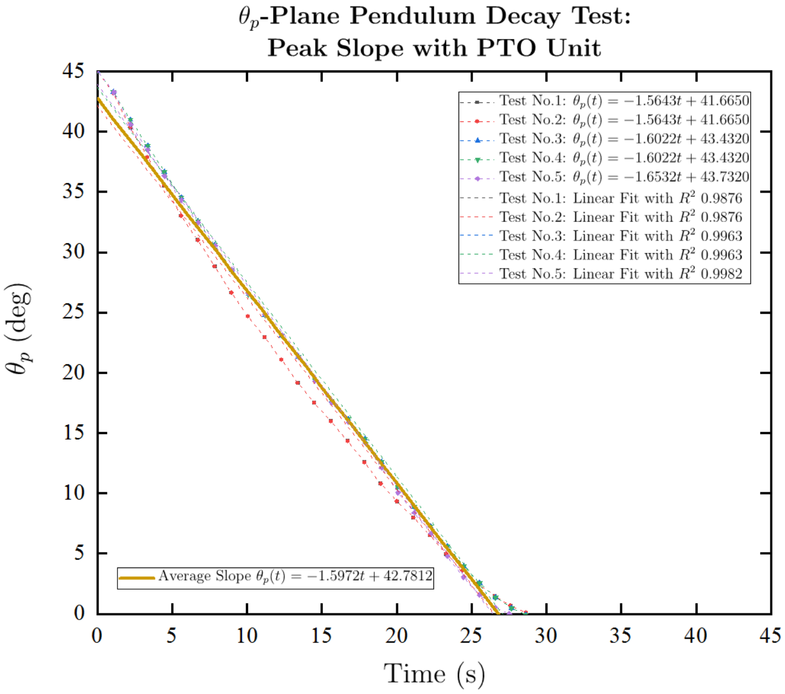

(b) θ_p-plane pendulum decay slopes.

Figure 5.13: θ_p-plane pendulum free decay tests with PTO unit.

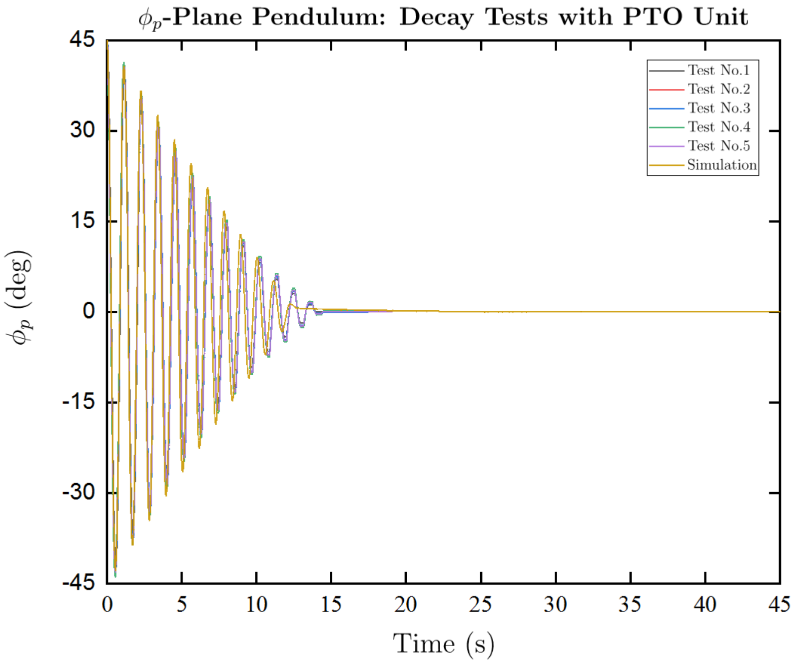

(a) ϕ_p-plane pendulum angular displacments.

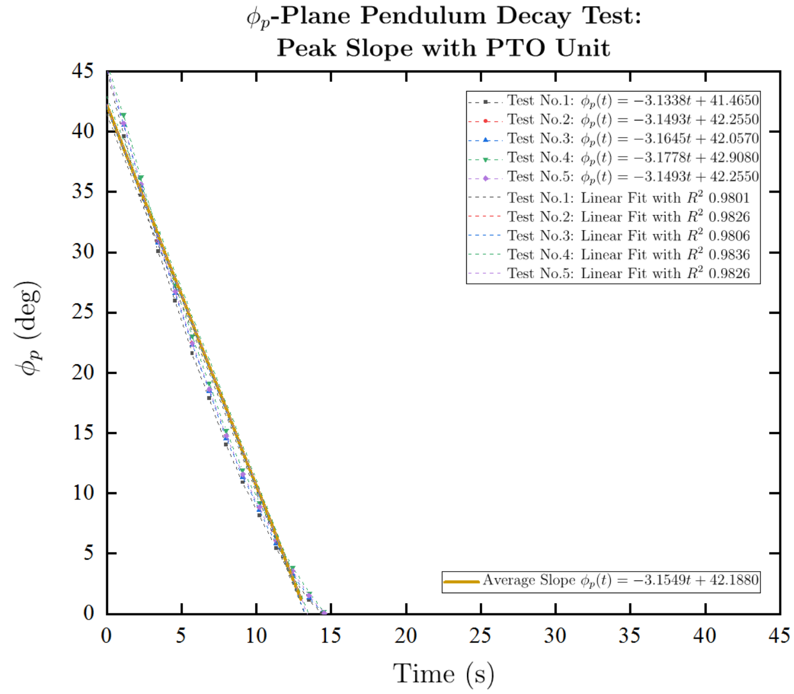

(b) ϕ_p-plane pendulum decay slopes.

Figure 5.14: ϕ_p-plane pendulum free decay tests with PTO unit.

Table 5.1: The Parameters of the Gimballed Pendulum System

Pendulum Reference	**Parameter**	**Symbol**	**Value**		**Unit**
			without Applied PTO	**with Applied PTO**	
θ_p-Plane	Pendulum Mass	m_{θ_p}	1.23934	1.23934	kg
	Pendulum Pivot-to-CG Length	l_{θ_p}	0.27801	0.27801	m
	Pendulum Mass Moment of Inertia	I_{θ_p}	0.10245	0.10249	$\text{kg}\cdot\text{m}^2$
	Natural Frequency (Uncoupled)	ω_{n,θ_p}	0.91416	0.91399	Hz
	Damping/Frictional Torque	$\tau_{\text{coulomb},\theta_p}$	0.01743	0.02779	N·m
ϕ_p-Plane	Pendulum Mass	m_{ϕ_p}	2.23593	2.24356	kg
	Pendulum Pivot-to-CG Length	l_{ϕ_p}	0.15347	0.15278	m
	Pendulum Mass Moment of Inertia	I_{ϕ_p}	0.10248	0.10254	$\text{kg}\cdot\text{m}^2$
	Natural Frequency (Uncoupled)	ω_{n,ϕ_p}	0.91217	0.91140	Hz
	Damping/Frictional Torque	$\tau_{\text{coulomb},\phi_p}$	0.02561	0.05623	N·m

5.4.4 Experimental Plan

Table 5.2: Test Conditions Matrix at $X_\circ = 0.01$ m

Damping Condition	**Case No.**	**Pendulum Reference**		**Dynamics Type**
		θ_p-Plane	**ϕ_p-Plane**	
without Applied PTOs	A1	Free	Locked	**1-DOF**
	A2	Locked	Free	
	A3	Free	Free	**Coupled-DOF**
with Applied PTOs	B1	Free	Locked	**1-DOF**
	B2	Locked	Free	
	B3	Free	Free	**Coupled-DOF**

[a] $\Omega = 0.7, 0.8, 0.9, 0.95, 1.0, 1.1, 1.2, 1.3$ Hz

[b] $\mu = 0°, 15°, 30°, 45°, 60°, 75°, 90°$

In this investigation, both 1- and coupled-DOFs pendulum dynamics were examined. The 1-DOF dynamics regarding two rotating references were experimentally tested as the pendulum was constrained to only swing about a particular axis. In other words, there was no rotation allowed about the constrained axis. For the coupled dynamics case, the prototype was tested based on that both pivots were fully unlocked. Both numerical and experimental investigations were performed across a range and external excitation frequencies[a] (Ω) with a constant excitation amplitude ($X_\circ = 0.01$ m) and a set of heading angle[b] (μ) as detailed in Table 5.2. Besides, the base excitation accelerations were measured using an inertial measurement unit (IMU), Xsens MTi-100, which was attached to the test rig. The good correlation between the simulated and measured acceleration signals are demonstrated in Figure 5.15.

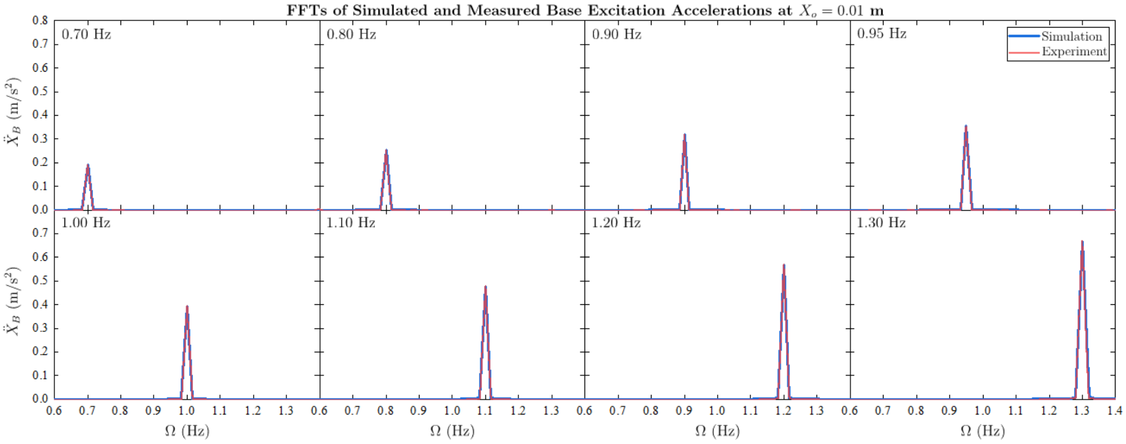

Figure 5.15: FFT diagrams of the simulated and measured base excitation acceleration signals.

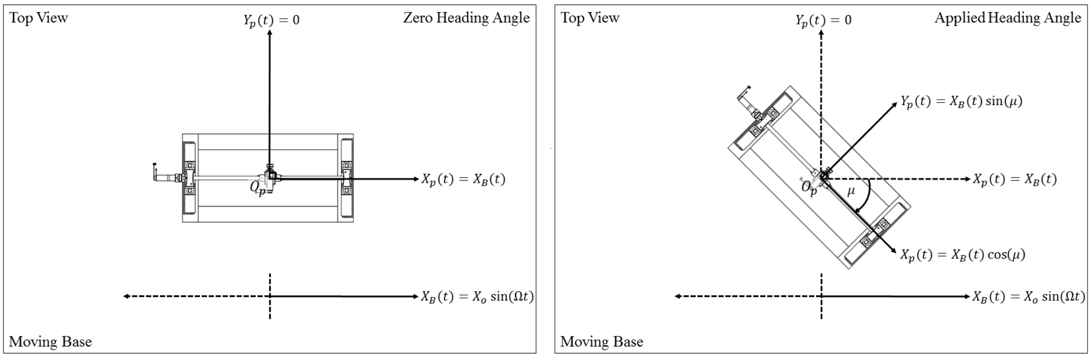

(a) with zero heading angle. (b) with applied heading angle.

Figure 5.16: Schematic diagrams of experimental testing and numerical representations of axial excitations.

Figure 5.16 demonstrates the top-view of schematic diagrams of the prototype on the test rig. According to the test conditions in Table 5.2, a horizontal harmonic motion is generated by the motion simulator. Hence, from Figure 5.16(a), the time-dependent position of the base (X_B) without applied heading angle is

$$X_B(t) = X_\circ \sin(\Omega t) \tag{5.28}$$

and, from Figure 5.16(b), the axial positions of the pivot(s) in global coordinate ($PX_pY_pZ_p$) with applied heading angle can be mathematically expressed as:

$$X_p(t) = X_B(t)\cos(\mu) = X_\circ \sin(\Omega t)\cos(\mu), \tag{5.29}$$

$$Y_p(t) = X_B(t)\sin(\mu) = X_\circ \sin(\Omega t)\sin(\mu), \tag{5.30}$$

$$Z_p(t) = 0. \tag{5.31}$$

Note that, the numerical solution for the 1-DOF pendulum dynamics can be quoted the standard equation of motion of a driven 1-DOF pendulum system, Equation D.19 in Appendix D.

5.5 Results and Discussion

5.5.1 Pendulum Responses

The comparisons of the numerical predictions and experimental results for the motion responses of the investigated pendulum prototype are shown in Figures 5.17 to 5.40.

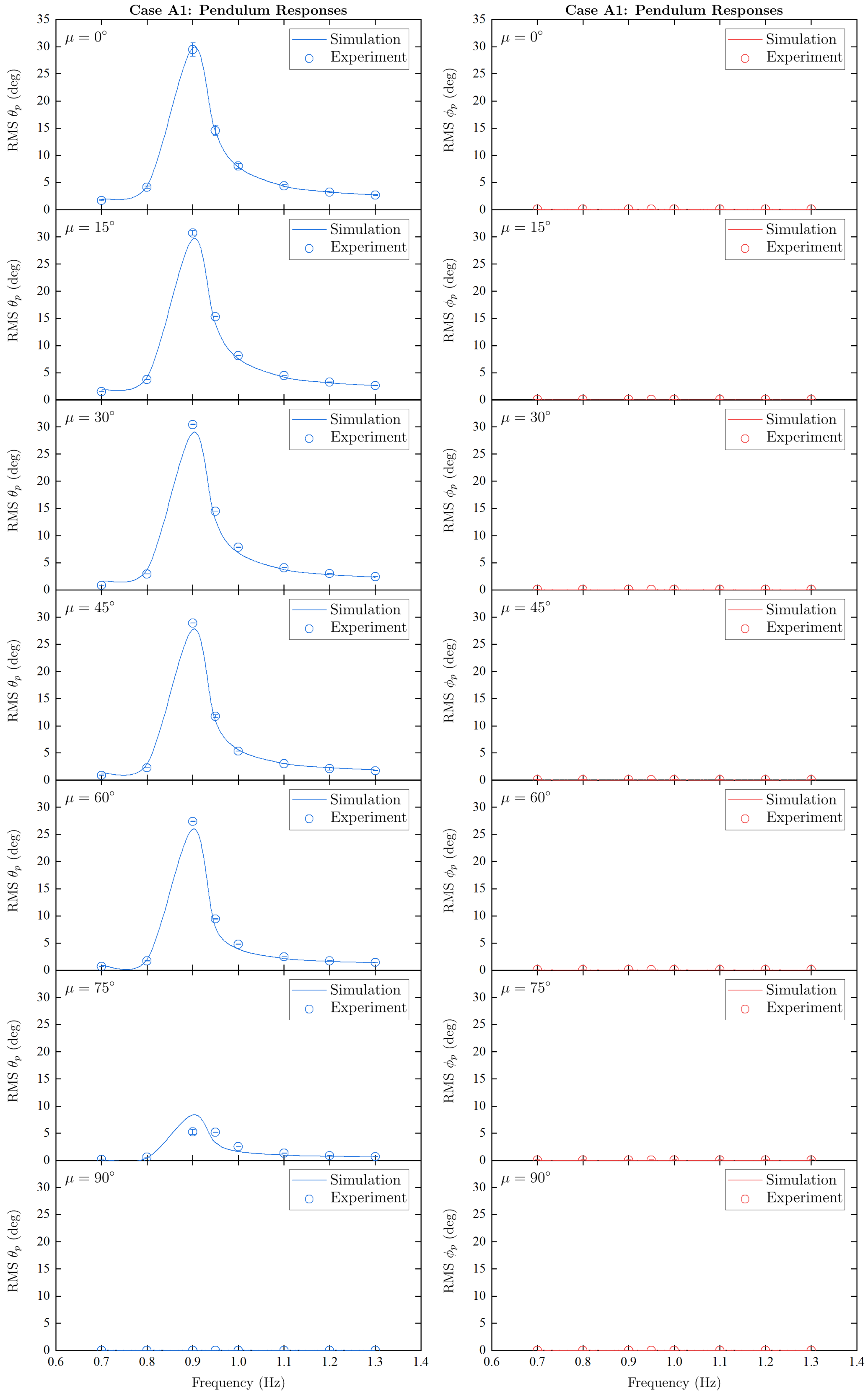

(a) θ_p-plane pendulum.

(b) ϕ_p-plane pendulum.

Figure 5.17: Case A1 - RMS of the last 30 seconds of pendulum responses without PTO units in the frequency-domain.

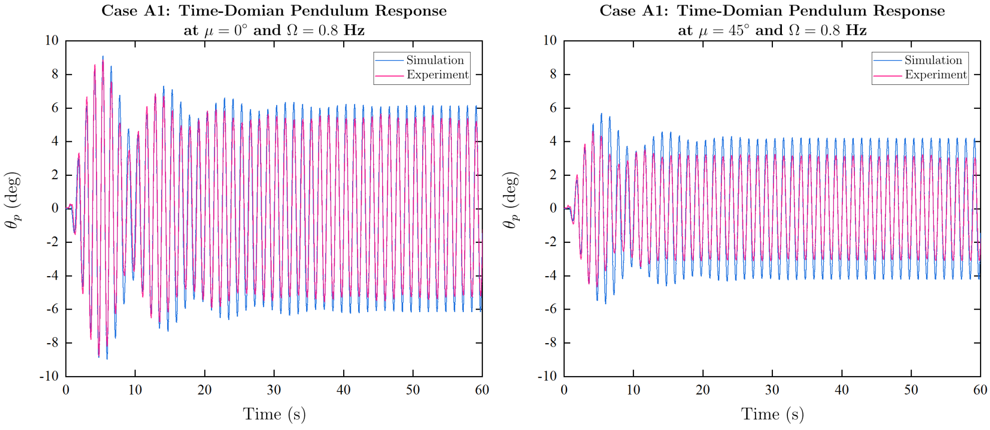

(a) at $\mu = 0°$.

(b) at $\mu = 45°$.

Figure 5.18: Case A1: Pendulum responses without PTO units at 0.8 Hz (before resonance region).

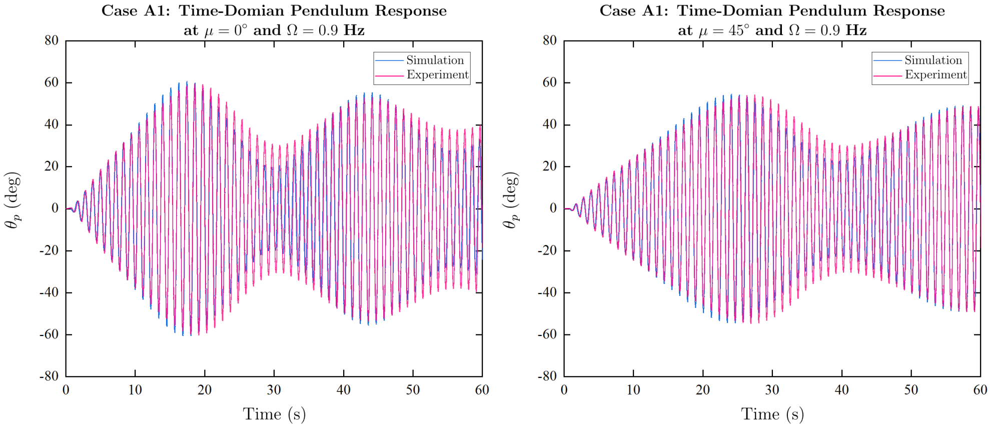

(a) at $\mu = 0°$.

(b) at $\mu = 45°$.

Figure 5.19: Case A1: Pendulum responses without PTO units at 0.9 Hz (at resonance region).

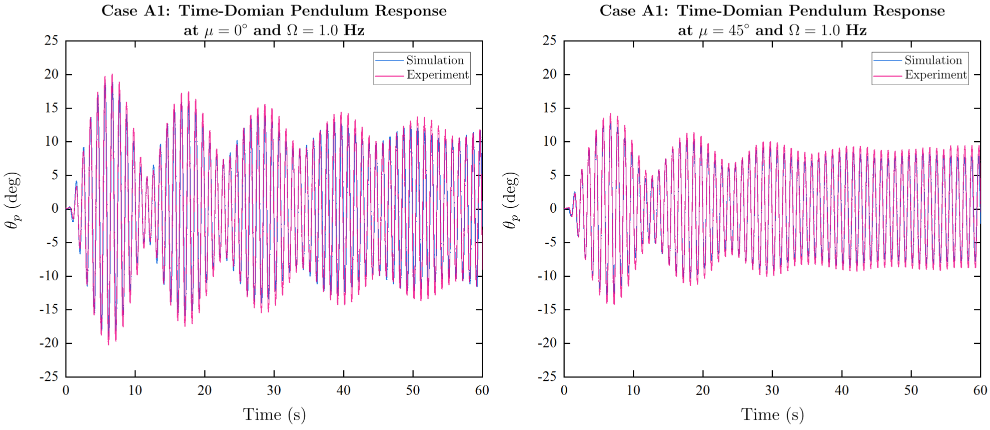

(a) at $\mu = 0°$.

(b) at $\mu = 45°$.

Figure 5.20: Case A1: Pendulum responses without PTO units at 1.0 Hz (after resonance region).

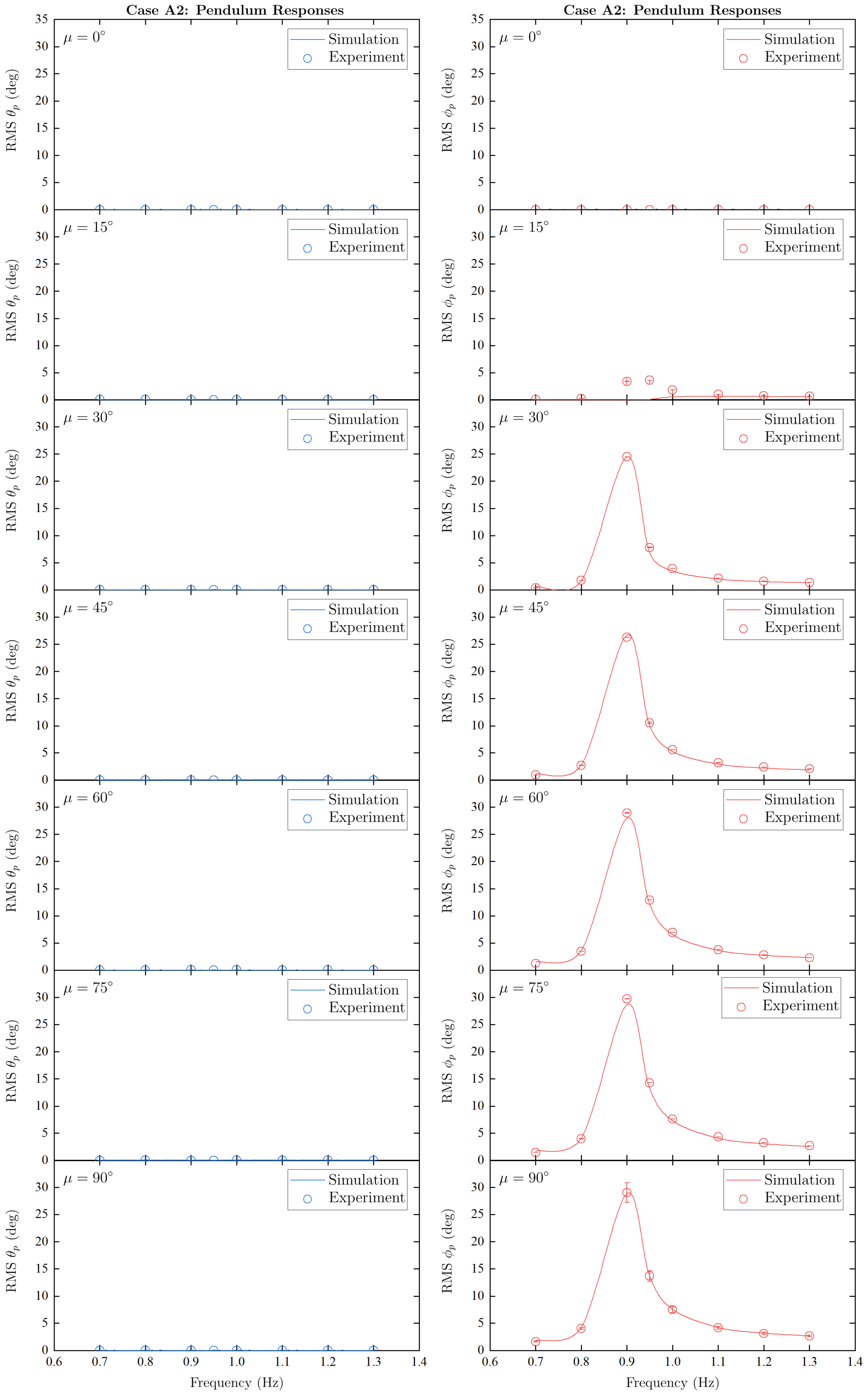

(a) θ_p-plane pendulum.

(b) ϕ_p-plane pendulum.

Figure 5.21: Case A2 - RMS of the last 30 seconds of pendulum responses without PTO units in the frequency-domain.

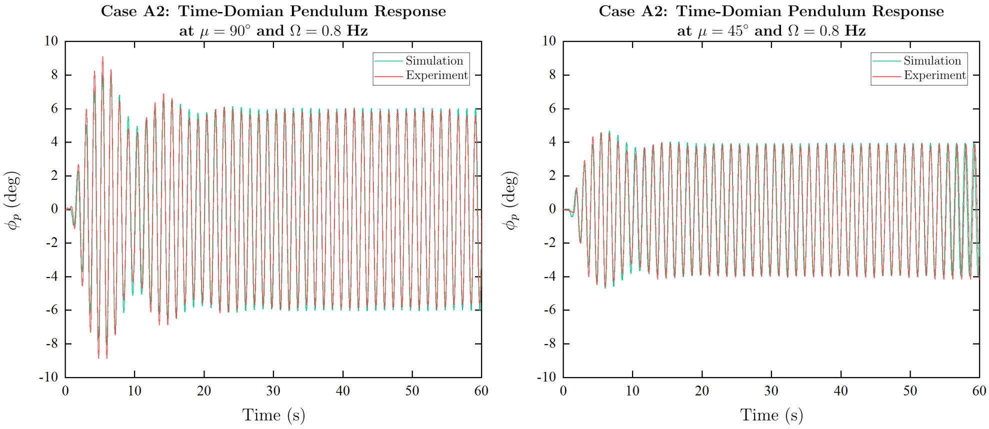

(a) at $\mu = 90°$.

(b) at $\mu = 45°$.

Figure 5.22: Case A2: Pendulum responses without PTO units at 0.8 Hz (before resonance region).

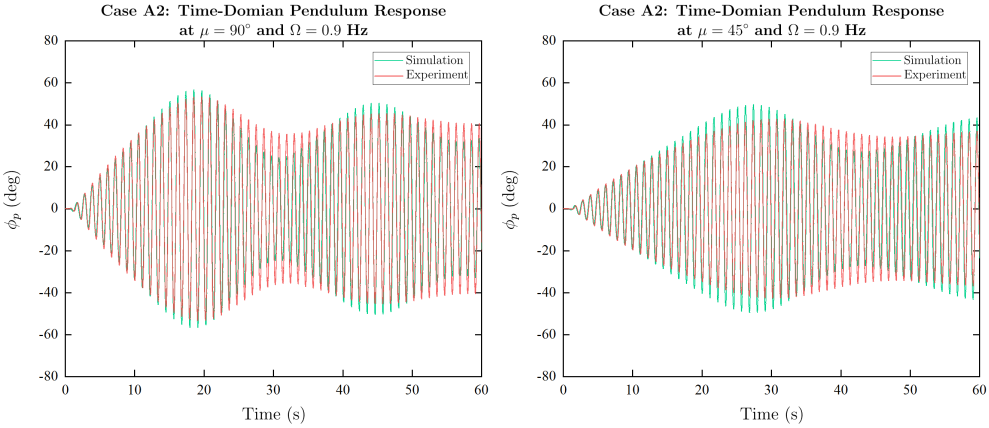

(a) at $\mu = 90°$.

(b) at $\mu = 45°$.

Figure 5.23: Case A2: Pendulum responses without PTO units at 0.9 Hz (before resonance region).

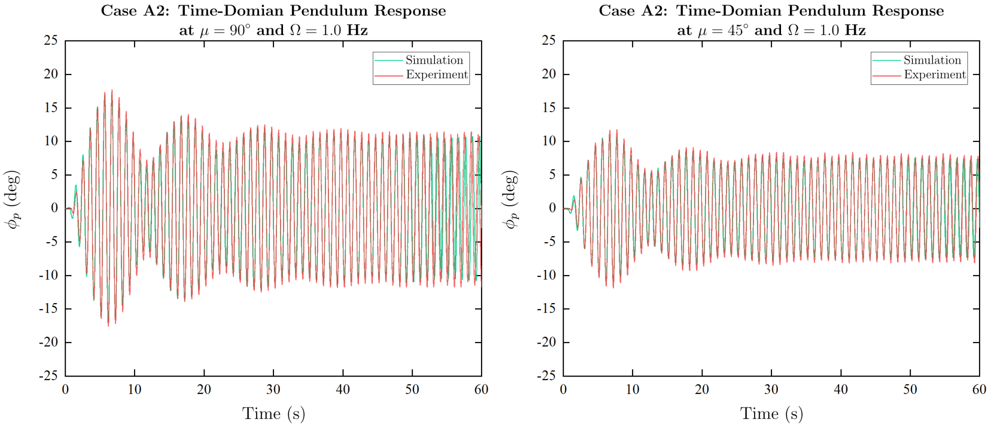

(a) at $\mu = 90°$.

(b) at $\mu = 45°$.

Figure 5.24: Case A2: Pendulum responses without PTO units at 1.0 Hz (before resonance region).

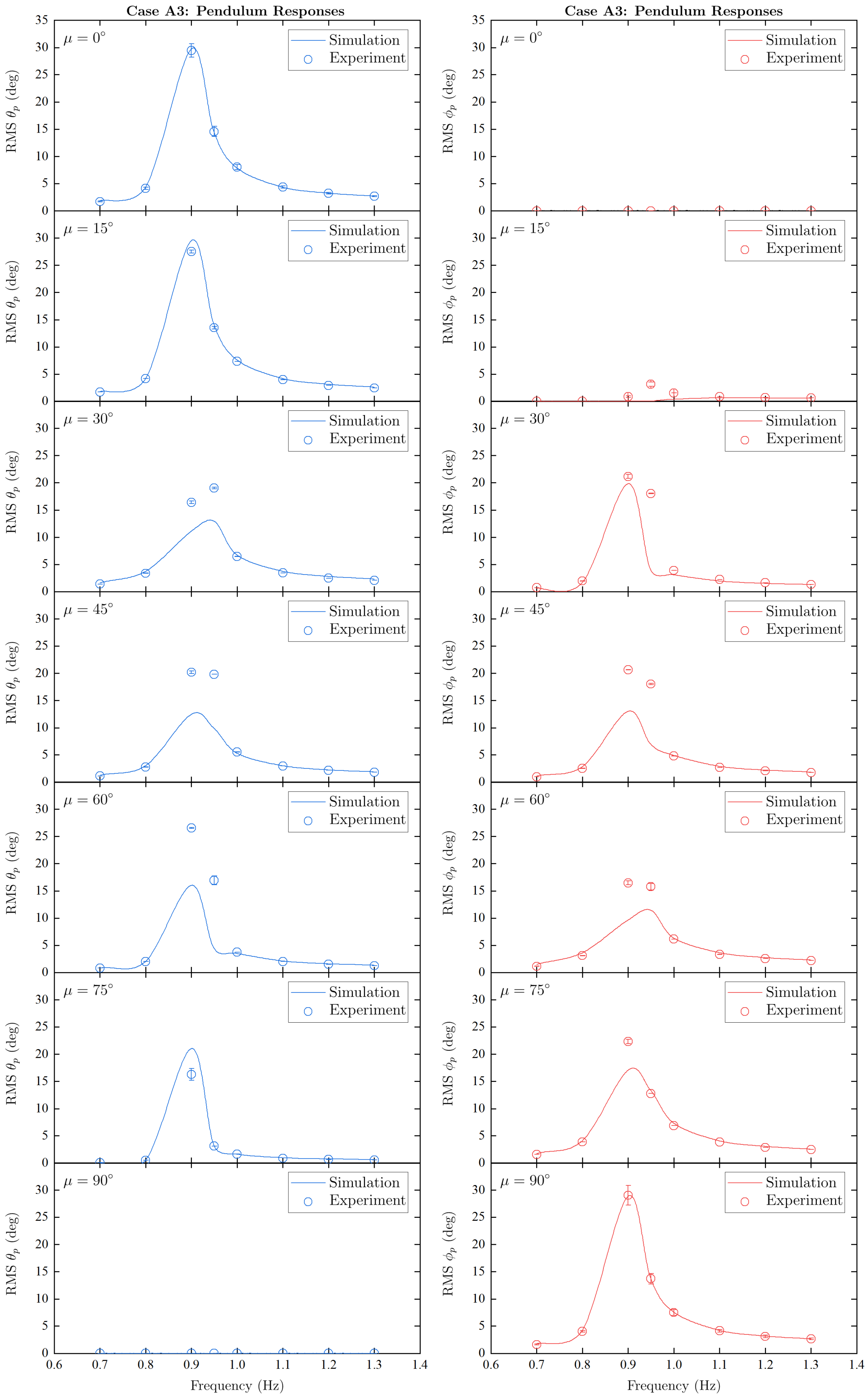

(a) θ_p-plane pendulum.

(b) ϕ_p-plane pendulum.

Figure 5.25: Case A3 - RMS of the last 30 seconds of pendulum responses without PTO units in the frequency-domain.

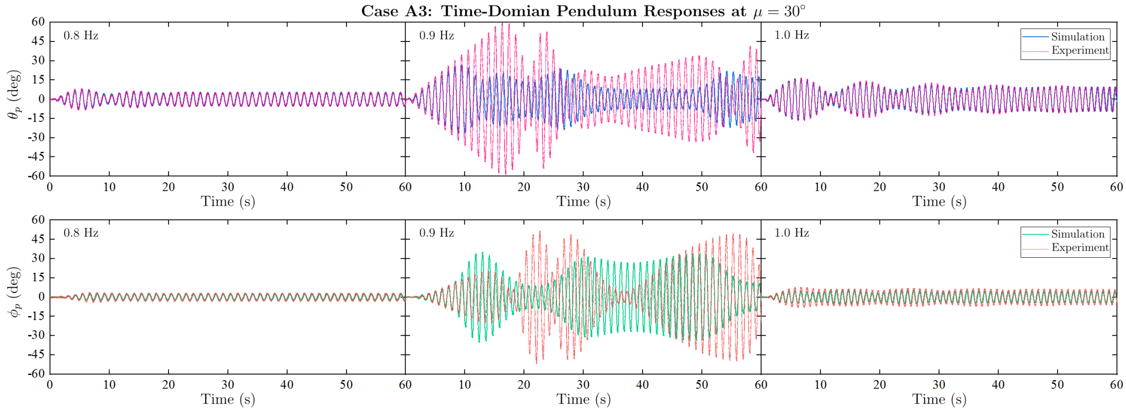

Figure 5.26: Case A3 - pendulum responses without PTO units at $\mu = 30°$ (upper row: θ_p-plane pendulum, lower row: ϕ_p-plane pendulum).

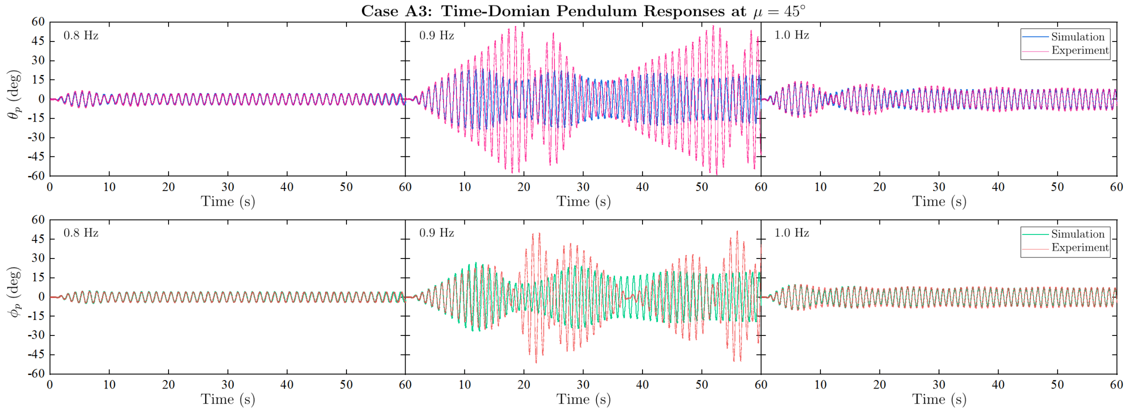

Figure 5.27: Case A3 - pendulum responses without PTO units at $\mu = 45°$ (upper row: θ_p-plane pendulum, lower row: ϕ_p-plane pendulum).

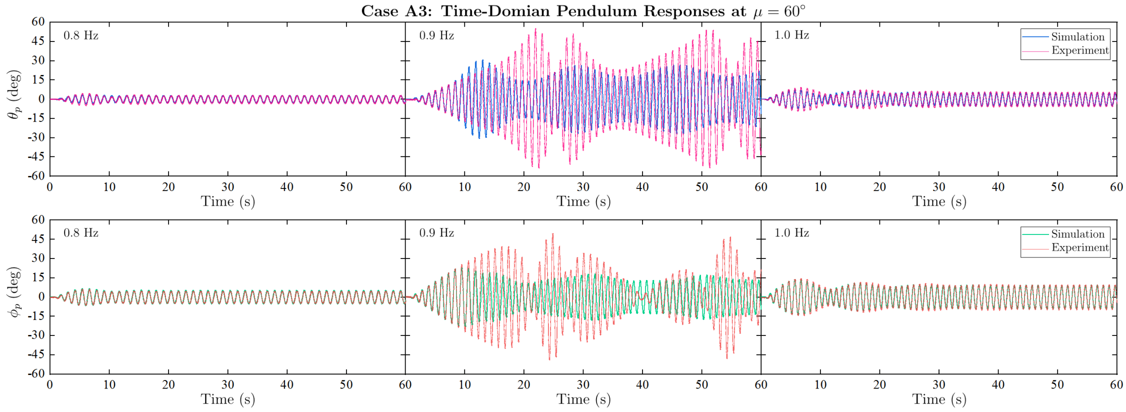

Figure 5.28: Case A3 - pendulum responses without PTO units at $\mu = 60°$ (upper row: θ_p-plane pendulum, lower row: ϕ_p-plane pendulum).

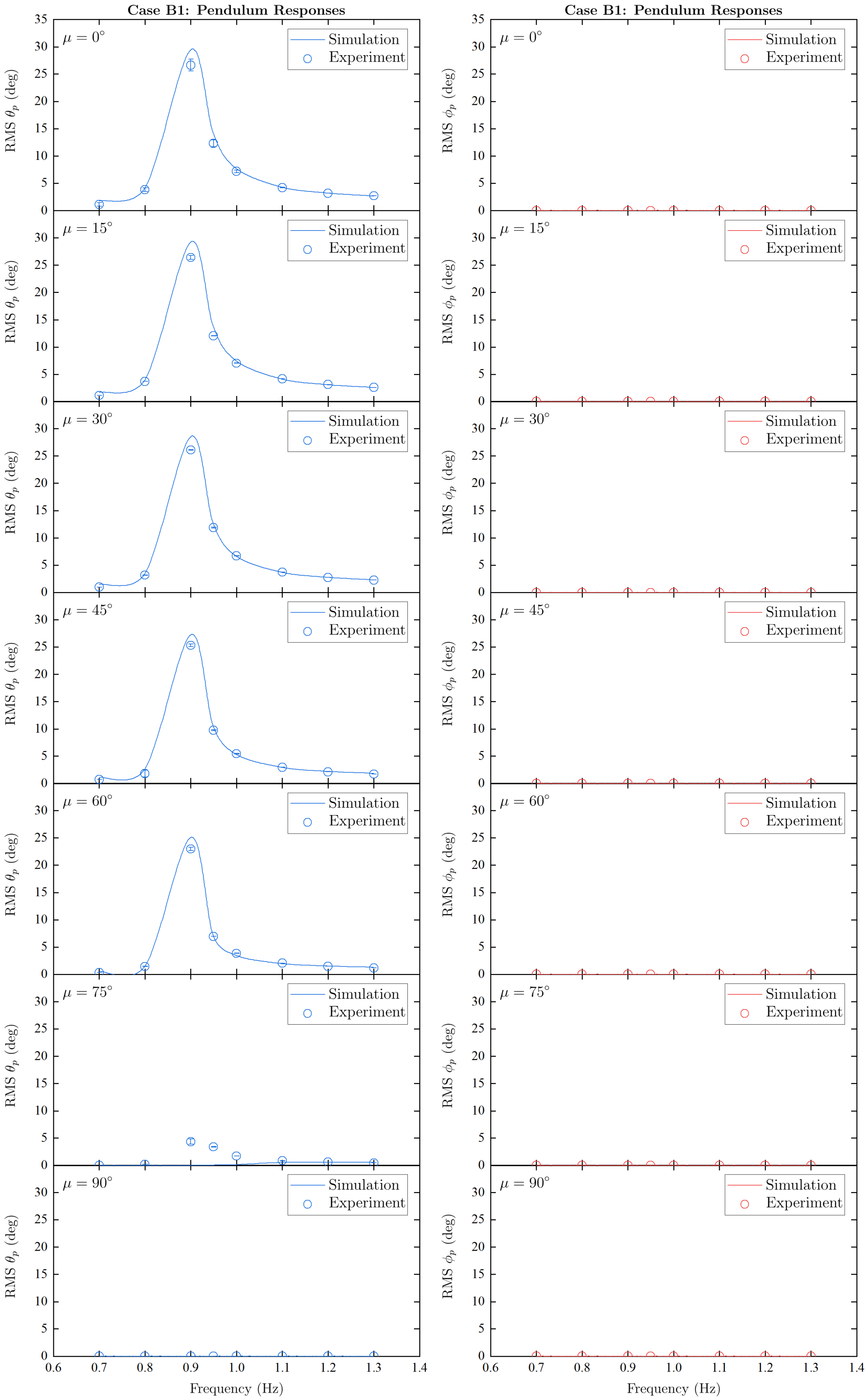

(a) θ_p-plane pendulum.

(b) ϕ_p-plane pendulum.

Figure 5.29: Case B1 - RMS of the last 30 seconds of pendulum responses with PTO units in the frequency-domain.

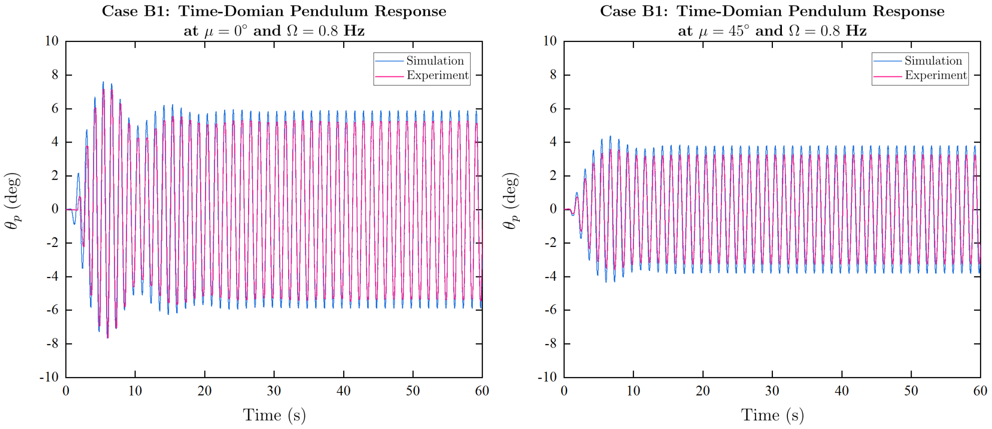

(a) at $\mu = 0°$.

(b) at $\mu = 45°$.

Figure 5.30: Case B1: Pendulum responses with PTO units at 0.8 Hz (before resonance region).

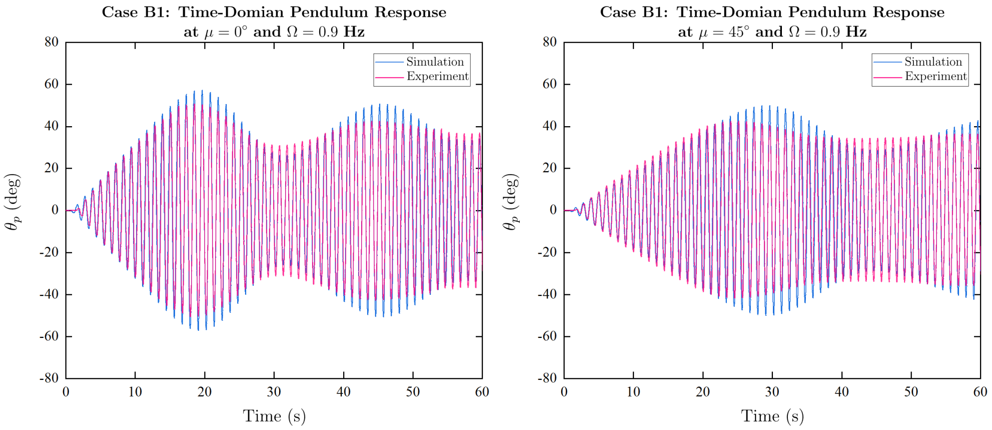

(a) at $\mu = 0°$.

(b) at $\mu = 45°$.

Figure 5.31: Case B1: Pendulum responses with PTO units at 0.9 Hz (at resonance region).

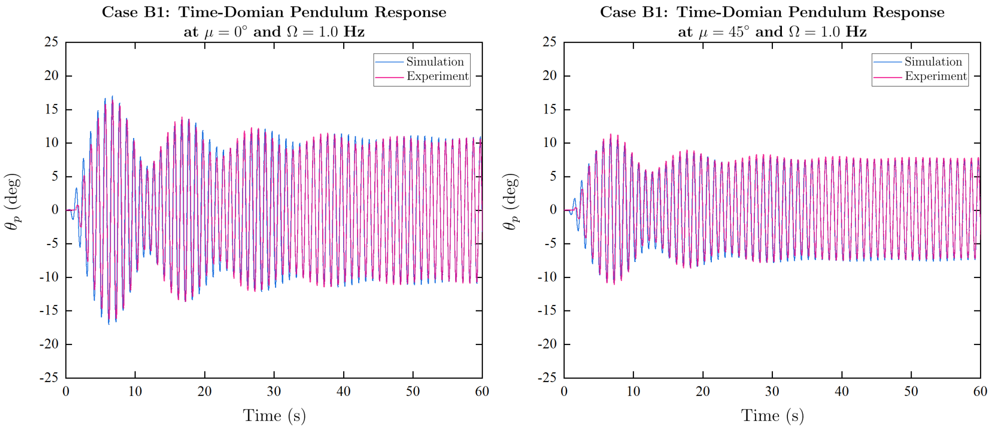

(a) at $\mu = 0°$.

(b) at $\mu = 45°$.

Figure 5.32: Case B1: Pendulum responses with PTO units at 1.0 Hz (after resonance region).

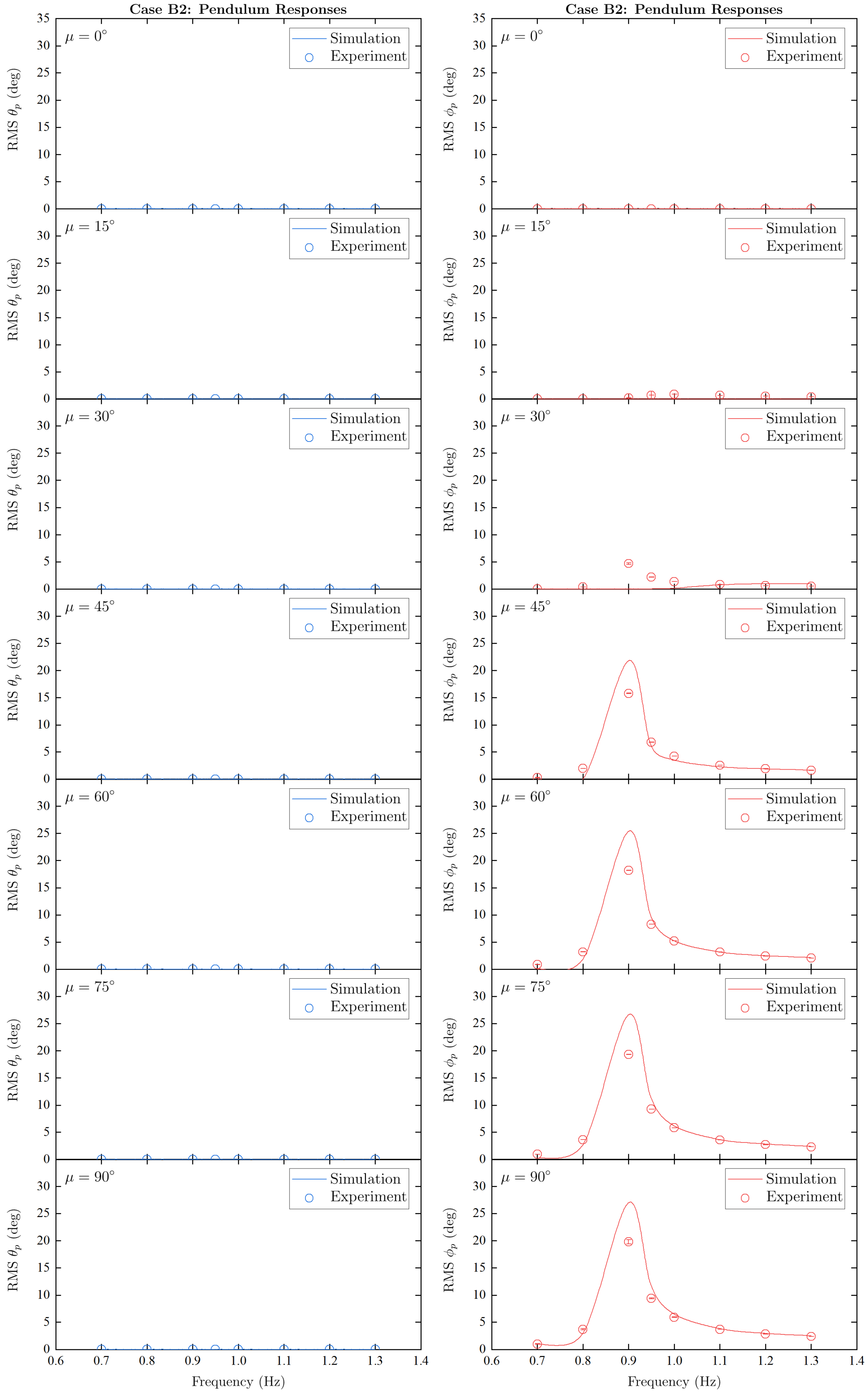

(a) θ_p-plane pendulum.

(b) ϕ_p-plane pendulum.

Figure 5.33: Case B2 - RMS of the last 30 seconds of pendulum responses with PTO units in the frequency-domain.

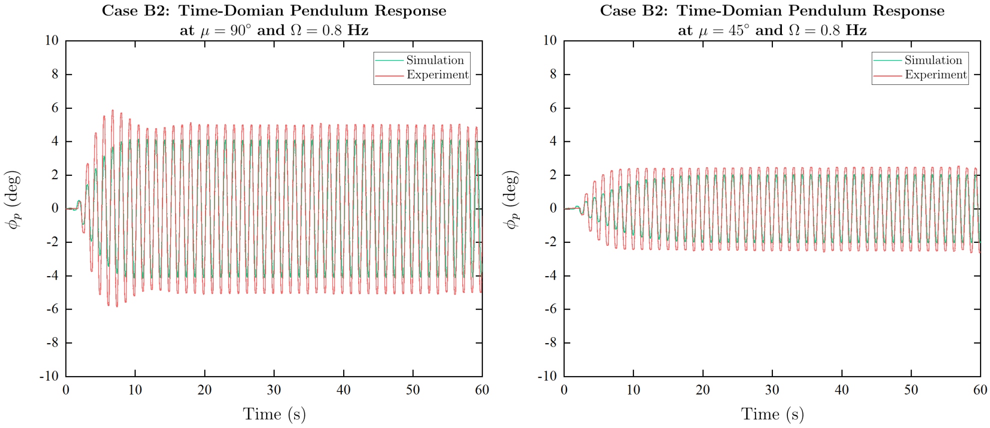

(a) at $\mu = 90°$.

(b) at $\mu = 45°$.

Figure 5.34: Case B2: Pendulum responses with PTO units at 0.8 Hz (before resonance region).

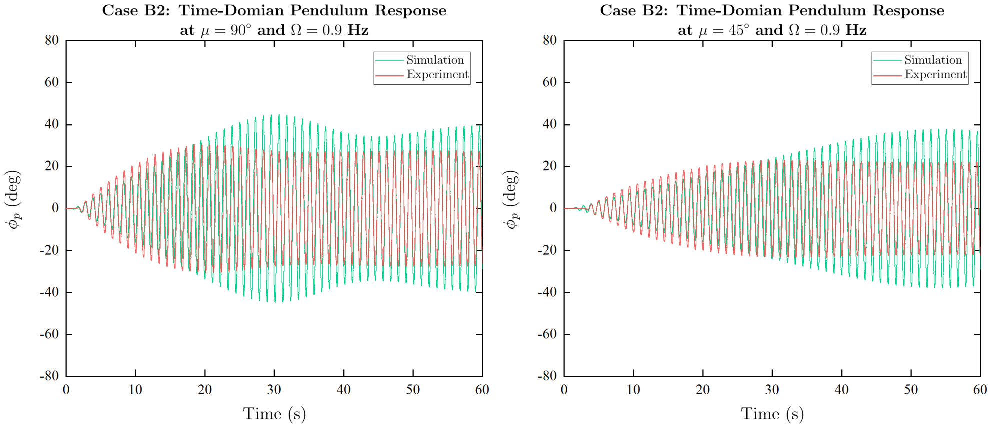

(a) at $\mu = 90°$.

(b) at $\mu = 45°$.

Figure 5.35: Case B2: Pendulum responses with PTO units at 0.9 Hz (before resonance region).

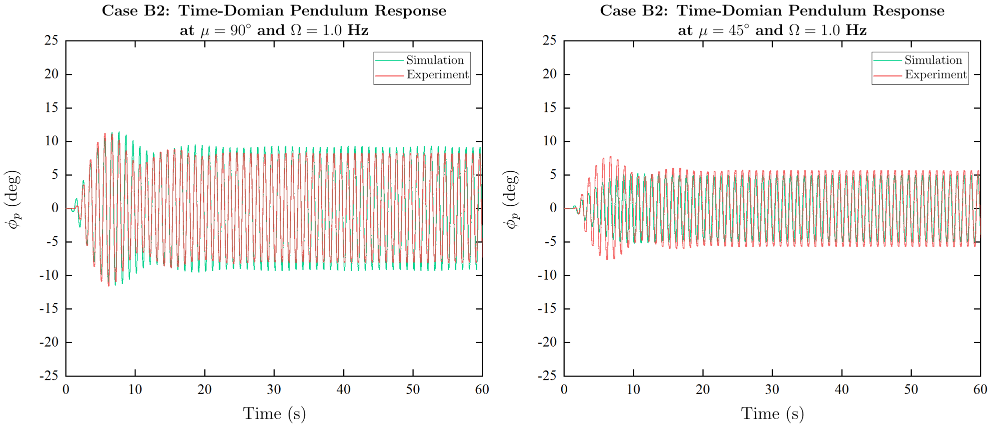

(a) at $\mu = 90°$.

(b) at $\mu = 45°$.

Figure 5.36: Case B2: Pendulum responses with PTO units at 1.0 Hz (before resonance region).

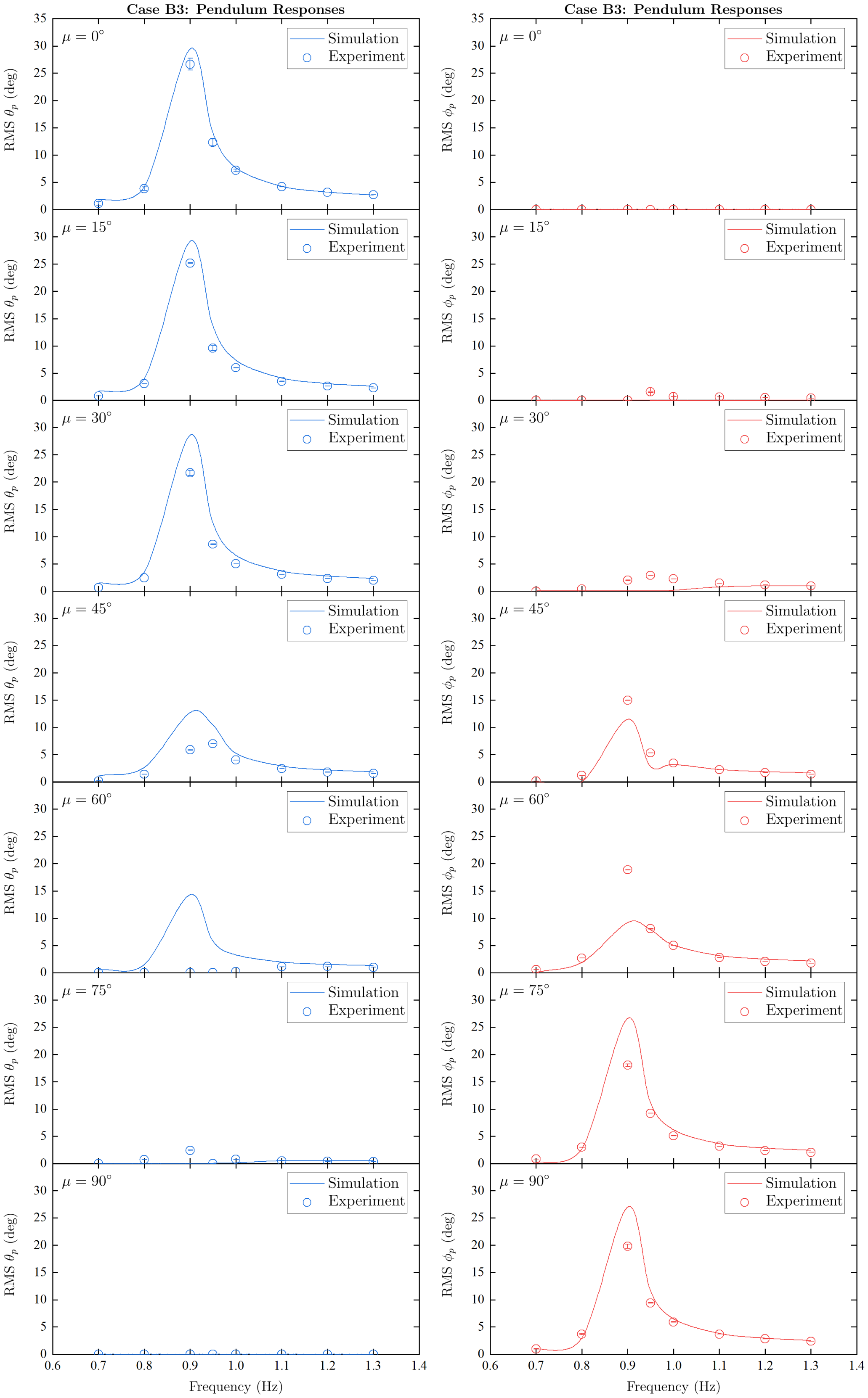

(a) θ_p-plane pendulum.

(b) ϕ_p-plane pendulum.

Figure 5.37: Case B3 - RMS of the last 30 seconds of pendulum responses with PTO units in the frequency-domain.

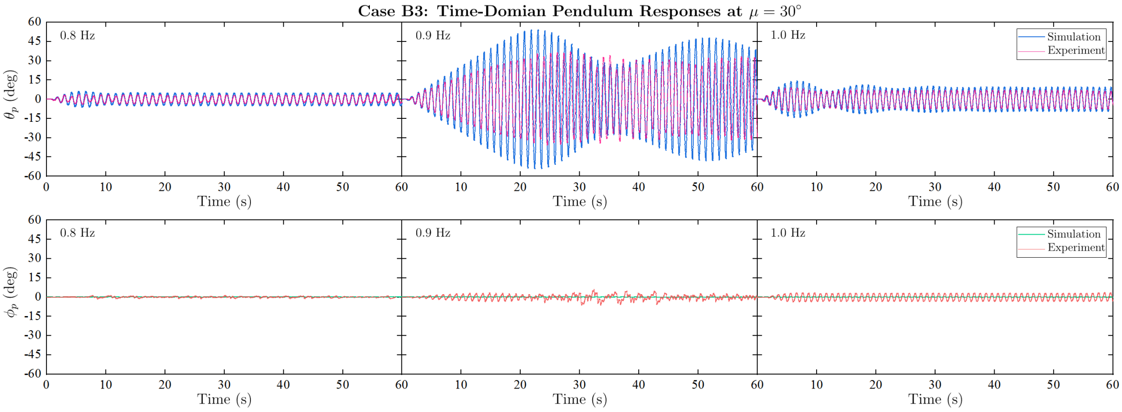

Figure 5.38: Case B3 - pendulum responses with PTO units at $\mu = 30°$ (upper row: θ_p-plane pendulum, lower row: ϕ_p-plane pendulum).

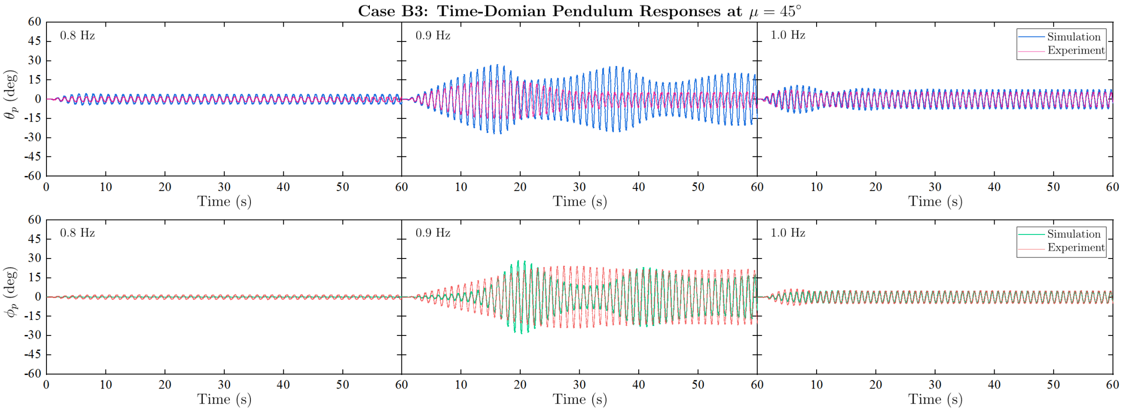

Figure 5.39: Case B3 - pendulum responses with PTO units at $\mu = 45°$ (upper row: θ_p-plane pendulum, lower row: ϕ_p-plane pendulum).

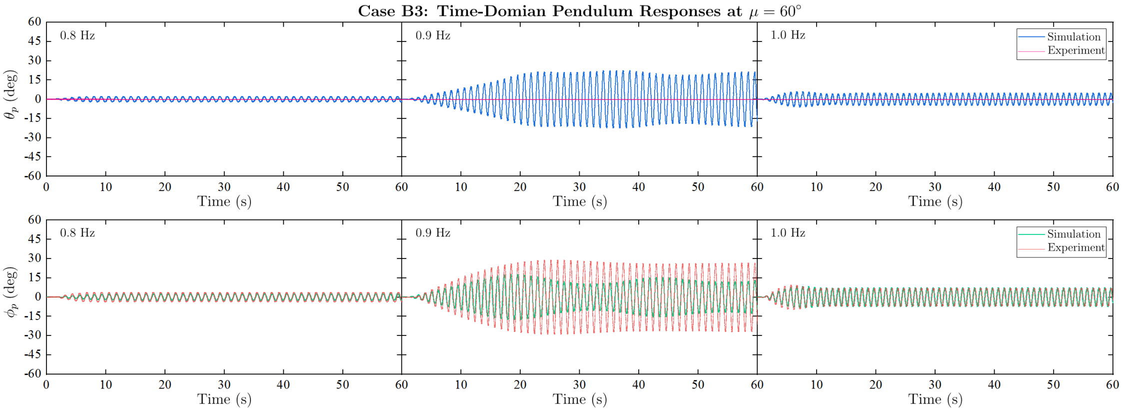

Figure 5.40: Case B3 - pendulum responses with PTO units at $\mu = 60°$ (upper row: θ_p-plane pendulum, lower row: ϕ_p-plane pendulum).

The RMS values of the constrained or 1-DOF pendulum responses without and with applied PTO units over the investigated frequency range and heading angles (μ) are presented in Figures 5.17, 5.21, 5.29, and 5.33. The overall comparisons of the 1-DOF motion responses in frequency-domain of the cases between numerical predictions by 1-DOF pendulum models, Equation D.19, and experimental results qualitatively and quantitatively show good agreement. The greatest motions emerge around resonance at 0.9 Hz as expected for both rotating references which are demonstrated in the time history responses in Figures 5.18 to 5.20, 5.22 to 5.24, 5.30 to 5.32, and 5.34 to 5.36.

These 1-DOF dynamic responses can also be compared to as the unconstrained pendulum, case A3 and B3, at $\mu = 0°$ and 90°. With the comparison to the case A1 and A2, the identical results proposed by the 2-DOF pendulum model, Equations 5.15 and 5.16, and the experimental results can be identified due to the pendulum ideally behave as a simple or 1-DOF pendulum system. This good correlation provides the confidence that the formed theoretical model is able to establish reasonable predictions when the excitation is parallel to a horizontal axis (x- or y-axes) is applied. In other words, for $\mu = 0°$ and 90° (a single directional excitation), the pendulum system behaves as a simple pendulum system as the coupling relationships/terms in the equations of motion, Equations 5.15 and 5.16, are not dominated as $\cos(0) = 1$ and $\sin(0) = 0$. Therefore, the equations of motion are reduced into a form of a simple pendulum system in Equation D.19. Moreover, the responded motion amplitudes by both numerical and experimental investigations in all conducted tests are lower when the PTO units are applied since the damping values for both rotating references are greater. When μ is applied ($0° < \mu < 90°$), the excitations along both horizontal axes (x_p- and y_p-axes) occur regarding the mathematical relationships in Equations 5.29 and 5.30. The θ_p-plane pendulum responses decrease followed the more angle until it dies out at 90°. Likewise, the ϕ_p-plane pendulum dynamically behaves in the opposite aspect.

Generally, the responded motion amplitudes of the θ_p-plane pendulum reference appear to be greater than the ϕ_p-plane pendulum in all tested circumstances. This is because of the combined perpendicular pivots created by the gimbal mechanism leads to non-equivalent mass distributions between the dynamic references, see Figure 5.9. For this case, the θ_p-plane pendulum comprises less mass, mass moment of inertia, and the parameters-related frictional torque as detailed in Table 5.1. Therefore, in this aspect, to design or to tune the system to have different natural frequencies between the reference planes is possible, e.g., for an asymmetric floating body as a marine vessel.

The overall 1-DOF pendulum dynamics have linear or normal sinusoidal responses as an example in Figure 5.41. The non-linearity of the exhibited motions from both the theoretical prediction and experiment can be observed during the test period as demonstrated in the time history plots, Figures 5.19, 5.20, 5.23, 5.31, and 5.35. The recorded motions, may, not finally reach steady-state responses or still in transient region. Thereby, the longer test duration is potentially required in order to cover all the characteristics of the oscillation response. Moreover, the small differences of the peak responded amplitudes between the numerical and experimental results at the resonance especially for ϕ_p-plane pendulum reference with applied PTO can be observed. This is attributed to the fact that the error made in the estimation of frictional damping constants (τ_{θ_p} and τ_{ϕ_p}) or experimental errors involving in the experiment configurations.

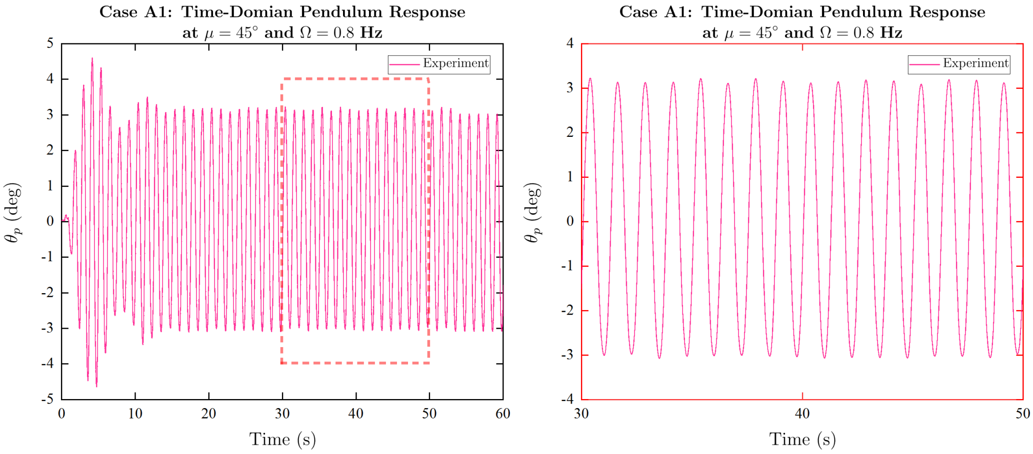

(a) Whole range view.

(b) Zoom-in view.

Figure 5.41: Example of a linear or regular sinusoidal response of the pendulum from the experiment case A1 at $\mu = 45°$ and $\Omega = 0.8$ Hz.

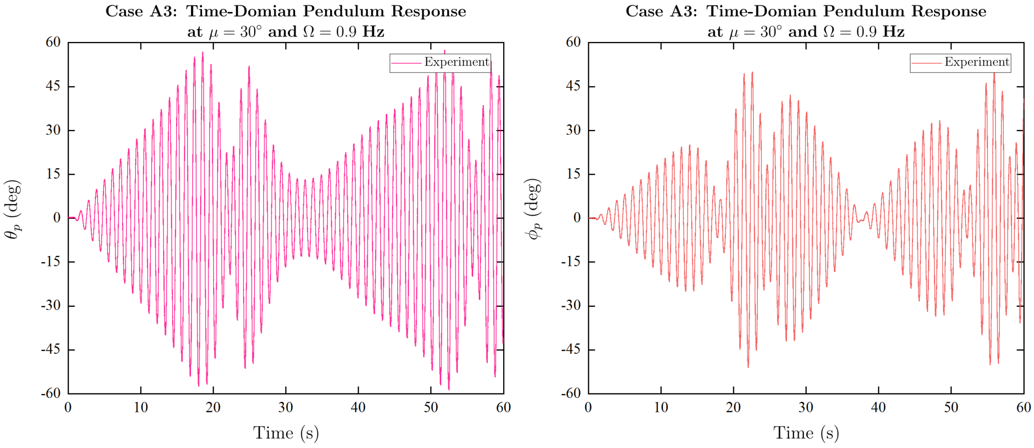

(a) θ_p-plane.

(b) ϕ_p-plane.

Figure 5.42: Example of non-linear responses of the coupled pendulum dynamics from the experiment case A3 at $\mu = 45°$ and $\Omega = 0.9$ Hz.

For the coupled pendulum dynamics without applied PTO units, case A3, the good agreements of the numerical and experimental results are found outside the resonance region with the comparable responded amplitudes to the planar responses as case A1 and A2 at the identical disturbed frequencies with regular sinusoidal responses. However, around resonance at 0.9 Hz, significant differences in the numerical predictions and experimental results are clearly observed as can be seen in Figures 5.26 to 5.28.

The pendulum responses form the experiment for this condition are abnormal wave forms, comlex non-linear responses, as an example in Figure 5.42. The observation also shows that the responded motions of the two rotating references are distinctively lower comparing to when it performed as a simple or 1-DOF pendulum with the duplicate disturbances due to the coupling effect between two dynamic references.

Further, when the PTO units are applied in case B3, the similar responded behaviour to case A3 (without PTO units) can be found with the modulated responses with regular wave forms. Outside the resonance, the agreeable comparisons are corroborated in the frequency ranges closing to the motion amplitudes of 1-DOF responses as examined in Figures 5.38 to 5.40. Therefore, these theoretically and experimentally imply that the domination of the coupling effect between two pendulum references at non-resonant regions is insignificant and potentially neglectable when the responded motion amplitudes are small. At and around the natural frequencies, the mathematical model could capture the expected trends of the coupled motions and tentatively indicate the effect of coupling phenomena that modulates both pendulum motions respecting the two referenced pivots where it becomes more influential. However, it provides the different responded amplitudes and characteristics compared to the experiment.

It can be therefore concluded that the mathematical model in Equations 5.15 and 5.16 based on geometrically coupled dynamics is unable to reflect all the particular aspect of the real physics of a gimballed pendulum system (especially at resonance). This is due to the fact that the assumption made in the numerical modelling simplified the dynamics of this type of pendulum with applied disturbance regarding only the dynamics of two inertial perpendicular reference planes in a 3-D Cartesian coordinate system which are the DOFs moving around two horizontal axes (x_p- and y_p-axes) or generalised coordinates (θ_p and ϕ_p). Hence, the dynamic definition around the vertical axis (z_p-axis) or the relationship relating to polar coordinate is required to fulfil the physics of this pendulum system. Nonetheless, with the potential asymmetric physical property of the pendulum using gimballed pivots, the determination of the equations of motion which are included all DOFs is theoretically complex and not straightforward.

5.5.2 Power Generations

The comparisons of the power generations between the 1- and coupled-DOFs pendulum dynamics are shown in Figures 5.43 to 5.45.

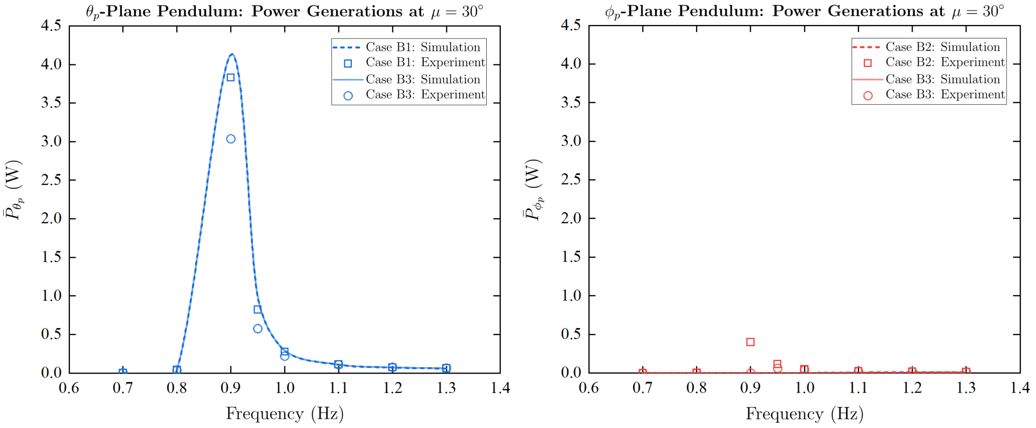

(a) θ_p-plane pendulum. (b) ϕ_p-plane pendulum.

Figure 5.43: Mean generated powers of the last 30 seconds of the pendulum responses at $\mu = 30°$.

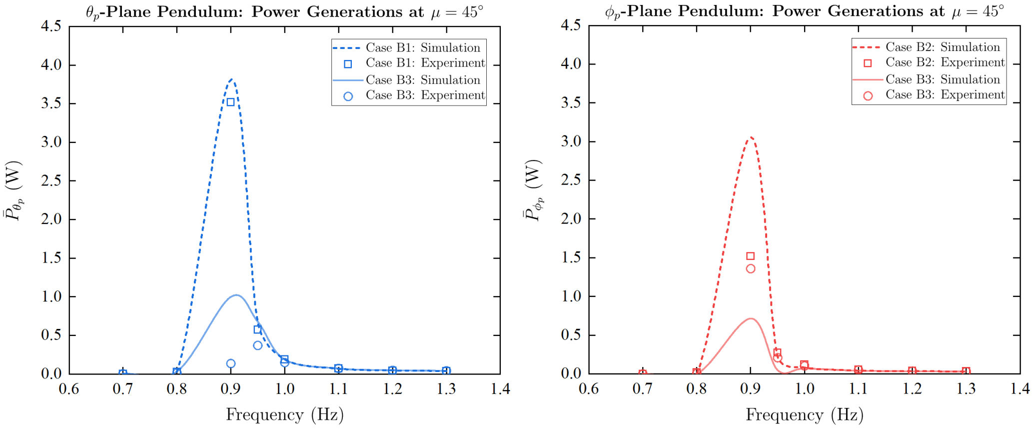

(a) θ_p-plane pendulum. (b) ϕ_p-plane pendulum.

Figure 5.44: Mean generated powers of the last 30 seconds of the pendulum responses at $\mu = 45°$.

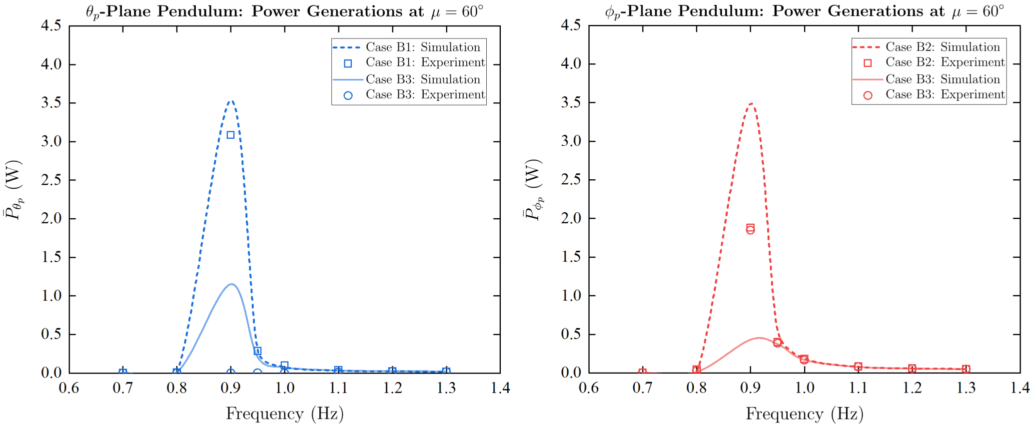

(a) θ_p-plane pendulum. (b) ϕ_p-plane pendulum.

Figure 5.45: Mean generated powers of the last 30 seconds of the pendulum responses at $\mu = 60°$.

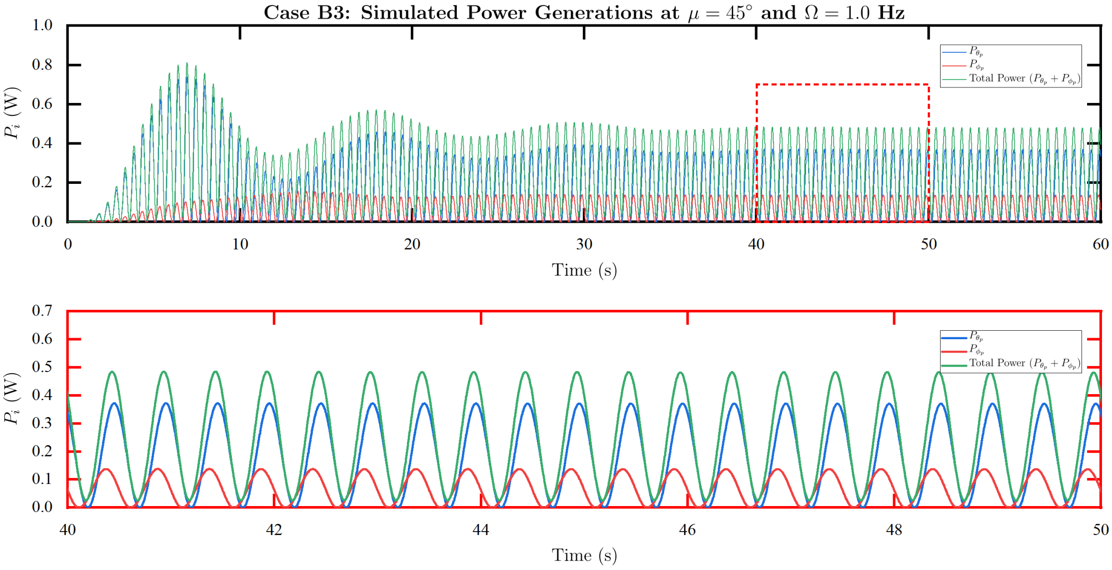

Figure 5.46: Example of simulated power generations of the coupled pendulum dynamics outside resonance region, case B3 at $\mu = 45°$ and $\Omega = 1.0$ Hz (blue - generated power by θ_p-plane pendulum, red - generated power by ϕ_p-plane pendulum, green - total generated power).

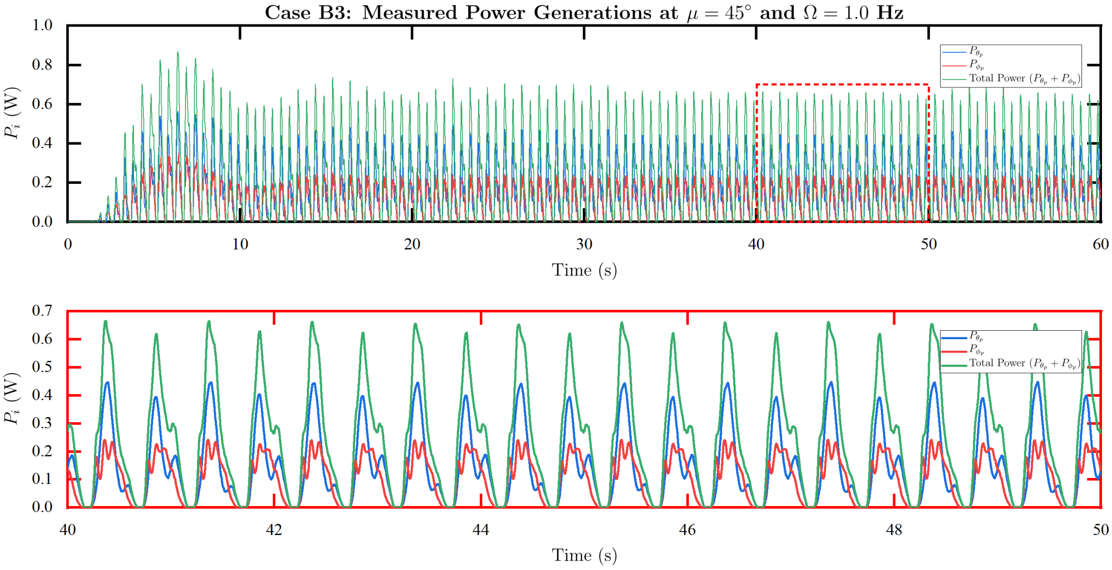

Figure 5.47: Example of measured power generations of the coupled pendulum dynamics outside resonance region, case B3 at $\mu = 45°$ and $\Omega = 1.0$ Hz (blue - generated power by θ_p-plane pendulum, red - generated power by ϕ_p-plane pendulum, green - total generated power).

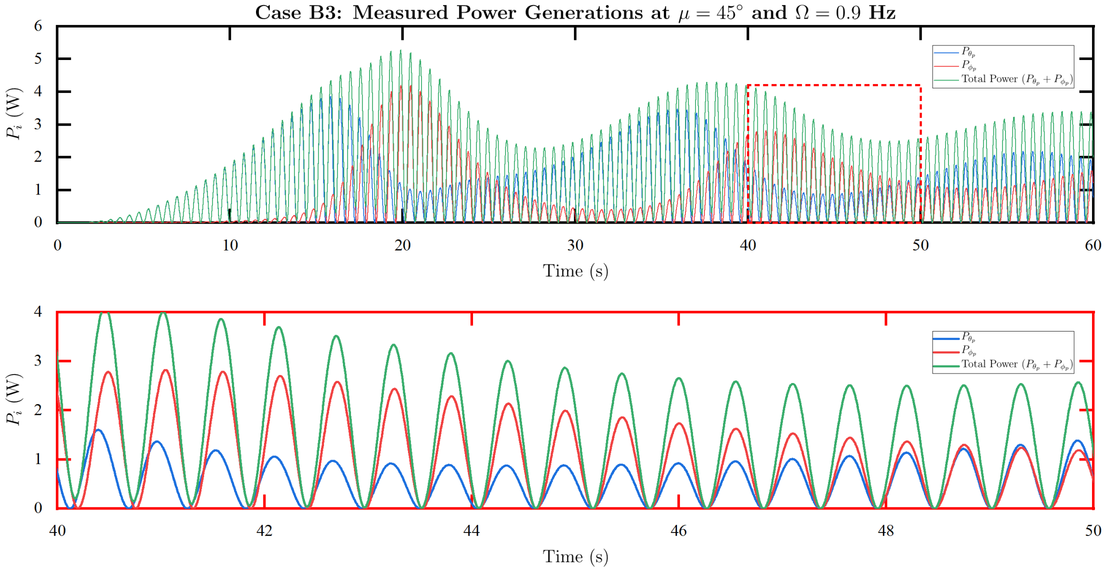

Figure 5.48: Example of simulated power generations of the coupled pendulum dynamics at resonance region, case B3 at $\mu = 45°$ and $\Omega = 0.9$ Hz (blue - generated power by θ_p-plane pendulum, red - generated power by ϕ_p-plane pendulum, green - total generated power).

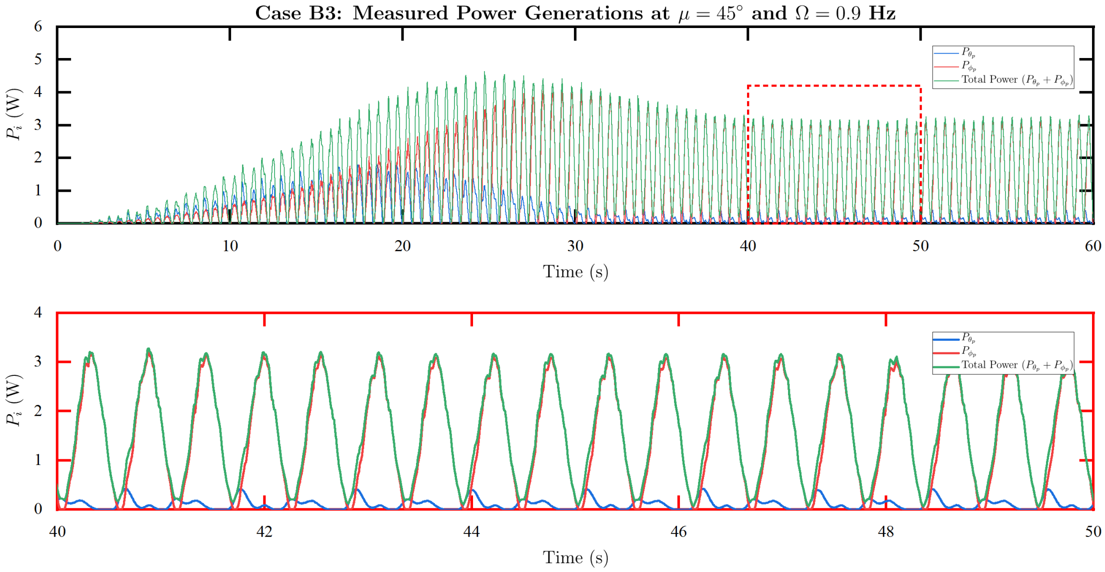

Figure 5.49: Example of measured power generations of the coupled pendulum dynamics at resonance region, case B3 at $\mu = 45°$ and $\Omega = 0.9$ Hz (blue - generated power by θ_p-plane pendulum, red - generated power by ϕ_p-plane pendulum, green - total generated power).

The maximum power generations by both simple pendulum and gimballed pendulum dynamics numerically and experimentally occur at the natural frequencies corresponding to the pendulum responses in all investigated heading angles. Generally, as expected, the comparisons of the power productions of 1-DOF dynamics between two pendulum references (case B1 for θ_p-plane pendulum and B2 for ϕ_p-plane pendulum) show that the θ_p-plane pendulum achieves higher power magnitude associated to the greater responded motions (due to the inertial property) which accommodates larger angular velocity to drive the DC generator.

For case B3, at $\mu = 0°$ and $90°$ both rotating references theoretically and physically perform the identical levels of power generations similar to case B1 and B2. In addition, it is worth noting that the coupled pendulum dynamics have not been clearly observed by either simulation and experiment at the heading angles of 15° and 75° as both pendulum references still comparably perform the power generations closing to the 1-DOF dynamics. At the applied heading angles of 30°, 45°, and 60°, the coupled pendulum motions are able to generate powers simultaneously. Similarly to the responded motions, the good correspondences of generated powers between the prediction and experimental validation are found outside the natural frequencies as the examples exhibited in Figures 5.46 and 5.47. Also, the power productions of the gimballed pendulum at these regions are magnified by the coupled pendulum motions comparing to when it operates as a 1-DOF system. However, at around resonance, The overall comparisons for the individual pendulum references between 1- and coupled-DOFs indicate that the coupled motions of the gimballed pendulum generate less powers due to the dominant coupling effect between two pendulum dynamics resulting in the modulated motion amplitudes and angular velocities. The similarity of the power generation relating to responded characteristics by numerical prediction and experiment has not been found as presented in Figures 5.48 and 5.49 even the domination of the coupling effect can be identified.

Overall, it may be stated that a gimbal mechanism is able to add compactness in design and directional responsiveness to a pendulum energy harvesting system. The maximum individual power generation level of each rotating reference could be achieved where the direction of applied excitation is parallel to a horizontal referenced axis (x_p- or y_p-axis) or, in this case, at $\mu = 0°$ and $90°$. In other words, the pendulum identically responds as a 1-DOF system. Outside resonance zone, the pendulum responses respecting two perpendicular rotating references comparably perform when they are constrained to rotate on a fixed plane as the responses are small, and the coupling effect is insignificant. This could be beneficial for the magnified power production by the coupled motions. Nevertheless, when the coupling effect is dominant at resonance in sufficient heading angles, the coupled pendulum dynamics create an undesired influence that results in lower response implying inferior power generation compared to when it performs as a planar or 1-DOF pendulum.

5.6 Summary

A novel theoretical model and a set of experimental validations and investigations of a gimballed pendulum energy harvesting system are described. Initially, the numerical model is developed using the governing equation (Lagrange's equation) with the simplified assumption that the presumed dual-perpendicular pendulum systems are created by a gimbal mechanism, and are treated as two driven planar or 1-DOF pendulum dynamic references, with geometric coupling relationships. By this method, the physical properties of the two rotating references are realistically allowed to be asymmetric. In addition, the natural frequencies of both rotating references are possible to be theoretically and practically tuned or designed differently.

The results from the mathematical and experimental investigations show qualitative and quantitative agreements over the tested frequency range as 1-DOF dynamic responses, in this case, the heading angles (μ) are equal to $0°$ and $90°$. For the condition that the applied excitation direction is not parallel to either rotating references, multi-directional responsiveness could be clearly achieved by a gimballed mechanism.

The coupled motions provided by the investigations show good agreement outside the resonance region with comparable responded motion magnitudes when it performs as a 1-DOF system, implying the coupling effect between the pendulum motions is insignificant and can be neglected. Therefore, the simultaneous power generations from both perpendicular pivots provide higher power output level compared to 1-DOF pendulum responses generated by a similar planar inertial pendulum property. At resonance, the dominant coupling effect is captured; however, the prediction of the pendulum motions by the mathematical model has been found to be inaccurate compared to the motions produced by the actual device test due to the simplified assumption that is made to form the equations of motion. Moreover, in this resonance condition, the coupled motions respecting the two perpendicular rotating references are significantly lower. This leads to an undesired lower simultaneous power production level compared to 1-DOF dynamic response at the identical excitation circumstance.

Chapter 6

Numerical Modelling and Experimental Validation of the Coupled Ship and Gimballed Pendulum Dynamics

The dynamics of motions of a ship in waves and the dynamics of a gimballed pendulum system are outlined in Chapters 3 and 5 respectively. Based on the identified dynamics, this chapter describes the coupled dynamics of a ship and an onboard gimballed pendulum energy harvester. The numerical model of the coupled dynamics consists of two main dynamics subsystems; the vessel and the pendulum motions. As the subsystems are coupled, the equations of motions of the ship and pendulum including the feedback dynamics are pointed out. Then, a set of experimental validations based on wave tank testing is presented. Finally, the results regarding numerical predictions and experimental validations are demonstrated and discussed.

6.1 Numerical Modelling of the Coupled Dynamics

6.1.1 Dynamics of the Coupled System

The numerical model aims to simulate the coupled dynamics of a ship and an onboard gimballed pendulum energy harvester. Both the ship and the pendulum motions are defined by sets of second-order differential equations (ODEs). Therefore, defining both dynamics together as a system, the system involves two sets of ODEs in which each set of equations can be referred to as a subsystem.

6.1.2 Assumptions and Limitations

The assumptions and limitations of linear wave theory and 2-D strip theory are applied as stated in Chapters 3 and 4. Additionally, the numerical model of the coupled dynamics also assumes that

- The overall mass distribution of the ship is not affected by the onboard pendulum.
- The displacement of the ship is not changed when the pendulum is installed, and therefore the hydrodynamic coefficients calculated by 2-D strip theory are not changed.
- The numerical model of the coupled dynamics only considers moments of the forces created by the swinging pendulum references as the feedback dynamics to the ship motions.
- The numerical model does not consider the change in the ship's centre of gravity during the pendulum is swinging.

6.1.3 Implemented Equations of Motions

According to the theoretical detail of a ship dynamics in waves in Chapter 3 and the assumption made in Chapter 4, the equations of the oscillatory ship motions including the feedback moments created by the onboard gimballed pendulum can be defined as:

- **Heave Motion**:

$$\begin{aligned}\big(\rho\nabla + a_{33}(\omega_e)\big)\ddot{z}(\omega_e,t) + b_{33}(\omega_e)\dot{z}(\omega_e,t) + c_{33}z(\omega_e,t)\\ +a_{35}(\omega_e)\ddot{\theta}(\omega_e,t) + b_{35}(\omega_e)\dot{\theta}(\omega_e,t) + c_{35}\theta(\omega_e,t)\\ = F_{wa_3}(\omega_e)\cos\big(\omega_e t + \varepsilon_3(\omega_e)\big)\end{aligned} \tag{6.1}$$

- **Roll Motion**:

$$\begin{aligned}\big(I_{xx} + a_{44}(\omega_e)\big)\ddot{\phi}(\omega_e,t) + b_{44}(\omega_e)\dot{\phi}(\omega_e,t) + c_{44}\phi(\omega_e,t)\\ = F_{wa_4}(\omega_e)\cos\big(\omega_e t + \varepsilon_4(\omega_e)\big) + \underbrace{F_{\phi_p}(\omega_e,t)}_{\text{Feedback Moment}}\end{aligned} \tag{6.2}$$

- **Pitch Motion**:

$$\begin{aligned}a_{53}(\omega_e)\ddot{z}(\omega_e,t) + b_{53}(\omega_e)\dot{z}(\omega_e,t) + c_{53}z(\omega_e,t)\\ \big(I_{yy} + a_{55}(\omega_e)\big)\ddot{\theta}(\omega_e,t) + b_{55}(\omega_e)\dot{\theta}(\omega_e,t) + c_{55}\theta(\omega_e,t)\\ = F_{wa_5}(\omega_e)\cos\big(\omega_e t + \varepsilon_5(\omega_e)\big) + \underbrace{F_{\theta_p}(\omega_e,t)}_{\text{Feedback Moment}}\end{aligned} \tag{6.3}$$

by heave motion is not affected by the moments created by the pendulum and therefore the equation of heave motion remains unchanged, and F_{θ_p} and F_{ϕ_p} are the feedback moments (N·m) created by the pendulum references on longitudinal and transverse planes. According to the schematic drawing of the coupled dynamics illustrated in Figure 6.1, the moments of the forces respecting the referenced planes can be calculated as:

- **Longitudinal-Plane**:

$$\begin{aligned} F_{\theta_p}(\omega_e,t) = {} & F_{H_{\theta_p}}(\omega_e,t)\big(z_{pp} - l_{\theta_p}\cos(\phi_p(\omega_e,t))\cos(\theta_p(\omega_e,t))\big) \\ & - F_{V_{\theta_p}}(\omega_e,t)\big(x_{pp} + l_{\theta_p}\cos(\phi_p(\omega_e,t))\sin(\theta_p(\omega_e,t))\big) \end{aligned} \tag{6.4}$$

- **Transverse-Plane**:

$$\begin{aligned} F_{\phi_p}(\omega_e,t) = {} & F_{H_{\phi_p}}(\omega_e,t)\big(z_{pp} - l_{\phi_p}\cos(\theta_p(\omega_e,t))\cos(\phi_p(\omega_e,t))\big) \\ & - F_{V_{\phi_p}}(\omega_e,t)\big(y_{pp} + l_{\phi_p}\cos(\theta_p(\omega_e,t))\sin(\phi_p(\omega_e,t))\big) \end{aligned} \tag{6.5}$$

where $F_{H_{\theta_p}}$, $F_{H_{\phi_p}}$, $F_{V_{\theta_p}}$, and $F_{V_{\phi_p}}$ are the horizontal and vertical forces created by the swinging pendulum on the referenced longitudinal- and transverse-planes respectively. In addition, x_{pp}, y_{pp}, and z_{pp} are the position of the pivot point of the pendulum away from the CG of the ship respecting x_b-, y_b-, and z_b-axes.

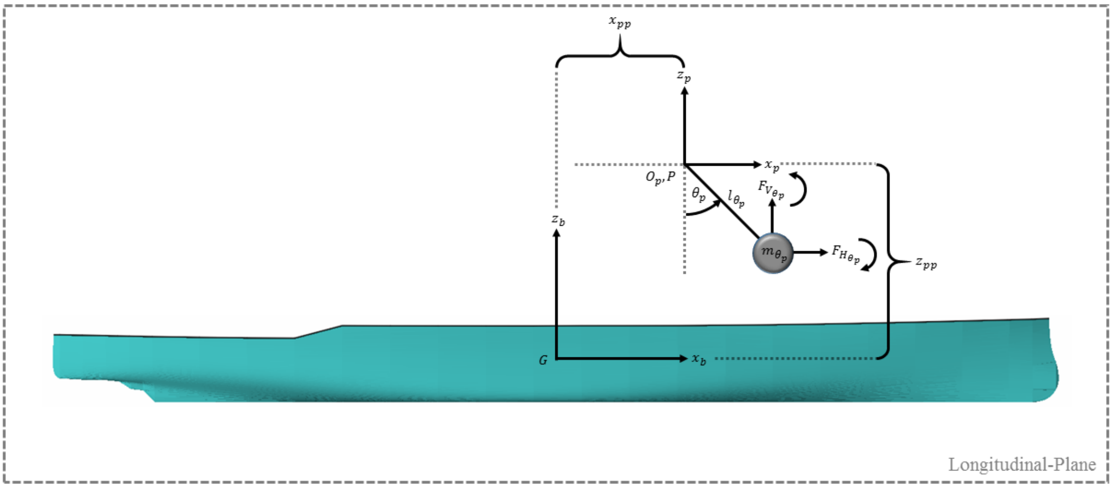

(a) Longitudinal-plane dynamics.

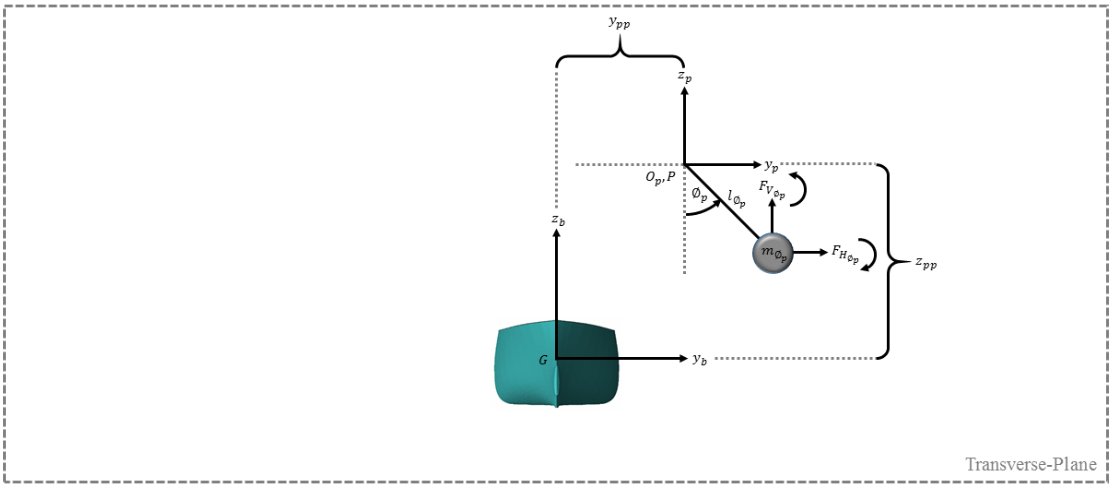

(b) Transverse-plane dynamics.

Figure 6.1: Schematic drawing of the coupled dynamics of the numerical model.

For the dynamics of the onboard gimballed pendulum system, the equations of motions of the pendulum references can be quoted Equations 5.15 and 5.16 detailed in Chapter 5 and the displacement of the excitations at the pendulum pivot along x_p-, y_p-, and z_p-axes at any point on the ship, see Journée and Massie (2001) for detail, regarding the assumptions can be obtained as:

- **Longitudinal Excitation**:

$$X_p(\omega_e,t) = z_{pp}\theta(\omega_e,t) \tag{6.6}$$

$$\dot{X}_p(\omega_e,t) = z_{pp}\dot{\theta}(\omega_e,t) \tag{6.7}$$

$$\ddot{X}_p(\omega_e,t) = z_{pp}\ddot{\theta}(\omega_e,t) - g\theta(\omega_e,t) \tag{6.8}$$

- **Lateral Excitation**:

$$Y_p(\omega_e,t) = -z_{pp}\phi(\omega_e,t) \tag{6.9}$$

$$\dot{Y}_p(\omega_e,t) = -z_{pp}\dot{\phi}(\omega_e,t) \tag{6.10}$$

$$\ddot{Y}_p(\omega_e,t) = -z_{pp}\ddot{\phi}(\omega_e,t) + g\phi(\omega_e,t) \tag{6.11}$$

- **Vertical Excitation**:

$$Z_p(\omega_e,t) = z - x_{pp}\theta(\omega_e,t) - y_{pp}\phi(\omega_e,t) \tag{6.12}$$

$$\dot{Z}_p(\omega_e,t) = \dot{z} - x_{pp}\dot{\theta}(\omega_e,t) - y_{pp}\dot{\phi}(\omega_e,t) \tag{6.13}$$

$$\ddot{Z}_p(\omega_e,t) = \ddot{z} - x_{pp}\ddot{\theta}(\omega_e,t) - y_{pp}\ddot{\phi}(\omega_e,t). \tag{6.14}$$

Ultimately, the numerical model of the coupled ship and gimballed pendulum dynamics can be therefore represented as a second-order ODE in a matrix form in a discretised time-step at a particular encountering frequency as:

$$M_{5\times5}\begin{bmatrix}\ddot{z}(\omega_e,t)\\ \ddot{\phi}(\omega_e,t)\\ \ddot{\theta}(\omega_e,t)\\ \ddot{\theta}_p(\omega_e,t)\\ \ddot{\phi}_p(\omega_e,t)\end{bmatrix} + C_{5\times5}\begin{bmatrix}\dot{z}(\omega_e,t)\\ \dot{\phi}(\omega_e,t)\\ \dot{\theta}(\omega_e,t)\\ \dot{\theta}_p(\omega_e,t)\\ \dot{\phi}_p(\omega_e,t)\end{bmatrix} + K_{5\times5}\begin{bmatrix}z(\omega_e,t)\\ \phi(\omega_e,t)\\ \theta(\omega_e,t)\\ \theta_p(\omega_e,t)\\ \phi_p(\omega_e,t)\end{bmatrix} = F_{5\times1} \tag{6.15}$$

where $M_{5\times5}$ is the 5 by 5 inertial matrix, $C_{5\times5}$ is the 5 by 5 damping matrix, $K_{5\times5}$ is the 5 by 5 restoring or stiffness matrix, and $F_{5\times5}$ is the 5 by 1 external excitation including the feedback moments matrix.

Note that, the hydrodynamic and hydrostatic coefficients of the ship in waves are calculated based on the 2-D strip theory (for coupled heave-pitch) and estimation based on the ship's hydrostatic property (for roll) which are implemented in the MAXSURF software package with the similar verified input parameter discussed in Chapter 4.

6.1.4 Numerical Algorithm

Figure 6.2 shows the flow chart of the numerical algorithm of the numerical model of the coupled dynamics. Again, this numerical model is solved using RK4 numerical method based on MATLAB software package with the similar verified time-step size mentioned in Section 5.3.1.

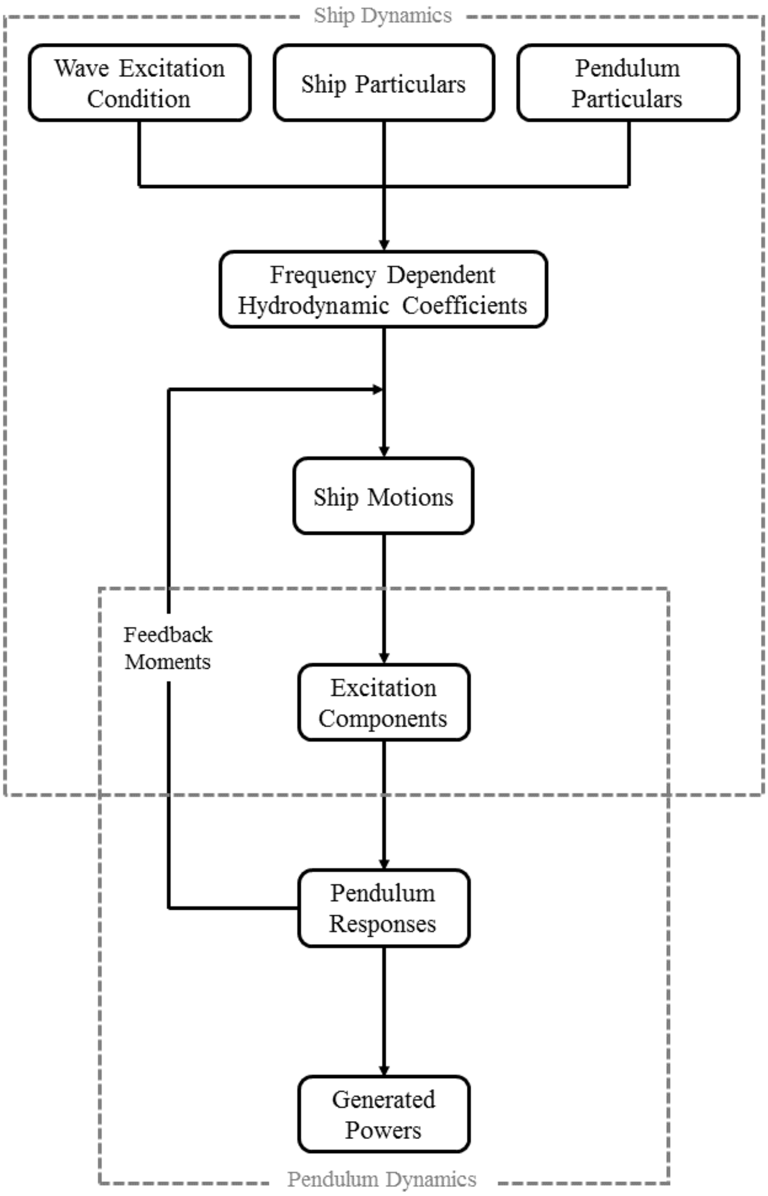

Figure 6.2: Flow chart of the numerical algorithm of the coupled ship and pendulum dynamics.

6.2 Experimental Validation of the Numerical Model of the Coupled Ship and Gimballed Pendulum Dynamics

6.2.1 Experimental Set-up

An existing ship model as shown in Figure 6.3(a), the HMS Queen Mary (QM) Battle Cruiser model, was modified for the purpose of the wave tank experiment aiming to validate the created numerical model of the coupled ship and gimballed pendulum energy harvester dynamics. The prototype of a gimballed pendulum detailed in Chapter 5 was attached to the model as can be seen in Figure 6.3(b). The combined weight of the pendulum prototype with the supporting frame was 8.5% of the total displacement of the ship model (at this waterline). Additionally, it is worth noting that the design of the ship and the onboard pendulum is not optimal. The model particulars are detailed in Table 6.1.

(a) ship hull.

(b) ship hull with installed gimballed pendulum system.

Figure 6.3: Investigated ship model.

Table 6.1: Experimental Particulars for the Investigated Model

Parameter	Symbol	Value	Unit
Length Overall	L_{OA}	2.470	m
Beam Overall	B_{OA}	0.315	m
Moulded Depth	D	0.190	m
Draft	d	0.112	m
Waterline Length	L_{WL}	2.462	m
Waterline Beam	B_{WL}	0.316	m
Displacement Weight	Δ	48.980	kg
Block Coefficient	C_B	0.562	-
Longitudinal Centre of Gravity (from Amidships)	LCG	-0.026	m
Vertical Centre of Gravity (from Baseline)	VCG	0.112	m
Transverse Metacentric Height	G_{MT}	0.274	m
Position of the Pendulum Pivot from the Ship's CG in x_b-Axis	x_{pp}	-0.141	m
Position of the Pendulum Pivot from the Ship's CG in y_b-Axis	y_{pp}	0.000	m
Position of the Pendulum Pivot from the Ship's CG in z_b-Axis	z_{pp}	0.414	m

6.2.2 Roll and Pitch Radii of Gyration Measurements

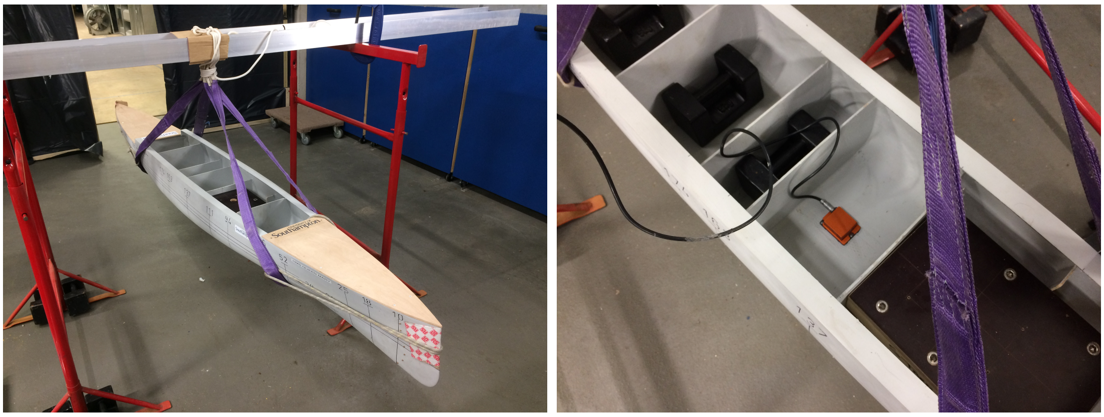

(a) Compound pendulum test rig.

(b) Motion sensor.

Figure 6.4: Radius of gyration test.

The roll and pitch moments of inertia were measured using the compound pendulum test rig (see Bhattacharyya (1978) or Lloyd (1989) for more detail) as illustrated in Figure 6.4. The model was suspended in a rigid structure with the distance from the CG of the model to the pivot (h, m) as, for this case, the value is 0.630 m. Then, this pendulum-like arrangement was released from a particular angle from resting position and the oscillation period which can be referred to the natural period of oscillation (T_*, s) was measured by the IMU, Xsens MTi-100. The moment of inertia of the pendulum rig regarding the referenced motion can be expressed as:

$$I = mk_{ii}^2 \quad \text{by} \quad ii = 44 \text{ or } 55 \tag{6.16}$$

where m is the mass of the model, and the stiffness of the compound pendulum is

$$c = mgh. \tag{6.17}$$

Therefore, the oscillation frequency can be calculated as:

$$\omega_{*,ii} = \frac{2\pi}{T_{*,ii}} = \sqrt{\frac{c}{I}} \quad \text{by} \quad ii = 44 \text{ or } 55 \tag{6.18}$$

and the radius of gyration of the model is given by

$$k_{ii} = \sqrt{\frac{ghT_{*,ii}^2}{4\pi^2} - h^2} \quad \text{by} \quad ii = 44 \text{ or } 55. \tag{6.19}$$

The time history and the oscillation period of roll and pitch radii of gyration tests of the model are presented in Figures 6.5 and 6.6 and the values of the radii of gyration is summarised in Table 6.2.

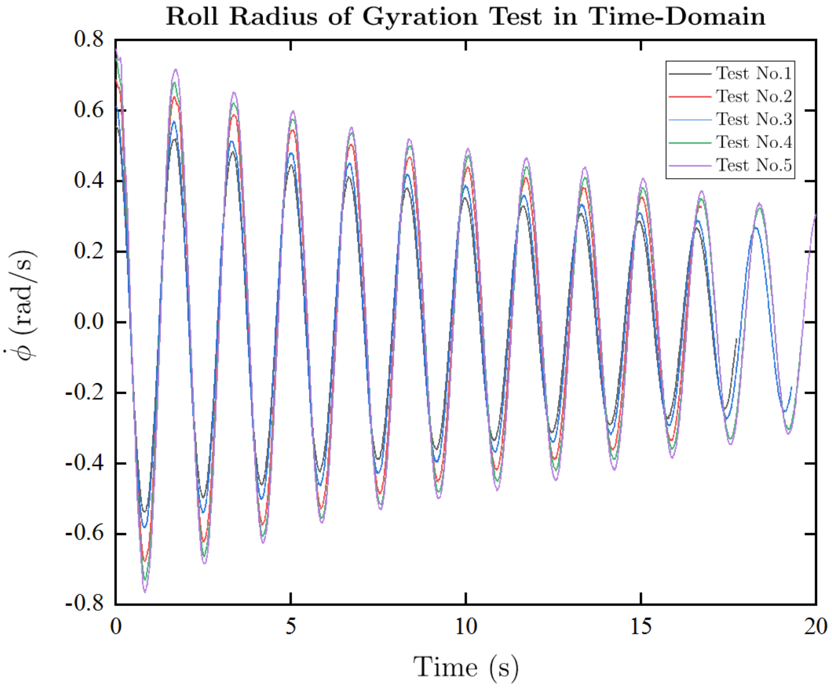

(a) Time-domain decay.

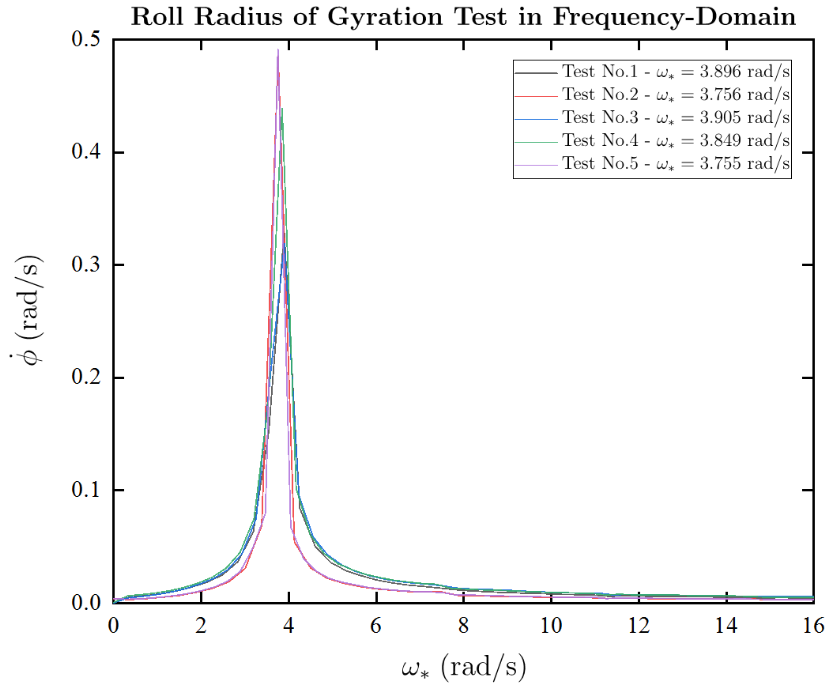

(b) FFTs of time-domain decay.

Figure 6.5: Roll radius of gyration tests.

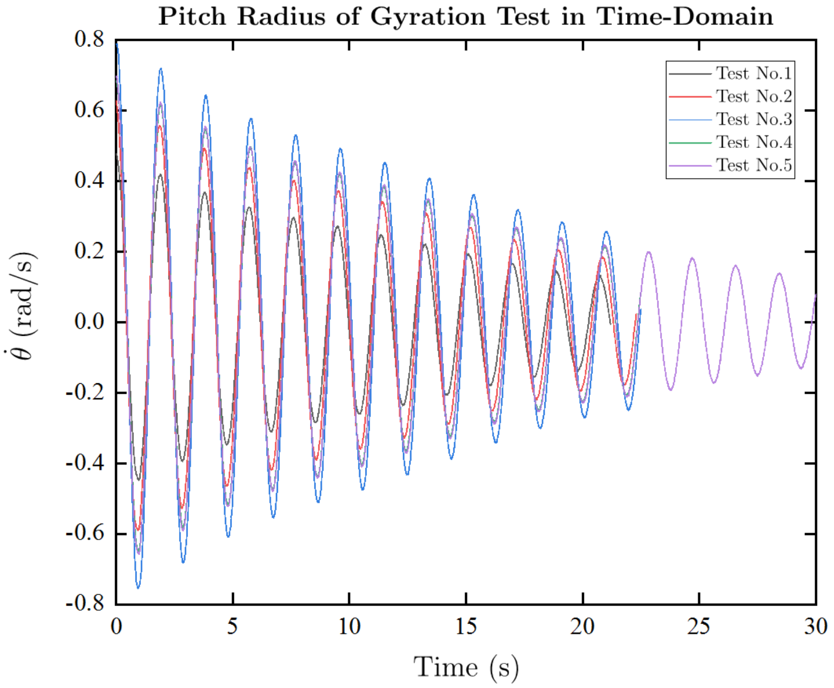

(a) Time-domain decay.

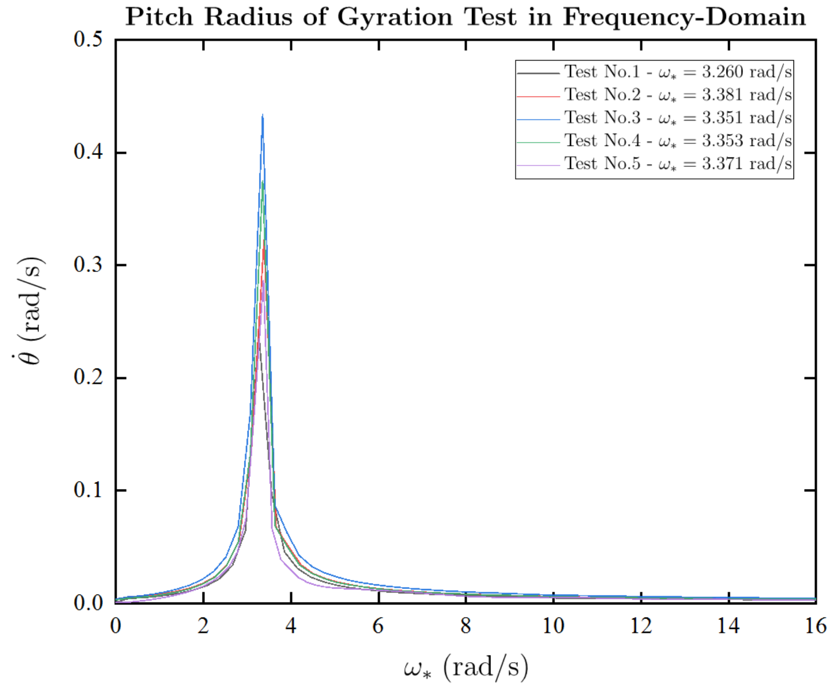

(b) FFTs of time-domain decay.

Figure 6.6: Pitch radius of gyration tests.

Table 6.2: Radii of Gyration Measurements.

Parameter	Symbol	Value		Unit
		Roll ($ii = 44$)	Pitch ($ii = 55$)	
Average Oscillation Frequency	$\bar{\omega}_{*,ii}$	3.832	3.343	rad/s
Oscillation Period	$T_{*,ii}$	1.640	1.879	s
Radius of Gyration	k_{ii}	0.155 (49.21 % of B_{OA})	0.395 (15.99 % of L_{OA})	m

6.2.3 Roll Damping Coefficient Measurement

The roll damping coefficient of the ship model was obtained from a set of roll decay tests of the roll motion. The method of this measurement has a similar approach compared to the pendulum decay tests discussed in Chapter 5 but, in this case, the vessel was tested in a water tank and was heeled over a particular initial angle and then released. The decay over the time of the roll motion was recorded and plotted as a slope of decaying successive peaks.

By using the average of the slope of the decay peaks from the tests, the non-dimensional roll damping coefficient or damping ratio is numerically modelled using the viscous damping assumption which can be estimated by Equation 5.23. The results from the roll decay tests and the simulated roll decay motion based on the average value from the measurement are shown in Figure 6.7 and the value of the calculated non-dimensional roll damping coefficient is summarised in Table 6.3. It should be noted that the unsmoothed decay slopes can be observed due to the experimental error that is the waves reflections created by the tank wall.

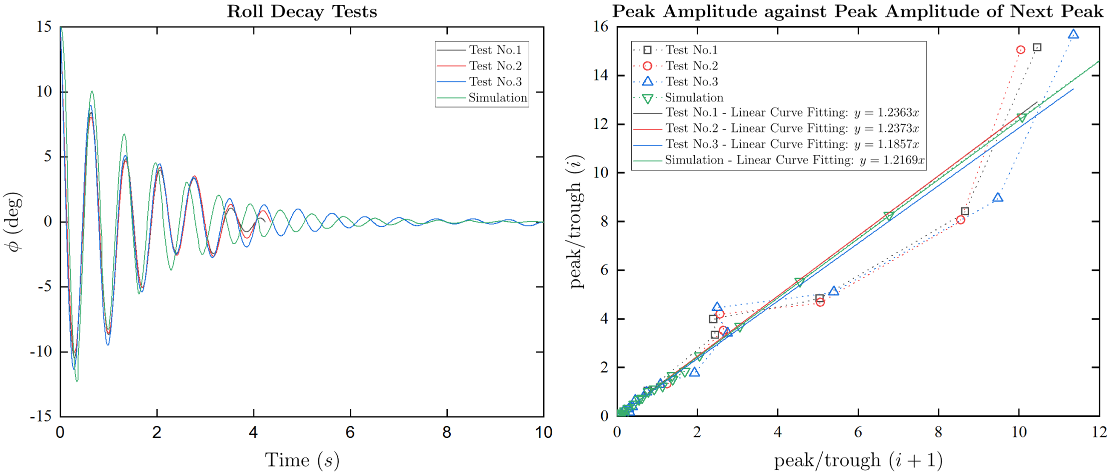

(a) Time-domain decay. (b) Decay slope.

Figure 6.7: Investigation of roll damping coefficient of the HMS QM model.

Table 6.3: Calculated Roll Damping Coefficient.

Parameter	Symbol	Value	Unit
Average Slope	-	1.220	-
Non-Dimensional Roll Damping Coefficient	ξ_{44}	0.063	-
Roll Damping Coefficient	b_{44}	1.758	$kg{\cdot}m^2/s$

6.2.4 Experimental Plan

A series of wave tank experimental testing was conducted in the Southampton Solent University towing tank which has the dimension of 60 m in length, 3.7 m wide and 1.8 m deep and capable of generating waves of up to 0.2 m amplitude and a frequency of 1.2 Hz. The ship model was constrained to a carriage via tow post at around 7 m away from the wave maker and 50 m away from the beach. The location of the tow post attached at the model is 25 cm from the model's LCG toward the bow. This tow post only allows the model to heave, roll, and pitch. Also, the motions of the model can be measured by the linear and rotary potentiometers connected to the tow post. Moreover, the applied wave profile was measured by a wave probe.

The experimental validation of the ship model with the onboard gimballed pendulum energy harvester was conducted based on that the ship was stationary and the pendulum was unlocked and allowed to swing around both perpendicular pivots without and with PTO units. The amplitudes of the regular waves (ζ_a) used were 0.035 m (0.07 m wave height (H)) with the wave frequencies from 0.5 to 1.2 Hz with 0.1 Hz increment. Moreover, due to the blockage issue with the carriage and the model, the greatest angle of the ship that can be practically investigated was 30° from the head waves condition or 150° relative to the direction of the waves. Therefore, three heading conditions were investigated which were 180°, 165°, and 150°. Also, it should be noted that all the motion responses results were measured based on around of 60-70 seconds range to avoid the effect of wave reflection by the tank end.

6.3 Results and Discussion

6.3.1 Ship Responses

Set of numerical and experimental results of the ship model responded transfer functions of the coupled heave-pitch and roll motions regarding the investigated heading conditions are shown in Figure 6.8 to 6.16.

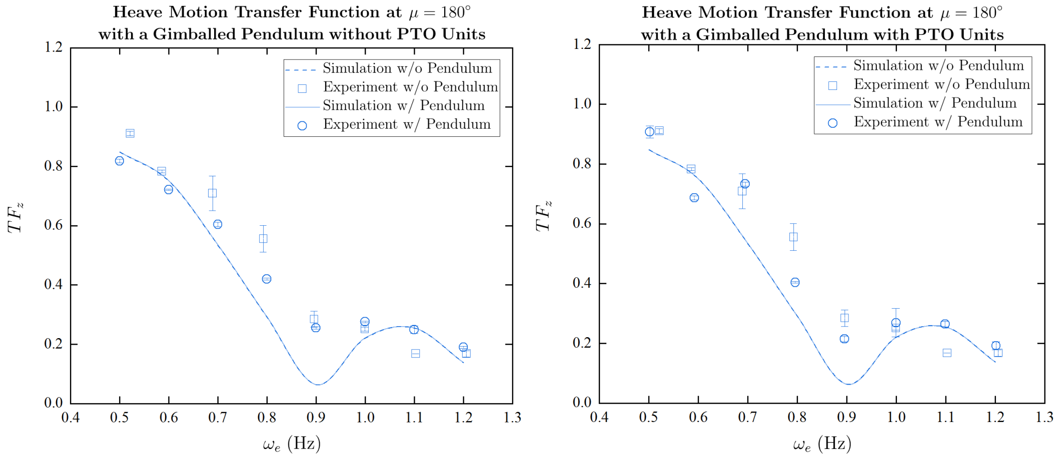

(a) with gimballed pendulum without PTOs.

(b) with gimballed pendulum with PTOs.

Figure 6.8: Heave motion transfer function at $\zeta_a = 0.035$ m and $\mu = 180°$.

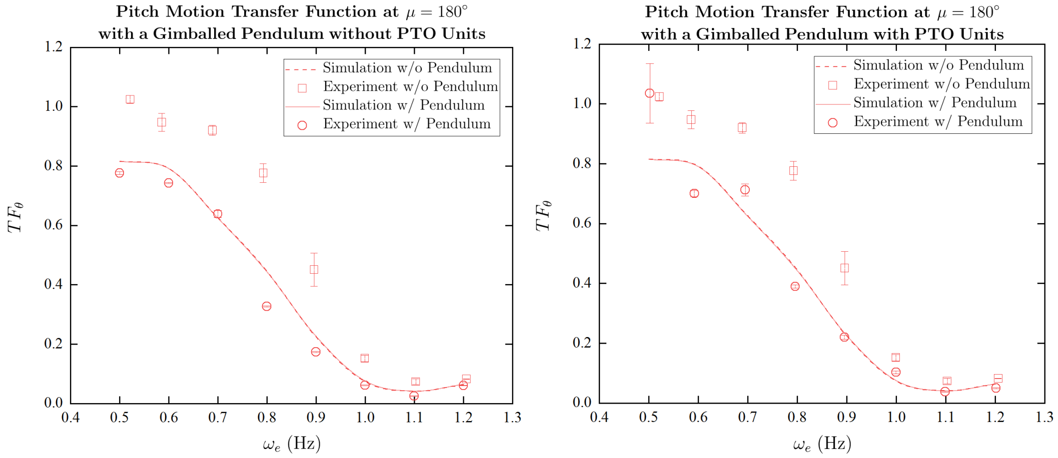

(a) with gimballed pendulum without PTOs.

(b) with gimballed pendulum with PTOs.

Figure 6.9: Pitch motion transfer function at $\zeta_a = 0.035$ m and $\mu = 180°$.

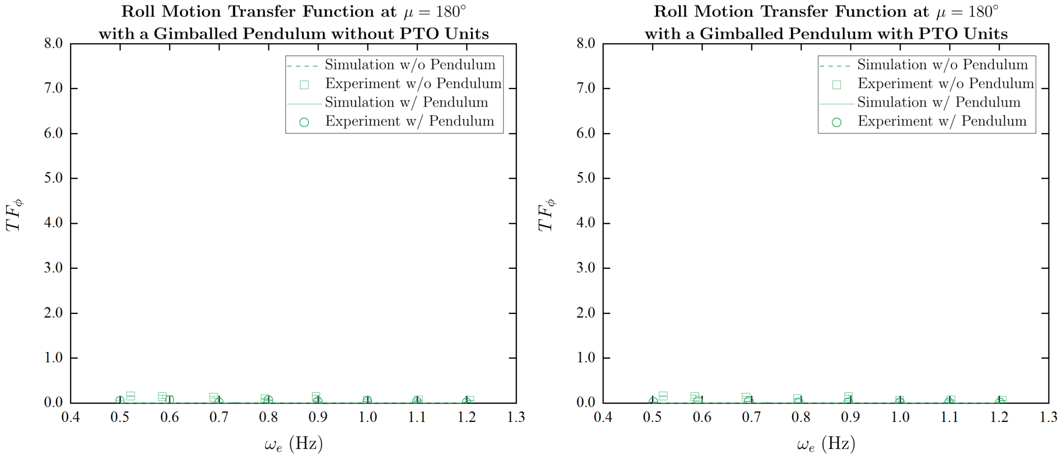

(a) with gimballed pendulum without PTOs.

(b) with gimballed pendulum with PTOs.

Figure 6.10: Roll motion transfer function at $\zeta_a = 0.035$ m and $\mu = 180°$.

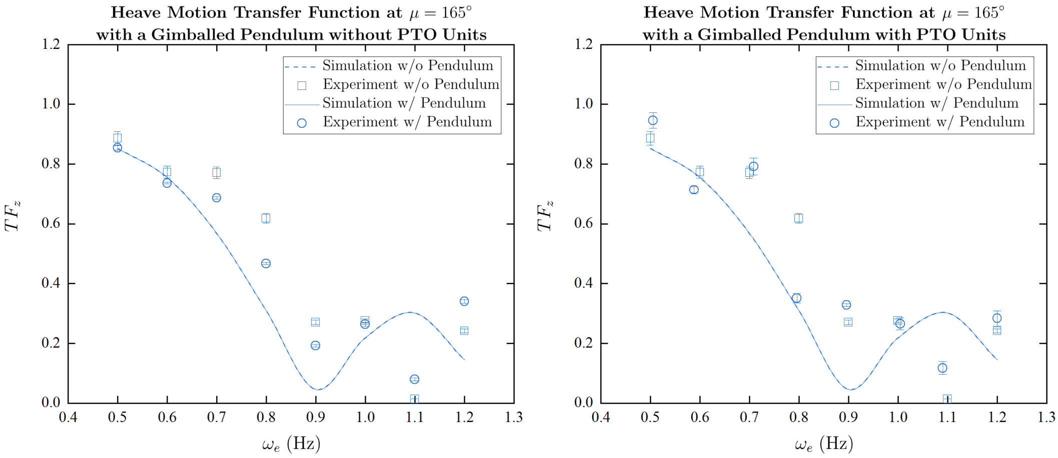

(a) with gimballed pendulum without PTOs.

(b) with gimballed pendulum with PTOs.

Figure 6.11: Heave motion transfer function at $\zeta_a = 0.035$ m and $\mu = 165°$.

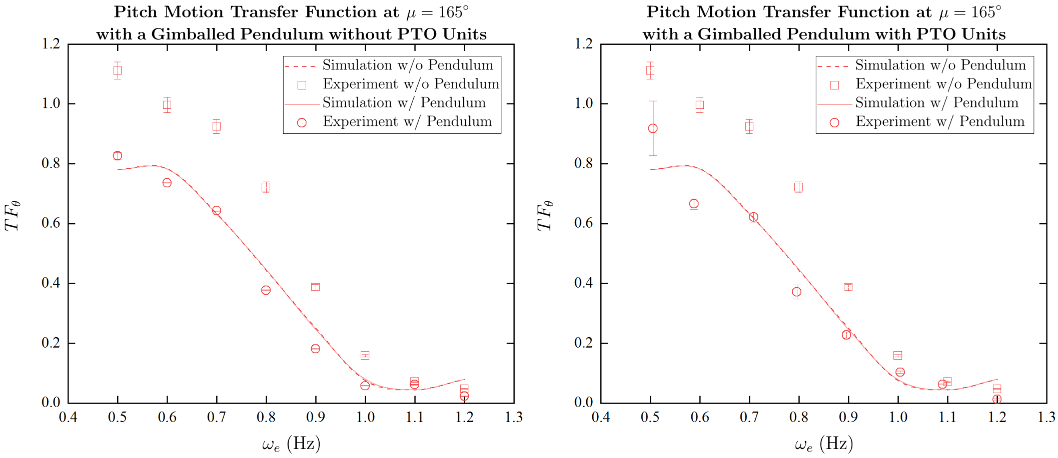

(a) with gimballed pendulum without PTOs.

(b) with gimballed pendulum with PTOs.

Figure 6.12: Pitch motion transfer function at $\zeta_a = 0.035$ m and $\mu = 165°$.

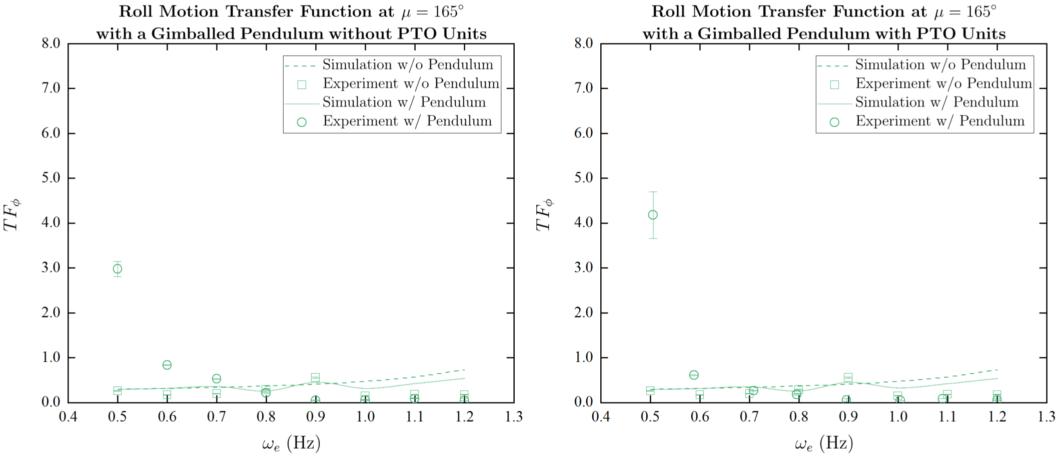

(a) with gimballed pendulum without PTOs.

(b) with gimballed pendulum with PTOs.

Figure 6.13: Roll motion transfer function at $\zeta_a = 0.035$ m and $\mu = 165°$.

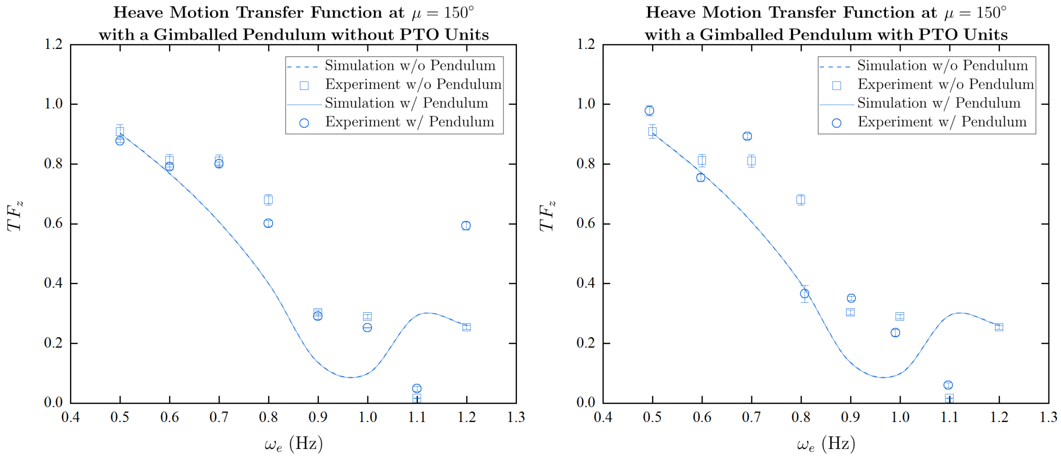

(a) with gimballed pendulum without PTOs. (b) with gimballed pendulum with PTOs.

Figure 6.14: Heave motion transfer function at $\zeta_a = 0.035$ m and $\mu = 150°$.

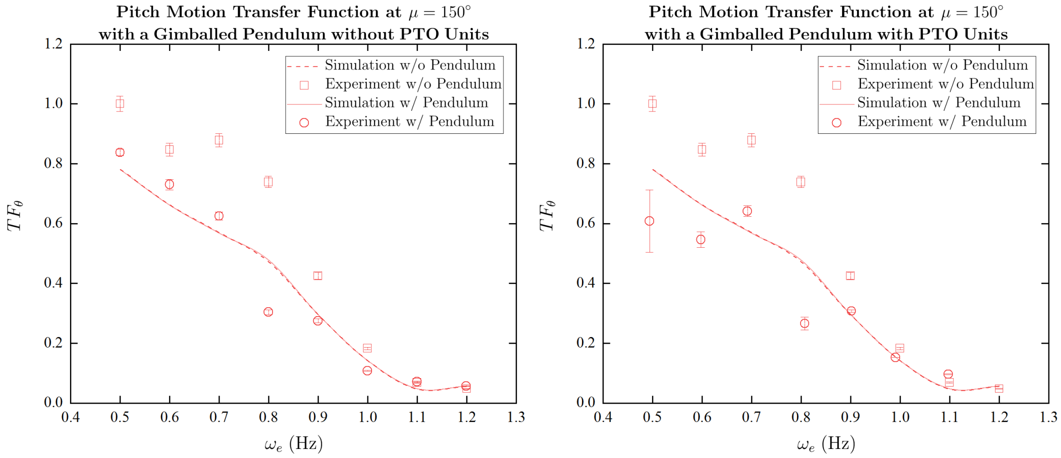

(a) with gimballed pendulum without PTOs. (b) with gimballed pendulum with PTOs.

Figure 6.15: Pitch motion transfer function at $\zeta_a = 0.035$ m and $\mu = 150°$.

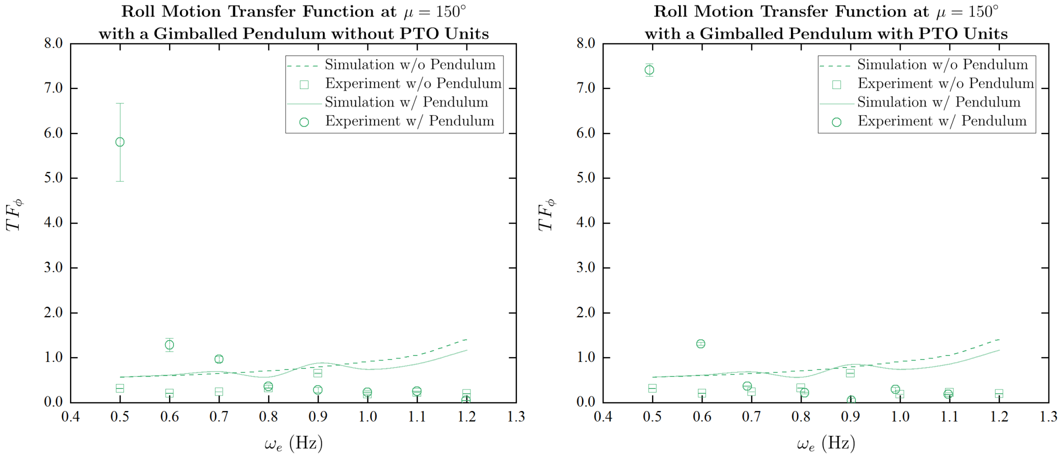

(a) with gimballed pendulum without PTOs. (b) with gimballed pendulum with PTOs.

Figure 6.16: Roll motion transfer function at $\zeta_a = 0.035$ m and $\mu = 150°$.

The motion transfer functions presented in Figures 6.8 to 6.16 were calculated based on the last 30 seconds of the 60-second time history motion responses which are considered as steady-state. The overall comparisons of numerical predictions and experimental results show reasonable agreement in heave, pitch, and roll motions across the investigated wave frequencies and heading angles for both bare hull and with onboard pendulum tests. There is no significant difference between the ship motions compared between the cases for the pendulum without and with PTO units. The discrepancies of the experimental results may be caused by the experimental error due to the uncertainty of the generated waves especially at high frequencies (1.0 to 1.2 Hz) as exhibited in Figure 6.17. Also, at these frequencies, the generated wave profiles were not entirely clean and stable as an example shown in Figure 6.18.

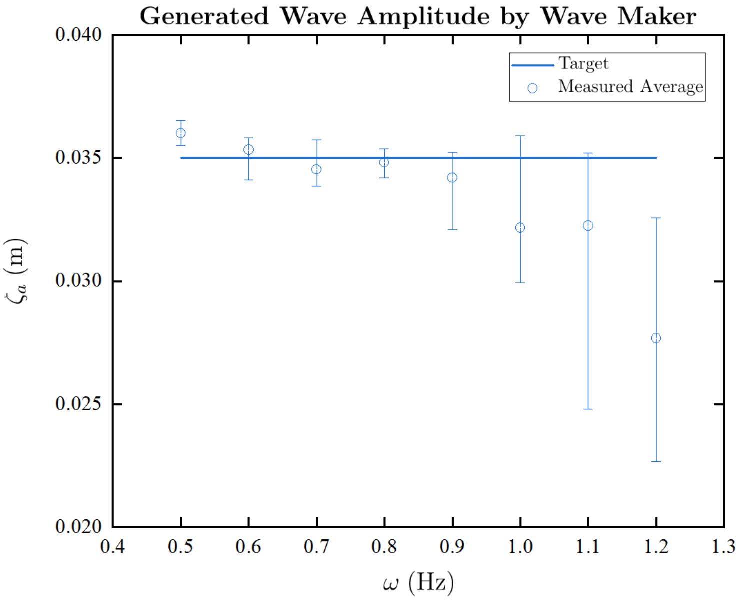

Figure 6.17: The errors of the generated waves by the wave maker.

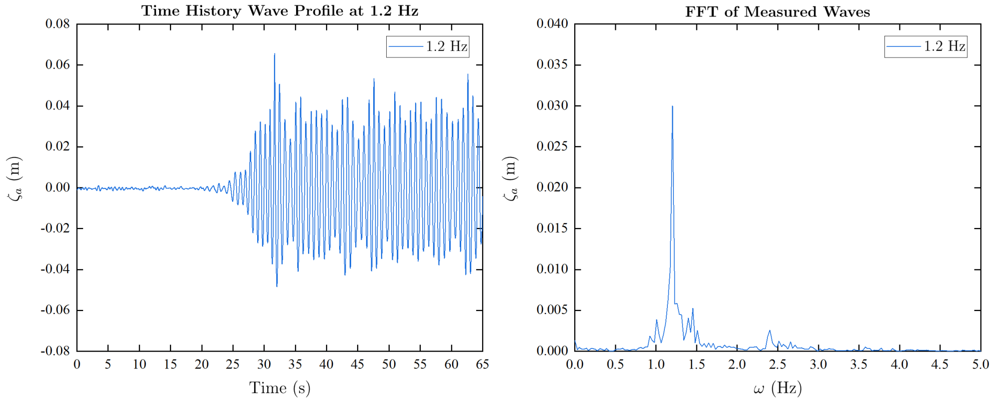

(a) Time-domain profile.

(b) FFT of the last 30 second.

Figure 6.18: Example of waves generated by the wave maker at 1.2 Hz.

In general, the onboard pendulum system theoretically and experimentally provide a minimal effect on the heave motion as can be seen in Figures 6.8, 6.11, and 6.14. For the pitch motions in Figures 6.9, 6.12, and 6.15, the numerical models based on the ship without and with the pendulum simulate comparable results as the effect from the pendulum cannot be identified. However, for the experimental results, the pitch motions across the tests are lower than that the bare hull. This could be due to the change in the mass distribution of the ship when the pendulum was installed and also during its oscillation while these are not included in the assumption of the numerical model.

For the roll motions in investigated headings (Figures 6.10, 6.13, and 6.16), the bare hull condition, the comparison of the results between the simulation and experiment show good correlation with the small overestimated offsets in the cases of heading angles at 165° and 150°. At the applied angles, the effect of the pendulum on the roll responses can be experimental observed at low frequencies at 0.5 to 0.7 Hz. At these frequencies, the pendulum had minimal reactions as it mostly remains vertically downward at the equilibrium position as demonstrated in Figure 6.19. Thus, the centre of gravity dynamically shifted to the port and starboard of the ship corresponding to the location of the pendulum mass, and so the roll motions were induced to be greater compared to when its behaved without pendulum attached. However, this dynamic characteristic not appears in the numerical prediction due to it is not taken into the assumption of the mathematical modelling of the coupled ship and gimballed pendulum dynamics described in Section 6.1. At higher frequencies, the numerical simulation can capture the influence of the onboard pendulum to the roll responses. The predicted roll motions show to be decreased at 0.8, and 1.0 to 1.2 Hz and to be amplified at 0.9 Hz. For the experimental results at these points, the insignificant differences in the results including the involved experimental error cannot conclude the precise effect of the pendulum on the roll motion of the ship.

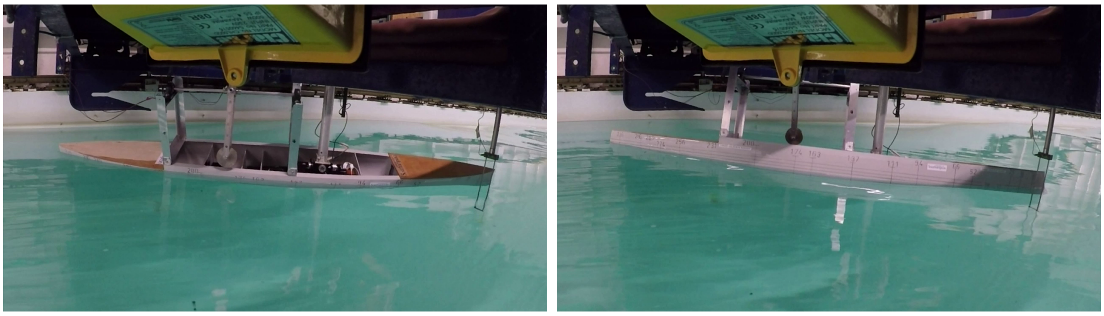

Figure 6.19: The model response at $\omega_e = 0.5$ Hz and $\mu = 150°$.

6.3.2 Pendulum Responses

The results of the pendulum responses are presented in Figures 6.20 to 6.25.

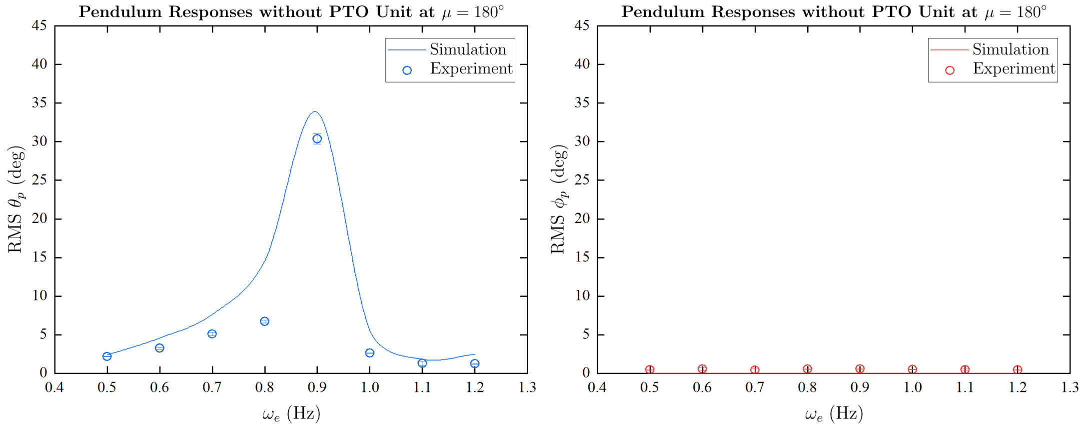

(a) θ_p-plane pendulum.

(b) ϕ_p-plane pendulum.

Figure 6.20: Pendulum RMS responses without PTO units at $\zeta_a = 0.035$ m and $\mu = 180°$.

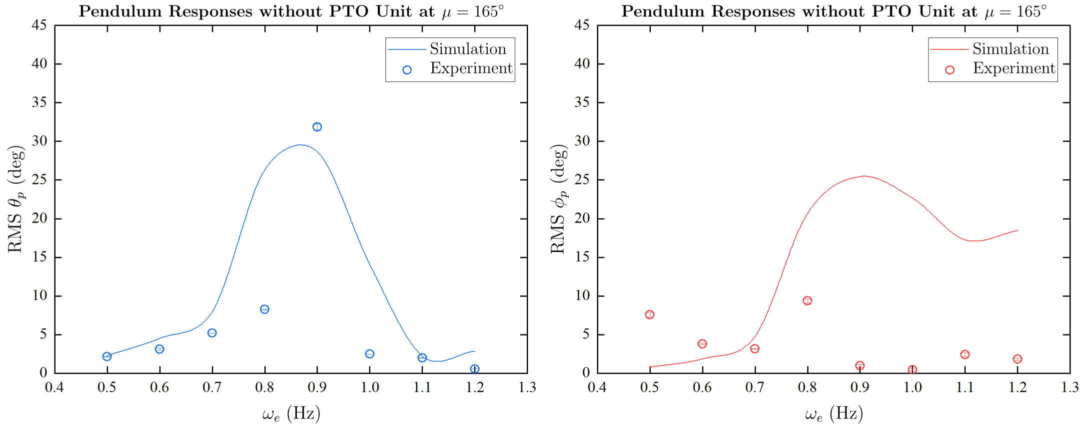

(a) θ_p-plane pendulum.

(b) ϕ_p-plane pendulum.

Figure 6.21: Pendulum RMS responses without PTO units at $\zeta_a = 0.035$ m and $\mu = 165°$.

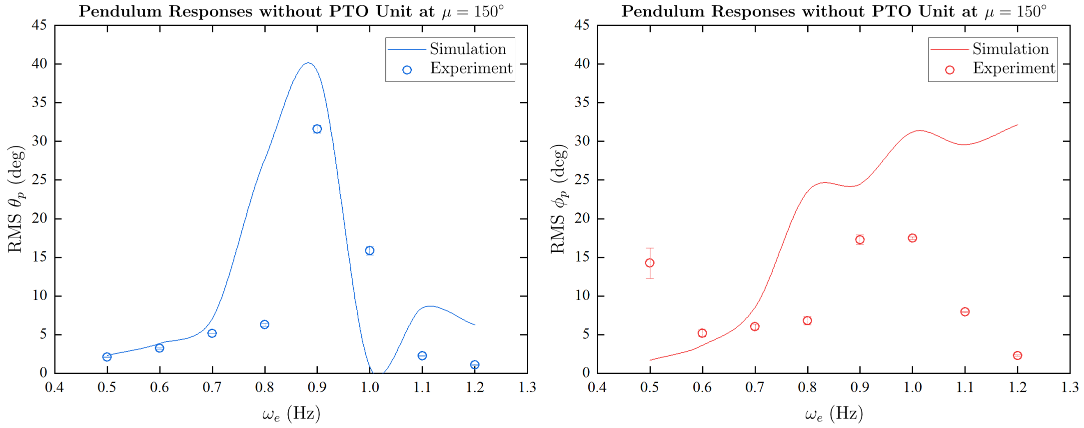

(a) θ_p-plane pendulum.

(b) ϕ_p-plane pendulum.

Figure 6.22: Pendulum RMS responses without PTO units at $\zeta_a = 0.035$ m and $\mu = 150°$.

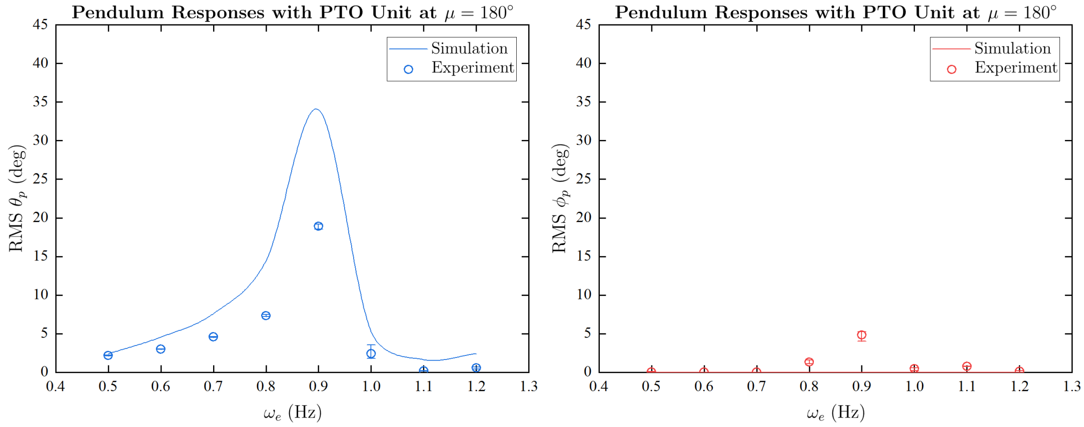

(a) θ_p-plane pendulum. (b) ϕ_p-plane pendulum.

Figure 6.23: Pendulum RMS responses with PTO units at $\zeta_a = 0.035$ m and $\mu = 180°$.

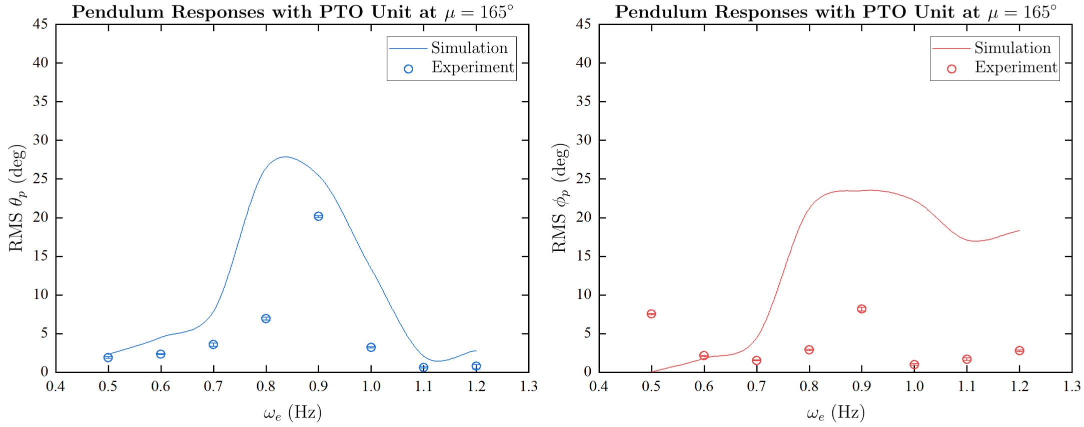

(a) θ_p-plane pendulum. (b) ϕ_p-plane pendulum.

Figure 6.24: Pendulum RMS responses with PTO units at $\zeta_a = 0.035$ m and $\mu = 165°$.

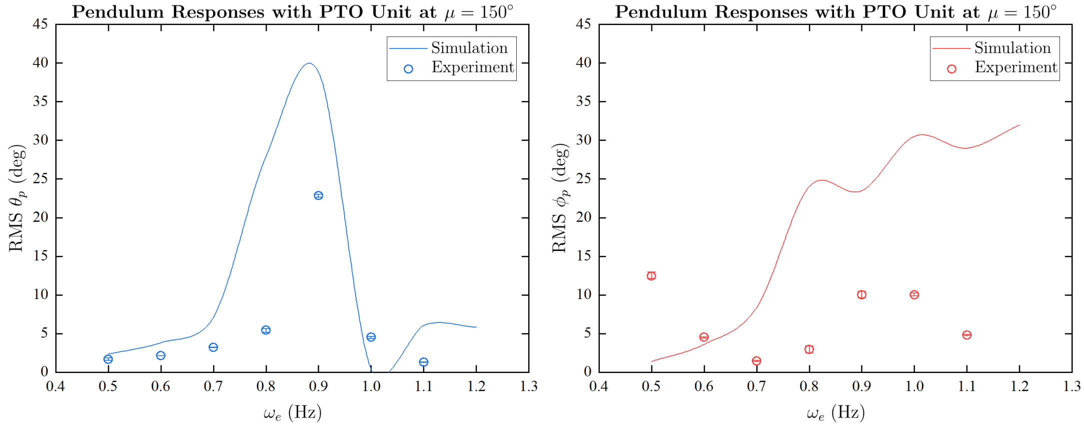

(a) θ_p-plane pendulum. (b) ϕ_p-plane pendulum.

Figure 6.25: Pendulum RMS responses with PTO units at $\zeta_a = 0.035$ m and $\mu = 150°$.

For the pendulum responses, the reasonable agreement between numerical prediction and experimental results only shows at the head waves condition ($\mu = 180°$) in both without and with applied PTO units as can be seen in Figures 6.20 and 6.23. The pendulum contributes the most significant responses at around resonance, 0.9 Hz. The overall pendulum responses are numerically and empirically lower when the PTO unit is applied since the added greater damping. At this heading, theoretically, the pendulum performs as a planar or 1-DOF pendulum as the excitation from the ship is uni-directional. Experimentally, the identical behaviour was confirmed with only small discrepancy providing the oscillation to the other perpendicular plane due to experimental error in some particular frequencies shown in Figure 6.23(b).

At applied heading angles, $\mu = 165°$ and $150°$, the comparison between the numerical and experimental results mainly show disagreement as displayed in Figures 6.21, 6.22, 6.24, and 6.25. At low frequencies (0.5 to 0.7 Hz), the pendulum at these points produces minimal responses. However, the recorded motions from the experimental were the relative angles between the barely moving pendulum and the ship riding on waves (more evident for ϕ-plane pendulum). This can be referred to as the dynamics explained in Section 6.3.1. Again, this characteristic does not present in the numerical simulation. In general, the overall simulations for the whole dynamics of the gimballed pendulum at these conditions are found to be inaccurate even the trend of the θ_p-plane responses is comparable to that the experiment. This is because of the simplified assumption of the numerical modelling of the pendulum system discussed in Chapter 5. Furthermore, the pendulum responses for both referenced planes are the results of asymmetric excitation from a combination of the 3-DOF ship dynamics. This is much greater than the investigated condition applied in Chapter 5 regarding excitation amplitude. Consequently, the resulting simulated pendulum motions significantly emerge, especially from 0.8 Hz. As from this excitation frequency, the coupling terms become more dominant in the equations of motions, Equations 5.15 and 5.16. This results in an inaccurate theoretical prediction. Therefore, it can also be concluded that the numerical model of a gimballed pendulum dynamics only valid under small pendulum dynamics where the coupling effects of two pendulum references are minimised.

6.3.3 Power Generations

As a reflection of inaccuracy of the pendulum responses predictions described in Section 6.3.2, only reasonable agreement between the simulation and the experiment is particularly found at the head waves condition as shown in Figures 6.26 to 6.26. The power generation level correlates to the pendulum responses with the peak at the resonance frequency. Nevertheless, the overall generated power predictions are overestimated compared to the measured data with apparently contradicting trends for the ϕ_p-plane pendulum at the headings of 165° and 150°.

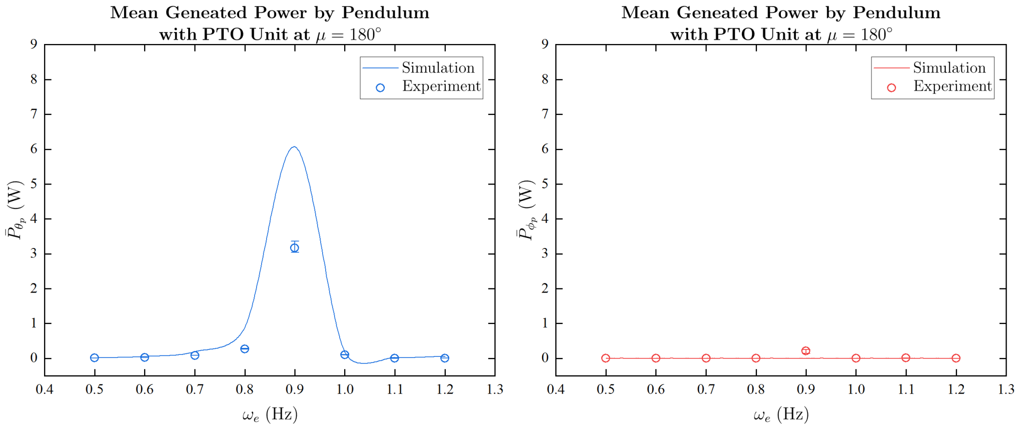

(a) θ_p-plane pendulum.

(b) ϕ_p-plane pendulum.

Figure 6.26: Average generated powers by the pendulum references at $\zeta_a = 0.035$ m and $\mu = 180°$.

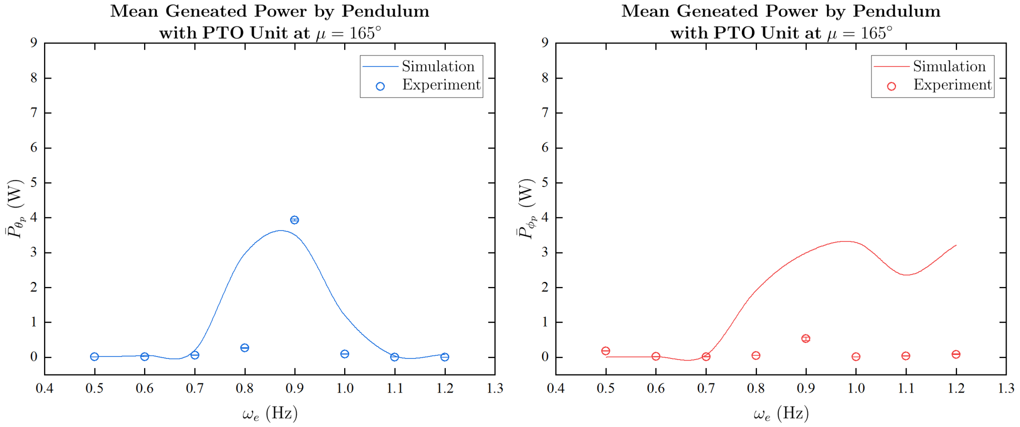

(a) θ_p-plane pendulum.

(b) ϕ_p-plane pendulum.

Figure 6.27: Average generated powers by the pendulum references at $\zeta_a = 0.035$ m and $\mu = 165°$.

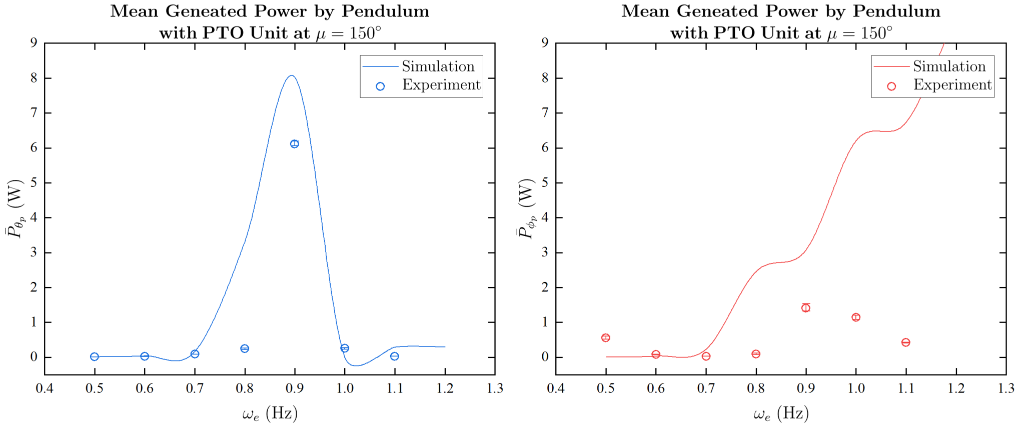

(a) θ_p-plane pendulum.

(b) ϕ_p-plane pendulum.

Figure 6.28: Average generated powers by the pendulum references at $\zeta_a = 0.035$ m and $\mu = 150°$.

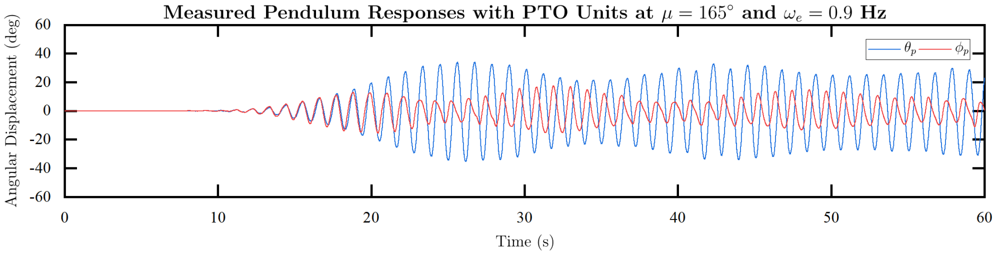

(a) Pendulum responses.

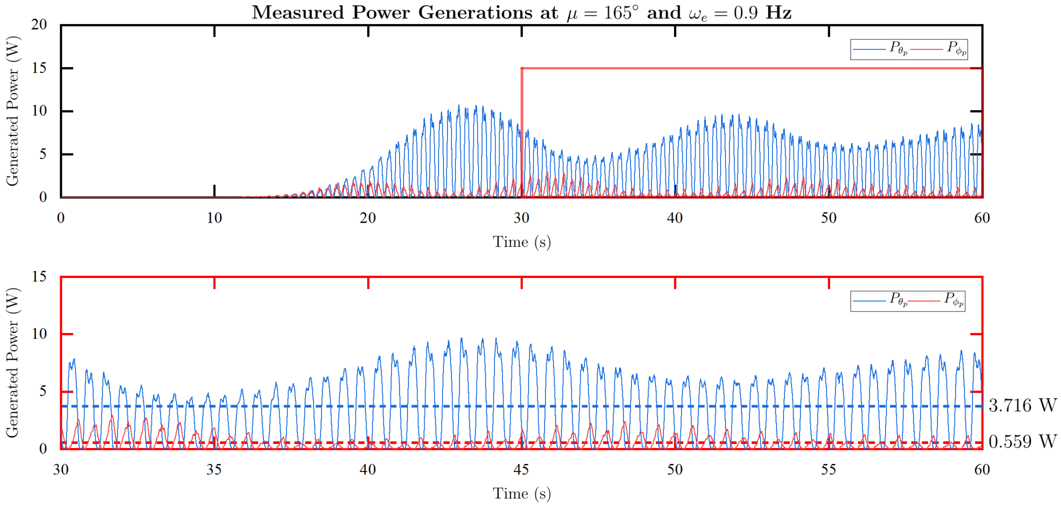

(b) Power generations by the pendulum references.

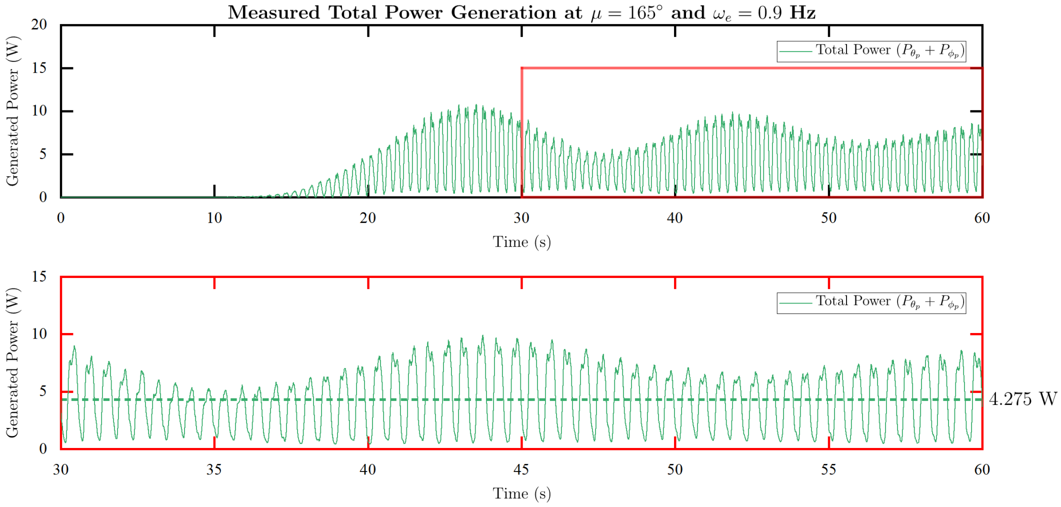

(c) Total power generation.

Figure 6.29: Measured pendulum responses and power generations by the gimballed pendulum energy harvester at $\mu = 165°$ and $\omega_e = 0.9$ Hz (Dash lines - mean power generations calculated based on the measured results at the last 30 seconds).

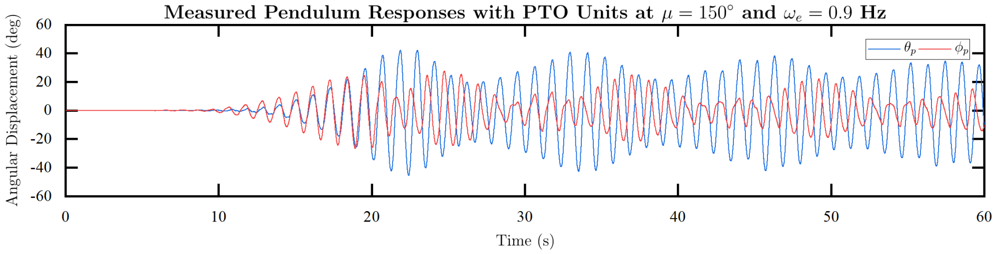

(a) Pendulum responses.

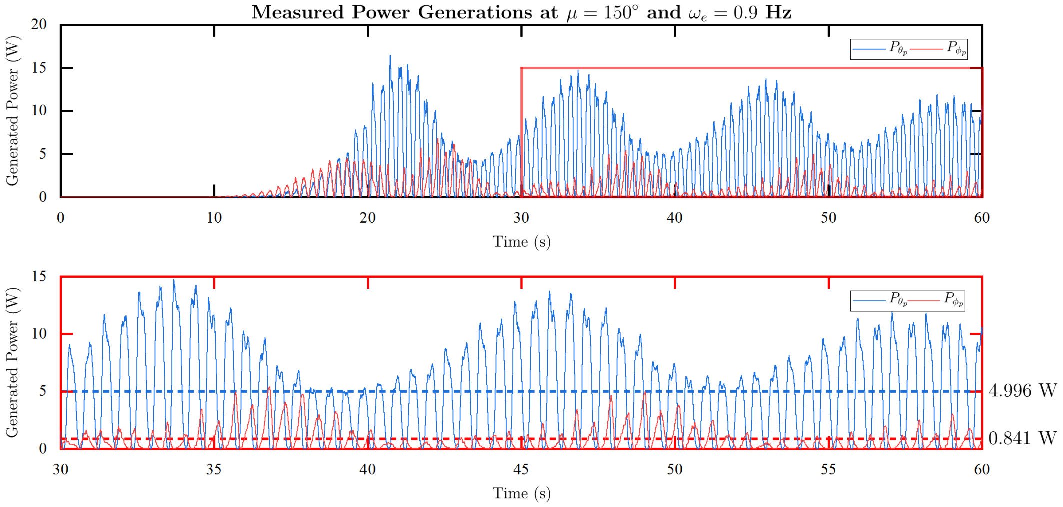

(b) Power generations by the pendulum references.

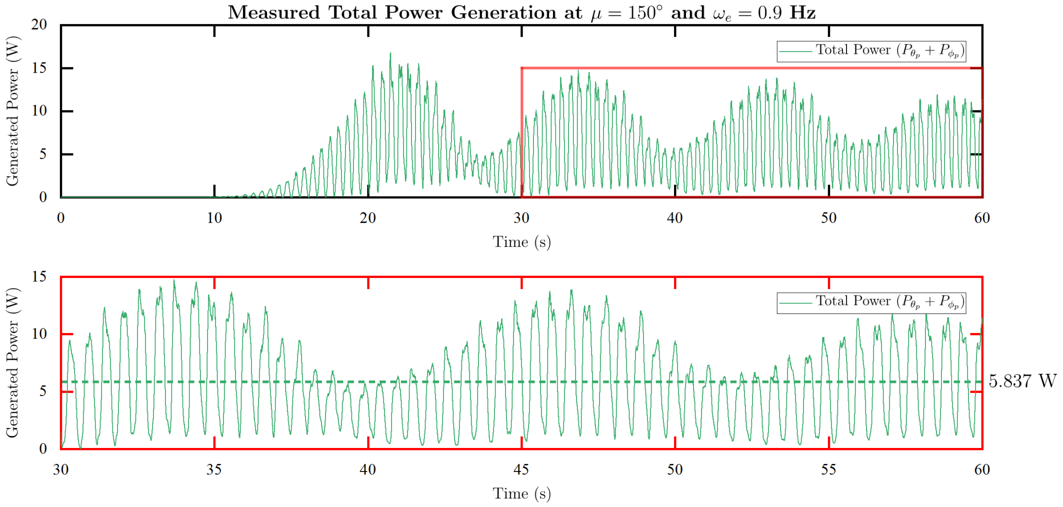

(c) Total power generation.

Figure 6.30: Measured pendulum responses and power generations by the gimballed pendulum energy harvester at $\mu = 150^\circ$ and $\omega_e = 0.9$ Hz (Dash lines - mean power generations calculated based on the measured results at the last 30 seconds).

Considering the experimental results at applied heading angles ($\mu = 165°$ and $150°$), the power generations at low frequencies (0.5 and 0.6 Hz) can be observed for ϕ-plane pendulum as shown in Figures 6.27(b) and 6.28(b). These power generations were the results of the contributed gravitational torques from the relative angles between the downward pendulum and the induced roll motions of the ship as explained in Section 6.3.2. At around natural frequencies of both pendulum references (0.9 Hz), the gimballed pendulum system created coupled motions as a result from the vessel heave, roll, and pitch. These coupled motions can be clearly seen with greater applied heading angle. Based on this pendulum dynamics, therefore, the electric powers from both referenced pendulum axes were simultaneously generated as exhibited in Figures 6.29 and 6.30. At $\mu = 165°$, the average power generations[1] of θ_p- and ϕ_p-planes pendulum references were 3.716 W (7.432 W average peak), 0.559 W (1.118 W average peak) respectively, and so the average total generated power can be summed up as 4.275 W (8.550 W average peak). Besides, at $\mu = 150°$, the average power generations[1] of θ_p- and ϕ_p-planes pendulum references were 4.996 W (9.992 W average peak), 0.841 W (1.682 W average peak) respectively, and the average total generated power was 5.837 W (11.674 W average peak).

6.4 Summary

A mathematical model of the coupled ship and onboard gimballed pendulum energy harvester is described. By defining the coupled dynamics as a system, the numerical model, therefore, consists of two main subsystems; the ship and the pendulum dynamics. These subsystems are coupled by feedback moments created by the pendulum motions. Then, a set of experimental testings based on wave tank experiment was organised to validate the numerical model.

A reasonable agreement is generally found in terms of the trends of the frequency dependent ship responses. The effect of the moving pendulum on the ship dynamics is numerically and experimentally confirmed to be meaningless to the heave response. For the pitch motion, the numerical model still shows that the effect of the onboard pendulum is insignificant. Experimentally, nevertheless, the reduction in pitch responses can be observed as this could be due to from the effect of the pendulum and the change in the mass distribution of the ship when the pendulum was attached as well as the involved experimental error. When the heading of the ship is not aligned with that the waves, the occurrence of roll motion can be expected as this theoretically and physically shows in the investigations. However, at low frequencies (0.5 to 0.7 Hz), the numerical model does not reflect the induced roll motion due to the shifting in the centre of gravity causing by the lateral translating position of the vertically downward pendulum on the rolling ship. This is due to that the effect is not included in the assumption made in the

---

[1] Based on the last 30 seconds of the measured results.

numerical modelling. At higher frequencies, the simulation is able to capture the effect of the created pendulum moment that affects the roll responses, but the experiment cannot precisely confirm the similar dynamics due to the experimental error.

Regarding the pendulum responses, a good corroboration between the numerical prediction and experimental result can only be confirmed at head waves condition. Elsewhere, the numerical model is considered inaccurate as it is found to be valid only for small dynamics. Nevertheless, based on the experimental results at applied heading angles, the gimballed pendulum prototype offered a benefit in power generation by gravitational torque at the low frequencies. At around resonance, the pendulum performed the coupled motions which were more significant at greater heading angle. These coupled motions could create simultaneous power generations from both two pendulum reference pivots. Therefore, this shows that harvesting energy from multiple-DOF dynamics offers the potential to generate more energy. In addition, it also proves that energy harvesting using multiple-DOF ship dynamics is practically possible.

Chapter 7

Discussion

7.1 Ship Motions Energy Harvesting

As demonstrated and discussed in Chapter 4 concerning the oscillatory motions for any wave direction, the magnitude of the available mechanical power contributed by the ship motions in a sea state varies proportionally to the scale of the ship. Based on the non-dimensional analysis of the scaling relationships relating to the mechanical powers, it shows that the ship in different scale contributes the power from the different dynamic determinants. The mechanical power from the larger size of a ship is dominated by its size, in terms of mass, and the velocity of the translational motion. Besides, the frequency response of a bigger scale vessel shifts toward low-frequency range. On the other hand, when the size becomes smaller, the magnitude of the power is principally controlled by the rotational motions and the ship responses more to the higher encountering frequency.

In an energy conversion aspect, it is generally difficult to convert the power of the low-frequency motions from a large-scale ship; even it offers a massive available power magnitude in the sea. On that regard, considering an onboard energy harvesting system as a conventional vibration device (e.g. mass-spring-damper or pendulum system), the size of the device is also required to be relatively large to ensure that the response will be created. Furthermore, as translational (heave) motion is proven to be the primary source of power for a large ship, by using the typical bottom-fixed approach for converting energy from a heaving body is not practical based on the operational basis of the ship in the deep water zone sea state. Besides, to harvest low-frequency motion by an outboard system as introduced by Sharon et al. (2011) as shown in Figure 2.20, an additional drag to the ship is a trade-off parameter to be concerned.

As stated earlier, the frequency response characteristics of a ship shift toward the high-frequency range followed the decreasing in size. Moreover, the rotational motions, pitch and roll in this case, are the main influential factors in the available mechanical power of a small-scale ship in waves. By considering this, the requirement of the energy conversion techniques concerning the system dimension could make energy harvesting using ship motions at a small scale fundamentally becoming more practical. Correspondingly, a number of energy harvesting concepts using rotational motion of a small-scale marine vessel are introduced as reviewed and discussed in Chapter 2. However, with the realisation of the dynamics of a ship in the real sea, to simultaneously harvest the energy from the ship directional responses could, therefore, elevate the resulting power production. It is because of the available mechanical power is magnified by the number of the involved ship DOFs as evidently confirmed by the assessment in Chapter 4.

7.2 A Gimballed Pendulum System as an Energy Conversion Mechanism

As discussed in Chapter 2, energy conversion mechanism for the WEC systems for marine vessels using rotational motion is potentially pendulum system. This system has several advantages. As the system is installed internally, it does not add any hydrodynamic resistance to the vessel and also it is able to prevent biofouling issue as it is not exposed to the external marine environment. Besides, pendulum response can be considered a free phenomenon. The frequency response of a pendulum system only depends on the excitation frequency the host body as it does not require any power to guarantee its responsiveness. However, the main limitation of the proposed energy conversion techniques based on typical pendulum system is the restricted directional responsiveness on the dynamics of a floating body as a ship in waves. This limit also constrains the potential to extract more power from the total available amount by the involved DOFs. Therefore, a gimballed pendulum mechanism is introduced in order to overcome the existing limit.

Regarding the numerical and experimental investigations of the dynamics of the gimballed pendulum system presented in Chapter 5, it is clear that the gimballed mechanism could add directional responsiveness to a pendulum energy harvesting system. With the benefit from the dual perpendicular pivots, the gimballed pendulum system is able to respond to the applied harmonic excitation from any angle. When the excitation is parallel to a particular referenced horizontal axis, the pendulum theoretically and experimentally performs as a 1-DOF pendulum. At the angles elsewhere, the coupled motions can be observed. These motions are found to be beneficial in the simultaneous power generations by the pivots outside resonance where the responded motions and the coupling effect are small.

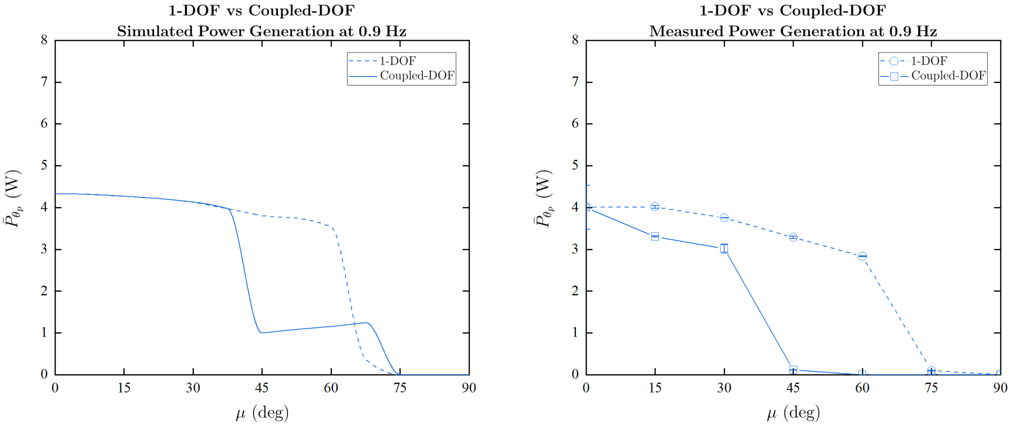

(a) Simulation.

(b) Experiment.

Figure 7.1: Comparison between the mean power generations of 1-DOF and coupled-DOF θ_p-plane pendulum references.

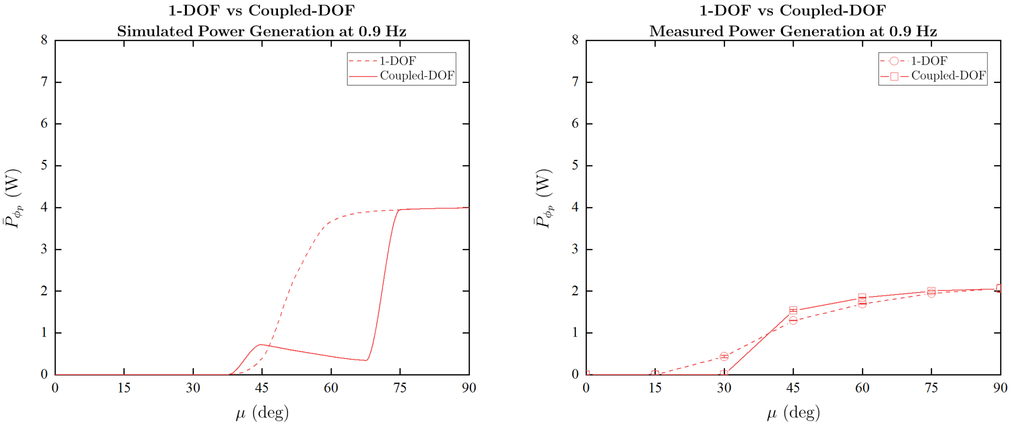

(a) Simulation.

(b) Experiment.

Figure 7.2: Comparison between the mean power generations of 1-DOF and coupled-DOF ϕ_p-plane pendulum references.

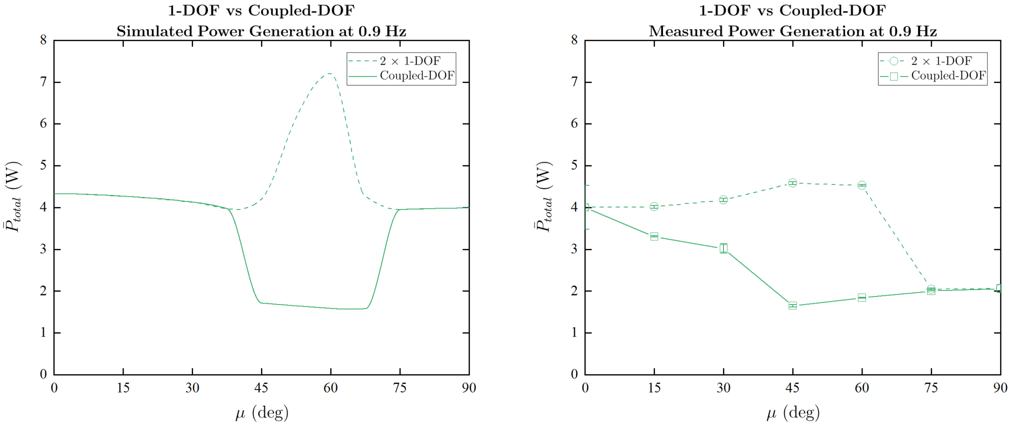

(a) Simulation.

(b) Experiment.

Figure 7.3: Comparison between the mean total power generations of two 1-DOF and coupled-DOF pendulum systems.

Nevertheless, at resonance, the coupling effect becomes more influential and diminishes the pendulum responses compared to when it performs as a 1-DOF system. These lower responses imply the inferior power generation levels as the comparisons in Figures 7.1 to 7.3. Although, the numerical model at this point is not found to be accurate. Both theoretical prediction and experimental result confirm the undesired effect concerning power generation of the coupling dynamics of the gimballed pendulum system.

For an example scenario, Figure 7.3 shows the comparison of the average total power generations by utilising two of 1-DOF pendulum as a system and that the gimballed pendulum system with the similar configuration and alignment. Clearly, to arrange two of 1-DOF pendulum energy harvesters for individual perpendicular DOFs could provide an identical coverage of directional responsiveness. Also, the average total power generation level of the combined single-DOF pendulum systems is more favourable. Furthermore, the theoretical prediction of the 1-DOF dynamics and power generation performance could be more accurate by the simpler numerical model. Therefore, this finding could be invaluable information for the design consideration of either the WEC system and energy harvesting using ship motions in waves concerning directional responsiveness or power generation from multiple-DOF dynamics with a pendulum system.

7.3 Energy Harvesting Using Ship Motions by an Onboard Pendulum System

This research has proved that the energy harvesting using multiple-DOF ship dynamics by applying a gimballed pendulum as an energy conversion mechanism to be practicable by the non-optimal design presented in Chapter 6. Assuming that the ship travelling at a constant encountering frequency at arbitrary speed, therefore, the average generated power as a percentage of the effective power at different speed of the ship model, HMS Queen Mary, can be presented in presented in Tables 7.1 to 7.3. Note that, the ship effecting power is numerically estimated using MAXSURF Resistance software package based on Holtrop method for displacement ships.

Table 7.1: Measured Power Generation as a Proportion of the Ship Effective Power at $\mu = 180°$ and $\omega_e = 0.9$ Hz.

Parameter	Symbol	Value					Unit
Ship Speed	U	1	2	3	4	5	Knot
Total Generated Power	P_{total}	3.3372	3.3372	3.3372	3.3372	3.3372	W
Effective Power	P_E	0.3704	2.7471	10.0162	32.0396	72.6138	W
Percentage of Total Generated Power to Ship Effective Power	$(P_{total}/P_E) \times 100$	900.9842	121.4810	33.3184	10.4160	4.5959	%

Table 7.2: Measured Power Generation as a Proportion of the Ship Effective Power at $\mu = 165°$ and $\omega_e = 0.9$ Hz.

Parameter	Symbol	Value					Unit
Ship Speed	U	1	2	3	4	5	Knot
Total Generated Power	P_{total}	4.4649	4.4649	4.4649	4.4649	4.4649	W
Effective Power	P_E	0.3704	2.7471	10.0162	32.0396	72.6138	W
Percentage of Total Generated Power to Ship Effective Power	$(P_{total}/P_E) \times 100$	1205.4368	162.5308	44.5770	13.9357	6.1489	%

Table 7.3: Measured Power Generation as a Proportion of the Ship Effective Power at $\mu = 150°$ and $\omega_e = 0.9$ Hz.

Parameter	Symbol	Value					Unit
Ship Speed	U	1	2	3	4	5	Knot
Total Generated Power	P_{total}	6.7061	6.7061	6.7061	6.7061	6.7061	W
Effective Power	P_E	0.3704	2.7471	10.0162	32.0396	72.6138	W
Percentage of Total Generated Power to Ship Effective Power	$(P_{total}/P_E) \times 100$	1810.5086	244.1135	66.9526	20.9307	9.2353	%

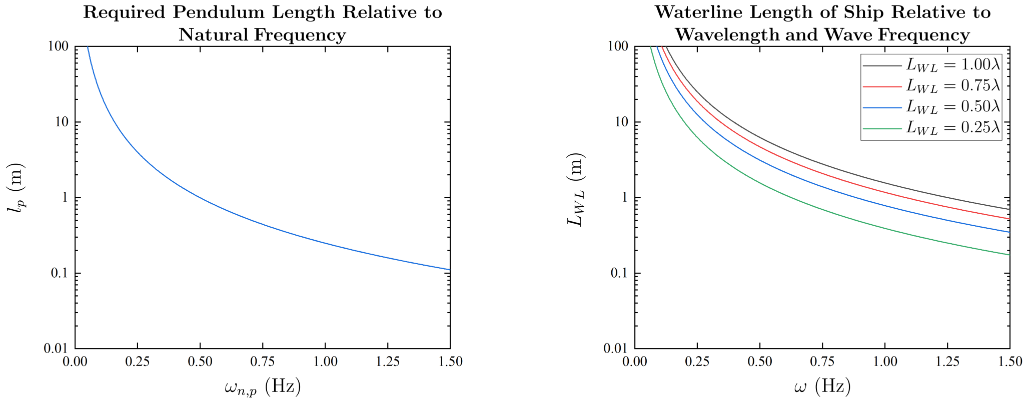

(a) Pendulum length relative to natural frequency. (b) Ship waterline length relative to wave frequency.

Figure 7.4: Pendulum and ship waterline lengths in the relations of frequencies.

To apply a pendulum system onboard a marine vessel, the size regarding the pendulum arm length relative to the vessel geometry or vice versa has to be included into the consideration. The relationships of the required pendulum length for achieving its natural frequency and the referenced ship waterline length relative to wave frequencies for ensuring the occurrence of the ship responses are demonstrated in 7.4(a) and 7.4(b) respectively. It is clear that both the required pendulum and the ship length are increasing followed the low target frequencies. However, to design a ship with an onboard pendulum system, the size of the pendulum is technically constrained by the vessel geometry. In other words, the required pendulum length to guarantee the pendulum response at a particular target operating frequency might be longer than that the ship beam and it is not practical to be operated onboard, presumably, due to the ship safety and stability reasons. Besides, the required volume for installing the pendulum system as shown in Figure 7.5 is needed to be considered.

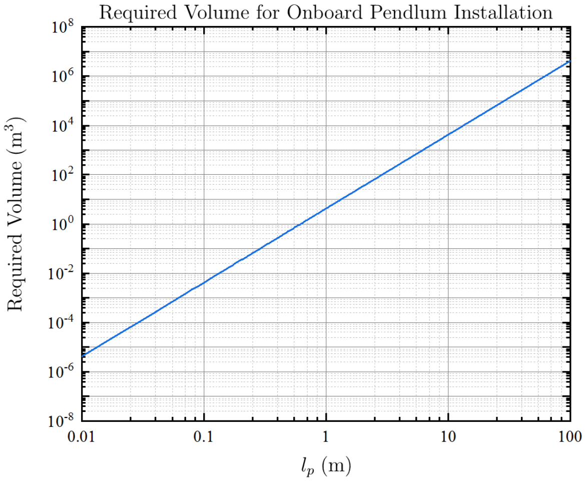

Figure 7.5: Required volume for onboard pendulum installation.

Therefore, if the required pendulum length is known based on target operating frequency, the geometry regarding the beam of a ship or the required length-to-beam ratio can be identified. By assuming the limit of the length of a pendulum system by half of a ship beam, the maximum length-to-beam ratios of the ship with different referenced waterline lengths that allow a pendulum to swing within the ship can be determined as shown in Figure 7.6. Based on the assumption, the maximum length-to-beam ratio for the ship in which waterline length equals to the frequency-dependent wavelength (Figure 7.6(a)) is around 3. With the reduction of referenced waterline length, the maximum length-to-beam ratio also decreases. This means the smaller ship requires greater lateral dimension for an onboard gimballed pendulum system.

It is worth noting that the pendulum length defines the natural frequency of a pendulum system. Accordingly, an energy harvester based on pendulum system requires the pendulum to have an optimum length to assure the pendulum response at a particular ambient frequency. This finite operating condition contrasts the behaviour of a floating body or a ship in the real sea. Therefore, a natural frequency tuning technique and PTO performance optimisation control algorithm (mentioned in Chapter 2) might be required which could improve the pendulum performance, increase the potential to generate more power, and expand the responsive band from the variation of disturbance.

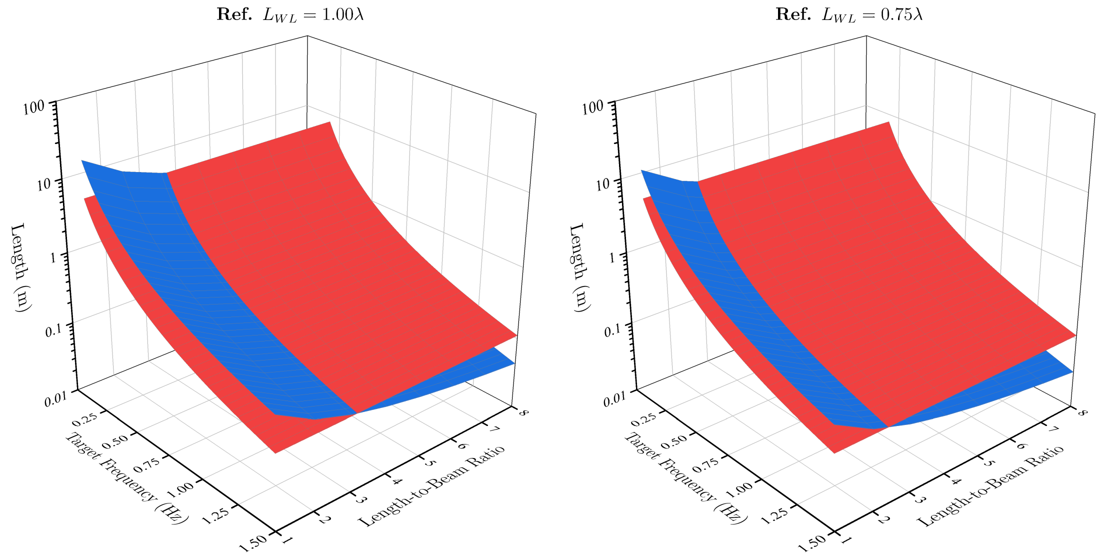

(a) at ref. $L_{WL} = 1.00\lambda$. (b) at ref. $L_{WL} = 0.75\lambda$.

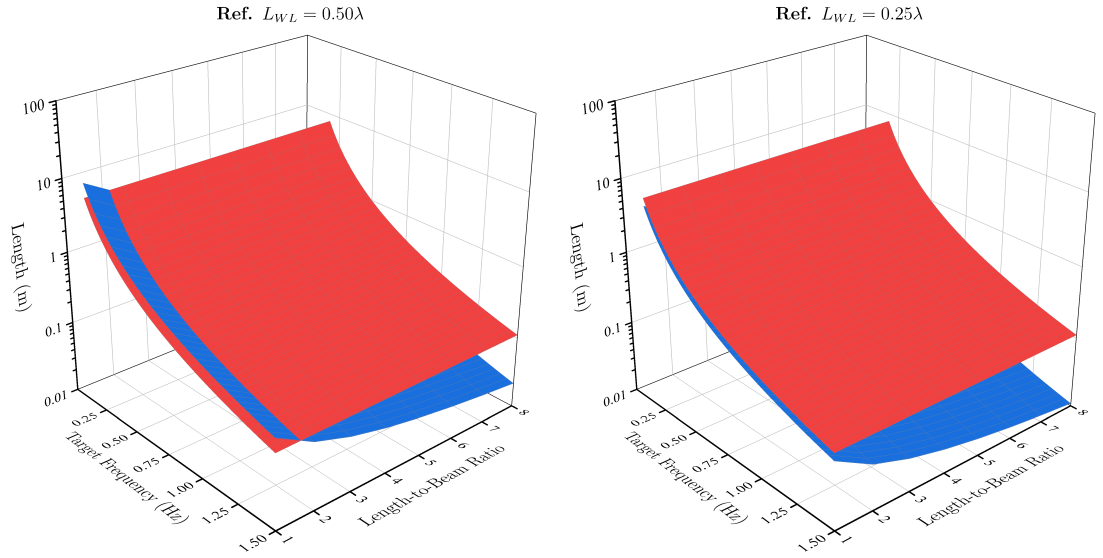

(c) at ref. $L_{WL} = 0.50\lambda$. (d) at ref. $L_{WL} = 0.25\lambda$.

Figure 7.6: The relationships of the required frequency-dependent pendulum length for achieving its natural frequency and the beam of the ships with different referenced waterline lengths relating to length-to-beam ratio (red - required pendulum length, blue - ship beam relative to length-to-beam ratio).

Chapter 8

Conclusions and Recommendations for Future Work

8.1 Conclusions

With the limited understanding of the potential use of the energy harvesting using wave-induced ship motions, therefore, the research provides a novel methodology for assessing the available mechanical power of motions of a ship in waves. By adopting the seakeeping analysis and statistical technique of describing the characteristic of a sea state, consequently, the available mechanical powers from the motions of a ship in a sea state can be determined. In general, the directional responses of a ship depends on the heading angles relative to the wave direction. With the consideration of the ship directional responses, the oscillatory motions, heave, pitch, and roll, have been taken into account for the investigation at zero speed condition. The frequency response and power contribution characteristics of a ship depend on the ship scale. A ship with the larger scale responds to low-frequency range, and its power is contributed by its mass and the translational motion. On the other hand, a smaller ship reacts to higher encountering frequency as the rotational motion mainly influences its power. It is also found that the number of the involved DOFs can magnify the available mechanical power of a ship in waves. Therefore, in energy conversion aspect, to simultaneously harvest the energy from the multiple-DOF of a ship concerning directional responses in the real sea could elevate the resulting power production.

Nevertheless, the main limitation of the typical energy conversion techniques for a floating body or a ship in waves is the limited DOF. Hence, this research has investigated a gimballed pendulum mechanism that is designed to overcome the limitation in directional responsiveness. The investigations are proposed in the comparison between

1- and coupled-DOFs pendulum dynamics. Based on the numerical and experimental investigations in the harmonic excitations at different angular alignments, it is clear that the gimballed pendulum is able to respond to the excitation at any angle and, at the sufficient angles, the coupled pendulum motions respecting the referenced perpendicular pivots are created. The coupled motions are theoretically and experimentally found to be beneficial in the simultaneous power generations by both pivots for the small pendulum responses outside resonance region. However, at resonance with the greater responses, the coupling effect between two pendulum references become significant. The gimballed pendulum at this point creates lower responses implying inferior power generation compared to when it performs as a 1-DOF at the identical applied angles.

Then, the dynamics of the coupled ship and onboard gimballed pendulum have been numerically and experimentally investigated. The numerical model of the coupled dynamics consists of two main sub-dynamics or subsystems, the ship and the pendulum. These subsystems are coupled with the excitation components and the feedback moments created by the ship to the pendulum and vice versa. Generally, the mathematical prediction provides a reasonable agreement to the experimental result in the frequency-dependent ship directional responses with comparable trends. However, the numerical model could not show the effect of the gimballed pendulum to the pitch and roll motions of the ship which showed in the experimental results. This is because of the simplifying assumption in the numerical modelling does not consider the change in the ship's mass distribution during the pendulum is swinging.

For the resulting responses of the onboard pendulum, a good corroboration between the numerical simulation and experiment result can be confirmed only at head waves condition where the pendulum technically performs 1-DOF responses. At the other investigated headings, the numerical model could not provide accurate result as it is found to be valid only for small pendulum dynamics. However, based on the experimental result, it shows that the multiple-DOF ship dynamics could benefit the simultaneous power generations by the coupled motions of the gimballed pendulum which can be evidently observed at greater heading angle. As a result, this confirms that harvesting energy from multiple-DOF dynamics offers the potential to generate more energy. This also proves that the energy harvesting using multiple-DOF ship dynamics by applying a gimballed pendulum as an energy conversion mechanism is practicable.

8.2 Main Contributions

The following contributions have resulted from the work presented in this thesis:

- A novel theoretical methodology of assessing available mechanical power from ship motions in seaway.

- A novel numerical model of the dynamics of a gimballed pendulum system validated by experimental testing with small applied excitation.
- Numerical and experimental investigations of the dynamics of a gimballed pendulum in an aspect of an energy conversion mechanism.
- Numerical and experimental investigations of the potential use of ship motions energy harvesting applying a gimballed pendulum as an energy conversion mechanism.

8.3 Recommendations Future Work

This thesis has identified a number of areas which would be challenge and beneficial for further research. Recommendations for future work can be listed as follows:

- An assessment of the available mechanical power of a ship in a specified sea route and speed including the effect of short-crested waves would provide a more realistic predicting scenario for the real sea condition.
- An improved numerical model of a gimballed pendulum system is recommended for the better or more accurate prediction of the coupled pendulum motions at any condition.
- An investigation of the interaction between a ship and an onobard multiple-DOF pendulum in an aspect of the ship stability.
- A sea-trial investigation in the real sea of a ship with an onboard multiple-DOF pendulum energy harvester.

8.4 Submitted Publication

- Anurakpandit, T., Townsend, N. C., Wilson, P. A., 'The Numerical and Experimental Investigations of a Gimballed Pendulum Energy Harvester', *International Journal of Non-Linear Mechanics* (under review).

Appendix A

All Directional Wave Record of the Global Wave Statistics

Global wave statistics that is used in the analysis in this research is the all directional wave record of Hogben et al. (1986). The summary of the wave record can be found in Figure A.1 and Tables A.1 to A.3.

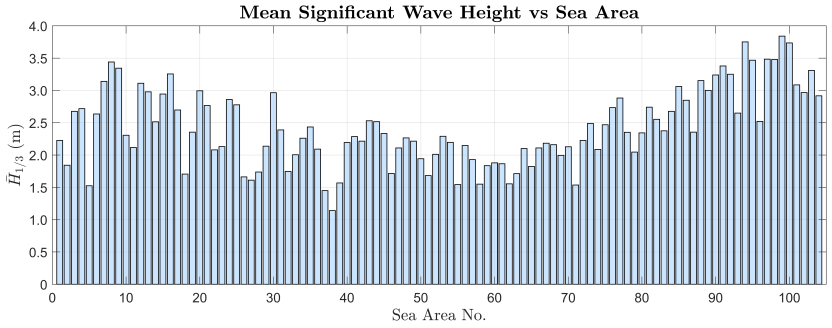

(a) Average significant wave height.

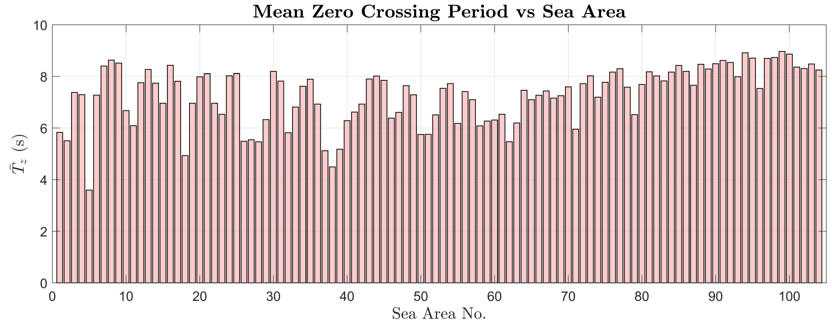

(b) Average zero crossing period.

Figure A.1: All directional wave record of individual sea areas (Hogben et al., 1986; BMT Fluid Mechanics Limited, 2011).

Table A.1: All directional wave record of sea area no. 1-35.

Sea Area No.	Coordinate				$\bar{H}_{1/3}$ (m)	$\bar{T}_z$ (s)
	Top Left		Bottom Right			
	Latitude	Longitude	Latitude	Longitude		
1	74.89 N	10.24 E	65.18 N	29.89 E	2.22527	5.83067
2	70.05 N	59.74 W	60.26 N	45.22 W	1.84300	5.50050
3	69.82 N	44.81 W	70.05 N	15.19 W	2.67618	7.37888
4	69.94 N	14.70 W	60.53 N	9.75 E	2.71822	7.28879
5	64.88 N	13.35 E	53.17 N	29.77 E	1.52398	3.59550
6	59.96 N	159.75 W	55.42 N	130.05 W	2.63586	7.27622
7	54.94 N	169.88 W	50.21 N	134.29 W	3.14100	8.40260
8	59.70 N	59.47 W	50.47 N	30.23 W	3.44106	8.62813
9	59.78 N	29.48 W	50.70 N	10.35 W	3.34331	8.51200
10	54.97 N	9.82 W	50.47 N	3.53 W	2.30558	6.67629
11	59.78 N	2.62 W	51.38 N	7.95 E	2.11569	6.09086
12	54.94 N	160.2 E	50.55 N	170.10 W	3.11039	7.75300
13	49.88 N	169.43 W	40.65 N	130.27 W	2.97848	8.26800
14	48.00 N	129.75 W	40.28 N	123.11 W	2.51400	7.73653
15	49.88 N	59.47 W	40.65 N	40.35 W	2.94444	6.96154
16	49.88 N	39.60 W	40.65 N	8.32 W	3.25524	8.42986
17	49.88 N	7.57 W	43.35 N	0.15 W	2.69620	7.81069
18	49.65 N	128.48 E	35.70 N	139.88 E	1.70582	4.93216
19	49.88 N	143.32 E	40.88 N	149.85 E	2.35371	6.96154
20	49.88 N	150.52 E	40.88 N	170.10 W	2.99449	7.98549
21	39.83 N	169.43 W	30.60 N	130.27 W	2.76627	8.10739
22	39.83 N	129.60 W	20.62 N	105.30 W	2.07942	6.95854
23	41.85 N	79.80 W	30.45 N	70.12 W	2.13137	6.52991
24	39.83 N	69.60 W	30.98 N	40.58 W	2.85836	8.02405
25	39.97 N	39.60 W	30.52 N	10.35 W	2.77700	8.11339
26	44.55 N	0.52 E	30.75 N	12.90 E	1.66267	5.48403
27	39.97 N	13.43 E	30.60 N	35.92 E	1.61100	5.54496
28	39.97 N	120.53 E	30.75 N	127.72 E	1.73653	5.46112
29	34.65 N	128.40 E	30.60 N	144.60 E	2.13754	6.32803
30	39.83 N	145.35 E	30.30 N	170.21 W	2.96507	8.19200
31	29.70 N	169.43 W	20.70 N	130.27 W	2.38777	7.81563
32	29.92 N	97.57 W	20.48 N	81.38 W	1.74700	5.81832
33	29.70 N	80.62 W	20.48 N	60.22 W	2.00401	6.81331
34	29.77 N	59.47 W	20.70 N	40.35 W	2.26052	7.61712
35	29.77 N	39.60 W	20.70 N	20.25 W	2.43493	7.89000

Table A.2: All directional wave record of sea area no. 36-70.

Sea Area No.	Coordinate				$\bar{H}_{1/3}$ (m)	$\bar{T}_z$ (s)
	Top Left		Bottom Right			
	Latitude	Longitude	Latitude	Longitude		
36	29.77 N	19.80 W	10.57 N	10.12 W	2.09159	6.92685
37	29.70 N	32.33 E	10.80 N	46.95 E	1.44910	5.12114
38	30.98 N	47.21 E	23.21 N	55.61 E	1.14024	4.49206
39	27.98 N	56.33 E	20.29 N	72.75 E	1.56766	5.17498
40	29.77 N	105.45 E	10.57 N	120.75 E	2.19483	6.28386
41	29.77 N	121.43 E	20.70 N	129.75 E	2.28478	6.62000
42	29.92 N	130.50 E	20.70 N	149.77 E	2.21471	6.92543
43	29.77 N	150.52 E	20.40 N	170.21 W	2.53006	7.89840
44	19.99 N	179.66 W	10.43 N	140.18 W	2.51600	8.00900
45	19.91 N	139.80 W	10.35 N	110.06 W	2.33483	7.84466
46	19.88 N	109.57 W	10.65 N	84.30 W	1.71343	6.38076
47	19.88 N	89.47 W	10.65 N	61.35 W	2.11000	6.60400
48	19.65 N	60.38 W	10.65 N	40.35 W	2.26453	7.64014
49	19.88 N	39.60 W	10.43 N	20.25 W	2.21471	7.28400
50	19.65 N	47.47 E	10.43 N	77.62 E	1.94246	5.74876
51	23.02 N	78.38 E	10.80 N	98.85 E	1.68136	5.75700
52	19.88 N	121.50 E	10.65 N	149.77 E	2.01198	6.50798
53	19.88 N	150.52 E	10.65 N	179.55 E	2.29079	7.53607
54	9.82 N	174.38 W	9.38 S	135.23 W	2.19630	7.71922
55	9.82 N	89.47 W	0.75 N	80.25 W	1.54200	6.18004
56	9.82 N	59.70 W	0.52 N	40.12 W	2.14865	7.41091
57	9.60 N	39.60 W	0.75 N	18.23 W	1.93000	7.09540
58	9.82 N	17.77 W	0.75 N	9.60 E	1.55005	6.07758
59	9.75 N	40.65 E	11.40 S	49.80 E	1.83634	6.27023
60	9.30 N	51.15 E	0.75 N	79.95 E	1.87962	6.30639
61	9.82 N	80.40 E	0.52 N	99.97 E	1.86573	6.53200
62	10.05 N	100.43 E	0.30 N	116.85 E	1.55384	5.46700
63	9.82 N	130.43 E	0.75 N	159.75 E	1.71300	6.19700
64	0.08 S	109.50 W	9.15 S	85.50 W	2.10160	7.46307
65	0.15 S	84.15 W	19.50 S	70.20 W	1.82432	7.09860
66	0.08 S	49.50 W	9.52 S	30.45 W	2.10961	7.26877
67	0.22 S	29.48 W	19.42 S	10.35 W	2.18268	7.43207
68	0.22 S	9.60 W	19.42 S	9.98 E	2.15998	7.15900
69	0.15 S	50.70 E	8.70 S	79.50 E	1.99449	7.25175
70	0.15 S	80.85 E	9.15 S	102.90 E	2.12863	7.59209

Table A.3: All directional wave record of sea area no. 71-104.

Sea Area No.	Coordinate				$\bar{H}_{1/3}$ (m)	$\bar{T}_z$ (s)
	Top Left		Bottom Right			
	Latitude	Longitude	Latitude	Longitude		
71	0.15 S	150.75 E	8.70 S	179.55 E	1.53600	5.95200
72	10.35 S	178.65 W	19.35 S	130.50 W	2.22673	7.72078
73	10.35 S	129.15 W	18.90 S	85.95 W	2.48999	8.02000
74	10.35 S	49.05 W	28.80 S	30.60 W	2.08576	7.19269
75	12.15 S	30.90 E	28.95 S	49.35 E	2.46800	7.76927
76	10.35 S	50.70 E	28.95 S	88.95 E	2.73400	8.16533
77	10.35 S	90.75 E	29.25 S	109.35 E	2.88262	8.29680
78	10.35 S	110.70 E	29.25 S	129.60 E	2.35200	7.58100
79	10.35 S	142.65 E	28.80 S	154.80 E	2.04491	6.51898
80	10.35 S	156.60 E	28.50 S	179.10 E	2.34269	7.68300
81	20.25 S	179.10 W	28.80 S	145.35 W	2.73948	8.17535
82	20.25 S	144.00 W	28.80 S	110.25 W	2.55400	8.01752
83	20.25 S	84.15 W	38.70 S	70.65 W	2.37387	7.82200
84	20.25 S	29.10 W	28.80 S	9.60 E	2.67718	8.16366
85	20.25 S	10.95 E	39.15 S	19.50 E	3.06012	8.42184
86	30.15 S	179.10 W	39.15 S	120.60 W	2.84870	8.19600
87	30.15 S	61.20 W	39.15 S	40.05 W	2.35471	7.65616
88	30.15 S	39.15 W	39.15 S	15.60 W	3.15100	8.46600
89	30.15 S	14.25 W	38.70 S	9.60 E	3.00100	8.28357
90	30.60 S	21.30 E	39.15 S	39.30 E	3.23926	8.49299
91	30.15 S	40.95 E	38.70 S	108.75 E	3.37900	8.61912
92	30.15 S	110.10 E	39.15 S	146.25 E	3.25000	8.53700
93	30.15 S	147.60 E	39.15 S	174.15 E	2.65015	7.98998
94	40.05 S	148.95 W	49.05 S	120.15 W	3.75150	8.91658
95	40.05 S	89.10 W	49.05 S	70.65 W	3.46794	8.70585
96	40.05 S	69.30 W	49.05 S	50.40 W	2.52202	7.53206
97	40.05 S	49.05 W	49.05 S	10.80 W	3.48297	8.69900
98	40.05 S	9.30 W	49.05 S	38.85 E	3.47900	8.73323
99	40.05 S	40.80 E	48.60 S	89.40 E	3.84100	8.96747
100	40.05 S	90.75 E	49.05 S	139.95 E	3.73547	8.86336
101	40.50 S	140.85 E	49.05 S	172.35 E	3.08617	8.35972
102	40.50 S	179.10 W	49.05 S	150.30 W	2.96794	8.30441
103	50.40 S	79.20 W	58.50 S	60.75 W	3.30900	8.47900
104	50.85 S	58.95 W	54.45 S	30.60 W	2.91642	8.24749

Appendix B

Hydrodynamic and Hydrostatic Coefficients Determination for Coupled Heave-Pitch and Roll Motions of a Ship in Waves

B.1 Coefficients Determination based on 2D-Strip Theory for Coupled Heave and Pitch Motions

The 2-D strip theory implemented in the MAXSURF Motions Advanced software package that is used in this resraech can be referred to the theory developed by Salvesen et al. (1970), see also Bentley Systems (2015b) for detail. The theory defines a 3-D underwater hull form by a series of 2-D underwater cross section areas or strips as illustrated in Figure B.1. The distances or gaps between strips are assumed to be small as each strip contains with local hydrodynamic properties such as added mass, damping, and stiffness. Moreover, the strip theory also assumes that the local hydrodynamic properties are identical to the strip of an infinite long cylinder with the same cross section area.

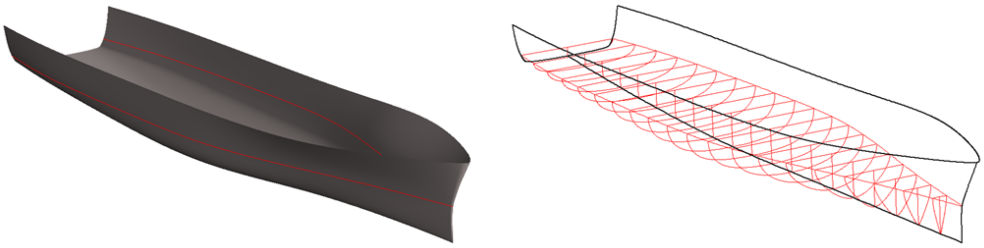

(a) 3-D Render of ship hull. (b) Ship hull with devided 2-D hull sections.

Figure B.1: Example of 3-D graphical ship hull and sectional underwater areas.

The ship heave and pitch motions are defined as coupled ODEs. Quoting the coupled heave-pitch equations of motions, Equations 3.41 and 3.43, as:

$$\begin{aligned}\big(\rho\nabla + a_{33}(\omega_e)\big)\ddot{z}(\omega_e,t) + b_{33}(\omega_e)\dot{z}(\omega_e,t) + c_{33}z(\omega_e,t)\\ +a_{35}(\omega_e)\ddot{\theta}(\omega_e,t) + b_{35}(\omega_e)\dot{\theta}(\omega_e,t) + c_{35}\theta(\omega_e,t)\\ = F_{wa_3}\cos\big(\omega_e t + \varepsilon_3(\omega_e)\big)\end{aligned} \tag{B.1}$$

$$\begin{aligned}\big(I_{yy} + a_{55}(\omega_e)\big)\ddot{\theta}(\omega_e,t) + b_{55}(\omega_e)\dot{\theta}(\omega_e,t) + c_{55}\theta(\omega_e,t)\\ a_{53}(\omega_e)\ddot{z}(\omega_e,t) + b_{53}(\omega_e)\dot{z}(\omega_e,t) + c_{53}z(\omega_e,t)\\ = F_{wa_5}\cos\big(\omega_e t + \varepsilon_5(\omega_e)\big)\end{aligned} \tag{B.2}$$

as for heave motion, Equation B.1, the global added mass, damping, and restoring coefficients are evaluated by integrating over the length of the ship as:

$$a_{33}(\omega_e) = \int a'_{33}(\omega_e)d\xi \tag{B.3}$$

$$b_{33}(\omega_e) = \int b'_{33}(\omega_e)d\xi \tag{B.4}$$

$$c_{33} = \rho g \int b_\xi d\xi = \rho g A_{WP} \tag{B.5}$$

$$a_{35}(\omega_e) = -\int \xi a'_{33}(\omega_e)d\xi - \frac{U}{\omega_e^2}b_{33}(\omega_e) \tag{B.6}$$

$$b_{35}(\omega_e) = -\int \xi b_{33}(\omega_e)d\xi + Ua_{33}(\omega_e) \tag{B.7}$$

$$c_{35} = -\rho g \int \xi b_\xi d\xi = -\rho g M_{WP} \tag{B.8}$$

and for pitch motion, Equation B.2, as:

$$a_{55}(\omega_e) = \int \xi^2 a_{33}(\omega_e)d\xi + \frac{U^2}{\omega_e^2}a_{33}(\omega_e) \tag{B.9}$$

$$b_{55}(\omega_e) = \int \xi^2 b_{33}(\omega_e)d\xi + \frac{U^2}{\omega_e^2}b_{33}(\omega_e) \tag{B.10}$$

$$c_{55} = \rho g \int \xi^2 b_\xi d\xi = \rho g I_{WP} \tag{B.11}$$

$$a_{53}(\omega_e) = -\int \xi a_{33}(\omega_e)d\xi + \frac{U}{\omega_e^2}b_{33}(\omega_e) \tag{B.12}$$

$$b_{53}(\omega_e) = -\int \xi b_{33}(\omega_e)d\xi - Ua_{33}(\omega_e) \tag{B.13}$$

$$c_{53} = c_{35} \tag{B.14}$$

where a'_{ij}, b'_{ij} are the frequency dependent sectional added mass (kg) and damping coefficient (kN/(m/s) or kN/(rad/s)), ξ is the sectional longitudinal distance (m) from longitudinal centre of gravity, and b_ξ is the sectional beam (m) of the ship.

The wave excitation force (for heave) and moment (for pitch) acting on the individual strip are induced by the effects of the sectional Froude-Krylov force (f_3) and the diffraction force (h_3). Thus, the global wave excitation forces and moments are calculated by integrating the Froude-Krylov and diffraction forces over the length of the ship (Salvesen et al., 1970) as:

$$F_{wa_3}(\omega_e) = \rho\zeta_a \int (f_3(\omega_e) + h_3(\omega_e))d\xi \tag{B.15}$$

$$F_{wa_5}(\omega_e) = -\rho\zeta_a \int \left[\xi(f_3(\omega_e) + h_3(\omega_e)) + \frac{U}{i\omega_e}h_3(\omega_e)\right] d\xi \tag{B.16}$$

by

$$f_3(\omega_e) = \rho\xi g e^{-ikx\cos(\mu)} \int_{C_s} \hat{z}e^{iky\sin(\mu)}e^{-kz}dl \tag{B.17}$$

$$h_3(\omega_e) = \rho g\omega e^{-ikx\cos(\mu)} \int_{C_s} \big(i\hat{z} - \hat{y}\sin(\mu)\big)e^{iky\sin(\mu)}e^{-kz}\phi_{30}(\omega_e)dl \tag{B.18}$$

where $\hat{y}$ and $\hat{z}$ are the outward normal vector of the section, C_s and dl are the sectional contour and element of arc along the hull section, and ϕ_{30} is the amplitude of frequency-dependent 2-D velocity potential of the section in heave, see Bentley Systems (2015b) for detail.

B.2 Coefficients Determination based on Ship Hydrostatic Property for Roll Motion

From Equation 3.42, the uncoupled roll motion equation of motion can be expressed as:

$$\big(I_{xx} + a_{44}\big)\ddot{\phi}(\omega_e, t) + b_{44}\dot{\phi}(\omega_e, t) + c_{44}\phi(\omega_e, t) = F_{wa_4}(\omega_e)\cos\big(\omega_e t + \varepsilon_4(\omega_e)\big). \tag{B.19}$$

Equation B.19 is in the form of uncoupled second-order ODE as it is described as a damped mass-spring with external force system (Bentley Systems, 2015b). Therefore, the solution of this equation can be expressed as:

$$\phi(\omega_e, t) = \frac{F_{wa_4}(\omega_e)}{\sqrt{\big(c_{44} - (I_{xx} + a_{44})\omega_e^2\big)^2 + b_{44}^2\omega_e^2}}\cos(\omega_e t + \varepsilon_4(\omega_e)) \tag{B.20}$$

and, hence, the natural frequency of roll motion of the ship is

$$\omega_{*4} = \sqrt{\frac{c_{44}}{(I_{xx} + a_{44})}} \tag{B.21}$$

as the phase lag relative to forcing function is

$$\varepsilon_4(\omega_e) = \frac{b_{44}\omega_e}{c_{44} - (I_{xx} + a_{44})\omega_e^2} \tag{B.22}$$

where I_{xx} is the mass moment of inertia of the ship in roll which can be estimated by Equation 3.33, a_{44} is the added inertia of roll which is approximated as:

$$a_{44} \approx 0.25 I_{xx}, \tag{B.23}$$

b_{44} is the damping ratio for roll, and c_{44} is the roll hydrostatic restoring coefficient that is

$$c_{44} = GM_T \nabla \rho g \tag{B.24}$$

as GM_T is the transverse metacentric height (m) of the ship.

The roll motion transfer function is assumed to be

$$TF_\phi(\omega_e) = \frac{\phi(\omega_e)}{\alpha(\omega_e)} = \frac{c_{44}\phi(\omega_e)}{F_{wa_4}(\omega_e)} = \frac{1}{\sqrt{\left(1 - (\omega_e/\omega_{*4})^2\right)^2 + 4b_{44}^2(\omega_e/\omega_{*4})^2}} \tag{B.25}$$

as the roll motion transfer function can be modified relating to the ship heading angle as:

$$TF_\phi(\mu) = TF_\phi \sin(\mu) \tag{B.26}$$

therefore the maximum value of roll motion transfer function occurs in beam waves and, on the other hand, the transfer function is zero in head and following waves (Bentley Systems, 2015b; Lloyd, 1989).

Appendix C

List of Scaling Laws

A comprehensive list of scaling laws based on the work of Lloyd (1989) is summarised in Table C.1. Note that, these scaling laws are expressed based on the assumption that the mass densities of the fluid or water between two different scaled ships are equivalent.

Table C.1: List of scaling laws.

Quantity of Parameter	Unit	Corresponding Scaling Laws
Mass	kg	$1/R^3$
Length	m	$1/R$
Time	s	$1/\sqrt{R}$
Velocity	m/s	$1/\sqrt{R}$
Acceleration	$\mathrm{m/s^2}$	1
Angular displacement	rad or deg	1
Angular velocity	rad/s or deg/s	$\sqrt{R}$
Angular acceleration	$\mathrm{rad/s^2}$ or $\mathrm{deg/s^2}$	R
Frequency	rad/s or Hz	$\sqrt{R}$
Force	N	$1/R^3$
Moment, torque	N·m	$1/R^4$
Moment of inertia	$\mathrm{kg{\cdot}m^2}$	$1/R^5$
Linear spectral density ordinate	$\mathrm{m^2/(rad/s)}$	$1/R\sqrt{R}$
Angular spectral density ordinate	$\mathrm{rad^2/(rad/s)}$	$1/\sqrt{R}$

Appendix D

Dynamics of Simple Pendulum Systems

D.1 Simple Pendulum System

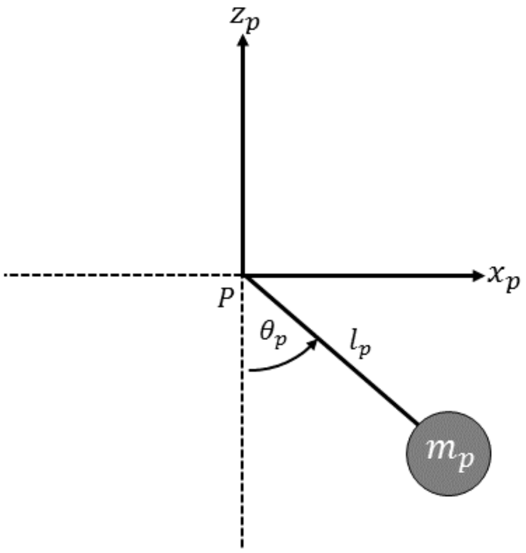

Figure D.1: Schematic diagram of a simple or 1-DOF pendulum system.

Considering a pendulum with a mass (m_p, kg) and a rigid arm with a length (l_p, m) hanged and free to swing around a pivot, the pendulum is released from the equilibrium or resting position with an angle (θ_p, rad) as illustrated in Figure D.1. Hence, the kinetic and potential energies in each discretised time step can be respectively expressed as:

$$KE(t) = \frac{1}{2}m_p v(t)^2 = \frac{1}{2}m_p\big(l_p\dot{\theta}_p(t)\big)^2 \tag{D.1}$$

$$PE(t) = m_p g h(t) = m_p g l_p\left(1 - \cos\big(\theta_p(t)\big)\right). \tag{D.2}$$

So, from Equation 5.2, the Lagrangian of this pendulum system is

$$L(t) = KE(t) - PE(t) = \frac{1}{2}m_p\big(l_p\dot{\theta}_p(t)\big)^2 - m_p g l_p\left(1 - \cos\big(\theta_p(t)\big)\right) \tag{D.3}$$

and, from Equation 5.1, in this case as:

$$\frac{d}{dt}\left(\frac{\partial L}{\partial \dot{\theta}_p}\right) - \frac{\partial L}{\partial \theta_p} = Q_{\theta_p} \tag{D.4}$$

and, therefore

$$\frac{d}{dt}\left(\frac{\partial L(t)}{\partial \dot{\theta}_p(t)}\right) = m_p l_p^2 \ddot{\theta}_p(t) \tag{D.5}$$

$$\frac{\partial L(t)}{\partial \dot{\theta}_p(t)} = m_p l_p^2 \dot{\theta}_p(t) \tag{D.6}$$

$$\frac{\partial L(t)}{\partial \theta_p(t)} = -m_p g l_p \sin\big(\theta_p(t)\big). \tag{D.7}$$

So, from Equation D.4, thus

$$m_p l_p^2 \ddot{\theta}_p(t) + m_p g l_p \sin\big(\theta_p(t)\big) = Q_{\theta_p}. \tag{D.8}$$

where $m_p l_p^2$ indicates the mass moment of inertia of the pendulum (kg·m^2), Q_{θ_p} is the generalised torque (N·m) that represents the control torque and damping component in the system, and the natural frequency (ω_n) of this simple pendulum is

$$\omega_n = \sqrt{\frac{g}{l_p}}. \tag{D.9}$$

Furthermore, in case of the pendulum mass is not uniformly distributed, it can be referred as a compound simple pendulum system and its equation of motion can be expressed as:

$$I_p \ddot{\theta}_p(t) + m_p g l_p \sin\big(\theta_p(t)\big) = Q_{\theta_p} \tag{D.10}$$

whilst I_p is the mass moment of inertia (kg·m^2), m represents the pendulum weight (kg), and l_p is the pivot-to-CG length (m) of the pendulum system as the undamped natural frequency is

$$\omega_n = \sqrt{\frac{mgl}{I}}. \tag{D.11}$$

D.1.1 Small Angle Approximation

For small angle oscillation ($\theta_p \to 0$), equation of motion of a pendulum system can be linearised ($\sin(\theta_p) \to \theta_p$). Therefore, for example, equation D.8 becomes

$$\ddot{\theta}_p(t) + \frac{g}{l_p}\theta_p(t) = Q_{\theta_p}. \tag{D.12}$$

Both non-linear and linear cases can be numerically solved by applying initial condition ($\theta_p(0)$). Figure D.2 shows planar motions of undamped pendulum system ($Q_{\theta_p} = 0$) with various initial angles. As can be seen, for small applied initial angle ($\theta_p(0) \leqslant \pi/9$ rad or 20°), good agreements between non-linear and linear equations of a pendulum system are valid over the oscillation period. However, for larger initial angle ($\theta_p(0) > \pi/9$ rad), the differences between the results by non-linear and linear equations can be noticed. The non-linear case provides phase shift growing with time. Therefore, it can be concluded that the approximation of linearising the pendulum equation is good for a small initial angel but that the approximation breaks down when the angle of oscillation is large.

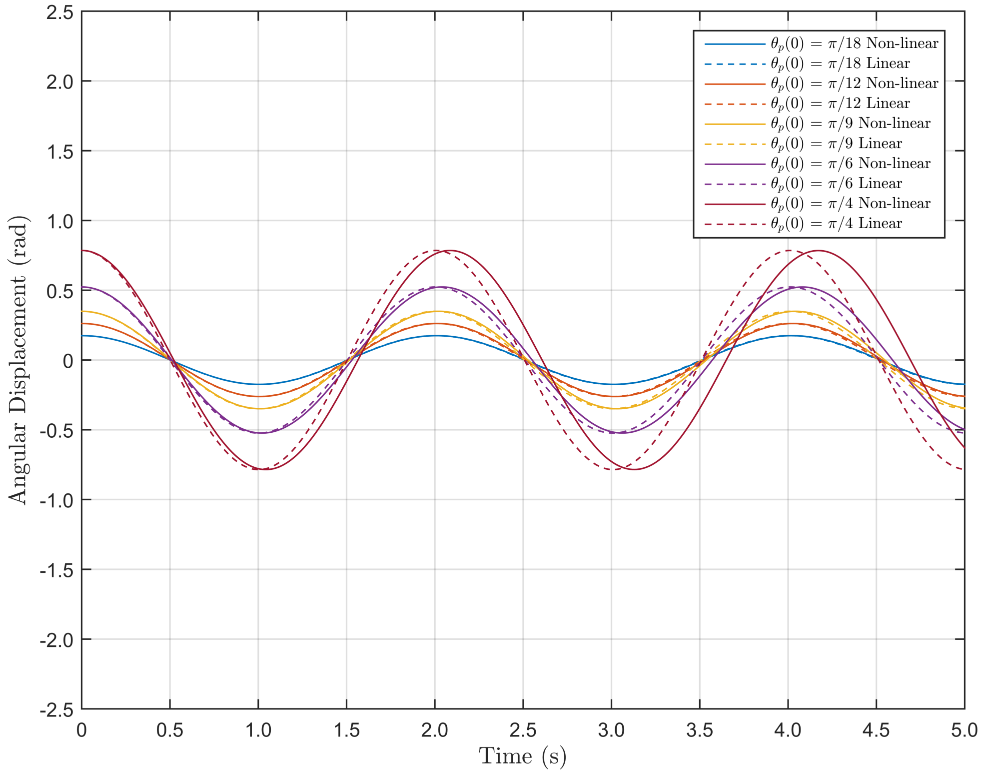

Figure D.2: Comparison of non-linear and linear analyses for undamped pendulum system with arbitrary weight and the length of of 1 m.

D.2 Simple Pendulum System with External Excitation

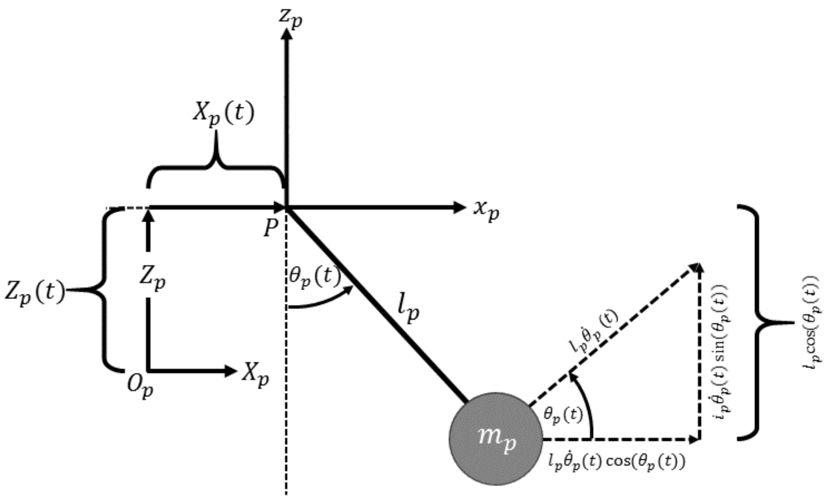

Figure D.3: Schematic diagram of a driven simple or 1-DOF pendulum system.

Considering the schematic diagram in Figure D.3, a pendulum system with a mass (m_p) hanging at the pivot or support point (P) at the local coordinate (Px_pz_p) with the length (l_p). The support point can be disturbed and moved in horizontal (X_p, m) and vertical (Z_p, m) directions from the global reference coordinate ($O_pX_pZ_p$) which will create the resultant angle (θ_p) respecting the equilibrium position. So, the horizontal velocity component ($\mathbf{v}_{x_p}$, m/s) can be expressed as:

$$\mathbf{v}_{x_p}(t) = \dot{X}_p(t) + l\dot{\theta}_p(t)\cos(\theta_p(t)) \tag{D.13}$$

and the vertical velocity component ($\mathbf{v}_{z_p}$, m/s) is

$$\mathbf{v}_{z_p}(t) = \dot{Z}_p(t) + l\dot{\theta}_p(t)\sin(\theta_p(t)) \tag{D.14}$$

and, hence, the kinetic energy (T) of this pendulum system can be represented as:

$$\begin{aligned} KE(t) &= \frac{1}{2}m_p v(t)^2 \\ &= \frac{1}{2}m_p\Big(\mathbf{v}_{x_p}(t) + \mathbf{v}_{z_p}(t)\Big)^2 \\ &= \frac{1}{2}m_p\Big(\dot{X}_p(t) + \dot{Z}_p(t) + l_p^2\dot{\theta}_p(t)^2 + 2l_p\dot{\theta}_p(t)\big(\dot{X}_p(t)\cos(\theta_p(t)) \\ &\qquad + \dot{Z}_p(t)\sin(\theta_p(t))\big)\Big) \end{aligned} \tag{D.15}$$

and, the potential energy (V) is

$$\begin{aligned} PE(t) &= m_p g h(t) \\ &= m_p g l_p \dot{Z}_p(t) + m_p g l_p\Big(1 - \cos(\theta_p(t))\Big) \end{aligned} \tag{D.16}$$

Therefore, from Equations D.15 and D.16, the Lagrangian of this driven pendulum system is

$$\begin{aligned} L(t) = \frac{1}{2} m_p \Big(\dot{X}_p(t) + \dot{Z}_p(t) + l_p^2 \dot{\theta}_p(t)^2 + 2 l_p \dot{\theta}_p(t) \big(\dot{X}_p(t) \cos(\theta_p(t)) + \dot{Z}_p(t) \sin(\theta_p(t)) \big) \Big) \\ - m_p g l_p \dot{Z}_p(t) - m_p g l_p \Big(1 - \cos(\theta_p(t)) \Big). \end{aligned} \tag{D.17}$$

Finally, from Equation D.4, the equation of motion of a driven 1-DOF pendulum system can be formulated as a second-order differential equation as:

$$m_p l_p^2 \ddot{\theta}_p(t) + m_p g l_p \sin(\theta_p(t)) + m_p l \Big(\ddot{X}_p(t) \cos(\theta_p(t)) + \ddot{Z}_p(t) \sin(\theta_p(t)) \Big) = Q_{\theta_p} \tag{D.18}$$

where $\ddot{X}_p$ and $\ddot{Z}_p$ are the horizontal and vertical accelerations (m/s^2) of the disturbance or external excitation and the natural frequency can be referred to Equation D.9. Additionally, the equation of motion of a compound pendulum with external excitation is expressed as:

$$I_p \ddot{\theta}_p(t) + m_p g l_p \sin(\theta_p(t)) + m_p l_p \Big(\ddot{X}_p(t) \cos(\theta_p(t)) + \ddot{Z}_p(t) \sin(\theta_p(t)) \Big) = Q_{\theta_p} \tag{D.19}$$

by the natural frequency of the system is indicated in Equation D.11.

Appendix E

Dynamics of Spherical Pendulum Systems

E.1 Spherical Pendulum System

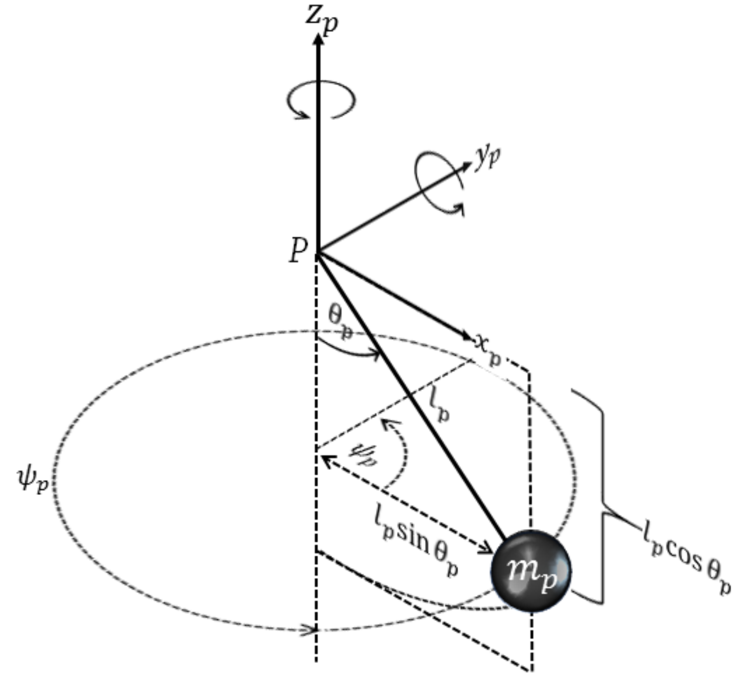

Figure E.1: Schematic diagram of a spherical pendulum system.

Consider a pendulum consisting of a mass m_p with the arm of length l_p, the pendulum is allowed to swing in any direction in spherical coordinate (r_p, θ_p, ψ_p). Hence, the position of the pendulum in the Cartesian coordinates (x_p, y_p, z_p) can be written in terms of the angular coordinates (θ_p, ψ_p) as:

$$x_p(t) = l_p \sin(\theta_p(t)) \cos(\psi_p(t)) \tag{E.1}$$

$$y_p(t) = l_p \sin(\theta_p(t)) \sin(\psi_p(t)) \tag{E.2}$$

$$z_p(t) = -l_p \cos(\theta_p(t)). \tag{E.3}$$

Therefore,

$$\dot{x}_p(t) = l_p\Big(\dot{\theta}_p(t) \cos(\theta_p(t)) \cos(\psi_p(t)) - \dot{\psi}_p(t) \sin(\theta_p(t)) \sin(\psi_p(t))\Big) \tag{E.4}$$

$$\dot{y}_p(t) = l_p\Big(\dot{\theta}_p(t) \cos(\theta_p(t)) \sin(\psi_p(t)) + \dot{\psi}_p(t) \sin(\theta_p(t)) \cos(\psi_p(t))\Big) \tag{E.5}$$

$$\dot{z}_p(t) = l_p\dot{\theta}_p(t) \sin(\theta_p(t)). \tag{E.6}$$

So, the kinetic and potential energies in each time step can be expressed as:

$$\begin{aligned} KE(t) &= \frac{1}{2} m_p v(t)^2 \\ &= \frac{1}{2} m_p \Big(\dot{x}_p(t)^2 + \dot{y}_p(t)^2 + \dot{z}_p(t)^2\Big) \\ &= \frac{1}{2} m_p l_p^2 \Big(\dot{\theta}_p(t)^2 + \dot{\psi}_p(t)^2 \sin(\theta_p(t))^2\Big) \end{aligned} \tag{E.7}$$

$$\begin{aligned} PE(t) &= m_p g h(t) \\ &= -m_p g l_p \cos(\theta_p(t)). \end{aligned} \tag{E.8}$$

Therefore, the Lagrangian of this pendulum system is

$$L(t) = KE(t) - PE(t) = \frac{1}{2} m_p l_p^2 \Big(\dot{\theta}_p(t)^2 + \dot{\psi}_p(t)^2 \sin(\theta_p(t))^2\Big) + m_p g l_p \cos(\theta_p(t)) \tag{E.9}$$

and, from Equation 5.1, the Lagrange equations of this pendulum system based on two generalised coordinates as:

$$\frac{d}{dt}\left(\frac{\partial L}{\partial \dot{\theta}_p}\right) - \frac{\partial L}{\partial \theta_p} = Q_{\theta_p}, \tag{E.10}$$

$$\frac{d}{dt}\left(\frac{\partial L}{\partial \dot{\psi}_p}\right) - \frac{\partial L}{\partial \psi_p} = Q_{\psi_p} \tag{E.11}$$

where

$$\frac{\partial L(t)}{\partial \theta_p(t)} = \dot{\psi}_p(t)^2 m_p l_p^2 \sin(\theta_p(t)) \cos(\theta_p(t)) - m_p g l_p \sin(\theta_p(t)), \tag{E.12}$$

$$\frac{\partial L(t)}{\partial \dot{\theta}_p(t)} = m_p l_p^2 \dot{\theta}_p(t), \tag{E.13}$$

$$\frac{d}{dt}\left(\frac{\partial L(t)}{\partial \dot{\theta}_p(t)}\right) = m_p l_p \ddot{\theta}_p(t), \tag{E.14}$$

$$\frac{\partial L(t)}{\partial \psi_p(t)} = 0, \tag{E.15}$$

$$\frac{\partial L(t)}{\partial \dot{\psi}_p(t)} = \dot{\psi}_p(t) m_p l_p^2 \sin(\theta_p(t))^2, \tag{E.16}$$

$$\frac{d}{dt}\left(\frac{\partial L(t)}{\partial \dot{\psi}_p(t)}\right) = \ddot{\psi}_p m_p l_p^2 \sin(\theta_p(t))^2 + 2\dot{\psi}_p(t) m_p l_p^2 \dot{\theta}_p \sin(\theta_p(t)) \cos(\theta_p(t)). \tag{E.17}$$

Then, substitute Equations E.12 to E.14 and E.15 to E.17 into Equations E.10 and E.11, therefore the 2-DOF equations of motion of a spherical pendulum system can be written as:

$$m_p l_p^2 \ddot{\theta}_p(t) + m_p g l_p \sin(\theta_p(t)) - m_p l_p^2 \sin(\theta_p(t)) \cos(\theta_p(t)) \dot{\psi}_p^2 = Q_{\theta_p}, \tag{E.18}$$

$$m_p l_p^2 \sin(\theta_p(t))^2 \ddot{\psi}_p(t) = Q_{\psi_p} \tag{E.19}$$

by the natural frequency of this system can be referred to Equation D.9.

E.2 Spherical Pendulum System with External Excitation

Regarding Figure E.2(a), a pendulum system with mass (m_p) and length (l_p) is hanging at an unconstrained pivot point (P) which ideally allows the pendulum to complete orbital rotation around the pivot. Once, the pendulum system is disturbed from the resting position in fixed global reference coordinate ($O_pX_pY_pZ_p$) with the distances in X_p-, Y_p-, and Z_p-directions, the referenced angles in generalised local coordinate ($Px_py_pz_p$) are given to be the swing angle acting on vertical axis (θ_p) and the angle rotating around the vertical axis (ψ_p) of the pendulum arm that projects to the horizontal plane (x_py_p-plane) respecting to x_p-axis.

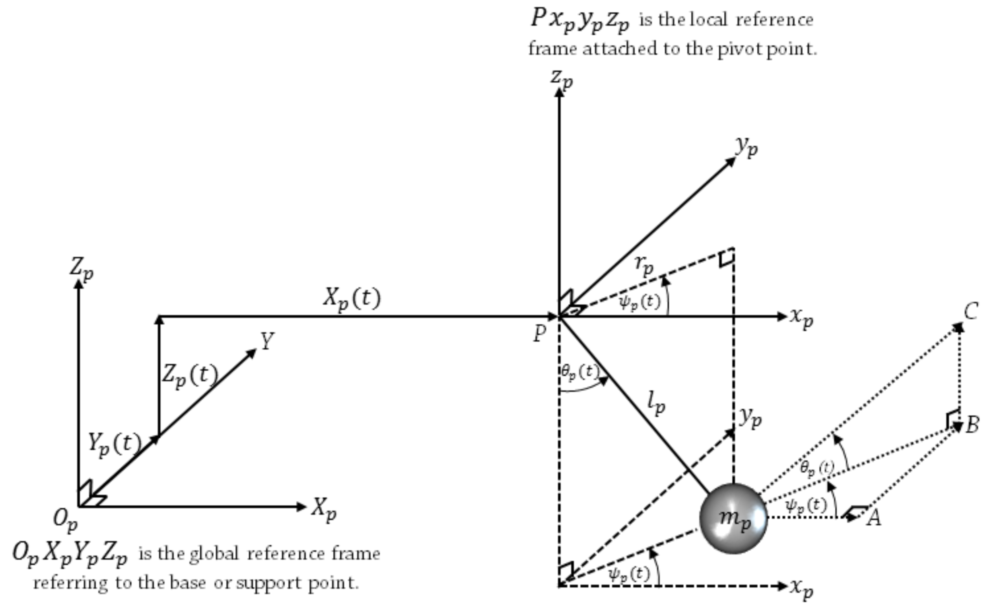

(a) Overview dynamics.

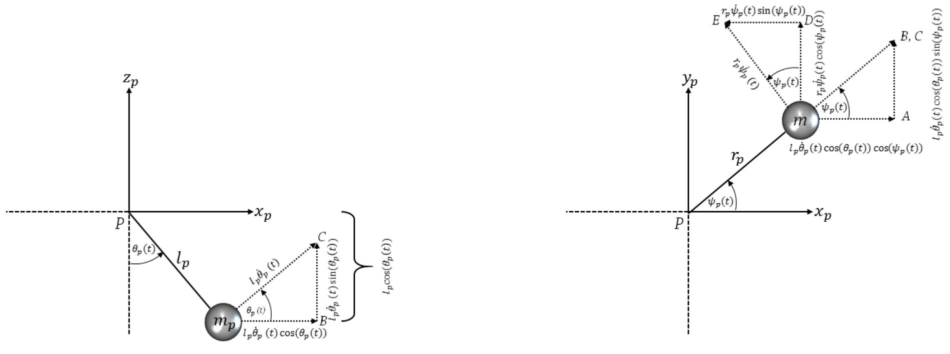

(b) x_pz_p-plane dynamics. (c) x_py_p-plane dynamics.

Figure E.2: Schematic diagram of a driven spherical pendulum system.

Consequently, from the trigonometric relations showing in Figures E.2(b) and E.2(c), the velocity vector components in x_p-, y_p-, and z_p-directions can be calculated as:

$$\mathbf{v}_{x_p}(t) = \dot{X}_p(t) + l_p\dot{\theta}_p(t)\cos(\theta_p(t))\cos(\psi_p(t)) - r_p\dot{\psi}_p(t)\sin(\psi_p(t)), \tag{E.20}$$

$$\mathbf{v}_{y_p}(t) = \dot{Y}_p(t) + l_p\dot{\theta}_p(t)\cos(\theta_p(t))\sin(\psi_p(t)) + r_p\dot{\psi}_p(t)\cos(\psi_p(t)), \tag{E.21}$$

$$\mathbf{v}_{z_p}(t) = \dot{Z}_p(t) + l_p\dot{\theta}_p(t)\sin(\theta_p(t)) \tag{E.22}$$

where r_p is the dynamic or projected pendulum length on horizontal plane (x_py_p-plane) which is

$$r_p = l_p\sin(\theta_p(t)). \tag{E.23}$$

Therefore, the kinetic energy (T) of this pendulum system can be represented as:

$$\begin{aligned} KE(t) &= \frac{1}{2}m_p v(t)^2 \\ &= \frac{1}{2}m_p\Big(\mathbf{v}_{x_p}(t) + \mathbf{v}_{y_p}(t) + \mathbf{v}_{z_p}(t)\Big)^2 \\ &= \frac{1}{2}m_p\Big(\dot{X}_p(t)^2 + \dot{Y}_p(t)^2 + \dot{Z}_p(t)^2 + l_p^2\dot{\psi}_p(t)^2\sin(\theta_p)^2 + l_p^2\dot{\theta}_p(t)^2 \\ &\qquad - 2l_p\dot{X}_p(t)\dot{\psi}_p(t)\sin(\theta_p(t))\sin(\psi_p(t)) + 2l_p\dot{X}_p(t)\dot{\theta}_p(t)\cos(\theta_p(t))\cos(\psi_p(t)) \\ &\qquad + 2l_p\dot{Y}_p(t)\dot{\psi}_p(t)\sin(\theta_p(t))\cos(\psi_p(t)) \; + 2l_p\dot{Y}_p(t)\dot{\theta}_p(t)\cos(\theta_p(t))\sin(\psi_p(t)) \\ &\qquad + 2l_p\dot{Z}_p(t)\dot{\theta}_p(t)\sin(\theta_p(t))\Big) \end{aligned} \tag{E.24}$$

and, from Figure E.2(b), the potential energy (V) is

$$\begin{aligned} PE(t) &= m_p g h(t) \\ &= m_p g l_p \dot{Z}_p(t) + m_p g l_p\Big(1 - \cos(\theta_p(t))\Big). \end{aligned} \tag{E.25}$$

and, based on the Lagrange equation, this pendulum system requires two governing equations regarding the two generalised coordinates as:

$$\frac{d}{dt}\left(\frac{\partial KE}{\partial\dot{\theta}_p}\right) - \frac{\partial KE}{\partial\theta_p} + \frac{\partial PE}{\partial\theta_p} = Q_{\theta_p}, \tag{E.26}$$

$$\frac{d}{dt}\left(\frac{\partial KE}{\partial\dot{\psi}_p}\right) - \frac{\partial KE}{\partial\psi_p} + \frac{\partial PE}{\partial\psi_p} = Q_{\psi_p}. \tag{E.27}$$

So, finalising the terms in Equations E.26 and E.27 as:

$$\begin{aligned} \frac{d}{dt}\left(\frac{\partial KE(t)}{\partial\dot{\theta}_p(t)}\right) = \frac{1}{2}m_p\Big(&2l_p^2\ddot{\theta}_p(t) + 2l_p\ddot{X}_p(t)\cos(\theta_p(t))\cos(\psi_p(t)) \\ &- 2l_p\dot{X}_p(t)\dot{\theta}_p(t)\sin(\theta_p(t))\cos(\psi_p(t)) \\ &- 2l_p\dot{X}_p(t)\dot{\psi}_p(t)\cos(\theta_p(t))\sin(\theta_p(t)) \\ &+ 2l_p\ddot{Y}_p(t)\cos(\theta_p(t))\sin(\psi_p(t)) \\ &- 2l_p\dot{Y}_p(t)\dot{\theta}_p(t)\sin(\theta_p(t))\sin(\psi_p(t)) \\ &+ 2l_p\dot{Y}_p(t)\dot{\psi}_p(t)\cos(\theta_p(t))\cos(\psi_p(t)) \\ &+ 2l_p\ddot{Z}_p(t)\sin(\theta_p(t)) + 2l_p\dot{Z}_p(t)\dot{\theta}_p(t)\cos(\theta_p(t))\Big), \end{aligned} \tag{E.28}$$

$$
\begin{aligned}
\frac{\partial KE(t)}{\partial \theta_p(t)} = \frac{1}{2} m_p \Big(& 2l_p^2 \dot{\psi}_p(t)^2 \sin(\theta_p(t)) \cos(\theta_p(t)) \\
& - 2l_p \dot{X}_p(t) \dot{\theta}_p(t) \sin(\theta_p(t)) \cos(\psi_p(t)) \\
& - 2l_p \dot{X}_p(t) \dot{\psi}_p(t) \cos(\theta_p(t)) \sin(\psi_p(t)) \\
& + 2l_p \dot{Y}_p(t) \dot{\psi}_p(t) \cos(\theta_p(t)) \cos(\psi_p(t)) \\
& - 2l_p \dot{Y}_p(t) \dot{\theta}_p(t) \sin(\theta_p(t)) \sin(\psi_p(t)) \\
& + 2l_p \dot{Z}_p(t) \dot{\theta}_p(t) \cos(\theta_p(t)) \Big),
\end{aligned} \tag{E.29}
$$

$$
\frac{\partial PE(t)}{\partial \theta_p(t)} = m_p g l_p \sin(\theta_p(t)), \tag{E.30}
$$

$$
\begin{aligned}
\frac{d}{dt} \left(\frac{\partial KE(t)}{\partial \dot{\psi}_p(t)} \right) = \frac{1}{2} m_p \Big(& 2l_p^2 \ddot{\psi}_p(t) \sin(\theta_p(t))^2 \\
& + 4l_p^2 \dot{\theta}_p(t) \dot{\psi}_p(t) \sin(\theta_p(t)) \cos(\theta_p(t) \\
& - 2l_p \ddot{X}_p(t) \sin(\theta_p(t)) \sin(\psi_p(t)) \\
& - 2l_p \dot{X}_p(t) \dot{\theta}_p(t) \cos(\theta_p(t)) \sin(\psi_p(t)) \\
& - 2l_p \dot{X}_p(t) \dot{\psi}_p(t) \sin(\theta_p(t)) \cos(\psi_p(t)) \\
& + 2l_p \ddot{Y}_p(t) \sin(\theta_p(t)) \cos(\psi_p(t)) \\
& + 2l_p \dot{Y}_p(t) \dot{\theta}_p(t) \cos(\theta_p(t)) \cos(\psi_p(t)) \\
& - 2l_p \dot{Y}_p(t) \dot{\psi}_p(t) \sin(\theta_p(t)) \sin(\psi_p(t)) \Big),
\end{aligned} \tag{E.31}
$$

$$\begin{aligned}\frac{\partial KE(t)}{\partial \psi_p(t)} =& \frac{1}{2} m_p \Big(- 2 l_p \dot{X}_p(t) \dot{\theta}_p(t) \cos(\theta_p(t)) \sin(\psi_p(t)) \\ & - 2 l_p \dot{X}_p(t) \dot{\psi}_p(t) \sin(\theta_p(t)) \cos(\psi_p(t)) \\ & + 2 l_p \dot{Y}_p(t) \dot{\theta}_p(t) \cos(\theta_p(t)) \cos(\psi_p(t)) \\ & - 2 l_p \dot{Y}_p(t) \dot{\psi}_p(t) \sin(\theta_p(t)) \sin(\psi_p(t)) \Big), \end{aligned} \tag{E.32}$$

$$\frac{\partial PE(t)}{\partial \psi_p(t)} = 0. \tag{E.33}$$

Eventually, substitute Equations E.28 to E.30 into Equation E.26 and Equations E.31 to E.33 into Equation E.27, two equations of motion of this driven 2-DOF spherical pendulum can be finalised as:

$$\begin{aligned}& m_p l_p^2 \ddot{\theta}_p(t) + m_p g l_p \sin(\theta_p(t)) - m_p l_p^2 \sin(\theta_p(t)) \cos(\theta_p(t)) \dot{\psi}_p(t)^2 \\ & + m_p l_p \Big(\ddot{X}(t) \cos(\theta_p(t)) \cos(\psi_p(t)) + \ddot{Y}(t) \cos(\theta_p(t)) \sin(\psi_p(t)) \\ & + \ddot{Z}(t) \sin(\theta_p(t)) \Big) = Q_{\theta_p}, \end{aligned} \tag{E.34}$$

$$\begin{aligned}& m_p l_p^2 \sin(\theta_p(t))^2 \ddot{\psi}_p(t) + 2 m_p l_p^2 \sin(\theta_p(t)) \cos(\theta_p(t)) \dot{\theta}_p(t) \dot{\psi}_p(t) \\ & - m_p l_p \sin(\theta_p(t)) \Big(\ddot{X}(t) \sin(\psi_p(t)) + m_p l_p \ddot{Y}(t) \cos(\psi_p(t)) \Big) = Q_{\psi_p} \end{aligned} \tag{E.35}$$

where $\ddot{X}_p$, $\ddot{Y}_p$, and $\ddot{Z}_p$ are the accelerations (m/s^2) along x_p-, y_p-, and z_p-axes of the disturbance or external excitation. Besides, Q_{θ_p} and Q_{ψ_p} are the generalised torques that representing control torques and damping components regarding referenced DOF. Likewise, the undamped natural frequency can be referred to Equation D.9.

Appendix F

Technical Drawing of the Gimballed Pendulum Energy Harvester

The technical drawings of the gimballed pendulum energy harvester can be found in Figures F.1 to F.13 and the DC generator detail is presented in Figures F.14 to F.23.

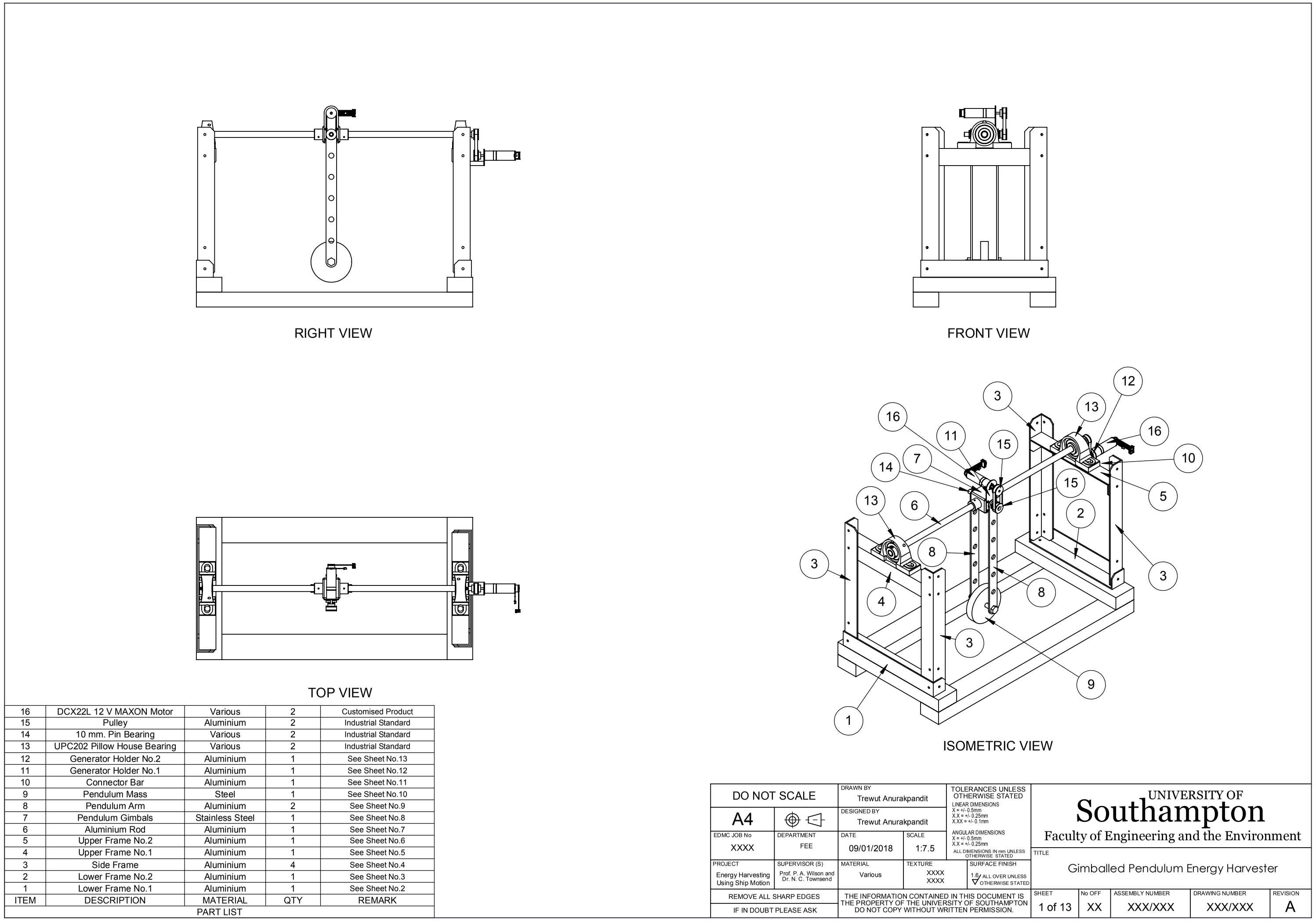

ITEM	DESCRIPTION	MATERIAL	QTY	REMARK
16	DCX22L 12 V MAXON Motor	Various	2	Customised Product
15	Pulley	Aluminium	2	Industrial Standard
14	10 mm. Pin Bearing	Various	2	Industrial Standard
13	UPC202 Pillow House Bearing	Various	2	Industrial Standard
12	Generator Holder No.2	Aluminium	1	See Sheet No.13
11	Generator Holder No.1	Aluminium	1	See Sheet No.12
10	Connector Bar	Aluminium	1	See Sheet No.11
9	Pendulum Mass	Steel	1	See Sheet No.10
8	Pendulum Arm	Aluminium	2	See Sheet No.9
7	Pendulum Gimbals	Stainless Steel	1	See Sheet No.8
6	Aluminium Rod	Aluminium	1	See Sheet No.7
5	Upper Frame No.2	Aluminium	1	See Sheet No.6
4	Upper Frame No.1	Aluminium	1	See Sheet No.5
3	Side Frame	Aluminium	4	See Sheet No.4
2	Lower Frame No.2	Aluminium	1	See Sheet No.3
1	Lower Frame No.1	Aluminium	1	See Sheet No.2

PART LIST

DO NOT SCALE
A4
DRAWN BY Trewut Anurakpandit
DESIGNED BY Trewut Anurakpandit
EDMC JOB No XXXX
DEPARTMENT FEE
DATE 09/01/2018
SCALE 1:7.5
TOLERANCES UNLESS OTHERWISE STATED
LINEAR DIMENSIONS
X = +/- 0.5mm
X.X = +/- 0.25mm
X.XX = +/- 0.1mm
ANGULAR DIMENSIONS
X = +/- 0.5mm
X.X = +/- 0.25mm
ALL DIMENSIONS IN mm UNLESS OTHERWISE STATED
PROJECT Energy Harvesting Using Ship Motion
SUPERVISOR (S) Prof. P. A. Wilson and Dr. N. C. Townsend
MATERIAL Various
TEXTURE XXXX XXXX
SURFACE FINISH 1.6 ALL OVER UNLESS OTHERWISE STATED
REMOVE ALL SHARP EDGES
IF IN DOUBT PLEASE ASK
THE INFORMATION CONTAINED IN THIS DOCUMENT IS THE PROPERTY OF THE UNIVERSITY OF SOUTHAMPTON DO NOT COPY WITHOUT WRITTEN PERMISSION.
UNIVERSITY OF Southampton
Faculty of Engineering and the Environment
TITLE Gimballed Pendulum Energy Harvester
SHEET 1 of 13
No OFF XX
ASSEMBLY NUMBER XXX/XXX
DRAWING NUMBER XXX/XXX
REVISION A

Figure F.1: General assembly of a gimballed pendulum energy harvester prototype.

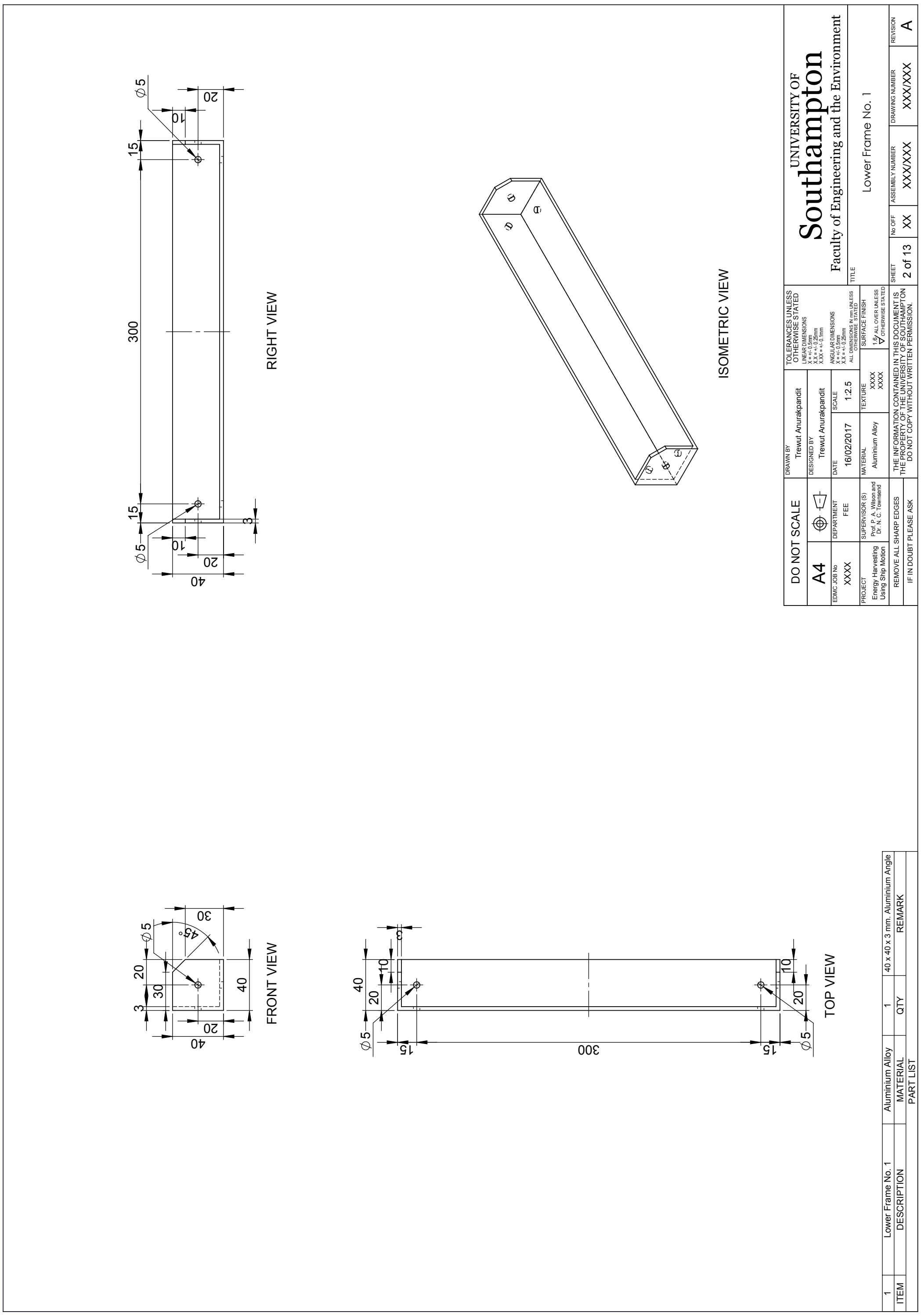

Figure F.2: Lower frame no.1.

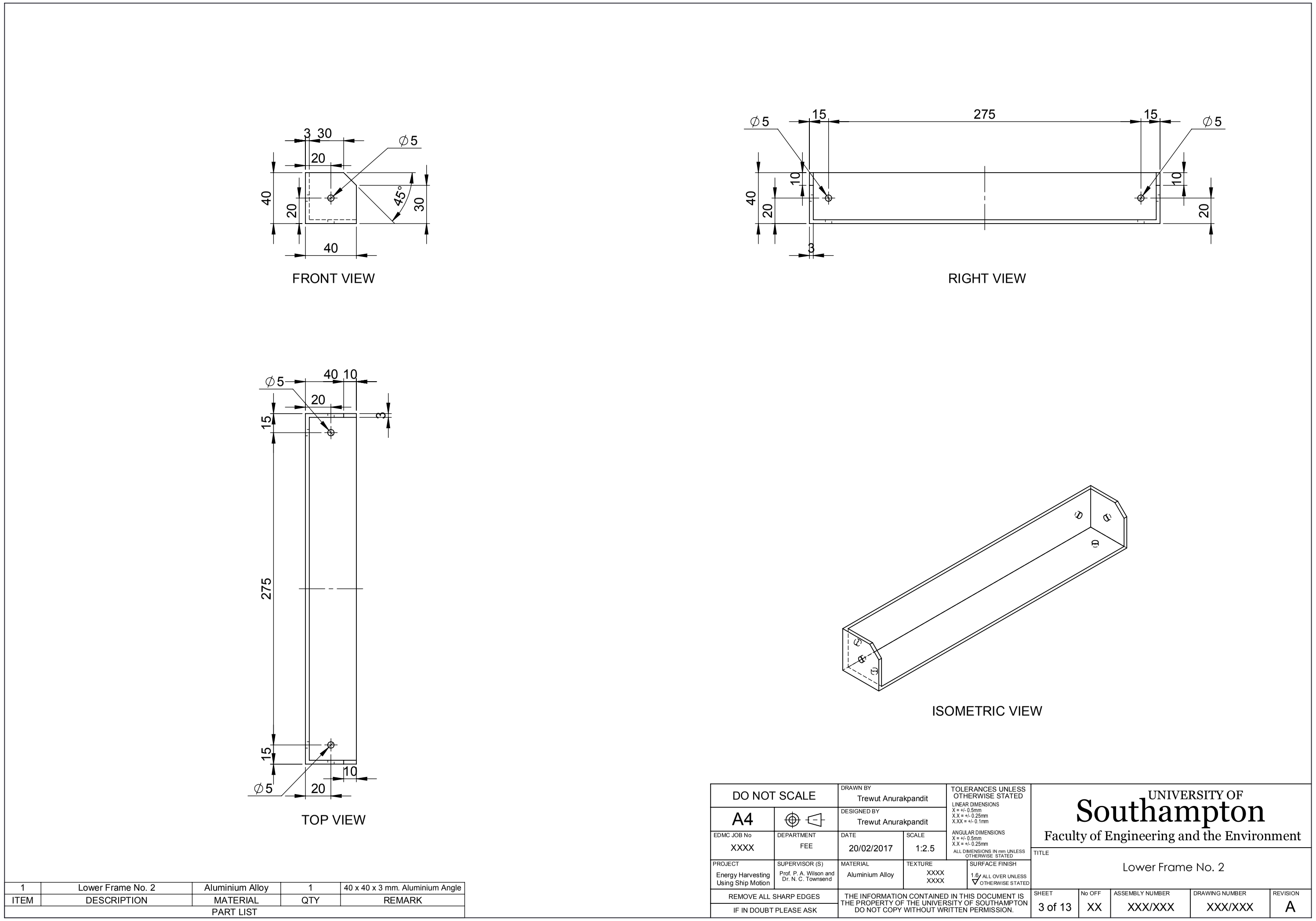

Figure F.3: Lower frame no.2.

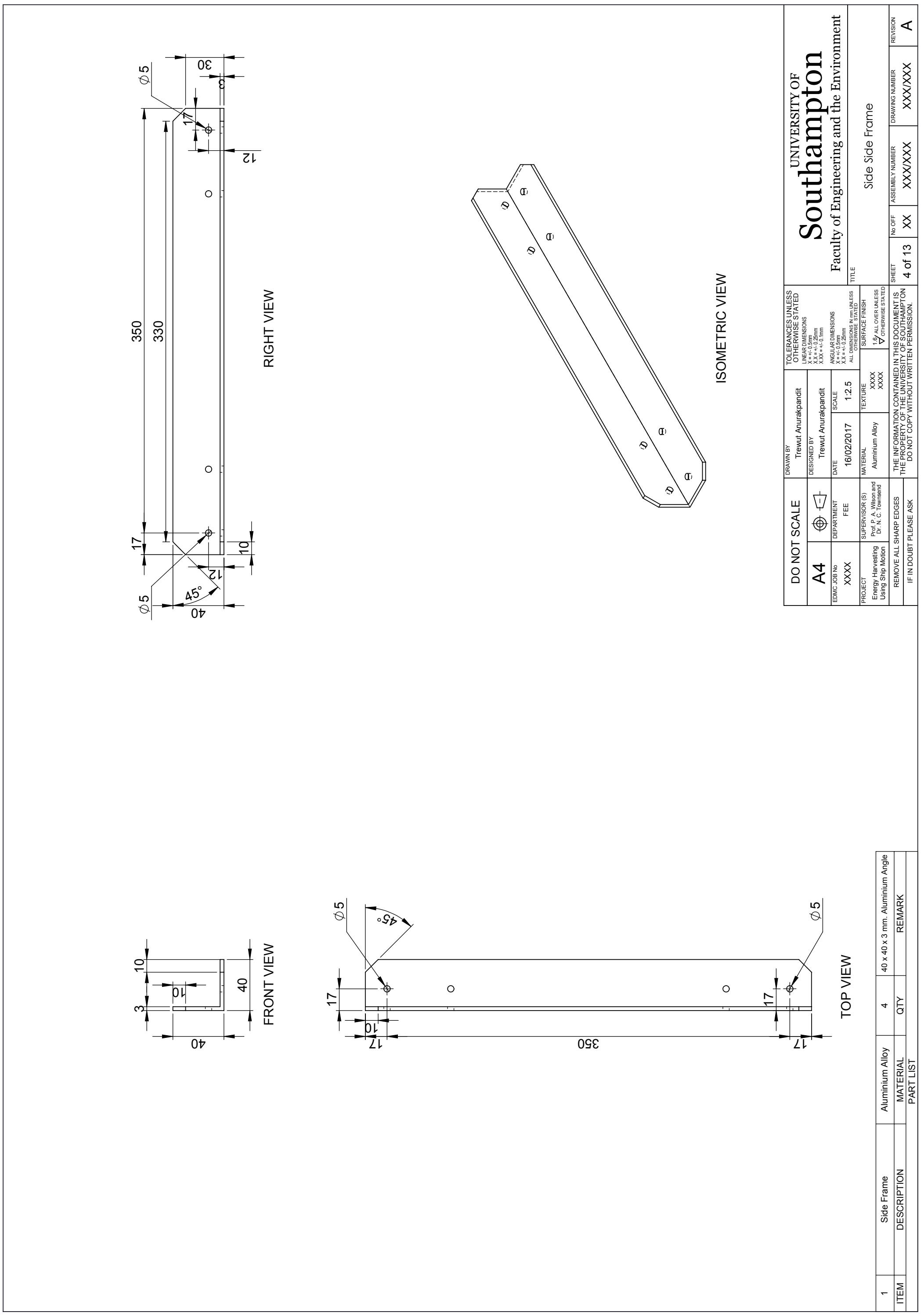

Figure F.4: Side frame.

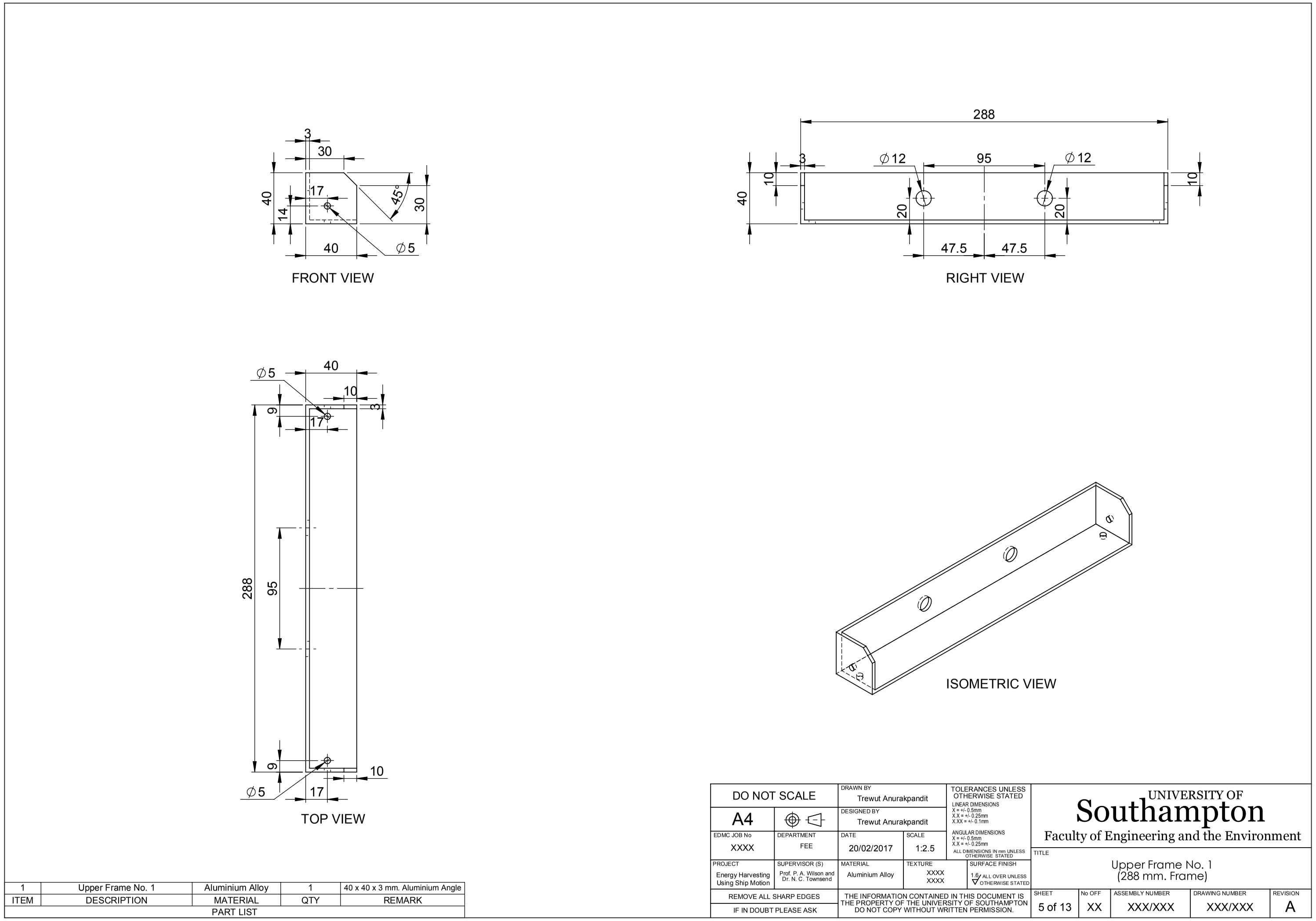

Figure F.5: Upper frame no.1.

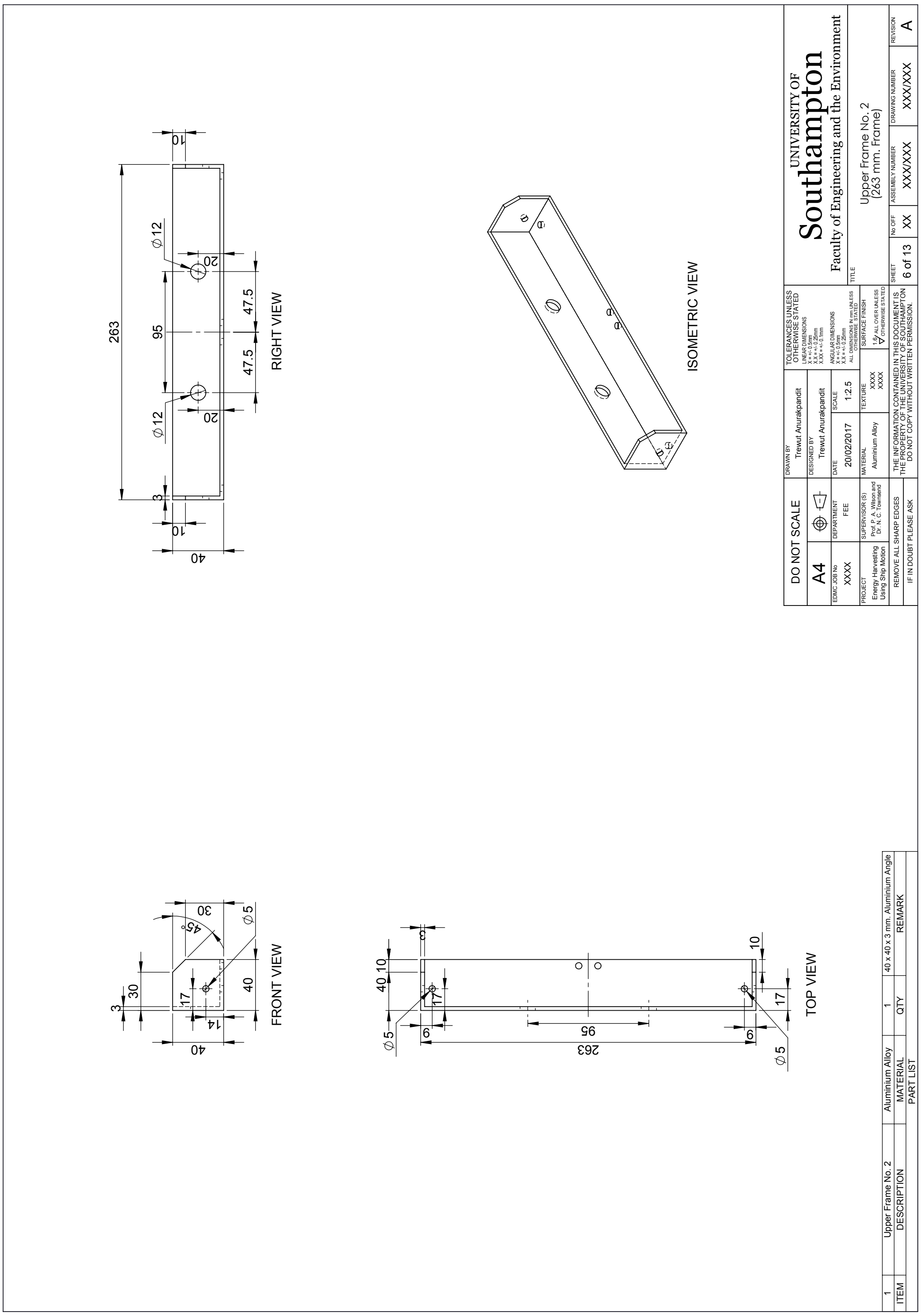

Figure F.6: Upper frame no.2.

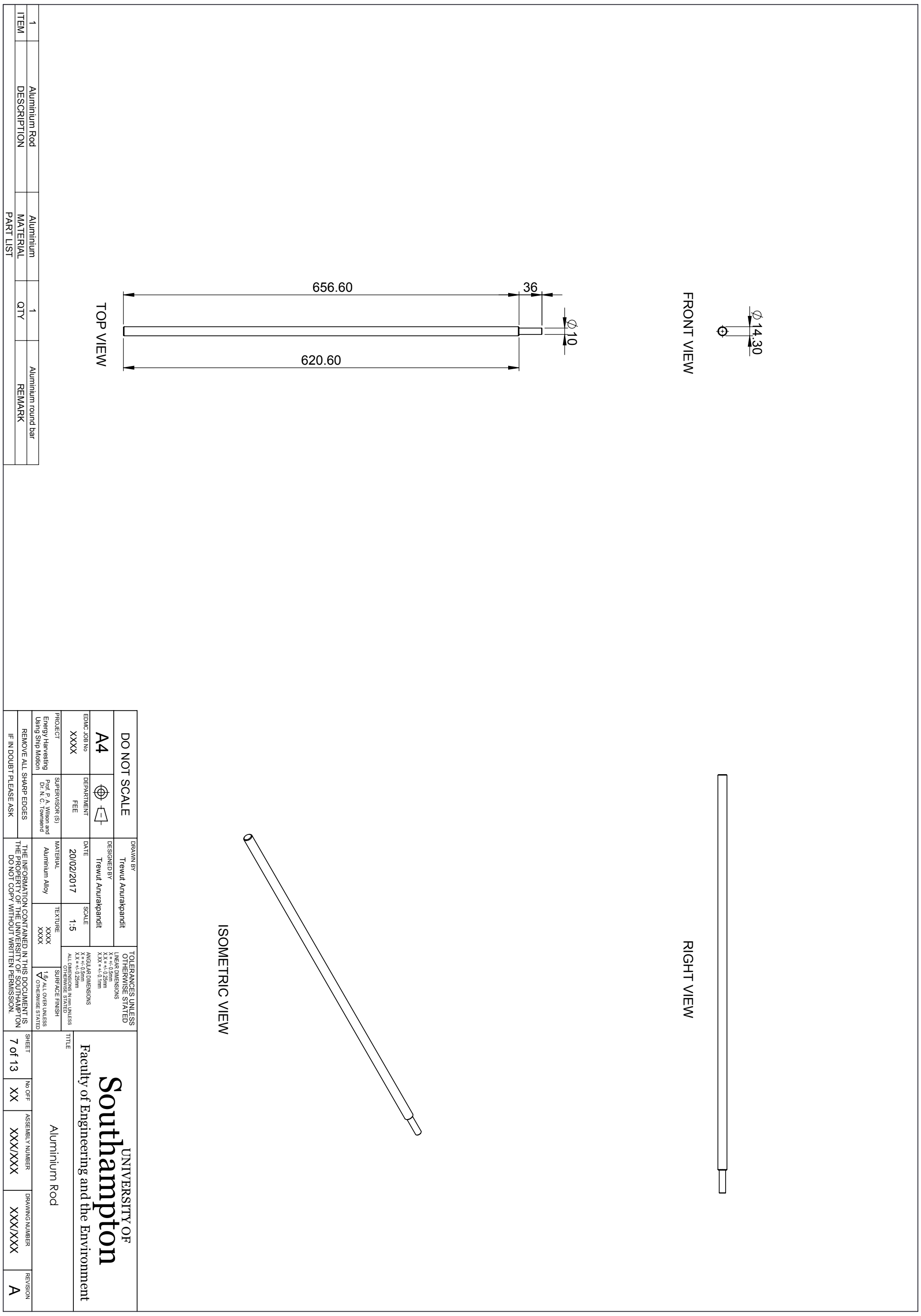

Figure F.7: Aluminium rod.

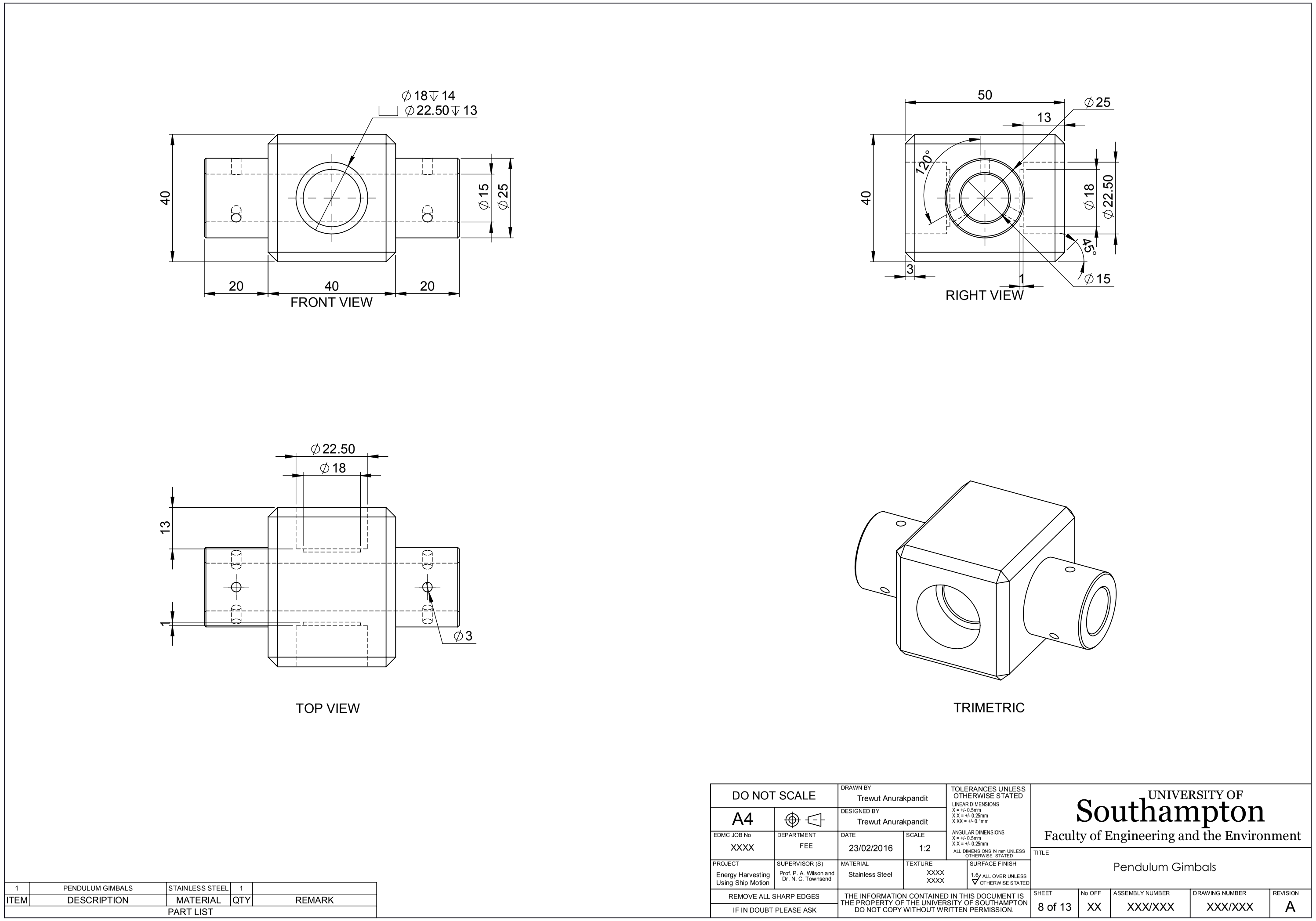

Figure F.8: Pendulum gimbals.

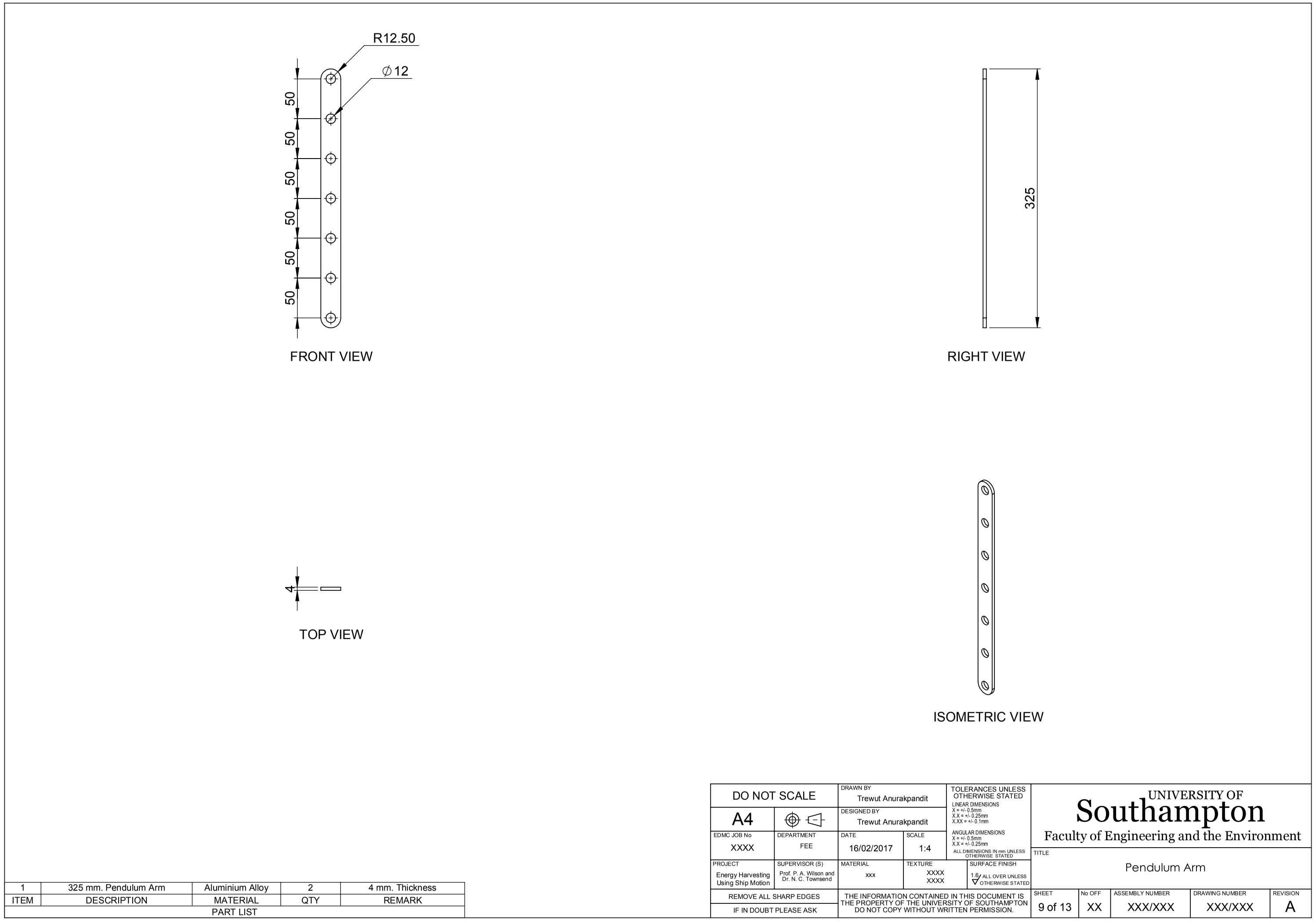

Figure F.9: Pendulum arm.

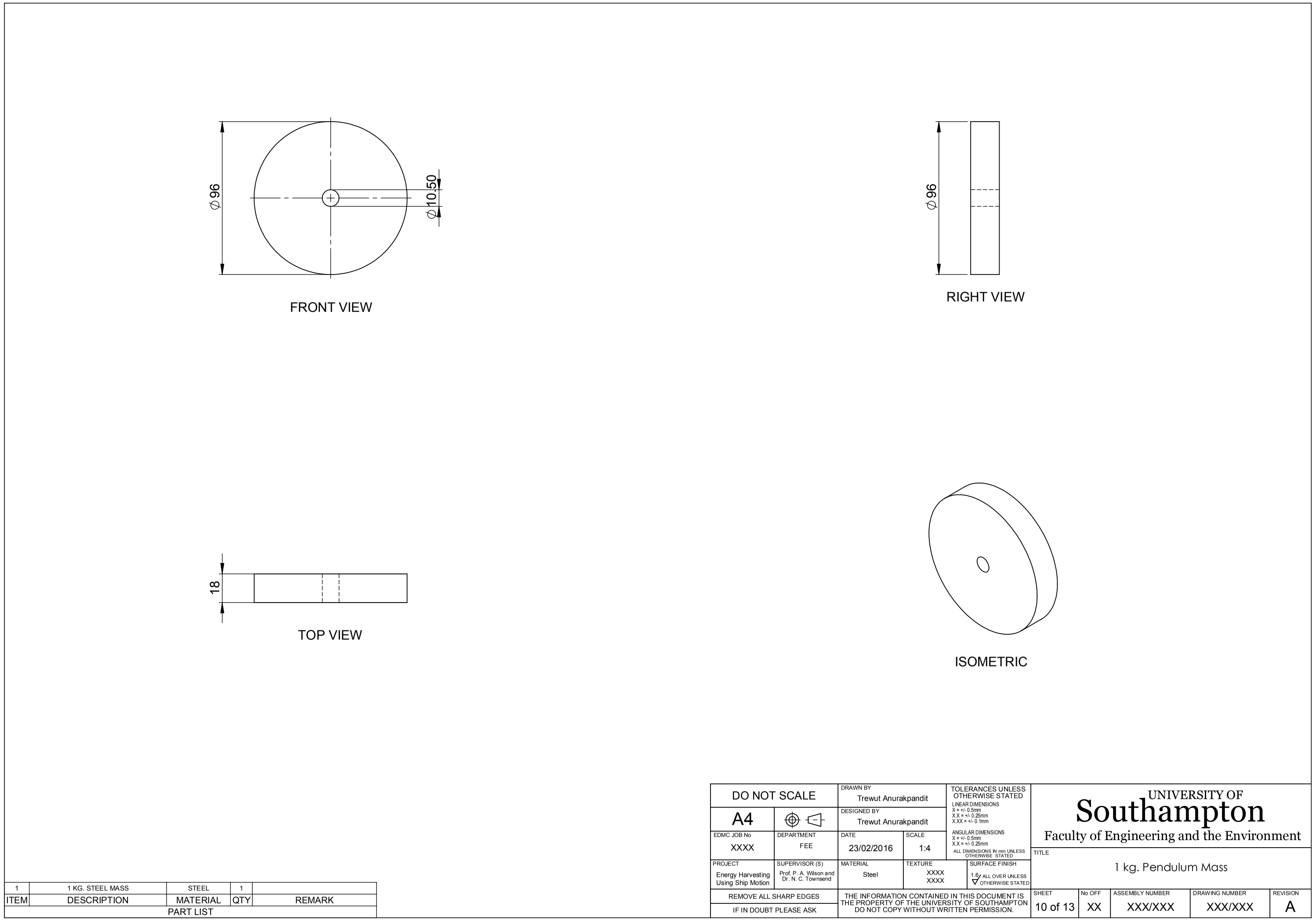

Figure F.10: Pendulum mass.

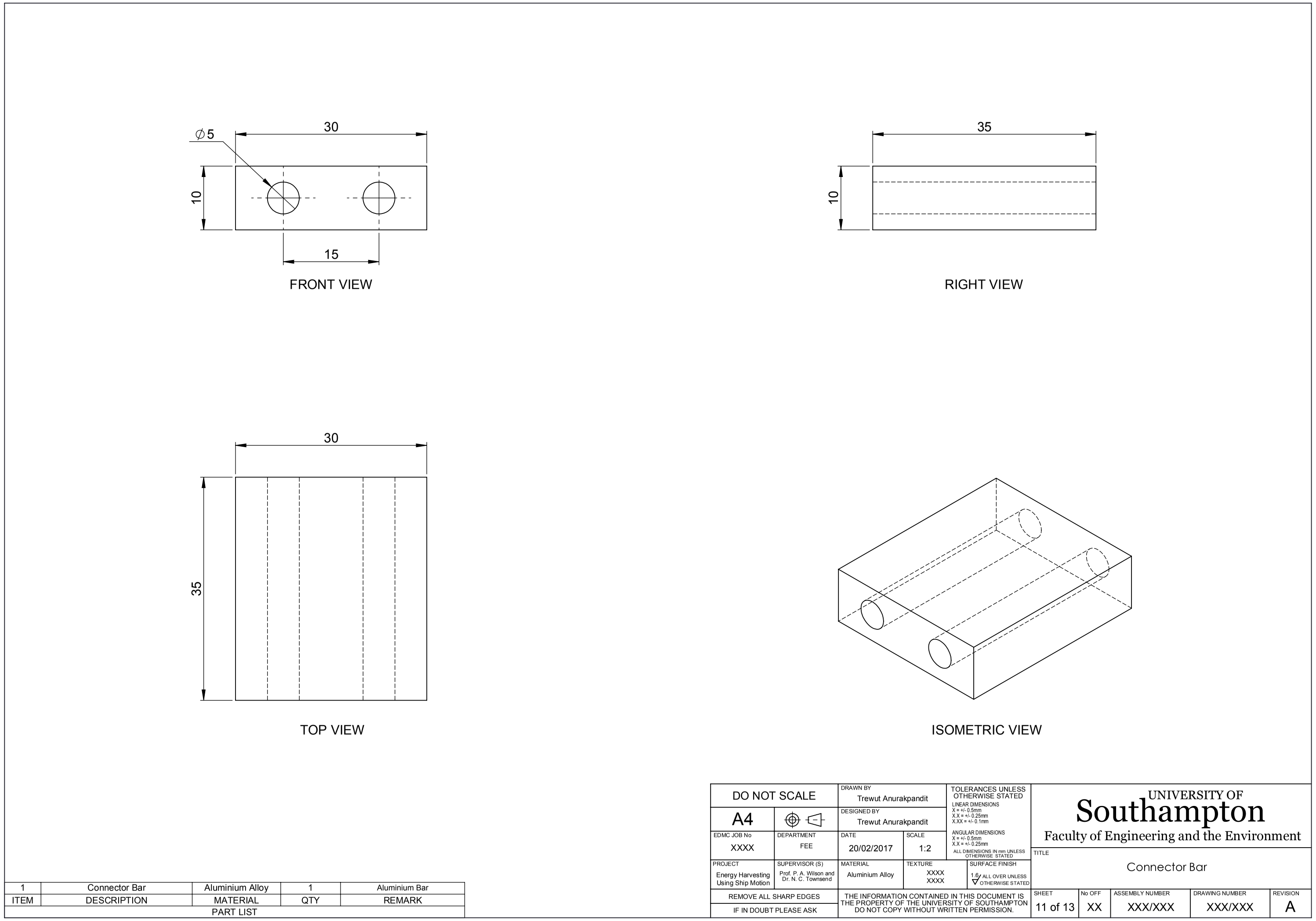

ITEM	DESCRIPTION	MATERIAL	QTY	REMARK
1	Connector Bar	Aluminium Alloy	1	Aluminium Bar

PART LIST

DO NOT SCALE
A4
DRAWN BY Trewut Anurakpandit
DESIGNED BY Trewut Anurakpandit
EDMC JOB No XXXX
DEPARTMENT FEE
DATE 20/02/2017
SCALE 1:2
TOLERANCES UNLESS OTHERWISE STATED
LINEAR DIMENSIONS
X = +/- 0.5mm
X.X = +/- 0.25mm
X.XX = +/- 0.1mm
ANGULAR DIMENSIONS
X = +/- 0.5mm
X.X = +/- 0.25mm
ALL DIMENSIONS IN mm UNLESS OTHERWISE STATED
PROJECT Energy Harvesting Using Ship Motion
SUPERVISOR (S) Prof. P. A. Wilson and Dr. N. C. Townsend
MATERIAL Aluminium Alloy
TEXTURE XXXX XXXX
SURFACE FINISH 1.6 ALL OVER UNLESS OTHERWISE STATED
REMOVE ALL SHARP EDGES
IF IN DOUBT PLEASE ASK
THE INFORMATION CONTAINED IN THIS DOCUMENT IS THE PROPERTY OF THE UNIVERSITY OF SOUTHAMPTON DO NOT COPY WITHOUT WRITTEN PERMISSION.
UNIVERSITY OF Southampton
Faculty of Engineering and the Environment
TITLE Connector Bar
SHEET 11 of 13
No OFF XX
ASSEMBLY NUMBER XXX/XXX
DRAWING NUMBER XXX/XXX
REVISION A

Figure F.11: Connector bar.

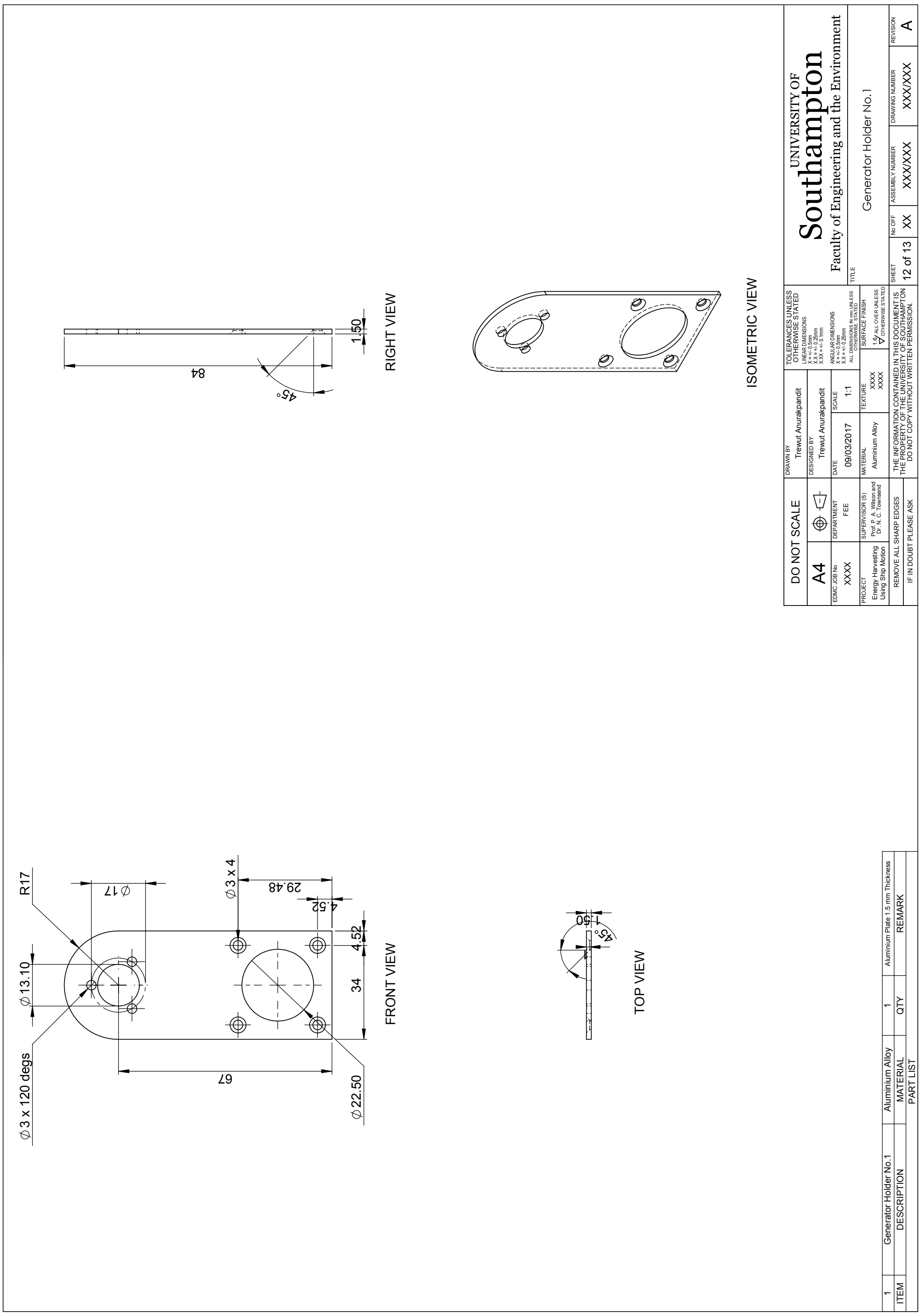

Figure F.12: Generator holder no.1.

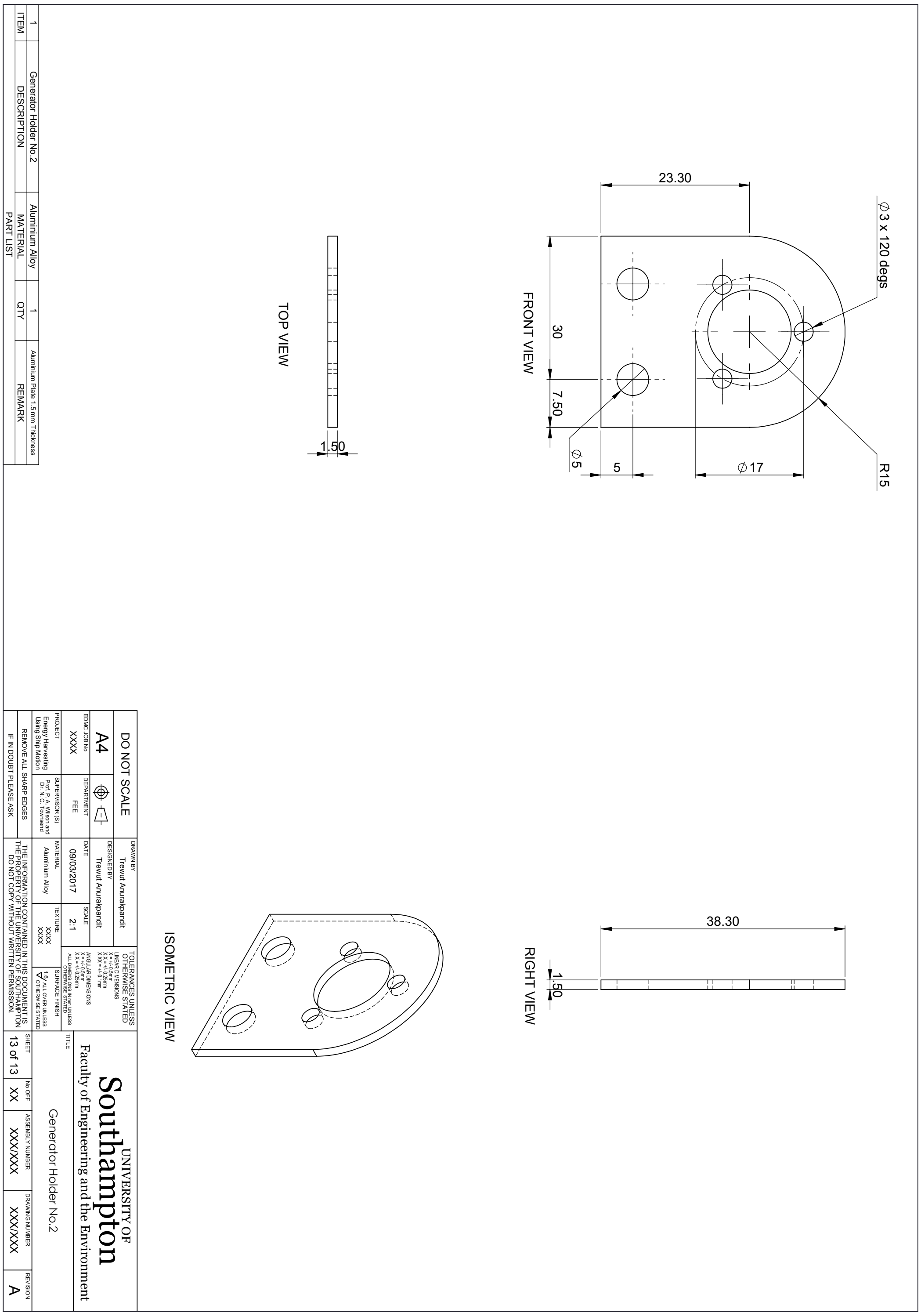

Figure F.13: Generator holder no.2.

maxon motor
driven by precision

Configured drive

Motor - DCX22L EB KL 12V
Planetary gearhead - GPX22 A 44:1
Sensor - ENX16 EASY 1024IMP

Part number: B772A87E4A0B Revision number 1

Orders are processed and shipped from Switzerland within 11 working days.
General Terms and Conditions: https://www.maxonmotor.ch/maxon/view/content/terms_and_conditions_page

To open the integrated CAD file, please save this document and open it in Acrobat Reader. The STEP file is available after a double-click on the pin icon.

B772A87E4A0B.stp (STP AP 214)

Open configuration: http://www.maxonmotor.ch/maxon/view/configurator/?ConfigID=B772A87E4A0B

05.10.2018 / Subject to change without notice / Part number: B772A87E4A0B / Revision number: 1 1 / 10

Figure F.14: Generator detail - 1.

Motor - DCX22L EB KL 12V
Planetary gearhead - GPX22 A 44:1
Sensor - ENX16 EASY 1024IMP

Drawing not to scale!

ISO 5456-1

maxon motor
driven by precision

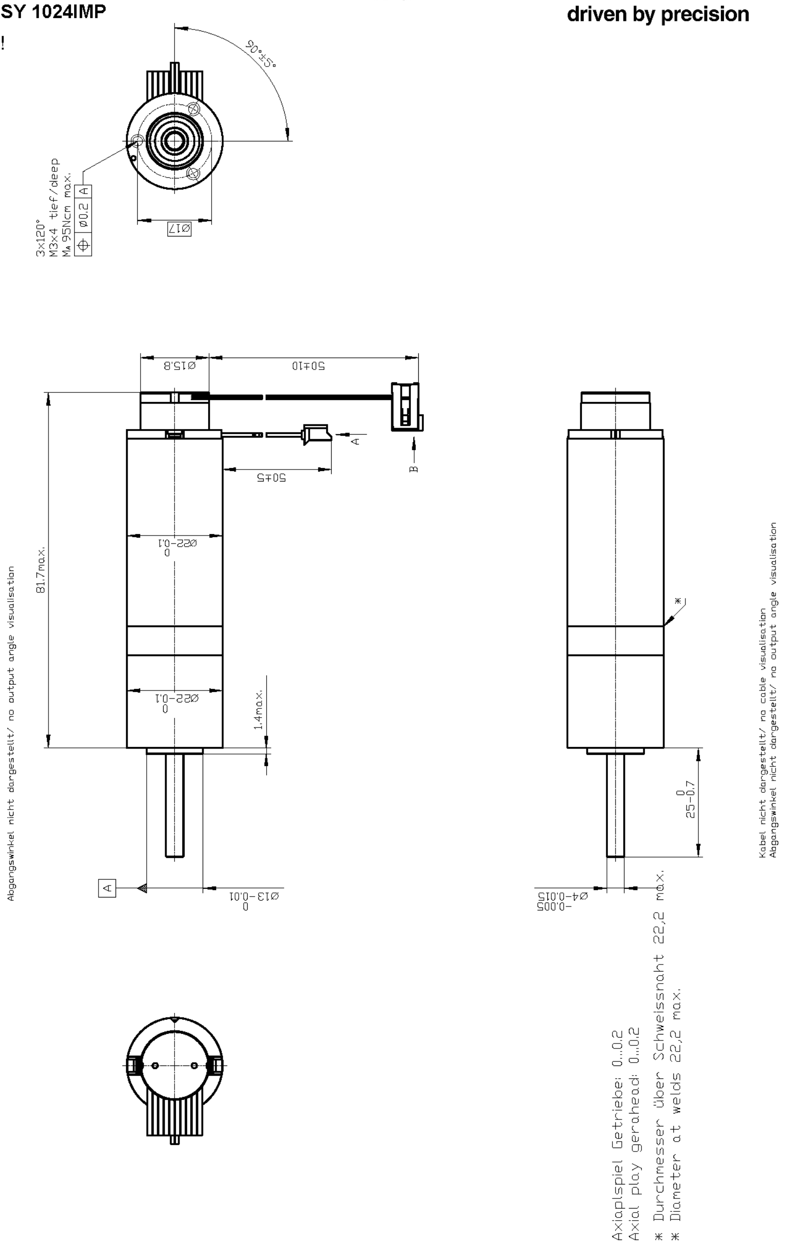

05.10.2018 / Subject to change without notice / Part number: B772A87E4A0B / Revision number: 1 2 / 10

Figure F.15: Generator detail - 2.

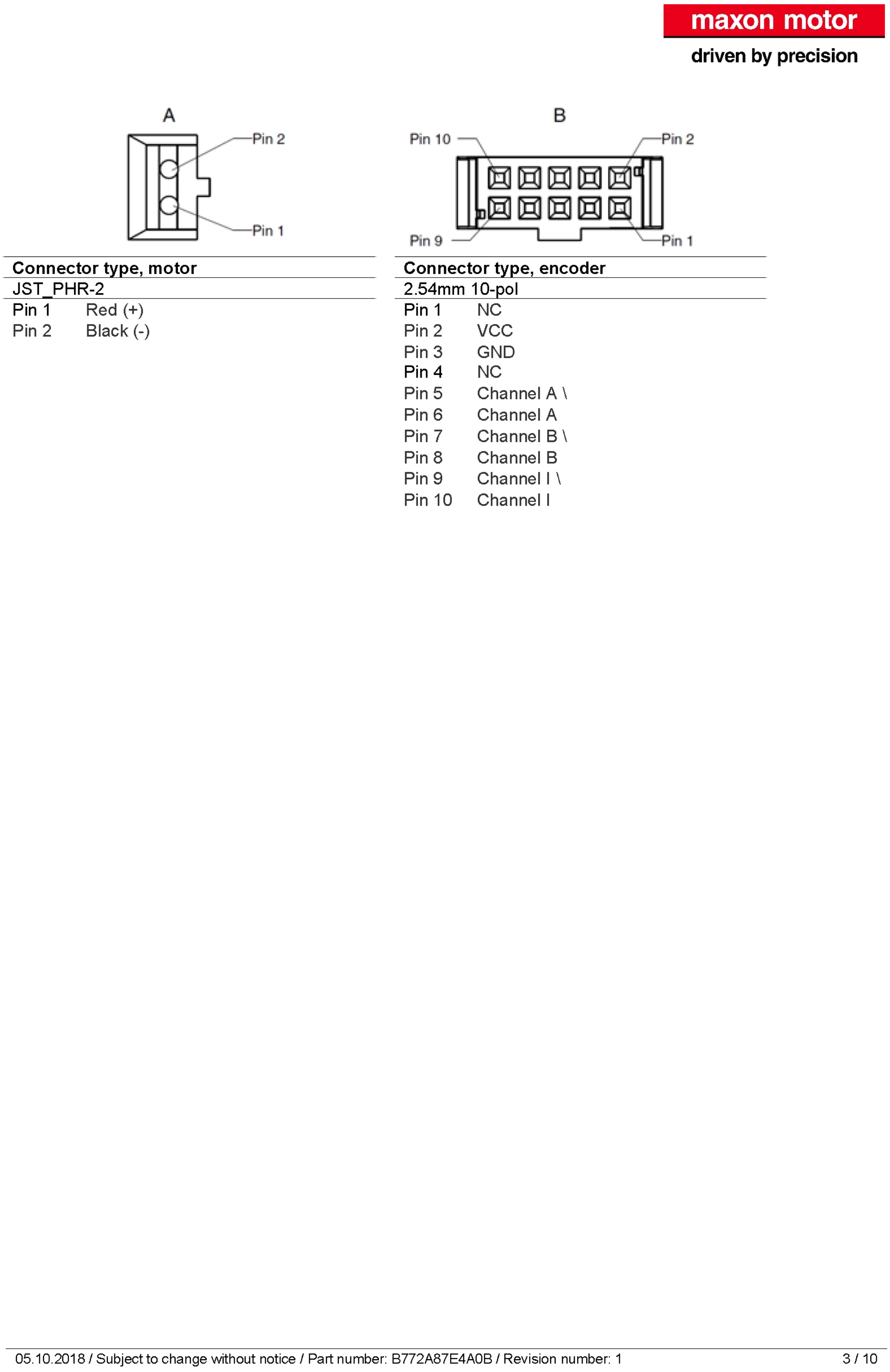

Connector type, motor	
JST_PHR-2	
Pin 1	Red (+)
Pin 2	Black (-)

Connector type, encoder	
2.54mm 10-pol	
Pin 1	NC
Pin 2	VCC
Pin 3	GND
Pin 4	NC
Pin 5	Channel A \
Pin 6	Channel A
Pin 7	Channel B \
Pin 8	Channel B
Pin 9	Channel I \
Pin 10	Channel I

05.10.2018 / Subject to change without notice / Part number: B772A87E4A0B / Revision number: 1 3 / 10

Figure F.16: Generator detail - 3.

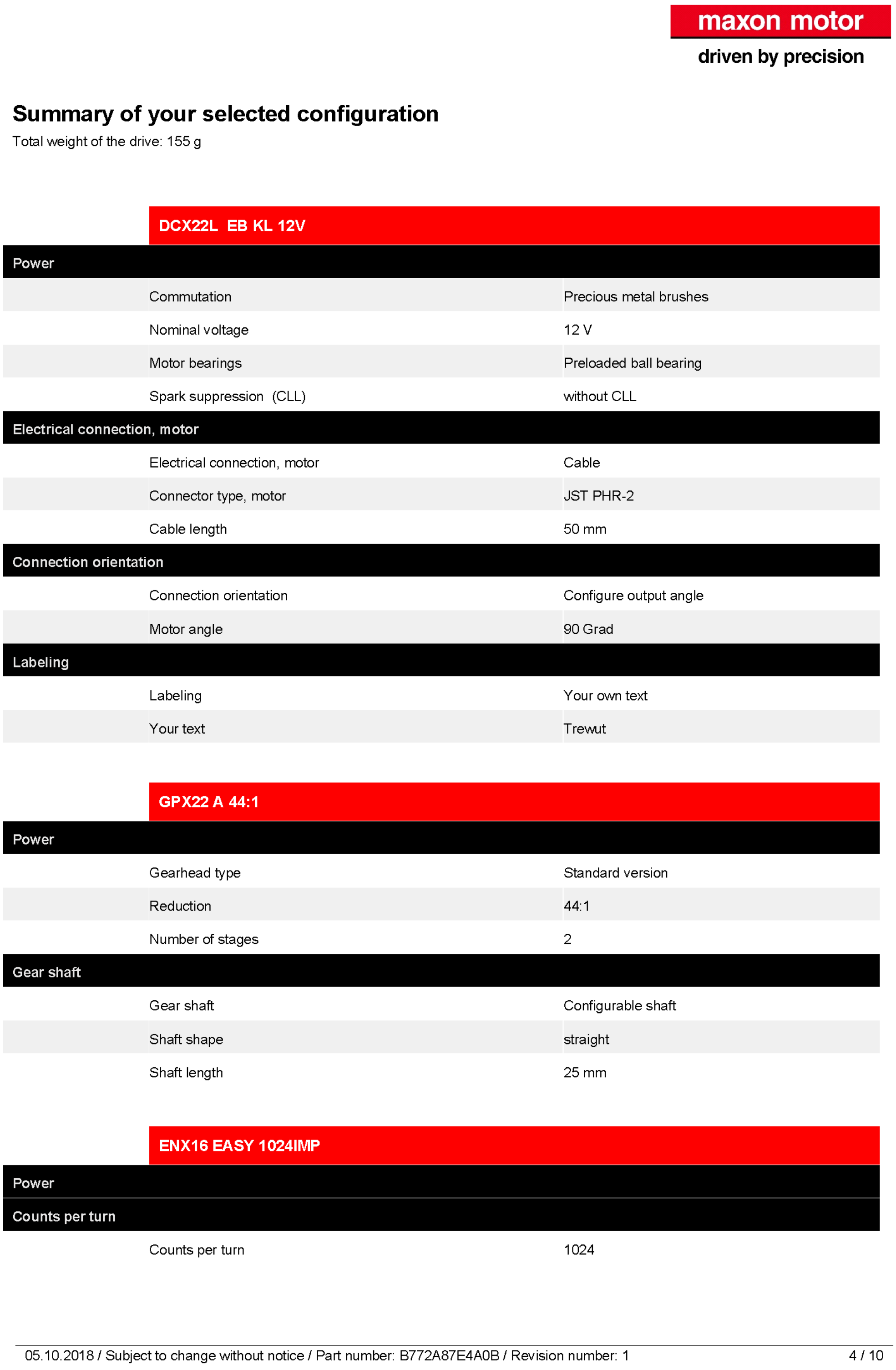

maxon motor
driven by precision

Summary of your selected configuration

Total weight of the drive: 155 g

DCX22L EB KL 12V

Power		
	Commutation	Precious metal brushes
	Nominal voltage	12 V
	Motor bearings	Preloaded ball bearing
	Spark suppression (CLL)	without CLL
Electrical connection, motor		
	Electrical connection, motor	Cable
	Connector type, motor	JST PHR-2
	Cable length	50 mm
Connection orientation		
	Connection orientation	Configure output angle
	Motor angle	90 Grad
Labeling		
	Labeling	Your own text
	Your text	Trewut

GPX22 A 44:1

Power		
	Gearhead type	Standard version
	Reduction	44:1
	Number of stages	2
Gear shaft		
	Gear shaft	Configurable shaft
	Shaft shape	straight
	Shaft length	25 mm

ENX16 EASY 1024IMP

Power		
Counts per turn		
	Counts per turn	1024

05.10.2018 / Subject to change without notice / Part number: B772A87E4A0B / Revision number: 1 4 / 10

Figure F.17: Generator detail - 4.

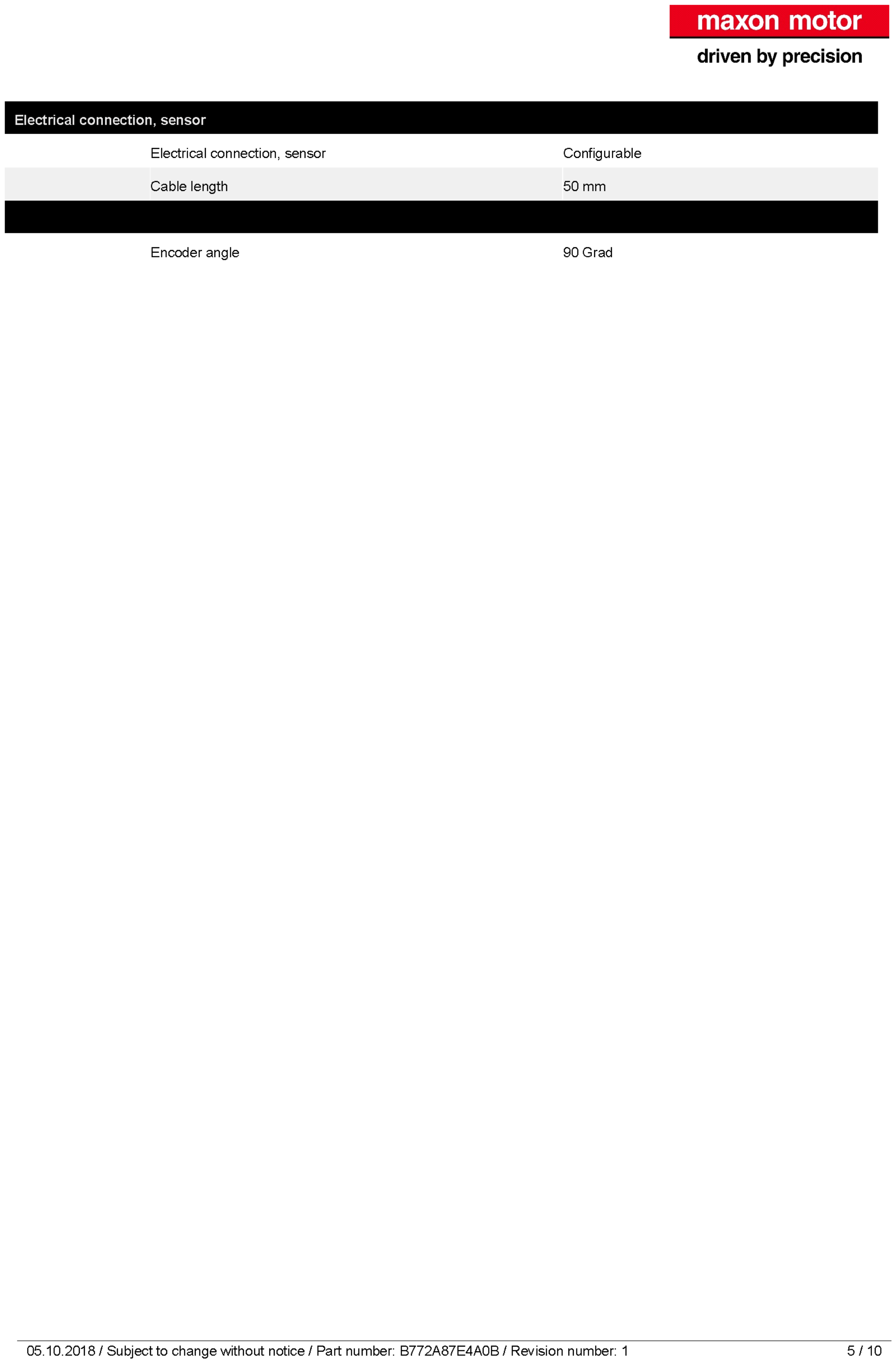

maxon motor
driven by precision

Electrical connection, sensor		
	Electrical connection, sensor	Configurable
	Cable length	50 mm
	Encoder angle	90 Grad

05.10.2018 / Subject to change without notice / Part number: B772A87E4A0B / Revision number: 1 5 / 10

Figure F.18: Generator detail - 5.

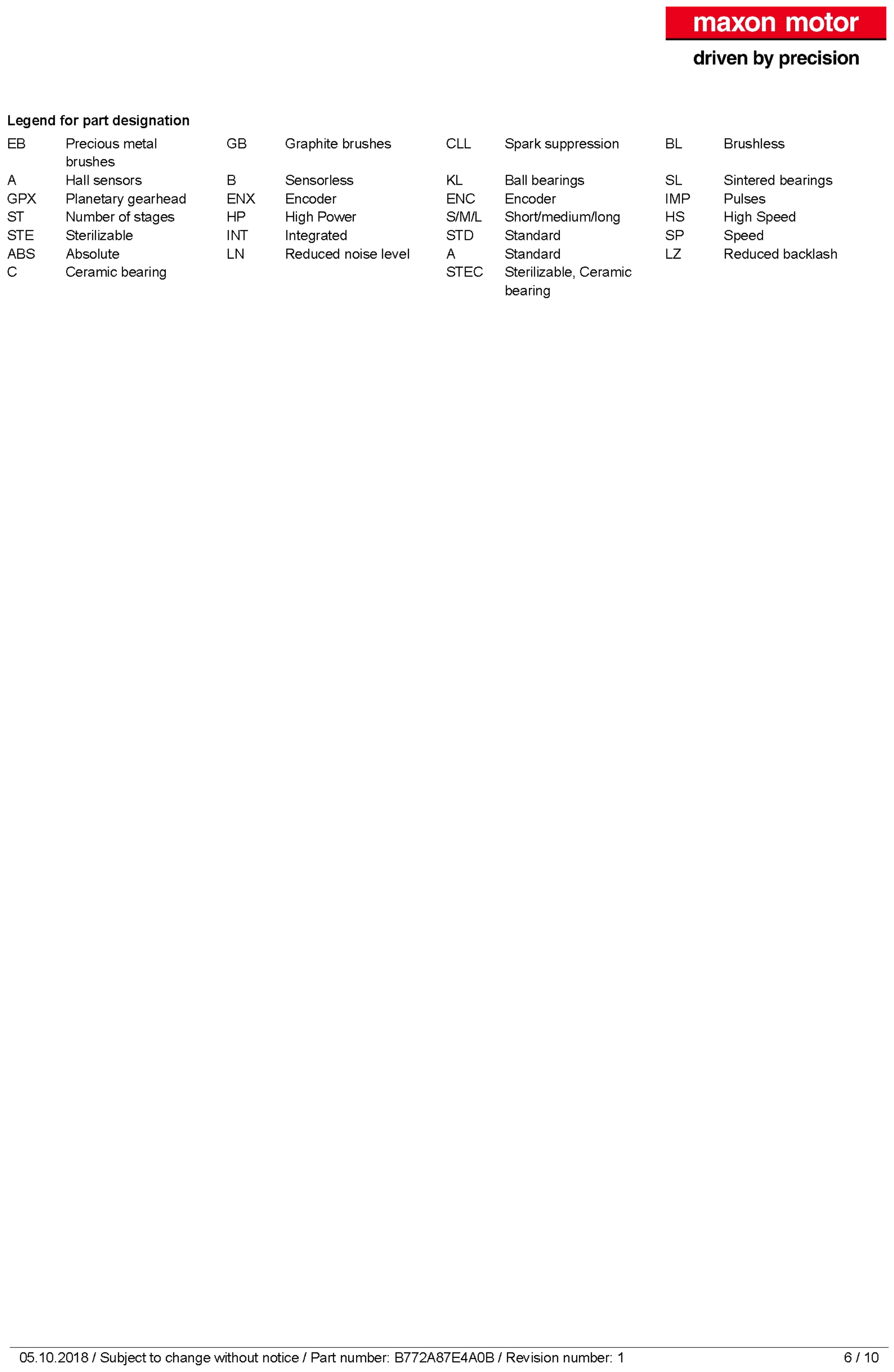

maxon motor
driven by precision

Legend for part designation

EB	Precious metal brushes	GB	Graphite brushes	CLL	Spark suppression	BL	Brushless
A	Hall sensors	B	Sensorless	KL	Ball bearings	SL	Sintered bearings
GPX	Planetary gearhead	ENX	Encoder	ENC	Encoder	IMP	Pulses
ST	Number of stages	HP	High Power	S/M/L	Short/medium/long	HS	High Speed
STE	Sterilizable	INT	Integrated	STD	Standard	SP	Speed
ABS	Absolute	LN	Reduced noise level	A	Standard	LZ	Reduced backlash
C	Ceramic bearing			STEC	Sterilizable, Ceramic bearing		

05.10.2018 / Subject to change without notice / Part number: B772A87E4A0B / Revision number: 1 6 / 10

Figure F.19: Generator detail - 6.

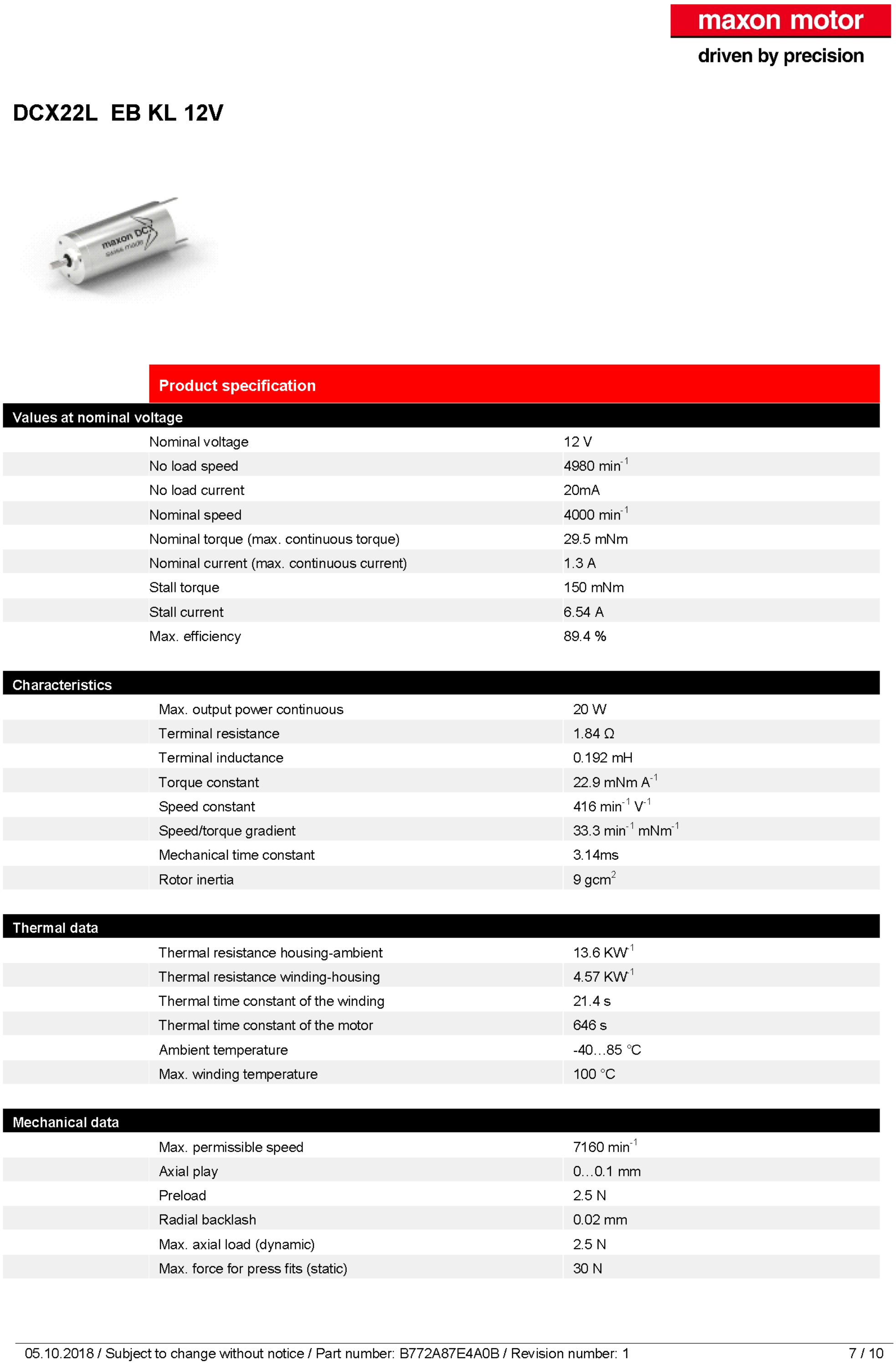

maxon motor
driven by precision

DCX22L EB KL 12V

Product specification

Values at nominal voltage	
Nominal voltage	12 V
No load speed	4980 min^{-1}
No load current	20mA
Nominal speed	4000 min^{-1}
Nominal torque (max. continuous torque)	29.5 mNm
Nominal current (max. continuous current)	1.3 A
Stall torque	150 mNm
Stall current	6.54 A
Max. efficiency	89.4 %

Characteristics	
Max. output power continuous	20 W
Terminal resistance	1.84 Ω
Terminal inductance	0.192 mH
Torque constant	22.9 mNm A^{-1}
Speed constant	416 min^{-1} V^{-1}
Speed/torque gradient	33.3 min^{-1} mNm^{-1}
Mechanical time constant	3.14ms
Rotor inertia	9 gcm^{2}

Thermal data	
Thermal resistance housing-ambient	13.6 KW^{-1}
Thermal resistance winding-housing	4.57 KW^{-1}
Thermal time constant of the winding	21.4 s
Thermal time constant of the motor	646 s
Ambient temperature	-40…85 °C
Max. winding temperature	100 °C

Mechanical data	
Max. permissible speed	7160 min^{-1}
Axial play	0…0.1 mm
Preload	2.5 N
Radial backlash	0.02 mm
Max. axial load (dynamic)	2.5 N
Max. force for press fits (static)	30 N

05.10.2018 / Subject to change without notice / Part number: B772A87E4A0B / Revision number: 1 7 / 10

Figure F.20: Generator detail - 7.

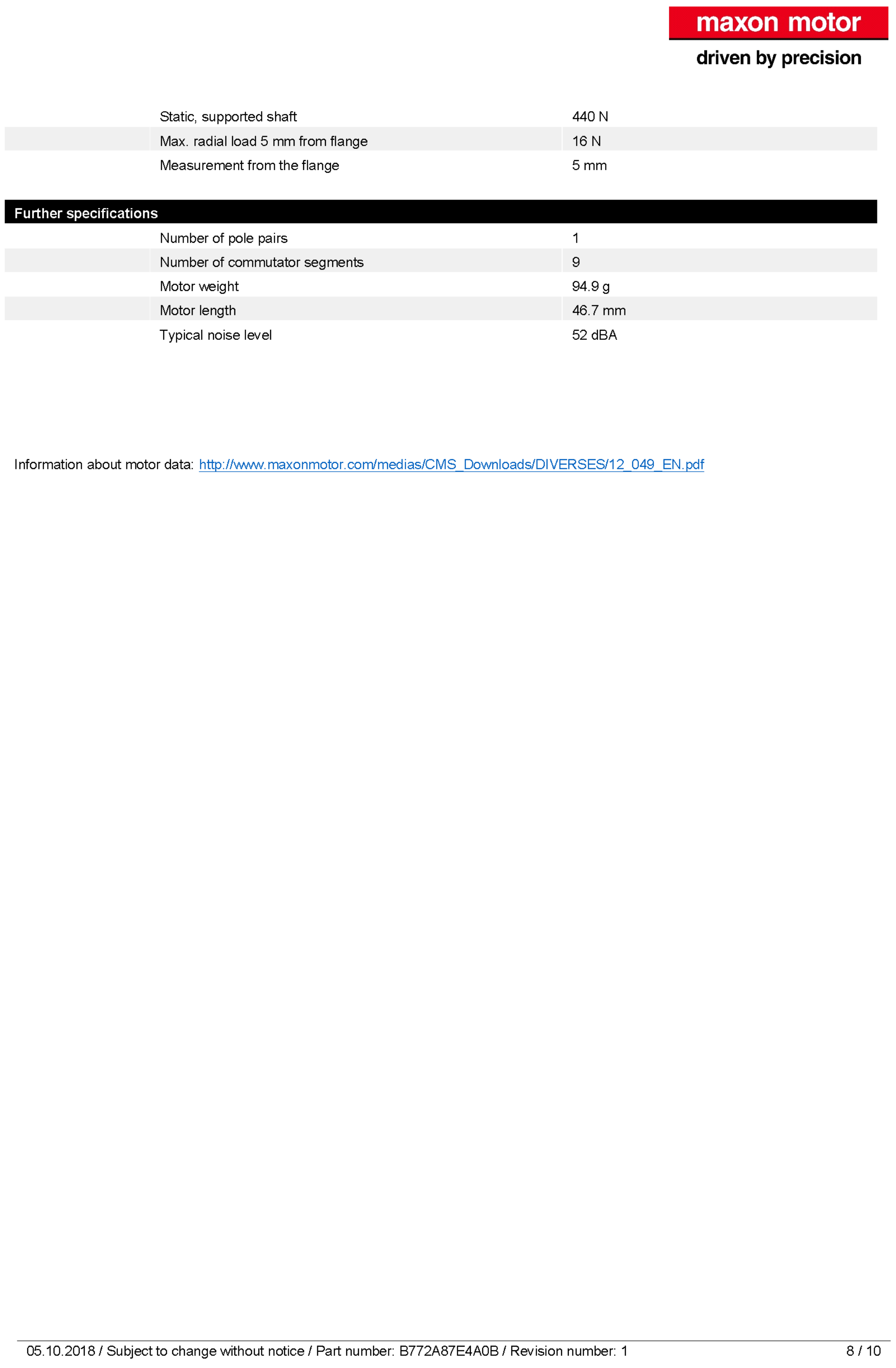

maxon motor
driven by precision

Static, supported shaft	440 N
Max. radial load 5 mm from flange	16 N
Measurement from the flange	5 mm

Further specifications	
Number of pole pairs	1
Number of commutator segments	9
Motor weight	94.9 g
Motor length	46.7 mm
Typical noise level	52 dBA

Information about motor data: http://www.maxonmotor.com/medias/CMS_Downloads/DIVERSES/12_049_EN.pdf

05.10.2018 / Subject to change without notice / Part number: B772A87E4A0B / Revision number: 1 8 / 10

Figure F.21: Generator detail - 8.

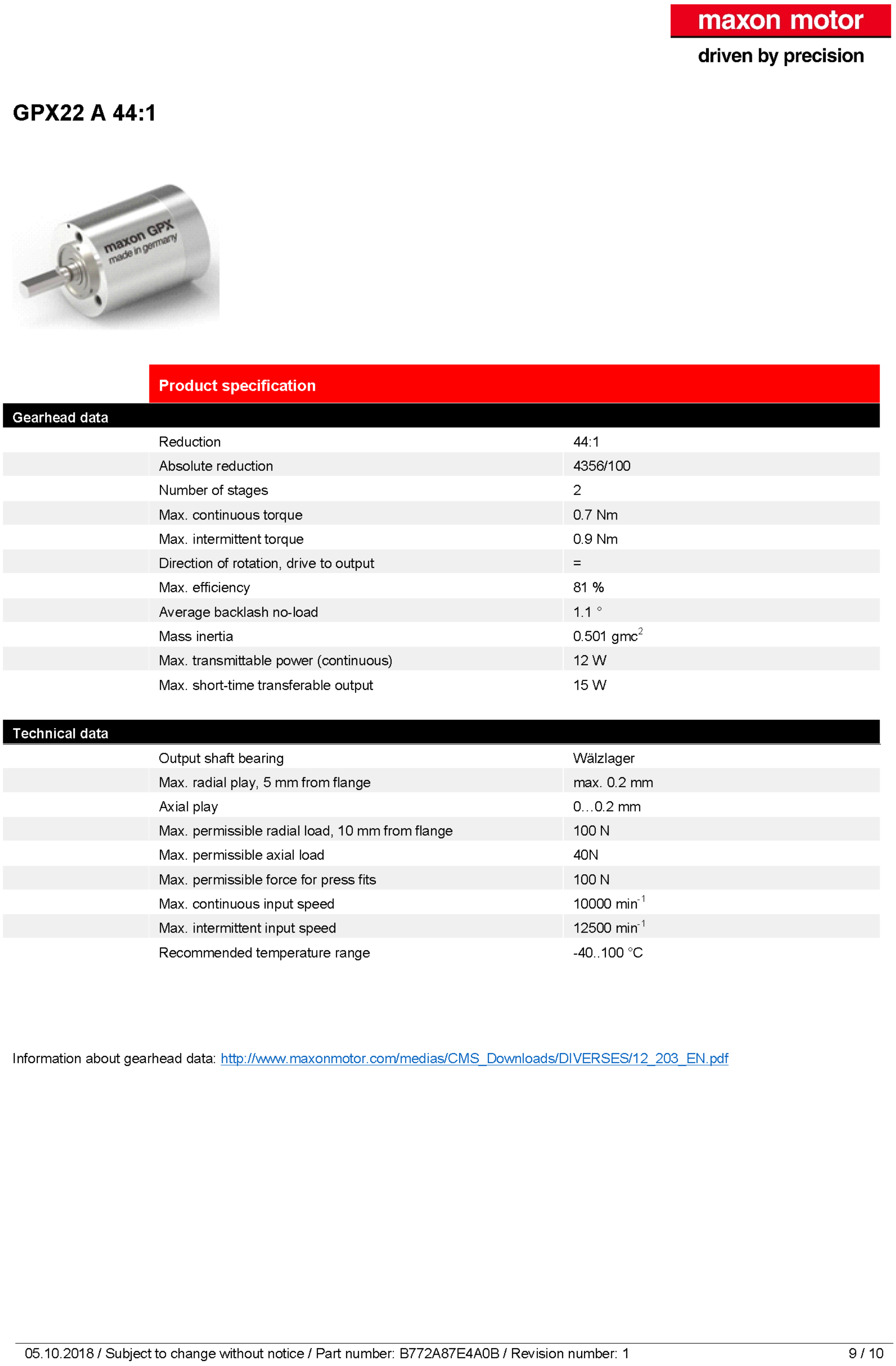

maxon motor
driven by precision

GPX22 A 44:1

Product specification

Gearhead data	
Reduction	44:1
Absolute reduction	4356/100
Number of stages	2
Max. continuous torque	0.7 Nm
Max. intermittent torque	0.9 Nm
Direction of rotation, drive to output	=
Max. efficiency	81 %
Average backlash no-load	1.1 °
Mass inertia	0.501 gcm^2
Max. transmittable power (continuous)	12 W
Max. short-time transferable output	15 W

Technical data	
Output shaft bearing	Wälzlager
Max. radial play, 5 mm from flange	max. 0.2 mm
Axial play	0...0.2 mm
Max. permissible radial load, 10 mm from flange	100 N
Max. permissible axial load	40N
Max. permissible force for press fits	100 N
Max. continuous input speed	10000 min^{-1}
Max. intermittent input speed	12500 min^{-1}
Recommended temperature range	-40..100 °C

Information about gearhead data: http://www.maxonmotor.com/medias/CMS_Downloads/DIVERSES/12_203_EN.pdf

05.10.2018 / Subject to change without notice / Part number: B772A87E4A0B / Revision number: 1 9 / 10

Figure F.22: Generator detail - 9.

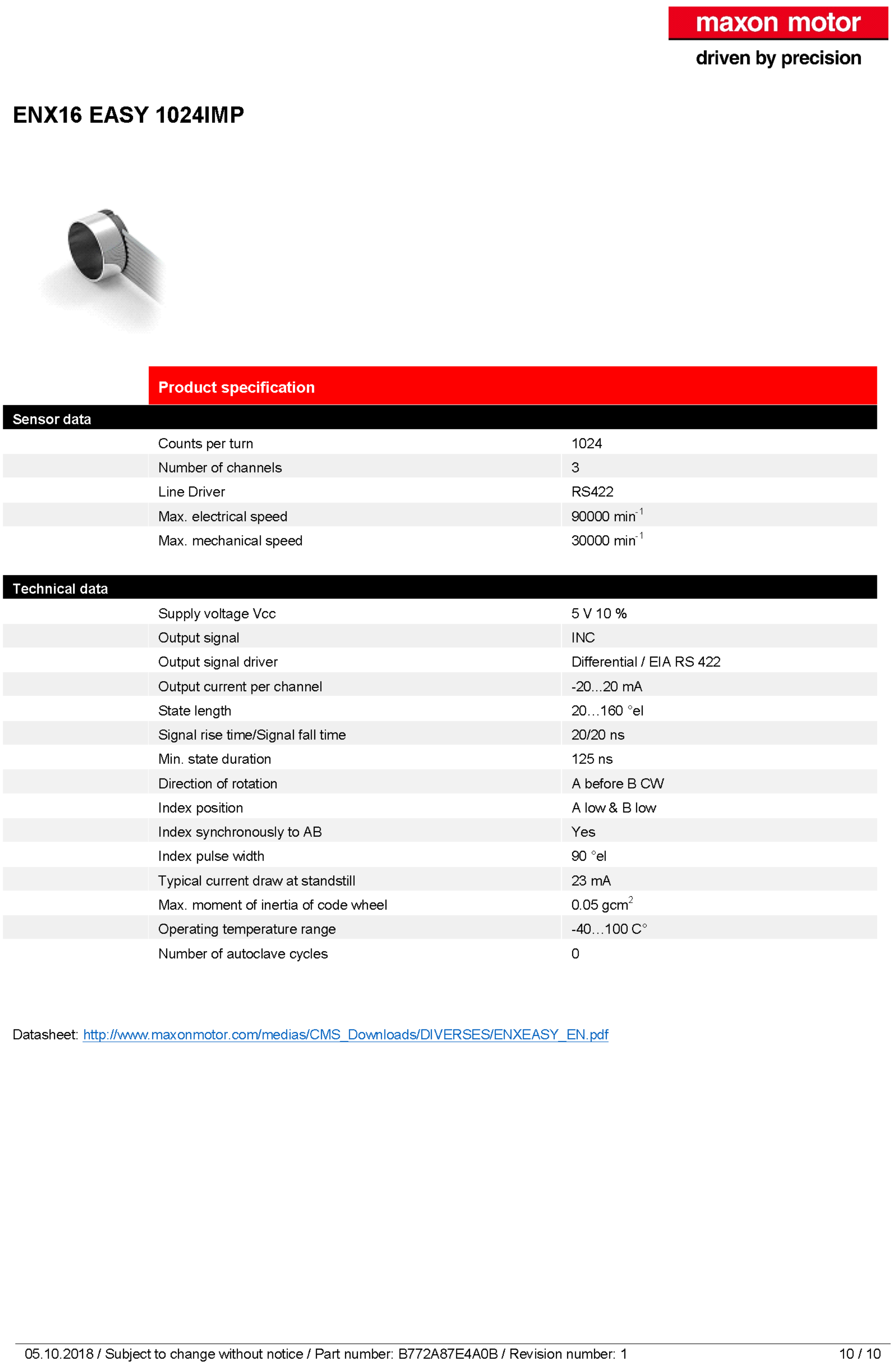

maxon motor
driven by precision

ENX16 EASY 1024IMP

Product specification

Sensor data

Counts per turn	1024
Number of channels	3
Line Driver	RS422
Max. electrical speed	90000 min^{-1}
Max. mechanical speed	30000 min^{-1}

Technical data

Supply voltage Vcc	5 V 10 %
Output signal	INC
Output signal driver	Differential / EIA RS 422
Output current per channel	-20...20 mA
State length	20…160 °el
Signal rise time/Signal fall time	20/20 ns
Min. state duration	125 ns
Direction of rotation	A before B CW
Index position	A low & B low
Index synchronously to AB	Yes
Index pulse width	90 °el
Typical current draw at standstill	23 mA
Max. moment of inertia of code wheel	0.05 gcm^2
Operating temperature range	-40…100 C°
Number of autoclave cycles	0

Datasheet: http://www.maxonmotor.com/medias/CMS_Downloads/DIVERSES/ENXEASY_EN.pdf

05.10.2018 / Subject to change without notice / Part number: B772A87E4A0B / Revision number: 1 10 / 10

Figure F.23: Generator detail - 10.

References

Anurakpandit, T., Townsend, N. C., and Wilson, P. A. The Numerical and Experimental Investigations of a Gimballed Pendulum Energy Harvester. *International Journal of Non-Linear Mechanics.*

Aqua-RET (2012). Aquatic Renewable Energy Technologies (Aqua-RET) Website (http://www.aquaret.com).

AutoNaut Ltd. (2018). AutoNaut - Wave Propelled Unmanned Surface Vessels (http://www.autonautusv.com).

AW-Energy Oy (2018). AW-Energy: WaveRoller - Plug into Wave Energy (http://aw-energy.com/waveroller/#technology).

Babarit, A. (2015). A Database of Capture Width Ratio of Wave Energy Converters. *Renewable Energy*, 80:610–628.

Bastankhah, M. and Porté-Agel, F. (2018). A New Miniature Wind Turbine for Wind Tunnel Experiments. Part I: Design and Performance. *Energies.*

Bentley Systems (2015a). *MAXSURF Modeller Program and User Manual.*

Bentley Systems (2015b). *MAXSURF Motions Program and User Manual.*

Bhattacharyya, R. (1978). *Dynamics of Marine Vehicles.* John Wiley & Sons, New York, USA.

BMT Fluid Mechanics Limited (2011). BMT Global Wave Statistics Online - Worldwide Wave Database (http://www.globalwavestatisticsonline.com/cgi-bin/analysis.exe).

Bowker, J. A. (2018). *Coupled Dynamics of a Flapping Foil Wave Powered Vessel.* Phd thesis, University of Southampton.

Bowker, J. A., Townsend, N. C., Tan, M., and Shenoi, R. A. (2015). Experimental Study of a Wave Energy Scavenging System Onboard Autonomous Surface Vessels (ASVs). In *OCEANS 2015 - Genova*, Genoa, Italy. IEEE.

Bowker, J. A., Townsend, N. C., Tan, M., and Shenoi, R. A. (2016). Experimental Analysis of Submerged Flapping Foils; Implications for Autonomous Surface Vehicles

(ASVs). In *OCEANS 2016 MTS/IEEE Monterey, OCE 2016*, Monterey, CA, USA. IEEE.

Brooke, J. (2003). *Wave Energy Conversion: Elsevier Ocean Engineering Book Series Volume 6*. Elsevier Science Ltd, Kidlington, Oxford, UK.

Bryden, I. G., Couch, S. J., Owen, A., and Melville, G. (2007). Tidal Current Resource Assessment. *Proceedings of the Institution of Mechanical Engineers, Part A: Journal of Power and Energy*, 221(2):125–135.

Budar, K. and Falnes, J. (1975). A Resonant Point Absorber of Ocean-Wave Power. *Nature*, 256(5517):478–479.

Burman, K. and Walker, A. (2009). Ocean Energy Technology Overview. Technical report, U.S. Department of Energy, Golden, CO, USA.

Cameron, L., Doherty, R., Henry, A., Doherty, K., Hoff, J. V., Kaye, D., Naylor, D., Bourdier, S., and Whittaker, T. (2010). Design of the Next Generation of the Oyster Wave Energy Converter. *3rd International Conference on Ocean Energy*, pages 1–12.

Chen, H. M. and DelBalzo, D. R. (2013a). Circular-Slide Wave Energy Converter. In *Ocean Waves Workshop 2013*, pages 22–25, New Orleans, USA.

Chen, H. M. and DelBalzo, D. R. (2013b). Circular-Slide Wave Energy Converter in Random Waves. In *Oceans 2013 (IEEE)*, pages 4–8, San Diego, California, USA.

Cheung, J. T. and Childress, E. F. (2007). Ocean Wave Energy Harvesting Devices. Technical report, Teledyne Scientific & Imaging, LLC, Thousand Oaks, CA.

Clare, R., Evans, D. V., and Shaw, T. L. (1982). Harnessing Sea Wave Energy by a Submerged Cylinder Device. *ICE Proceedings*, 73(3):565–585.

Coe, R. G., Bacelli, G., Wilson, D. G., and Abdelkhalik, O. (2017). A Comparison of Control Strategies for Wave Energy Converters. *International Jonrnal of Marine Energy*, 20:45–63.

Como, S., Meas, P., Stergiou, K., and Williams, J. (2015). *Ocean Wave Energy Harvesting: Off-Shore Overtopping Design*. Undergraduate dissertation, Worcester Polytechnic Institute.

Cordonnier, J., Gorintin, F., De Cagny, A., Clément, A. H., and Babarit, A. (2015). SEAREV: Case Study of the Development of a Wave Energy Converter. *Renewable Energy*, 80:40–52.

Crowley, S., Porter, R., Taunton, D. J., and Wilson, P. A. (2018). Modelling of the WITT Wave Energy Converter. *Renewable Energy*, 115:159–174.

Crowley, S. H., Porter, R., and Evans, D. V. (2013). A Submerged Cylinder Wave Energy Converter. *Journal of Fluid Mechanics*, 716:566–596.

Crowley, S. H., Porter, R., and Evans, D. V. (2014). A Submerged Cylinder Wave Energy Converter with Internal Sloshing Power Take Off. *European Journal of Mechanics - B/Fluids*, 47:108–123.

Drew, B., Plummer, A. R., and Sahinkaya, M. N. (2009). A Review of Wave Energy Converter Technology. *Proceedings of the Institution of Mechanical Engineers, Part A: Journal of Power and Energy*, 223(8):887–902.

Durand, M., Babarit, A., Pettinotti, B., Quillard, O., Toularastel, J. L., and Clément, A. H. (2007). Experimental Validation of the Performances of the SEAREV Wave Energy Converter with Real Time Latching Control. In *Proceedings of 7th European Wave and Tidal Energy Conference*, Porto, Portugal.

Edelstein, W. A., Walcek, C. J., Cox, D. L., and Davis, L. C. (2003). Wind Energy. Technical report, American Physical Society.

Evans, D. V. and Falcão, A. F. d. O., editors (1986). *Hydrodynamics of Ocean Wave-Energy Utilization: IUTAM Symposium Lisbon/Portugal 1985.* Springer Berlin Heidelberg, Berlin, Heidelberg.

Evans, D. V., Jeffrey, D. C., Salter, S. H., and Taylor, J. R. M. (1979). Submerged Cylinder Wave Energy Device: Theory and Experiment. *Applied Ocean Research*, 1(1):3–12.

Fadaeenejad, M., Shamsipour, R., Rokni, S. D., and Gomes, C. (2014). New Approaches in Harnessing Wave Energy: With Special Attention to Small Islands. *Renewable and Sustainable Energy Reviews*, 29(January):345–354.

Faizal, M., Ahmed, M. R., and Lee, Y. H. (2014). A Design Outline for Floating Point Absorber Wave Energy Converters. *Advances in Mechanical Engineering*, 2014:1–18.

Falcão, A. F. d. O. (2010). Wave Energy Utilization: A Review of the Technologies. *Renewable and Sustainable Energy Reviews*, 14(3):899–918.

Falcão, A. F. d. O. (2014). *Modelling of Wave Energy Conversion.* Instituto Superior Técnico, Universidade de Lisboa, Lisboa.

Falnes, J. (2002). *Ocean Waves and Oscillating Systems - Linear Interactions Including Wave-Energy Extraction.* Cambridge University Press, Cambridge, United Kingdom.

Falnes, J. (2007). A Review of Wave-Energy Extraction. *Marine Structures*, 20(4):185–201.

Gebreslassie, M. G., Tabor, G. R., and Belmont, M. R. (2013). Numerical simulation of a new type of cross flow tidal turbine using OpenFOAM - Part I: Calibration of energy extraction. *Renewable Energy*, 50:994–1004.

Gebreslassie, M. G., Tabor, G. R., and Belmont, M. R. (2015). Investigation of the Performance of a Staggered Configuration of Tidal Turbines Using CFD. *Renewable Energy*, 80:690–698.

Hagerman, G. (1995). Wave Power. In Bisio, A. and Boots, S., editors, *Encyclopedia of Energy Technology and the Environment*, pages 2859–2907. John Wiley & Sons, Inc., New York, USA.

Heath, T. V. (2012). A Review of Oscillating Water Columns. *Philosophical Transactions. Series A, Mathematical, Physical, and Engineering Sciences*, 370(1959):235–245.

Henderson, R. (2006). Design, Simulation, and Testing of a Novel Hydraulic Power take-off System for the Pelamis Wave Energy Converter. *Renewable Energy*, 31(2):271–283.

Hernández, C. V., Telsnig, T., and Pradas, A. V. (2017). JRC Wind Energy Status Report 2016 Edition. Technical report, Joint Research Centre - Directorate for Energy, Transport and Clmate, Petten, Netherlands.

Hogben, N., Dacunha, N. M. C., and Olliver, G. F. (1986). *Global Wave Statistics*. British Maritime Technology Limited, Middlesex, UK.

Holthuijsen, L. H. (2007). *Waves in Oceanic and Coastal Waters*. Cambridge University Press, New York, USA, first edition.

IEA (2014). Technology Roadmap Solar Photovoltaic Energy. Technical report, International Energy Agency, Paris, France.

Inman, D. J. (2014). *Engineering Vibration*. Pearson Education Limited, Essex, England, fourth edition.

Journée, J. M. J. and Massie, W. W. (2001). *Offshore Hydromechanics*. Delft University of Technology, Delft, The Netherlands, first edition.

Kanki, H., Arii, S., Furusawa, T., and Otoyo, T. (2009). Development of Advanced Wave Power Generation System by Applying Gyroscopic Moment. In *Proceedings of the 8th European Wave and Tidal Energy Conference*, pages 280–283, Uppsala, Sweden.

Kaphengst, N. F., Toh, T. T., Mitcheson, P. D., Holmes, A. S., Wright, S. W., and Yeatman, E. M. (2012). Adaptive Load Synthesis for Autonomous Resonant Frequency Tuning of Electromagnetic Energy Harvesters. In *PowerMEMS 2012*, pages 420–423, Atlanta, GA, USA.

Karami, M. A. and Inman, D. J. (2012). Hybrid Rotary-translational Energy Harvester for Multi-axis Ambient Vibrations. In *Proceedings of the ASME 2012 Conference on Smart Materials, Adaptive Structures and Intelligent Systems*, Stone Mountain, Georgia, USA.

Khan, J. and Bhuyan, G. S. (2009). Ocean Energy: Global Technology Development Status. Technical report, International Energy Agency - Ocean Energy Systems, British Columbia, Canada.

Koh, S. J. A., Keplinger, C., Li, T., Bauer, S., and Suo, Z. (2011). Dielectric Elastomer Generators: How Much Energy Can Be Converted? *IEEE/ASME Transactions on Mechatronics*, 16(1):33–41.

Lagoun, M. S., Benalia, A., and Benbouzid, M. E. H. (2010). Ocean Wave Converters: State of the Art and Current Status. In *2010 IEEE International Energy Conference*, pages 636–641, Manama. IEEE.

Levitan, D. (2014). Why Wave Power Has Lagged Far Behind as Energy Source (https://e360.yale.edu).

Liquid Robotics Inc. (2018). Wave Glider - Energy Harvesting Ocean Robot (http://www.liquid-robotics.com/wave-glider/how-it-works).

Lloyd, A. R. J. M. (1989). *Seakeeping: Ship Behaviour in Rough Weather.* Ellis Horwood Ltd, Sussex, UK.

Lu, C. H., Wang, Y. J., Sung, C. K., and Chao, P. C. P. (2011). A Hula-Hoop Energy-Harvesting System. *IEEE Transactions on Magnetics*, 47(10):2395–2398.

Margheritini, L., Vicinanza, D., and Kofoed, J. P. (2007). Hydraulic Characteristics of Seawave Slot-Cone Generator Pilot Plant at Kvitsøy (Norway). In *7th European Wave and Tidal Energy Conference.*

Masuda, Y. (1971). Wave-activated Generator. In *International Collquium on the Exposition of the Oceans*, Bordeaux, France.

Masuda, Y. (1979). Experimental Full-scale Results of Wave Power Machine Kaimei in 1978. In *First Symposium on Wave Energy Utilization*, pages 349–363, Gothenburg, Sweden.

McCabe, A. P., Bradshaw, A., Meadowcroft, J. A. C., and Aggidis, G. (2006). Developments in the Design of the PS Frog Mk 5 Wave Energy Converter. *Renewable Energy*, 31(2):141–151.

McCormick, M. E. (2007). *Ocean Wave Energy Conversion.* Dover Publications, Inc., Mineola, New York, USA, dover edition.

McCormick, M. E. (2010). *Ocean Engineering Mechanics with Applications.* Cambridge University Press, Cambridge, UK.

Mitcheson, P. D., Toh, T. T., Wong, K. H., Burrow, S. G., and Holmes, A. S. (2011). Tuning the Resonant Frequency and Damping of an Electromagnetic Energy Harvester Using Power Electronics. *IEEE Transactions on Circuits and Systems II: Express Briefs*, 58(12):792–796.

Muetze, A. and Vining, J. G. (2006). Ocean Wave Energy Conversion - A Survey. In *Conference Record of the 2006 IEEE Industry Applications Conference 41st IAS Annual Meeting*, pages 1410–1417, Tampa, FL. IEEE.

Multon, B., editor (2012). *Marine Renewable Energy Handbook*. ISTE Ltd, London, UK.

National Grid (2006). Transmission and Wind Energy: Capture the Prevailing Winds for the Benefit of Customers. Technical report, National Grid plc.

Ocean Power Technologies Inc. Global Resources, Ocean Power Technologies Website (http://www.oceanpowertechnologies.com/resources.html).

Oceanlinx Ltd. Oceanlinx: Powering a Sustainable Future (http://www.oceanlinx.com).

Papini, G. P. R., Vertechy, R., and Fontana, M. (2013). Dynamic Model of Dielectric Elastomer Diaphragm Generators for Oscillating Water Column Wave Energy Converters. In *ASME 2013 Conference on Smart Materials, Adaptive Structures and Intelligent Systems*, volume 21, Snowbird, Utah, USA.

Priya, S. and Inman, D. J., editors (2009). *Energy Harvesting Technologies*. Springer US, Boston, MA.

Rahm, M. (2010). *Ocean Wave Energy - Underwater Substation System for Wave Energy Converters*. Phd dissertation, Uppsala Universitet, Uppsala, Sweden.

REN21 (2012). Renewables 2012 - Global Status Report. Technical report, Renewable Energy Policy Network for the 21st Century, Paris.

REN21 (2017). Renewables 2017 - Global Status Report. Technical report, Renewable Energy Policy Network for the 21st Century.

Ringwood, J. V., Bacelli, G., and Fusco, F. (2014). Control, Forecasting and Optimisation for Wave Energy Conversion. In *The 19th World Congress - The International Federation of Automatic Control*, pages 7678–7689, Cape Town, South Africa.

Rodrigues, L. (2008). Wave Power Conversion Systems for Electrical Energy Production. In *International Conference on Renewable Energies and Power Quality (ICREPQ'08)*, Santander, Spain.

Romero-Ramirez, E. (2010). *Energy Harvesting from Body Motion Using Rotational Micro-Generation*. Phd thesis, Michigan Technological University.

Ruellan, M., BenAhmed, H., Multon, B., Josset, C., Babarit, A., and Clement, A. (2010). Design Methodology for a SEAREV Wave Energy Converter. *IEEE Transactions on Energy Conversion*, 25(3):760–767.

Salter, S. H. (1974). Wave Power. *Nature*, 249(5459):720–724.

Salvesen, N., Tuck, E. O., and Faltinsen, O. (1970). Ship Motions and Sea Loads. *Transactions of the Society of Naval Architects and Marine Engineers*, (78):250–287.

Sharon, A., Briggs, J., and Wirz, H. (2011). Mobile Wave Energy Harvesting System. In *Clean Technology 2011*, Boston, MA.

Sun, X., Huang, D., and Wu, G. (2012). The Current State of Offshore Wind Energy Technology Development. *Energy*, 41(1):298–312.

Taylor, J. (2009). Edinburgh Wave Power Group - Evolution of Duck Full-scale Engineering Design (http://www.homepages.ed.ac.uk/v1ewaveg).

The Queen's University of Belfast (2002). Islay LIMPET Wave Power Plant. Technical report, The Queen's University of Belfast.

Thorpe, T. W. (1999). An Overview of Wave Energy Technologies: Status, Performance and Costs. In *Wave Power: Moving towards Commercial Viability*, number November, London, UK.

Toh, T. T., Mitcheson, P. D., Dussud, L., Wright, S. W., and Holmes, A. S. (2011). Electronic Resonant Frequency Tuning of a Marine Energy Harvester. In *PowerMEMS 2011*, pages 383–386, Seoul, Republic of Korea.

Townsend, N. C. (2016). Self-Powered Autonomous Underwater Vehicles: Results from a Gyroscopic Energy Scavenging Prototype. *IET Renewable Power Generation*, 10(8):1078–1086.

Townsend, N. C. and Shenoi, A. (2012). A Gyroscopic Wave Energy Recovery System for Marine Vessels. *IEEE Journal of Oceanic Engineering*, 37(2):271–280.

Townsend, N. C. and Shenoi, A. (2013). Recharging Autonomous Underwater Vehicles from Ambient Wave Induced Motions. In *Oceans 2013 (IEEE)*, pages 2159–2168, San Diego, California, USA.

Townsend, N. C. and Shenoi, R. A. (2016). Feasibility Study of a New Energy Scavenging System for an Autonomous Underwater Vehicle. *Autonomous Robots*, 40(6):973–985.

University of Southampton (2018). Human Factors Research Unit - Laboratory Facilities (https://www.southampton.ac.uk/hfru/laboratory-facilities/index.page).

Vertechy, R. and Fontana, M. (2015). Dielectric Elastomers for Wave Energy Harvesting. *SPIE Newsroom*, pages 148–156.

Vertechy, R., Fontana, M., Papini, G. P. R., and Bergamasco, M. (2013). Oscillating-Water-Column Wave-Energy-Converter based on Dielectric Elastomer Generator. In Bar-Cohen, Y., editor, *Electroactive Polymer Actuators and Devices (EAPAD) 2013*, volume 8687, San Diego, California, USA.

von Sydow, T. (2014). *Investigating the Impact of Wave Energy in the Electric Power System - A Case Study of Southern Sweden.* Master thesis, Chalmers University of Technology, Göteborg, Sweden.

Wang, Y. J. and Hao, Y. T. (2014). Harvesting Energy from Ship Rolling Using an Eccentric Disk Revolving in a Hula-hoop Motion. In *2014 International Power Electronics Conference (IPEC-Hiroshima 2014 - ECCE ASIA)*, pages 1420–1424, Hiroshima. IEEE.

Washio, Y., Osawa, H., and Ogata, T. (2001). The Open Sea Tests of the Offshore Floating Type Wave Power Device “Mighty Whale” - Characteristics of Wave Energy Absorption and Power Generation. *MTS/IEEE Oceans 2001. An Ocean Odyssey. Conference Proceedings (IEEE Cat. No.01CH37295)*, 1:579–585.

Waters, R. (2008). *Energy from Ocean Waves - Full Scale Experiment Verification of a Wave Energy Converter.* Phd dissertation, Uppsala Universitet, Uppsala, Sweden.

Waters, R., Stålberg, M., Danielsson, O., Svensson, O., Gustafsson, S., Strömstedt, E., Eriksson, M., Sundberg, J., and Leijon, M. (2007). Experimental Results from Sea Trials of an Offshore Wave Energy System. *Applied Physics Letters*, 90(3):10–13.

Watkins, R. (2013). *The Origin of Self-Winding Watches 1773-1779.* Ligare, Australia.

Wave Energy Centre (WavEC) (2006). OWC Pico Wave Power Plant Website (http://www.pico-owc.net).

WITT Energy Ltd. (2018). WITT Energy Website (http://www.witt-energy.com).

Xie, L., Menet, C. G., Ching, H., and Du, R. (2009). The Automatic Winding Device of a Mechanical Watch Movement and Its Application in Energy Harvesting. *Journal of Mechanical Design*, 131(7):071005.

Xu, X. (2005). *Nonlinear Dynamics of Parametric Pendulum for Wave Energy Extraction.* PhD thesis, University of Aberdeen.

Yan, H. S. and Wang, H. T. (2007). Configuration Design of Novel Manually Operated Dynamo Flashlights. *Journal of Advanced Mechanical Design, Systems, and Manufacturing*, 1(5):616–627.

Yeatman, E. M. (2006). Rotating and Gyroscopic MEMS Energy Scavenging. In *International Workshop on Wearable and Implantable Body Sensor Networks (BSN’06)*, pages 42–45, Cambridge, MA. IEEE.

Yeatman, E. M. (2008). Energy Harvesting from Motion Using Rotating and Gyroscopic Proof Masses. *Proceedings of the Institution of Mechanical Engineers, Part C: Journal of Mechanical Engineering Science*, 222(1):27–36.

Yerrapragada, K., Ansari, M. H., and Karami, M. A. (2017). Enhancing Power Generation of Floating Wave Power Generators by Utilization of Nonlinear Roll-Pitch Coupling. *Smart Materials and Structures*, 26(9).

Zheng, C., Shao, L., Shi, W., Su, Q., Lin, G., Li, X., and Chen, X. (2014). An Assessment of Global Ocean Wave Energy Resources Over the Last 45 A. *Acta Oceanologica Sinica*, 33(1):92–101.

Zhu, D. (2011). Vibration Energy Harvesting: Machinery Vibration, Human Movement and Flow Induced Vibration. In Tan, Y. K., editor, *Sustainable Energy Harvesting Technologies - Past, Present and Future*, pages 25–54. InTech Europe, Rijeka, Croatia.